University of Mons
Faculty of Engineering

UMONS

Understanding of rock cutting mechanism under confinement

Nicolas Gonze

Thesis presented on 30th September 2022 for the degree of
PhD in Engineering Sciences & Technology

Jury

Prof. Edouard RIVIÈRE-LORPHEVRE, UMONS, Chairman
Prof. Jean-Pierre TSHIBANGU, UMONS, Supervisor
Prof. Fanny DESCAMPS, UMONS, Secretary
Prof. Frédéric COLLIN, ULiège, Member
Dr. Pascal LONGUEMARE, Ifpen-Paris, Member

In memory of my grandfather

Lionel Duwez alias Baba

Acknowledgements

First and foremost, I am incredibly grateful to my supervisor, Professor Jean-Pierre Tshibangu, who gave me the opportunity to achieve the beautiful journey of the PhD thesis. I have benefited greatly from your immense knowledge and rich experience helped me to grow as a scientist and also as a person.

I would like to express my sincere gratitude to the members of my accompanying committee, Prof. Edouard Rivière-Lorphèvre (UMONS), Prof. Frédéric Collin (ULiège), and Prof. Fanny Descamps (UMONS), the members of my thesis committee for their insightful comments and suggestions provided throughout this thesis. I also thank Dr. Pascal Longuemare (Ifpen), who accepted to be part of my thesis Jury.

I also thank all the members of the mining engineering department for the excellent atmosphere and their goodwill. I especially want to thank Fanny, with whom I had the chance to share the office. She offered me a calm and peaceful working environment where it was always possible to discuss, during the afternoon cookie, our latest recipes or the newest restaurants we tried.

As an assistant under mandate, I also want to thank the students I supervised during these years for different projects or master thesis. Even if they were not aware of it, they were often my breathing space during this long journey.

I would like to express my gratitude to the members of my family and especially my parents, who have always trusted me since I was young and who have never ceased to support me throughout all the steps of my life. Thanks to my brother Kevin for his encouragement; I miss our lunches since you left university. I also thank my friends for their encouragement

Finally, I would like to express my special thanks to my wife, Camille. You are the one who has experienced all the ups and downs of this journey but you have never stopped supporting me. Thank you for constantly listening to me rant, talk and doubt and for proofreading me over and over again. I think you even know my thesis better than I do now...

Abstract

Since the income of PDC (Polycrystalline Diamond Compact) drill bits, understanding the cutting mechanism of rocks has always been an important issue for optimizing drilling performances. However, while the depths reached by wells get deeper and deeper, it appears that the understanding of this destruction mechanism with high-depth conditions is not yet fully mastered.

Research in this field is mainly based on experimental and numerical methods. Among numerical ones, the Discrete Element Method has already shown promising results. Therefore, this numerical method has been implemented in this thesis to address the problem of the evolution of the cutting mechanism in high-depth conditions with a focus on the effects of confinement.

To address this issue, this thesis addressed firstly the calibration of a numerical model representing as accurately as possible the behavior of the Vosges Sandstone, chosen as the reference rock. For this purpose, a calibration protocol based on uniaxial and polyaxial tests has been developed. Then, the effects of confinement and cutting parameters were studied. The objective was twofold: on the one hand, to better understand the evolution of the cutting mechanism under confinement and, on the other hand, to ensure the accuracy of the numerical results compared to the experimental ones.

The results of this thesis are interesting for several reasons. Firstly, the new calibration procedure allowed to determine numerical parameters reproducing the evolution of the Vosges Sandstone behavior. Secondly, the comparative analysis of the numerical results with the experimental ones highlighted their qualitative and quantitative consistency. Thirdly, this thesis highlighted the evolution of the cutting mechanism as a function of the two essential parameters, the confinement and the depth of cut. While the mechanism is generally considered to be composed of two regimes, the existence of three distinct regimes is demonstrated, namely: friction, brittle, and ductile regimes. The boundaries of these regimes are governed by rock behavior, confinement, and cutting parameters

Finally, an analytical model that estimates the Optimal Specific Energy of cutting according to the confinement is proposed. This model is based on rock properties and a parameter characterizing the rock-tool interaction.

Résumé

Depuis la création des outils PDC (Polycrystalline Diamond Compact), la compréhension du mécanisme de coupe des roches a toujours été un enjeu important en vue d'optimiser les performances de forage. Cependant, à l'heure où les forages atteignent des profondeurs de plus en plus importantes, il apparaît que la compréhension de l'évolution du mécanisme de coupe en conditions de grandes profondeurs n'est pas encore complètement maîtrisée.

Les recherches dans ce domaine s'axent essentiellement sur des méthodes expérimentales et numériques. Parmi les secondes, la méthode des éléments discrets a déjà montré des résultats encourageants. Cette méthode numérique a donc été sélectionnée pour répondre à la problématique du mécanisme de coupe en conditions de grandes profondeurs, en se concentrant sur les effets du confinement.

Pour répondre à cette problématique, la première étape fut de retranscrire dans le modèle numérique l'évolution du comportement du Grès des Vosges, choisi comme roche de référence, en fonction du confinement. A cette fin, un protocole de calibration basé sur des essais uniaxiaux et polyaxiaux a été mis au point.
Par la suite, les effets du confinement et des paramètres de coupe ont été étudiés. L'objectif était double : d'une part, mieux comprendre l'évolution du mécanisme de coupe sous confinement et d'autre part, s'assurer de la représentativité des résultats numériques par rapport aux résultats expérimentaux.

Les résultats obtenus sont intéressants à plus d'un titre.
Premièrement, la procédure de calibration a permis de déterminer les paramètres numériques reproduisant l'évolution du comportement du Grès des Vosges. Deuxièmement, l'analyse comparative des résultats a mis en évidence leur cohérence aussi bien qualitative que quantitative par rapport aux résultats expérimentaux. Troisièmement, les résultats ont permis de mettre en évidence l'évolution du mécanisme de coupe en fonction des deux paramètres essentiels que sont le confinement et la profondeur de coupe. Alors que généralement, le mécanisme est considéré comme étant composé de deux régimes, l'existence de trois régimes distincts est démontrée, à savoir : le frottement, le régime fragile et le régime ductile. Les limites entre ces régimes sont dictées par le comportement de la roche, le confinement et les paramètres de coupe.

Enfin en se basant sur les résultats obtenus, une première ébauche d'un modèle analytique permettant d'estimer l'Energie Spécifique Optimale en fonction du confinement est proposée. Celui-ci se base sur les propriétés mécaniques du matériau étudié ainsi que sur un paramètre caractérisant l'interaction roche-outil.

Table of contents

Table of contents ..... *i*

List of figures ..... *v*

List of tables ..... *xiii*

Nomenclature ..... *xv*

Chapter I Introduction *1*

1 Background **1**

2 Problem statement and objectives of the thesis **2**

2.1 Position of the problem 2

2.2 Previous research in the Mining Department of the UMONS – FPMs 2

2.3 Objectives of the thesis 3

3 Outline of the thesis **4**

Chapter II State of the art *5*

1 Drilling generalities **6**

1.1 Rotary drilling 6

1.2 Extreme Drilling 7

1.3 Drill bits 9

2 Rock behavior in high-depth conditions **13**

2.1 Definition of high-depth conditions 13

2.2 Evolution of rock behavior with confinement 15

2.3 Effects of pore pressure on rock behavior 21

2.4 Effects of temperature on rock behavior 23

2.5 Thermo-hydro-mechanical coupling 25

3 Rock cutting mechanism **26**

3.1 Characteristics of rock cutting mechanism in drilling 26

3.2 Rock cutting mechanism in atmospheric conditions 32

3.3 Rock cutting mechanism under confinement 59

3.4 Rock cutting mechanism in real drillings conditions 77

4 Conclusions **80**

Chapter III Methodology 83

1 Research approach 83
1.1 Numerical method choice 84
1.2 Reference rock choice 85

2 Discrete Element Method in PFC 86
2.1 Calculation cycle 86
2.2 Constitutive models 87
2.3 Calibration of constitutive models 91

3 Vosges Sandstone description 92
3.1 Petrophysical properties 92
3.2 Geomechanical properties 93

4 Research steps 96

Chapter IV Calibration, building and validation of rock cutting models 97

1 Calibration of synthetic rock models 97
1.1 Constitutive model choice 97
1.2 Calibration procedure building 100
1.3 Failure envelope of 3D synthetic rock model 105

2 Rock cutting models 107
2.1 Conceptual model of rock cutting under confinement 107
2.2 Two-dimensional rock cutting model 108
2.3 Three-dimensional rock cutting model 113

3 Quantities determined from cutting forces 119

4 Validation of rock cutting models 122
4.1 Laboratory tests 122
4.2 Numerical models of slab test 123
4.3 Results of the validation process 124

5 Simulation protocols 126

Chapter V Results of numerical modeling 131

1 The effects of the confinement on the rock cutting mechanism 131
1.1 Evolution of destruction mechanism 132
1.2 Evolution of cutting forces 136
1.3 Evolution of Specific Energy 138

2 The effects of cutting parameters 139
2.1 Impact of the depth of cut 139
2.2 Impact of the side rake angle 141
2.3 Impact of the back rake angle 144

3 The cutter geometry effects on the rock cutting mechanism 146
3.1 2D modeling 146
3.2 3D modeling 147

4 The groove geometry effects on rock cutting mechanism 155
4.1 Case of fully overlapped grooves 155
4.2 Case of partially overlapped grooves 156

5 Summary 157

Chapter VI Comparative analyses and interpretations 161

1 Comparative analyses 161
1.1 Cutting forces 162
1.2 Impact of cutting parameters 164
1.3 Impact of cutter geometries 166
1.4 Evolution of E with confinement 166
1.5 Conclusions of comparative analyses 167

2 Interpretations 168
2.1 Evolution of cutting mechanism with confinement 168
2.2 Optimal depth of cut 170
2.3 Evolution of cutting energies with confinement 173
2.4 Attempt to model the evolution of the Optimal Specific Energy versus confinement 174

3 DEM models as a tool to optimize cutting parameters 178

Chapter VII Conclusions and outlook 179

1 General conclusions 179

2 Outlook 181
2.1 Validation of the methodology and results 182
2.2 Integration of thermo-hydro-mechanical coupling in cutting models 182
2.3 Transposition of the results to the drill bit scale 182
2.4 Application of the work methodology to other destruction mechanisms 183

References 185

Appendices I

Appendix A: database of numerical studies dealing with rock cutting I

Appendix B: calibration procedure XII

Appendix C: results of 3D numerical modeling XVIII

List of figures

Figure II.1. Simplified representation of a drilling rig (modified from Leine and Van Campen (2005)). _____ *6*

Figure II.2. The worldwide deep wells and extended-reach wells (Ma et al., 2016). *7*

Figure II.3. Simplified views of punching and cutting mechanism involved by drilling bits. _____ *9*

Figure II.4. Example of roller-cone bits with a Tungsten Carbide Insert bit on the left and a Milled-Tooth bit on the right. _____ *10*

Figure II.5. Different types of fixed cutters bits (Menand, 2001). _____ *11*

Figure II.6. Measured horizontal and vertical stresses around the world. (a) Evolution of the vertical stress with the depth. (b) Evolution of the stress ratio K with the depth (from Brown and Hoek (1978)). _____ *14*

Figure II.7. Pore pressure gradient. _____ *14*

Figure II.8. Illustration of brittle to ductile transition with increasing confining pressure (modified from Helmons (2017)). _____ *16*

Figure II.9. Theoretical rock behavior evolution from brittle to hardening one with the increase of confinement (modified from Yu et al. (2019)). _____ *17*

Figure II.10. Brittle fracture modes. _____ *18*

Figure II.11. Coalescence of microcracks in a shear band (modified from Winterwerp and van Kesteren (2004)). _____ *19*

Figure II.12. Evolution of the volumetric strain with respect to the confinement. At confinement up to 40 MPa, Vosges Sandstone exhibits a dilatant behavior at failure and above this confinement the behavior is dilatant (Bésuelle et al., 2000). _____ *20*

Figure II.13. Mohr diagram showing possible modes of failure, fracturing and brittle-ductile deformation (modified from Nygård et al. (2006)). _____ *21*

Figure II.14. Mohr diagram including Mohr-Coulomb failure envelope. Increasing fluid pressure shifts the initial stress state closer to the failure envelope. _____ *22*

Figure II.15. Effect of pore pressure (given in MPa by the numbers on the curves) on the stress-strain behavior of a limestone tested at a constant confining pressure of 69 MPa (after Robinson, in Brady and Brown, 2004). _____ *23*

Figure II.16. Stress-strain curve and failure photographs of rock samples as a function of temperature: (a) sandstone samples, (b) marble samples, (c) granite samples, and (d) failure photograph (Gu et al., 2020). _____ *24*

Figure II.17. Thermo-hydro-mechanical coupling (modified from Descamps (2007)). _____ *25*

Figure II.18. 2D schematic view of the cutting parameters. _____ *27*

*Figure II.19. Definition of negative and positive rake angle.*_____ *27*

*Figure II.20. Illustration of non-planar cutters: (a) Conical cutter, (b) Axe cutter and (c) 3-RDE cutter (Liu et al., 2019).*_____ *31*

*Figure II.21. Schematic views of scratching (left) and chipping (right) cutting regimes and associated force signals. Modified from Richard et al. (2012).*_____ *32*

Figure II.22. Destruction cycle in chipping regime and associated force signal (Richard, 1999a). _____ *33*

Figure II.23. Evolution of cutting mechanism from grinding to chipping, after Chaput (1991). _____ *35*

Figure II.24. Evolution of cutting forces with the depth of cut: (a), data from Richard et al. (1998) obtained with rectangular cutters and (b), data from Doshvarpassand et al. (2017) with the cutting surface for circular cutters. _____ *36*

Figure II.25. Schematic evolution of cutting force (black line) and Specific Energy (green line) with the depth of cut (modified from He and Xu (2016)). _____ *37*

Figure II.26. Evolution of the Specific Energy with the depth of cut: (a), data from Cheng et al. (2018) and (b), data from Rajabov et al. (2012). _____ *38*

Figure II.27. Traditional relationship between Rate of Penetration and Weight on Bit. _____ *39*

Figure II.28. Normalized Specific Energy at different back rake angles (Rostamsowlat et al., 2018b). _____ *40*

Figure II.29. The flow of the crushed material (cuttings) at different back rake angles in scratching mode (Rostamsowlat et al., 2018b). _____ *40*

Figure II.30. Evolution of Specific Energy with side rake angle. Tests were performed on Carthage marble at a depth of cut of 1.15 mm (Rajabov et al., 2012). _____ *41*

Figure II.31. Laboratory test results of a six bladed PDC bit in Carthage limestone during increasing stages of wear (Sinor et al., 1998). _____ *43*

Figure II.32. Impact of cutter wear: (a) Rate of penetration (V) versus Weight on Bit (W), (b) Evolution of E-S diagram with the cutter wear (Dagrain and Richard, 2006a). _____ *43*

*Figure II.33. Variation of the tangential cutting force component with the vertical position of the cutter at atmospheric pressure on the Vosges Sandstone (Amri et al., 2016).*_____ *44*

Figure II.34. Decomposition of the total force applied on the cutter in Detournay & Defourny (1992) model. _____ *46*

Figure II.35. Theoretical E-S diagram of Detournay and Defourny (a) and E-S Diagram based on results of Glowka (1989) (b). Images modified from Dagrain (2001). _____ *47*

Figure II.36. Cutting model of Wojtanowicz & Kuru (1993). _____ *48*

Figure II.37. Cutting model of Pelfrene (2010). _____ *50*

Figure II.38. Cracks propagation and chip formation with FEM based on LEFM (Ingraffea, 1987). _____ *53*

*Figure II.39. Continuous mining simulation with 3D FEM: (a) total model, (b) grooves geometry and (c) deleted rock element highlighted in red (Yu, 2005).*___ *53*

Figure II.40. Comparison of fracture patterns (a) in scratching mode (b) in chipping mode (Jaime, 2011). _____ *54*

Figure II.41. Cutting simulations with FEM in scratching mode in (a) 2D linear cutting and (b) 3D circular groove cutting (Fontoura et al., 2012). _____ *55*

Figure II.42. Numerical results obtained by Huang et al. (1999) with Discrete Element Method: (a) and (b) show the transition between scratching and chipping mode and (c) plots the evolution of maximum and mean cutting forces with respect to the depth of cut. _____ *56*

*Figure II.43. 3D DEM modeling of rock cutting tests (a) in groove mode (Rizo, 2013) and (b) in slab mode (Lin et al., 2012).*_____ *57*

*Figure II.44. Sketch of the Single Cutter Tester of Mines ParisTech laboratory (Pelfrene et al., 2011).*_____ *59*

Figure II.45. 3D representation of single cutter test under confinement. _____ *60*

Figure II.46. Cuttings morphology obtained during (a) test in atmospheric conditions and (b), under a confinement of 3.44 MPa. Depth of cut was not mentioned by authors (Kaitkay and Lei, 2005). _____ *60*

Figure II.47. Sides of cutting obtained under confinement (Rafatian et al., 2009). 61

Figure II.48. Schematic representation of cutting mechanism under pressurized conditions (Rafatian et al., 2009). 62

Figure II.49. Evolution of the cutting forces and Specific Energy with respect to the confinement obtained by: (a), Kaitkay & Lei (2005) and (b), Rafatian et al. (2009). 63

Figure II.50. Impact of cutting parameters on rock cutting under confinement: (a) impact of depth of cut (Akbari and Miska, 2017), (b) impact of back rake angle (Rajabov et al., 2012). 63

Figure II.51. Cutting Model of Cheatham & Daniels (1979). 64

Figure II.52. Cutting model of Detournay & Atkinson (2000). 65

Figure II.53. Cutting model of Sellami (1990). 68

Figure II.54. Cutting model of Gerbaud et al. (2006). 69

Figure II.55. Cuttings formation for cutting simulations with DEM: (a) at atmospheric conditions and (b) under a confinement of 34.5 MPa (Lei and Kaitkay, 2003). 72

Figure II.56. Comparison of tangential cutting forces between experimental and simulation results (Lei and Kaitkay, 2003). 73

Figure II.57. Stress versus axial and volumetric strain curves of the generated PFC rock model by Ledgerwood III (2007). 73

Figure II.58. PFC cutting simulation at (a) atmospheric pressure, and (b) 20 MPa (Ledgerwood III, 2007). 74

Figure II.59. Comparison of MSE calculated results and testing CCS in vertical section (Chen et al., 2018). 78

Figure II.60. Comparison of MSE calculated results and testing CCS in horizontal section (Chen et al., 2018). 79

Figure III.1. Time-stepping algorithm implemented in DEM (Itasca Consulting Group, 2008b). 87

Figure III.2. Components at contacts. 88

Figure III.3. Rheological model of the different components constituting contact model at ball-ball contact. 88

Figure III.4. Graphical representation of contact behavior in the shear direction. 89

Figure III.5. force-displacement behavior between two particles when contact bond is activated. 90

Figure III.6. The polyaxial device of the Mining Department of UMONS: (a) Full device with polyaxial cell, hydraulic bench and computer and (b) cross-section of the cell. Modified from Descamps (2007). 93

Figure III.7. Stress-strain curves of the Vosges sandstone under conventional triaxial compression conditions. Data from Descamps (2007). _____ *94*

Figure III.8. Failure envelopes of Vosges Sandstone: (a) 2D envelope in Mohr plane and (b) 3D envelope according to the Mohr-Coulomb criterion in three-dimensional principal stresses plane. Modified from Descamps (2007). _____ *95*

Figure IV.1. Rheological model of Bonded Particle Model. The parallel bond part is represented in black, while the linear contact model is in grey. _____ *98*

*Figure IV.2. Constitutive behavior of the Bonded Particle Model in shear and tension when particles are bonded (A is the cross-section of the parallel bond).*_____ *99*

*Figure IV.3. Triaxial tests environment in 2D (a) and 3D (b).*_____ *101*

Figure IV.4. Calibration procedure based on uniaxial and triaxial tests used to find micro-properties of DEM model. _____ *102*

Figure IV.5. Strain-stress curve of uniaxial and triaxial tests obtained at the end of the calibration process compared to experimental ones. _____ *104*

Figure IV.6. Failure envelope of synthetic 3D rock model (black lines) of Vosges Sandstone compared to experimental one (dashed grey lines). _____ *106*

Figure IV.7. Conceptual model of rock cutting under confinement used to build numerical models. _____ *107*

Figure IV.8. 2D model of rock cutting. _____ *108*

*Figure IV.9. Cutter geometries used for 2D simulations: (a) sharp cutter, (b) chamfered cutter, (c) blunt cutter.*_____ *109*

*Figure IV.10. Implementation of confinement in 2D models: (a) membrane at the beginning of the test and orientation of the pressure along the surface and (b) evolution of the membrane during the test.*_____ *110*

Figure IV.11. Raw 2D cutting force signals. _____ *111*

Figure IV.12. Snapshots of 2D cutting modeling at different length of cut: (a) 0.03 cm, (b) 0.77 cm, (c) 0.83 cm, and (d) 1.42 cm. _____ *112*

Figure IV.13. 2D cutting force signals after processing. _____ *113*

Figure IV.14. 3D model of rock cutting: the three-particle colors represent the three size distribution zones. _____ *114*

Figure IV.15. Cutter geometries used for 3D simulations: (a) sharp circular cutter, (b) circular chamfered cutter, (c) rectangular sharp cutter, (d) rectangular chamfered cutter, and (e) rectangular blunt cutter. _____ *115*

Figure IV.16. Schematic view of the shining lamp-algorithm. Applied particle forces (F) are proportional to the projected areas (A_i). Light grey particles are not illuminated. _____ *116*

Figure IV.17. Raw 3D cutting force signals from the cutting face of a circular cutter. _____ *117*

Figure IV.18. Number of cracks evolution during 3D cutting simulation. _____ *117*

Figure IV.19. 3D cutting force signals for each face of a circular chamfered cutter and their summation. _____ *118*

Figure IV.20. Determination of mean tangential and normal cutting forces based on force signals. _____ *119*

Figure IV.21. Active surface for a rectangular cutter. _____ *120*

Figure IV.22. Active surface for a circular cutter. _____ *121*

Figure IV.23. Slab tests: (a) fake 3D representation of 2D rock cutting simulation by DEM, (b) Schematic view of a slab test (Dagrain et al., 2001), (c) slab tests performed in the laboratory. _____ *122*

Figure IV.24. Rock Strength Device used to perform slab tests. _____ *123*

Figure IV.25. The 3D model used to simulate slab tests. _____ *124*

Figure IV.26. Validation of cutting models through slab tests in atmospheric conditions. _____ *125*

Figure IV.27. Comparison between scratching (A (Richard, 1999) and B) and chipping (C (Richard, 1999) and D) destruction mechanisms observed in lab and during numerical modeling. _____ *125*

Figure IV.28. Schematic diagrams of cutting simulations of overlapping groove: (a) same path but different depth (b) partial overlap at the same cutting depth. ____ *129*

Figure V.1. Evolution of cutting mechanism at 0.5 (a, b, c) and 1.5 mm (d, e, f) depth of cut for different confinements: (a) and (d) = atmospheric conditions; (b) and (e) 10 MPa confinement; (c) and (f) 30 MPa confinement. _____ *132*

Figure V.2. Formation of a ribbon of crushed rock during the simulation at a depth of cut of 1.5 mm and confinement of 30 MPa. _____ *134*

Figure V.3. Evolution of crack numbers during tests at different confinements for cutting tests at 1.5 mm depth of cut. _____ *135*

Figure V.4. Registered cutting forces during simulations at 0.5 and 1.5 mm depth of cut and confinement of 0, 20, and 40 MPa. _____ *136*

Figure V.5. Evolutions of mean tangential cutting force and its standard deviation versus confinement at a depth of cut of (a) 0.5 mm and (b) 1.5 mm. _____ *137*

Figure V.6. Evolution of Specific Energy versus confinement for different depths of cut. _____ *138*

Figure V.7. Evolution of mean and maximum cuttings forces and Specific Energy versus depths of cut and confinements. _____ *140*

Figure V.8. Evolutions of normalized Specific Energy and distribution of tangential cutting force between cutting and lateral faces of the cutter depending on the side rake angle for different values of confinement and depth of cut. _____ *142*

Figure V.9. Evolutions of normal cutting force between cutting and lateral faces of the cutter depending on the side rake angle for different values of confinement and depth of cut. _____ *143*

Figure V.10. Effects of side rake angle (ωs) on the exposition on the lateral face of the circular cutter during a linear cutting test. The blue line represents the 0.5 mm depth of cut, while the red one represents the 1.5 mm depth of cut. _____ *144*

Figure V.11. Evolution of normalized Specific Energy and Aggressiveness depending on the back rake angle. _____ *145*

Figure V.12. Distribution of the contact forces near the cutting face of sharp (a), chamfered (b) and wear cutters (c) in atmospheric conditions. _____ *146*

Figure V.13. Comparison between Specific Energies developed by circular and rectangular cutters under the same test conditions (depths of cut and confinements). _____ *147*

Figure V.14. Comparison of the evolution of Specific Energy versus depth of cut for circular and rectangular cutters in atmospheric and under 20 MPa of confinement. _____ *149*

Figure V.15. Distribution of tangential and normal forces on the different faces of a circular cutter for tests performed under atmospheric conditions and confinement of 20 MPa. _____ *152*

Figure V.16. Ft - Fn diagrams built from simulations carried out with increasing wear flat length for depths of cut of 1 and 2 mm and confinements of 0, 20, and 40 MPa. _____ *154*

Figure V.17. Cross-section of the model after the first cut exhibiting damage to the material under the surface of the groove by the loss of parallel bonds (represented by black lines). _____ *156*

Figure VI.1. Comparison between (a - c) experimentally (Che et al. (2016) - Kaitkay and Lei (2005)) and (b - d) numerically measured forces under atmospheric conditions and under confinement. _____ *162*

Figure VI.2. Evolution of Specific Energy with the depth of cut: (a) experimental results on Carthage Marble (Akbari and Miska, 2017), (b) numerical ones. ___ 164

Figure VI.3. Impact of the back rake angle on the Specific Energy: (a) experimental results on Carthage Marble (Rajabov et al., 2012) and (b) numerical ones.____ 165

Figure VI.4. Impact of the side rake angle on the Specific Energy: (a) experimental results on Carthage Marble (Rajabov et al., 2012) and (b) numerical ones.____ 165

Figure VI.5. Diagram of the evolution of the cutting mechanism for Vosges Sandstone according to the confinement and the depth of cut. _____ 169

Figure VI.6. Curve fitting of the evolution of Specific Energy with confinement for different confinement values. _____ 171

Figure VI.7. Graphical representation of the evolution of the optimum depth of cut with the confinement based on numerical simulations. _____ 172

Figure VI.8. Evolution of the optimum Specific Energy with the confinement. The discontinued grey line is the curve fitting of the data, while orange and purple ones are two segments piecewise model._____ 173

Figure VI.9. Mohr-Coulomb criterium of numerical model in (τ, σ) and ($\sigma 1$, $\sigma 3$) planes. _____ 174

Figure VI.10. Schematic representation of the model determining the evolution of the optimal Specific Energy with the confinement._____ 175

Figure VI.11. Analytical model of the evolution of the Optimal Specific Energy with the confinement compared to simulation data._____ 177

Figure VI.12. 3D mappings of E (a -b) and Fn (c-d) for a fixed confinement of 20 MPa. _____ 178

List of tables

Table II-1. Brittle-ductile transitions: some examples observed in triaxial compression tests at room temperature (Paterson and Wong, 2005; Cai, 2009). _ 17

Table III-1. Results of polyaxial tests on Vosges Sandstone. Data from Descamps (2007). _____ 95

Table IV-1. Definition of micro-properties of the Bonded Particles Model. _____ 99

Table IV-2. Links between macro and micro -properties of PFC models using Bonded-Particle Model. _____ 103

Table IV-3. Parallel bond's micro-properties to create synthetic Vosges Sandstone models._____ 104

Table IV-4. Comparison of compressive strength and Young's modulus between calibrated models and Vosges Sandstone. _____ 105

Table IV-5. Comparison between compressive strength and Young's modulus values obtained with the calibrated model and the laboratory tests from Descamps (2007). _____ 105

Table IV-6. Comparison of failure envelope parameters of Vosges Sandstone and 3D model. _____ 106

Table IV-7. Cutting parameters used during the first phase of simulations to study the effect of confinement on the rock cutting mechanism. _____ 126

Table IV-8. Cutting parameters used during the second phase of simulations to study the relative effect of confinement and cutting parameters on the cutting mechanism. _____ 127

Table IV-9. Geometrical parameters used in the third phase of simulation to study the impact of cutter shape on cutting mechanisms in 2D models. _____ 127

Table IV-10. Geometrical parameters used in the third phase of simulation to study the impact of cutter shape on cutting mechanisms in 3D models. _____ 128

Table V-1. Comparison of mean DOCs and active surface between circular and rectangular cutters for different theoretical DOCs. _____ 148

Table V-2. Evolution of E and M depending on the chamfer length and the depth of cut for circular cutters. _____ *150*

Table V-3. The proportion of the active surface covered by the cutting face and the chamfer, depending on the cutter geometry, the chamfer length, and the depth of cut. _____ *151*

*Table V-4. Effects on the chamfer length of circular cutter on E and M.*_____ *153*

Table V-5. Comparison of Specific Energy and Aggressiveness between first and second run of the fully overlapped groove at different confinement values. ____ *155*

Table V-6. Comparison of Specific Energy and Aggressiveness for each overlapping scenario. _____ *157*

Table VI-1. Comparison of tangential cutting force between simulations and various lab tests available in the literature. _____ *163*

Table VI-2. Friction coefficient μ between the wear flat and the rock for different confinements and depths of cut. _____ *166*

Table VI-3. Evolution of the optimum depth of cut and its associated Specific Energy with the confinement. _____ *172*

Nomenclature

A_c	Cross section of the groove
A_f	Wear flat area
A_{ch}	Chamfer surface area of cut
b	Biot coefficient
c	Cohesion
$CONF$	Confinement
C_f	Fluid compressibility
$c_{n(s)}$	Normal (shear) viscous damping at contact
C_S	Circular segment of the cutter in contact with the rock
d	Depth of cut
D	Cutter diameter
DOC	Depth of cut
$\mathcal{D}$	Diffusivity coefficient
e	Specific Energy of Teale
E	Specific Energy in rock cutting / Young's Modulus
E_c	Young Modulus at particles contact point
$\bar{E}_c$	Young Modulus of parallel bond
E_{norm_SR}	Normalized Specific Energy for side rake angle
E_{norm_BR}	Normalized Specific Energy for back rake angle
$E_{opt\_p_m}$	Optimum Specific Energy at confinement p_m

E_{i-j}	Coefficient of piecewise model in of Optimum Specific Energy for confinement comprises between i and j MPa.
EFF_m	Efficiency factor of drilling
F_{ij}^n	Normal force acting on particle i from j
F_{ij}^s	Shear force acting on particle i from j
$F_c^{n(s)}$	Normal (shear) strength of contact bond
F	Total cutting force
F_t	Tangential cutting force
F_n	Normal cutting force
F_l	Lateral cutting force
F^c	Force acting upon the cutting face
F^{ch}	Force acting upon the chamfer
F^f	Force acting upon the wear flat
F^b	Force acting upon the back cutter face
k	Permeability
k_{i-j}	Slope coefficient of Optimum Specific Energy model between i and j MPa of confinement
k_g	Projection factor of Gerbaud
k^s	Contact shear stiffness
$\bar{k}^s$	Parallel bond shear stiffness
K	Ratio between horizontal and vertical stress
k^n	Contact normal stiffness
$\bar{k}^n$	Parallel bond normal stiffness
L_{ch}	Chamfer length
m_i	Hoek Brown material constant
M	Cutter Aggressiveness
MSE	Mechanical Specific Energy

MSE_{adj}	Adjusted Mechanical Specific Energy
p	Pore pressure
p_m	Mud pressure
p_g	Ground pressure
p_0	Initial pore pressure
p_b	Pore pressure along the failure plane
p_b	Pore pressure along the failure plane
r_{ij}	Vector connecting the center of particle i with the contact point with particle j
q	Slope coefficient of Mohr-Coulomb envelope in σ_1-σ_3 plane
R	Ball/particle radius
R_c	Rock resistance to compression
R_{eq}	Rock equivalent strength
R_s	Rock resistance to shearing
R_p	Rock resistance to punching
ROP	Rate of penetration
$\bar{R}$	Radius of parallel bond
S	Drilling Strength
S_G	Section of the groove
U^n	Normal displacement component of contact displacement vector
U^s	Shear displacement component of contact displacement vector
V_c	Cutter velocity
W_c	Rectangular cutter width
WOB	Weight on bit
z	Depth
α	Local damping constant
ε	Intrinsic Specific Energy

$\bar{\lambda}$	Radius multiplicator of parallel bond
θ_f	Friction angle at the cutting face
μ	Friction coefficient at the wear flat
ν	Poisson ratio
φ	Internal friction angle
φ_{i-j}	Internal friction angle between i and j MPa of confinement
φ'	Friction angle between crushed rock and virgin rock
ϕ	Porosity
σ	Stress
σ'	Effective stress
σ_0	Rock equivalent strength
σ_h	Horizontal stress
σ_v	Vertical stress
σ_c	Uniaxial compressive strength
σ_t	Tensile Strength
$\bar{\sigma}_n$	Parallel bond tensile strength
$\bar{\sigma}_s$	Parallel bond shear strength
ψ	Chip failure angle
ω_c	Back rake angle
ω_s	Side rake angle
ω_{ch}	Chamfer angle
ω_d	Relief angle
ω_r	Repression angle
ω_p	Penetration angle

Chapter I Introduction

1 Background

The economic and industrial development of the last century has been driven by the increasing capacity to extract mineral resources from the earth's crust. Oil has been a significant component of this development among the various underground resources. Easily transportable and storable, oil became an essential energy source during the 20th century.

If oil has become predominant as an energy source over the last century, it is thanks to the continuous evolution of drilling techniques. Since the first commercial oil drilling in 1895 using the percussion drilling method, the techniques have never stopped to evolve. The first evolution was rotary drilling which improved drilling efficiency. Subsequently, the need to reach deep reservoirs that were more and more difficult to access led to directional, horizontal and deep drilling technique developments.

One example of this need for new techniques is the development of offshore oil fields. To reduce the number of drilling platforms required, the reuse of the platform was implemented to reach different underground targets from the same point on the surface.

In addition to access oil resources, deep drilling can have other economic and environmental interests, such as geothermal energy recovery and CO_2 storage. Furthermore, new projects also investigate the possibility of recovering dissolved metals contained in geothermal waters.

Moreover, even though rich countries are trying to turn to greener energy sources, hydrocarbon will still be needed for many years. Many countries still rely on oil as the primary source of their economic development, while many industrial fields remain dependent on this black liquid (aviation, maritime transport,

petrochemistry). Based on their necessity, drilling techniques still have a bright future and will know further improvements.

2 Problem statement and objectives of the thesis

2.1 Position of the problem

The uncertainty surrounding the evolution of oil and gas prices, the development of numerous deep geothermal projects, or the innovative projects mentioned before require optimizing drilling operations. Indeed, with a daily drilling operations rate that varies from $50,000 for an onshore platform to $700,000 for an offshore one (Santos et al., 2021), drilling operations are a significant factor in the overall expenses of this type of project. It is then essential to have an optimal management and optimization of drilling operations to ensure the feasibility of those projects.

Optimizing the drilling operations implies, inter alia, an appropriate choice of the drill bit and a correct setting of the drilling parameters. The choice of the drill bit depends essentially on the properties and the mechanical behavior of the rocks to be drilled through. In the case of deep wells, the rock is subjected to specific conditions, among which confinement plays an important role. It is then essential to know how constitutive laws of geomaterials evolve with confinement.

Furthermore, the change in rock behavior and the confinement applied to the rock-tool interface will also impact the involved destruction mechanisms. However, while PDC drill bits are currently the most widely used, the cutting mechanism has been extensively studied under atmospheric conditions without confinement. The impact of high-depth conditions on this mechanism is not yet fully known and understood. Therefore, an important work remains to be done to have a complete understanding of the evolution of the cutting mechanism with confinement in order to be able to optimize the drilling operations in such conditions.

2.2 Previous research in the Mining Department of the UMONS – FPMs

The Mining Engineering Department of Mons University (UMONS) has followed two main axes of research: the evolution of constitutive laws of rocks with confinement and destruction mechanisms of rocks.

The work on the rock behavior under confinement has allowed the development of two in-house test benches to carry out tests under confinement: a true triaxal compressive frame (Tshibangu, 1993) and a classical triaxial one (Descamps, 2007). The true triaxial (or polyaxial) device developed in the beginning of the 1990's is able to apply different stresses in the three orthogonal directions of a cubic sample. This device can reproduce complex confinement conditions to study their impact on the behavior of the rock. To go a step further, Descamps (2007) developed a triaxial device featuring pore fluids connecters and a heating jacket. The objective was to get closer to high depth conditions by considering pore pressure and temperature. The development of these machines allowed to study the behavior of rocks in high-depth conditions. It led to the publication of many scientific articles.

The second main axis of research, the study of rock destruction mechanisms, aims to understand more in detail interactions between rock and drill bits. This work also led to the development of test benches and the creation of a standardized abrasiveness test (Brison and Brych, 1971). All these benches allowed to study the whole destruction mechanisms and different types of tools. This research axis has been the subject of numerous scientific publications and a thesis on the cutting mechanism (Dagrain, 2006).

2.3 Objectives of the thesis

The main motivation of this thesis is to contribute to a better understanding of the cutting mechanism under confinement, combining knowledges about rock behavior and rock cutting developed through the years in the Mining Engineering Department of the University of Mons. Indeed, these two axes of research are not separated but communicate with each other and a good understanding of the rock behavior is essential to analyze the interactions with the cutting tool.

This thesis aims to integrate the knowledge related to the evolution of the mechanical behavior of rocks and their constitutive laws in the study of the cutting mechanism under high-depth conditions by the use of numerical modeling. This approach should explain the phenomena observed experimentally such as the modifications of the cuttings shape or the increase of the cutting energies with confinement.

3 Outline of the thesis

This manuscript is divided into four main sections.

The first part, Chapter II, will review the state of the art concerning the mechanical behavior of rocks in high-depth conditions and the cutting mechanism. Regarding the cutting mechanism, this chapter will focus on experimental approaches and the development of analytical and numerical models of rock cutting with a distinction between atmospheric and confined conditions.

The second part focuses on presenting the methods used to achieve the objectives of this work. Chapter III presents the methodology and the tools used in this work in a general way. Chapter IV discusses and presents the construction of the synthetic rock model and the cutting models for simulation.

The third part of the work encompasses the results of the numerical models (Chapter V). The first sections of Chapter VI are used to validate previous results and interpret them. The last section of Chapter VI is then devoted to developing analytical models based on previous results.

Finally, Chapter VII will present the overall conclusions of this thesis and further perspectives of improvement for future research.

Chapter II State of the art

To understand and model the evolution of the cutting mechanism under confinement, it requires, on the one hand, to have a global vision of the evolution of the mechanical behavior of rocks under confinement and, on the other hand, to have a clear vision of the current knowledge on the cutting mechanism.

This chapter will start with a general presentation of drilling, introducing the subject in its globality. Afterward, it will enter the subject's core with a second part presenting the state of the art on the evolution of rocks mechanical behavior under high-depth conditions, focusing on the impact of confinement.

In the third part, the current state of the art of the cutting mechanism will be presented. The main cutting parameters in drilling will be defined and the different test benches and test analysis parameters will be presented. Thereafter, particular interest will be given to present the current knowledge about the cutting mechanism in atmospheric conditions and under confinement. This section will end with an analysis of the phenomena observed in real drilling conditions with PDC drill bits.

Finally, this chapter will conclude with a comparison of the actual state of knowledge of the mechanical behavior of rocks on the one hand and those concerning the cutting mechanism on the other.

1 Drilling generalities

The following sections will introduce the current state of drilling techniques and their evolution to face the challenges to deeper and deeper access reservoirs.

1.1 Rotary drilling

The rotary drilling technique is used industrially since the beginning of the 1900s. It has been a key element in developing the oil and gas industry, increasing the drilling efficiency. Rotary drilling is the most widely used method to drill wells requiring reaching several hundreds of meters in depth. Figure II.1 is a schematic representation of a rotary drilling rig and its main components.

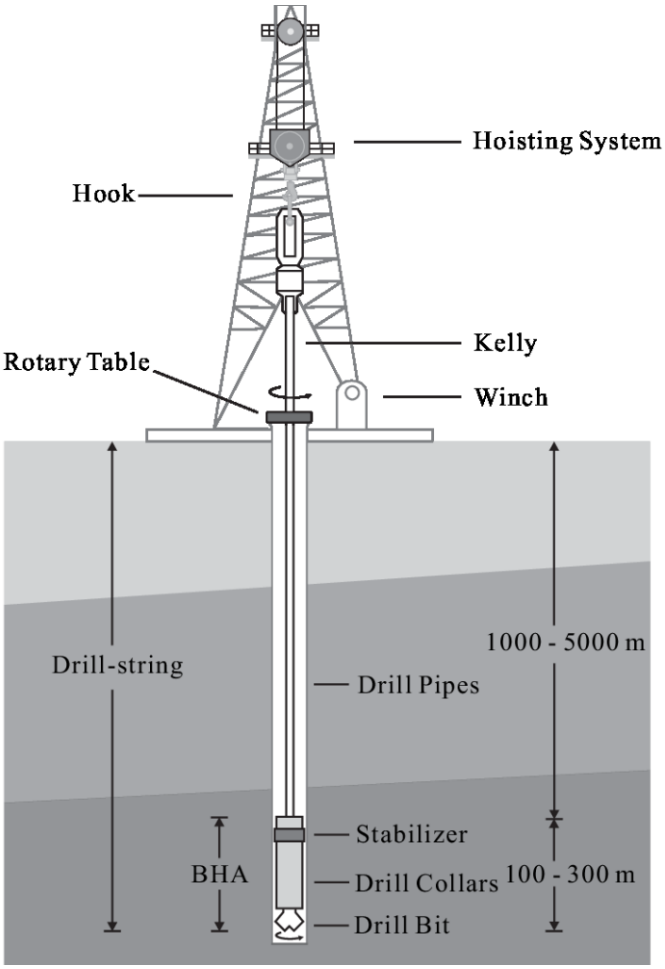

Figure II.1. Simplified representation of a drilling rig (modified from Leine and Van Campen (2005)).

The general principle of rotary drilling consists in a rotating bit to which a thrust force is applied. The rotation is generally generated at the surface by the rotary table and transmitted to the drill bit through a drill string to the bottom. The weight on the drill bit is obtained by inserting heavier drill pipes, called drill collars, just above the bit. The drill collars - drill bits combination is called BHA for Bottom Hole Assembly. Rock chips formed by the destruction process are brought to the surface by the circulation of the drilling fluid. The drilling fluid is pumped from the surface through the drill rods and the drill bit onto the cutting face. The mud then rises into the annular space between drill pipes and the well wall, carrying the chips to the surface.

1.2 Extreme Drilling

Once easily accessible reservoirs were exploited, the drilling industry had to adapt to access more profound targets increasingly challenging to access (Ma et al., 2016). Indeed, as shown in Figure II.2, wells are getting deeper and deeper with increasing horizontal offsets. This has led to significant developments in rotary drilling.

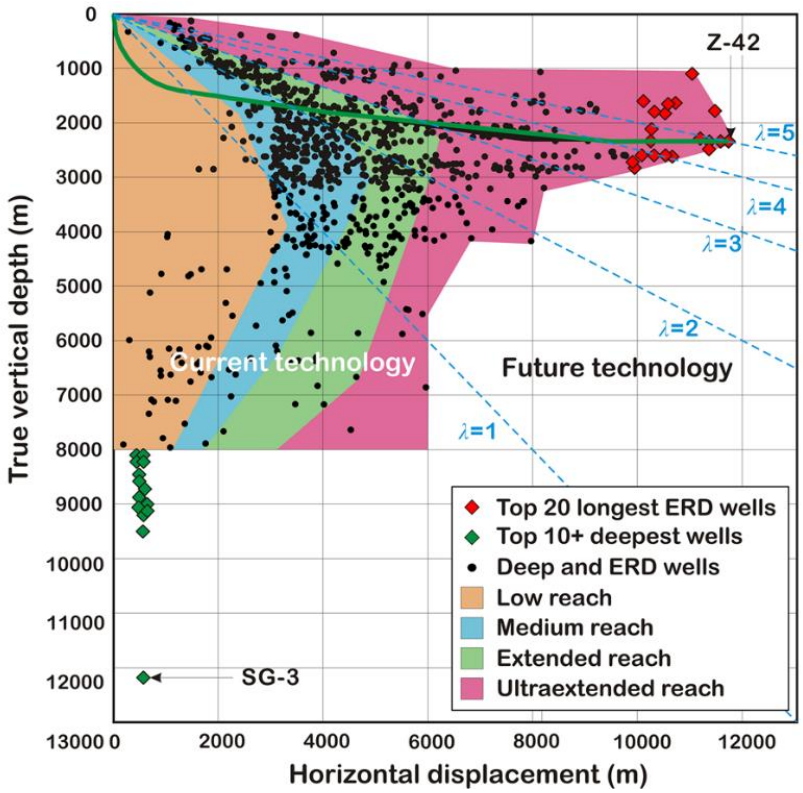

Figure II.2. The worldwide deep wells and extended-reach wells (Ma et al., 2016).

Firstly, from the point of view of vertical depth, it became common to reach vertical depths up to 4000 meters both for wells in the oil and gas industry and for geothermal energy production, while some wells can reach 8000 meters. The few deeper boreholes were for scientific purposes, such as the “Kola Superdeep Borehole” (SG -3), reaching 12.262 meters. The access to such depths means that the rock and drill bit are subjected to high temperatures and pressures. It means that it is necessary to have drill bits resistant to such constraints while being optimized to drill the rock under these conditions.

Secondly, some considerations have led to the development of directional and horizontal drilling techniques (Downton et al., 2000). These methods are used in offshore drilling, where the goal is to maximize the number of drilled wells from a same surface point. For onshore drilling, these techniques are used when there exist important surface constraints such as mountains, cities where environmental (drilling beneath cities or protected environmental areas), geographic (reservoirs under mountains), or geopolitical (reservoirs on the border between two countries) constraints are strong. The horizontal drilling technique is also used to maximize the “pay zone” between the well and the reservoir in the shale gas industry.

Finally, the most recent development in drilling techniques concerns three-dimensional drilling techniques. These techniques allow reaching tiny reservoirs while avoiding crossing geological formations that are difficult to drill (salt domes). These techniques are also helpful for redeveloping old reservoirs with preexisting wells constraints.

The implementation of complex trajectories required the creation of dedicated directional systems (Beccari and Romano, 2005). The oldest technique consists in positioning stabilizers along the Bottom Hole Assembly. Stabilizers act as support points and allow the BHA to bend in the desired direction. During the 1960s, downhole mud motors and turbines were introduced to the market (Pelfrene, 2010). These downhole devices are powered by the drilling mud circulating into the drill string. Generally situated just above the bit, these units drive the drill bit. Using these motors or turbines (the difference between the two is the speed of rotation given to the drill bit) allows dissociating the rotation of the drilling bit from the drill string. When these motors are coupled with bent subs, it is possible to modify the drill's path by imposing a deviation angle.

However, these systems did not allow precise control or change of the drilling trajectory from the surface. To overcome this problem, Rotary Steerable Systems (RSS) were invented in the 90s. These devices, which operate in rotary mode, were

developed to replace the mud motors that had to be pushed into the well. The main advantage of RSS is that it can be controlled from the surface while it was then necessary to adapt the bent sub to change the angle of attack of the mud motor. Based on the information received by the Measurement-while-Drilling (MWD) tools, the engineer or directional driller can transmit commands to gradually change the drill bit's orientation to reach the desired direction. The commands are usually transmitted to the RSS either by pressure fluctuations in the mud column or by variations in the rotation of the drill string.

1.3 Drill bits

The drill bit, which will destroy the rock, is one of the most critical elements for the success and optimization of drilling operations. Its choice and the definition of its appropriate drilling parameters (Weight on Bit and Rotation per Minute) are essential elements contributing to the success of any drilling operation. The choice of the drill bit is mainly based on the nature of the rocks to be crossed and their properties (strength, abrasiveness and mechanical behavior).

The drill bits can be classified into two major categories according to their involved destruction mechanism (Figure II.3):

- Roller-cone bits whose teeth work according to the punching mechanism. Teeth of the bits crush the rock following a normal force and create craters and chips. It is known as the “punching mechanism”.
- Fixed cutter bits whose cutting elements work according to the cutting/shearing mechanism. This mechanism is obtained by the displacement of a cutter at a specified depth of cut, under the effect of a normal force and a tangential force. It is called the “cutting mechanism”.

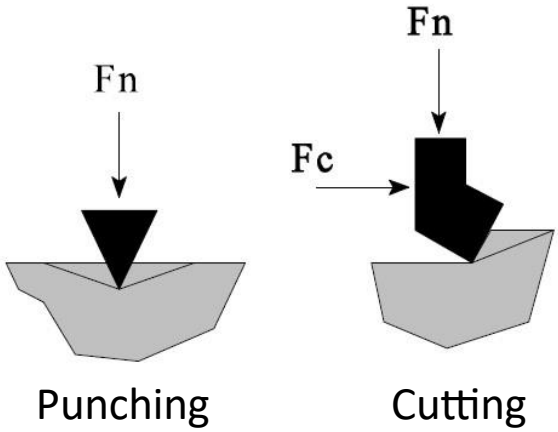

Figure II.3. Simplified views of punching and cutting mechanism involved by drilling bits.

1.3.1 Roller-cone bits

Roller-cone bits are generally composed of three independent cones, although we can find some roller-cones bits with four elements. The first one was developed by Howard R Hugues and employed two conical steel rolling elements. These drill bits can be classified into two categories according to the nature of the teeth, also called cutting elements. On one side, we have the Milled-Tooth bits where the wedge-shaped teeth are directly milled on the cone steel. On the other side are the Tungsten Carbide Insert (TCI) bits whose cutting elements are sintered tungsten carbide inserts pressed into drilled holes in the bit cones (Figure II.4).

Figure II.4. Example of roller-cone bits with a Tungsten Carbide Insert bit on the left and a Milled-Tooth bit on the right.

Cone axes are generally separated by 120° when roller-cones are composed of three cones and thanks to roller bearings linking the body of the bit and each cone, they can rotate independently. As a result of the weight on bit and the bit's rotation, cones roll on the rock's surface while the teeth penetrate the rock and crush it by punching mechanism creating chips of variable sizes.

1.3.2 Fixed cutter bits

This category of bits includes all drill bits made up of fixed cutting elements. These bits do not have moving elements such as roller-cone bits but are composed of bit bodies made from steel or tungsten carbide matrix on which are fixed the cutting elements.

This family of drill bits is divided into three according to the type of cutting elements (Figure II.5):

- Polycrystalline Diamond Compact (PDC) Bits.
- Natural or synthetic diamond bits.
- Thermally Stable Polycrystalline (TSP) bits.

Figure II.5. Different types of fixed cutters bits (Menand, 2001).

*1.3.2.1 **PDC bits***

These drilling bits are composed of Polycrystalline Diamond Compact (PDC) cutters. These cutters, created in 1971 by General Electric, are made of a diamond table and a tungsten carbide substrate. The diamond table is obtained by sintering a powder of randomly oriented fine and ultrafine synthetic diamond particles with cobalt [Co] under extreme pressure and heat to produce a thin cylinder of polycrystalline diamond. With its randomly oriented synthetic diamond matrix, polycrystalline diamond has no preferred cleavage planes, thus making the PDC cutter extremely hard and resistant to impact and wear.

Once produced, the diamond table is sintered onto a substrate made of tungsten carbide. This substrate is used to attach the PDC table to the bit body. Indeed, Tungsten carbide is one of the few substances materials that can be bonded to diamond while being able to be brazed on the bit body.

Even if PDC cutters can have multiple sizes, PDC cutters generally have a diameter of 13mm, with a diamond table presenting a typical thickness from 2 to 4 mm and

a substrate thickness of 10 mm. Generally sharp when introduced on the markets in the 70's, now diamond tables present a chamfer on the cutting face to reduce the stress on the edge when the cutter is in contact with the rock. Although the chamfered edge can reduce bit aggressiveness, it increases its durability and impact resistance.

1.3.2.2 TSP bits

These bits consist of diamond cutters treated to make them more resistant to high temperatures by removing cobalt catalyst (typically contained in PDC cutters) that can create differential thermal expansion problems at high temperatures. This modification makes TSP stable up to 1200°C, while the maximum safe operating temperature for PDC materials is 750°C. TSP cutters generally have small triangular or cubic shapes and do not need substrate.

TSP bits are generally used for applications where the operating temperature of the bit cannot be reliably controlled.

1.3.2.3 Diamond bits

Diamond drill bits are composed of natural or, more frequently, synthetic diamonds trapped in a tungsten carbide matrix. The type and quantity of diamonds depend on the rocks to be drilled. These bits are generally used to drill very hard and abrasive rocks. The destruction mechanism is cutting mechanism at a very shallow depth of cut, also known as abrasion. Currently, these drilling tools are mainly used for core drilling.

1.3.3 Evolution of drill bits market

Developed at the same time as rotary drilling, roller-cone bits were essential for the rising of rotary drilling. They had a monopoly on the drill bits market until the arrival of a new game changer, the PDC drill bits. Indeed, at this time, the roller-cone bits represented more than 90% of the total distance drilled annually. PDC bits that were first mainly used in soft rock have seen their market share increase thanks to the different evolutions of the PDC cutters. These evolutions allowed them to drill harder and more abrasive rocks. Their market share has increased from a few percent of the distance drilled in 1980 to about 20% in the 90's and finally represents today 90% of the distance drilled per year (Scott and Hughes, 2015).

2 Rock behavior in high-depth conditions

As mentioned in the introduction chapter, rocks are subjected to high pressure and temperature at high depths. These conditions modify the mechanical behavior of the rocks. This section defines the terminology " high depth conditions " as a first step. Subsequently, the impact of confinement, temperature and pore pressure on rock behavior will be presented. A particular emphasis will be given to the impact of confinement as this is the main topic of this work. Finally, a brief overview of thermo-hydro-mechanical coupling will conclude this section.

2.1 Definition of high-depth conditions

As presented in Figure II.2, it is current that drillholes reached vertical depth up to 4000m and sometimes even more. It can be inferred that vertical and horizontal stresses, pore pressure (pressure of fluids within the pores of rock) or temperature will increase with depth. It is essential to know the order of magnitude of this increase.

Regarding the evolution of vertical and horizontal stresses, the database of measured underground stresses collected by Brown and Hoek (1978) indicates their evolution with depth. Although the results in Figure II.6 (a) show a slight scatter, vertical stresses follow the line $\sigma_v = \rho g z$ with a density of 2700 kg/m³ corresponding to the average weight of the overlying lands. Different geologies can explain deviations from this linear relationship at the different measurement points as well as local variations in topography.

On the other hand, the horizontal stress evolution with depth does not follow a linear relationship and presents a greater dispersion. The evolution of the stress ratio K, the ratio between the horizontal and vertical stresses, as a function of the depth, is presented in Figure II.6 (b). Up to 500 m, this ratio ranges between 1 and 4, while for greater depths, it decreases significantly to less than one after 2000m.

Based on the dataset, Brown and Hoek (1978) have determined two envelopes that surround the data and allow the estimation of K as a function of depth such that:

$$0.3 + \frac{100}{z} \leq K \leq 0.5 + \frac{1500}{z} \qquad \text{(II.1)}$$

Where z is expressed in meters.

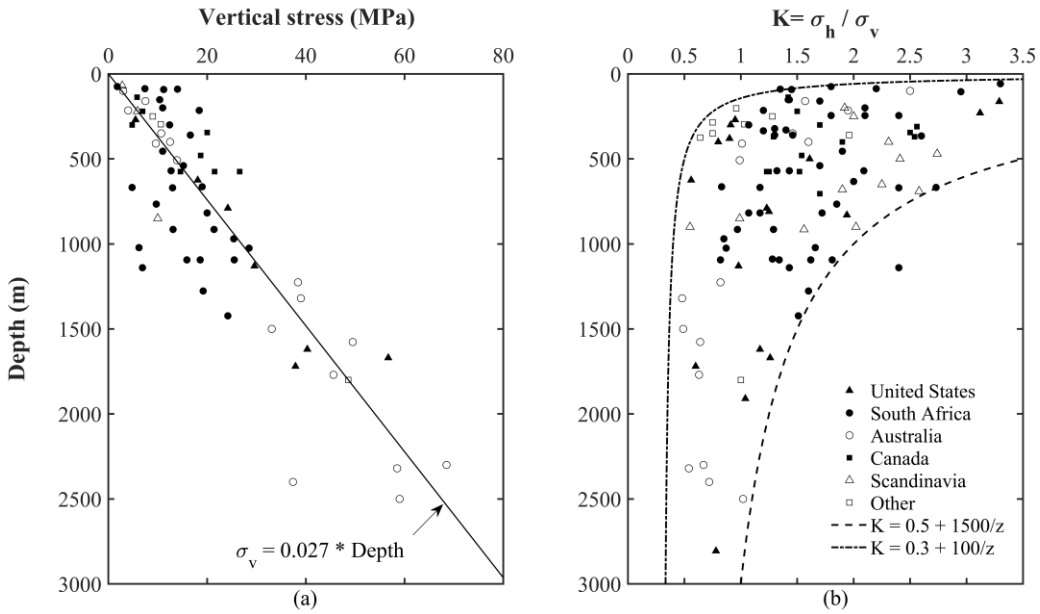

Figure II.6. Measured horizontal and vertical stresses around the world. (a) Evolution of the vertical stress with the depth. (b) Evolution of the stress ratio K with the depth (from Brown and Hoek (1978)).

Concerning the evolution of pore pressure with depth, Fertl (1976) explained that the normal pore pressure in any geological formation is equal to the hydrostatic pressure considering that the pores are filled with water from the surface to the concerned geological formation. Depending on the salinity of the water, the normal gradient of the pore pressure ranges from 0.098 to 0.105 bar/m (Figure II.7).

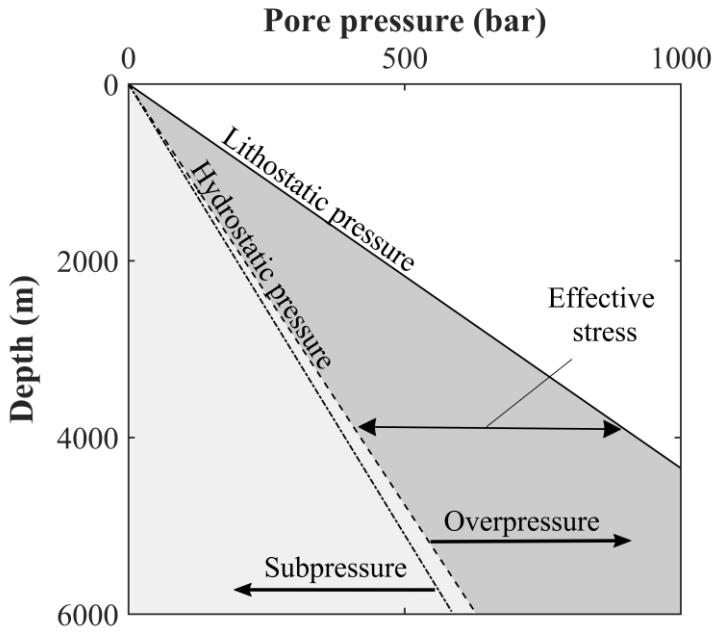

Figure II.7. Pore pressure gradient.

Naturally, this gradient varies depending on the geological conditions and the water table depth. It is called abnormal pore pressure. The terms “overpressure” and “subpressure” are used respectively when the pore pressure is abnormally high or low.

Abnormal overpressures can have several explanations. First, cap rocks (geological layers of low permeability) can trap reservoirs (e.g., oil and gas reservoirs) by preventing the movement of substantial amounts of fluid. Secondly, this phenomenon can occur in zones of active tectonics, generating numerous faults (Obradors-Prats et al., 2017). Finally, this overpressure also occurs in geothermal areas or hotspots. On the other hand, subpressure conditions can be encountered when the water table is located at a depth of several hundred meters, as it can be the case in arid areas (Fertl, 1976).

Finally, the temperature evolution with depth is governed by the geothermal gradient. It defines the rate of increase in temperature per unit depth in the Earth and averages 25 to 30°C/km. However, this gradient can increase drastically near mid-ocean ridge or volcanic area.

As an example, at a depth of 3000 meters, the following conditions can be expected:

- Vertical stress: 81 MPa.
- Horizontal stress: between 27 to 81 MPa.
- Pore pressure: between 29.4 MPa and 31.5 MPa.
- Temperature: 90°C.

2.2 Evolution of rock behavior with confinement

Confinement's effects on rock behavior are known since the end of the nineteenth century. Indeed, Becker (1892) and Adams (1912) explained already that the increase of confining stress σ_3 applied during triaxial test increases the axial stress σ_1 required to generate the failure of the sample (Jaeger et al., 2007). Moreover, due to the increase of confinement, some rocks that present a brittle behavior (section 2.2.1) in atmospheric conditions show a tendency of greater ductility (section 2.2.2). Figure II.8 illustrates these effects with respect to the increase of the confining pressure.

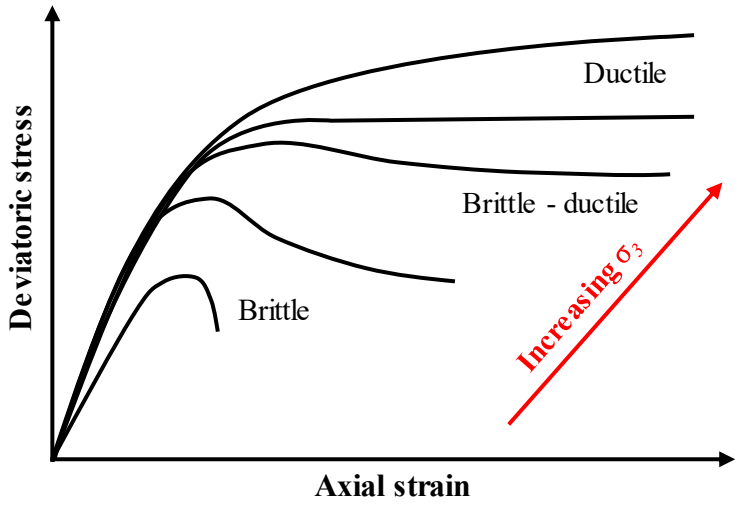

Figure II.8. Illustration of brittle to ductile transition with increasing confining pressure (modified from Helmons (2017)).

The failure mode encountered depends on the rock properties and the stress conditions applied to the sample. A good tool for estimating the behavior of rock under confinement is the strength ratio R, defined as the ratio between the uniaxial compressive strength σ_c and uniaxial tensile strength σ_t:

$$R = \frac{\sigma_c}{|\sigma_t|} \tag{II.2}$$

Strength ratio R is often used to estimate the Hoek-Brown material constant m_i (Cai, 2009; Sari, 2010). Rocks presenting low strength ratio values will exhibit ductile behavior from low confinement values (e.g., shale (R = 6 ± 2), chalk (R = 7 ± 2), gypsum (R = 8 ± 2)). On the other hand, rocks with a high strength ratio (e.g., granite (R = 32 ± 3), quartzite (R = 20 ± 3)) are qualified as brittle rocks and will require high confinement values to exhibit ductile behavior. Moreover, some rocks, such as granite (R = 32±3), still present brittle behavior over the whole range of confining pressure reachable at the laboratory scale. Indeed, some researchers have shown that granite can be brittle at pressures as high as 3000 MPa at ambient temperature (Paterson and Wong, 2005).

Table II-1 gives the values of m_i and confining pressure at the brittle-ductile transition for some typical rocks.

Table II-1. Brittle-ductile transitions: some examples observed in triaxial compression tests at room temperature (Paterson and Wong, 2005; Cai, 2009).

Rock type	m_i	Approximative confining pressure at transition (MPa)
Chalk	7 ± 2	< 10
Rock salt	12 ± 2	< 20
Gypsum	8 ± 2	40
Limestones and marbles	12 ± 3	30 - 100
Siltstones and shales	7 ± 2	< 100
Anhydrite	12 ± 2	100
Dolomite	9 ± 2	100 – 200 or higher
Sandstones (≈ 10% porosity)	17 ± 4	200 - 300
Quartzite	20 ± 3	600
Granite	32 ± 3	> 1000

2.2.1 Brittle behavior

A competent rock is considered brittle when it fails violently due to the quick propagation of fractures when its peak strength is reached. The rock strength could then drop abruptly to zero or a residual strength depending on the confinement (Figure II.9). For some rocks, peak stress can be followed by a softening phase before reaching its residual strength.

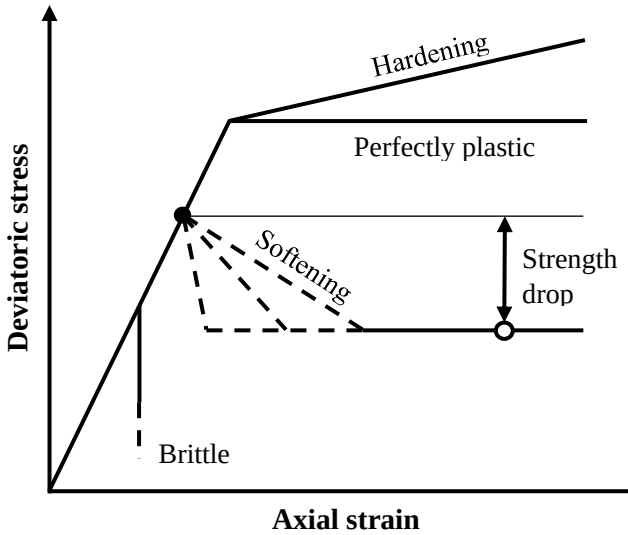

Figure II.9. Theoretical rock behavior evolution from brittle to hardening one with the increase of confinement (modified from Yu et al. (2019)).

Brittle behavior is characterized by three different modes of fracture propagation as presented in Figure II.10 (Anderson, 2017). In opening mode (Mode I), the fracture is propagated due to tensile stress normal to the plane of crack. In shearing mode (Mode II), the shear stress acting parallel to the plane of the crack and perpendicular to the crack front leads to the propagation of fracture. Finally, tearing mode (Mode III) is characterized by shear stress acting parallel to the plane of the crack and parallel to the crack front. This last mode is rarely observed in standard rock mechanics tests.

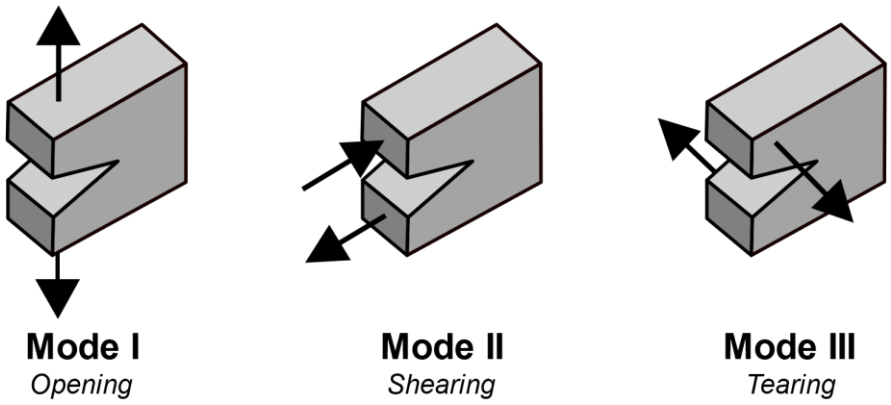

Figure II.10. Brittle fracture modes.

2.2.2 Ductile behavior

The ductile behavior of rock is defined as its capacity to change shape substantially without major fracturing. This change of the shape of the rock due to compression, also called compressive failure, can be caused by two different types of failure at the micro-scale level (Winterwerp and van Kesteren, 2004):

- Failure of the particles, called particle crushing
- Failure of the skeleton, called pore collapse

Some rocks may exhibit a ductile behavior from a sufficiently high confinement value. In contrast to brittle behavior, where rocks lose all or part of their total strength after reaching their peak strength, rocks exhibiting a ductile behavior will keep or even increase their bearing capacity after reaching peak strength (Jaeger et al., 2007). These phenomena, called perfect plasticity and hardening, are due to ruptures at the microscopic level and the free displacement of particles within the rock structure. It densifies the internal rock structure (decrease in porosity), which increases its compressive strength (Figure II.9).

2.2.3 Transition brittle-ductile

The brittle-to-ductile transition is not a simple switchover but a continuous change. This transitional phase is characterized by the formation of simple or conjugated shear bands. It is due to the increased confinement which prevents the formation of macro-cracks while stabilizing the formation of micro-cracks (Figure II.11). This stabilization of the micro-cracks leads to their coalescence as the loading increases. Finally, it results in the formation of simple or conjugated shear bands (Karato and Wong, 1995).

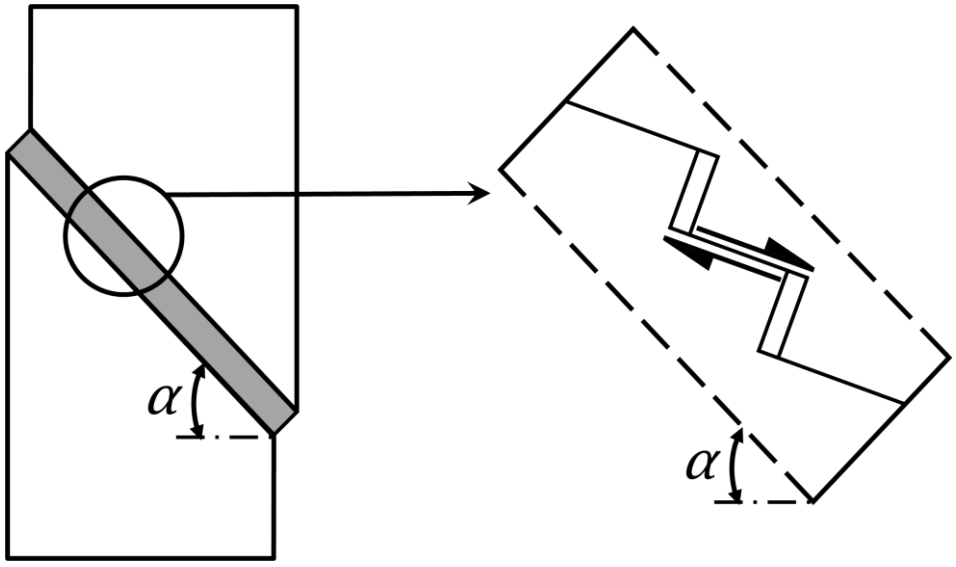

Figure II.11. Coalescence of microcracks in a shear band (modified from Winterwerp and van Kesteren (2004)).

The brittle-ductile transition also marks a change in the evolution of the volumetric strain rate at failure (Paterson and Wong, 2005). Indeed, at low confinement, volumetric strain increases to a maximum and then decreases at failure. The negative volumetric strain rate[1] at failure is due to the fracture opening when the sample reaches its peak strength, which increases the porosity and volume of the sample. The rock is therefore described as exhibiting dilatant behavior.

When confinement is sufficient for the rock to exhibit ductile behavior, the evolution of the volumetric strain changes to become compactant. Indeed, the volumetric deformation increases continuously during loading, even after failure due to pore collapse (Figure II.12).

[1] By convention in rock mechanics, the volumetric strain rate and the volumetric strain are considered positive when the volume of the sample decreases. They become negative when its volume increases.

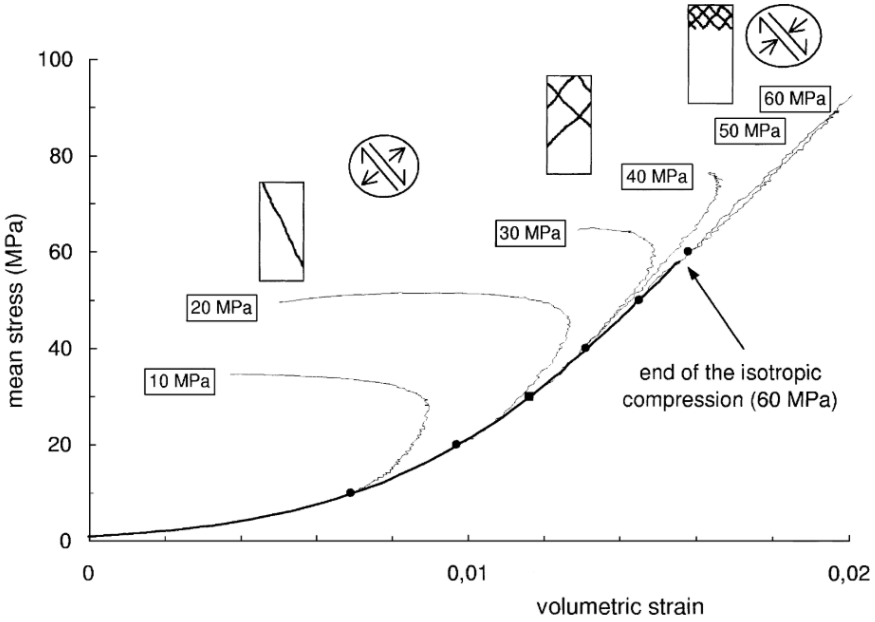

Figure II.12. Evolution of the volumetric strain with respect to the confinement. At confinement up to 40 MPa, Vosges Sandstone exhibits a dilatant behavior at failure and above this confinement the behavior is dilatant (Bésuelle et al., 2000).

2.2.4 Evolution of failure modes with confinement

An overview of the evolution of failure modes with changes in confining stress is presented in Figure II.13. Tensile failure is associated with tension stress generated in the rock sample in direct tension test or Brazilin test. This failure mode can also occur during uniaxial tests on very hard rocks like granite. It is then called axial splitting. For less resistant rocks such as sedimentary rocks, samples will only fail in tension when submitted to tension stress.

The sample will fail along a clearly defined fracture plane for uniaxial and low confinement tests. This plane is characterized by shearing displacement along its surface and is referred as a shear fracture. Further increase in confinement could result in the formation of simple or conjugated shear bands marking the transition between brittle and ductile behavior of the rock. Finally, the sample will fail in a fully compressive ductile fashion at sufficiently high confinement.

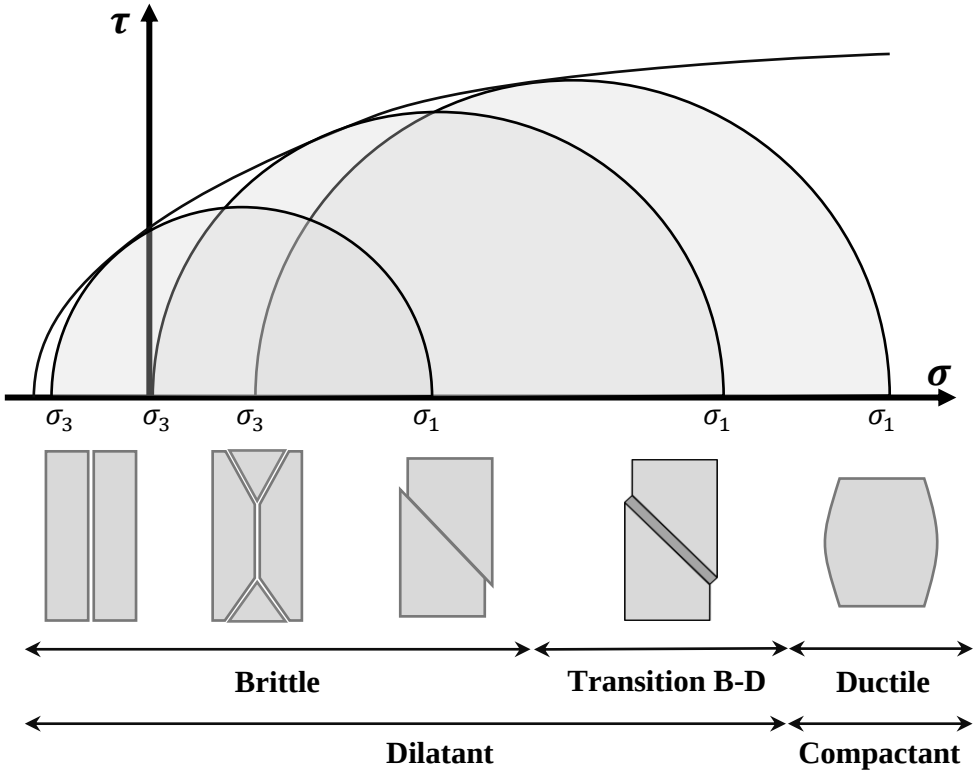

Figure II.13. Mohr diagram showing possible modes of failure, fracturing and brittle-ductile deformation (modified from Nygård et al. (2006)).

2.3 Effects of pore pressure on rock behavior

The pressure of fluids (water, oil, gas) in porous rock, called pore pressure, significantly affects the rocks mechanical behavior by reducing the rock's compressive strength. To explain this impact, it is first necessary to define the concept of effective stress introduced by Terzaghi (1943) in soil mechanics. Following Terzaghi, pore pressure supports a part of the load applied to the soil and only a portion of this load is supported by the soil skeleton. The relation between effective stress and total stress is then given by:

$$\sigma' = \sigma - p \tag{II.3}$$

Where σ' is the effective stress, σ the total stress and p is the pore pressure. Terzaghi uses the terminology “effective” to emphasize that only a fraction of the total stress is effective in causing changes in volume, shape, or strength of the solid matrix. This theory assumed that the soil matrix is rigid.

Developed empirically for soil mechanics, the concept of effective stress was later verified and adapted to rock mechanics by Biot (1941) to consider the compressibility of the rock matrix. Effective stress tensor is expressed as:

$$[\sigma'] = [\sigma] - b\,p\,[1] \quad \text{(II.4)}$$

Where $[\sigma']$ is the tensor of effective stress, $[\sigma]$ the tensor of total stress, b the Biot's coefficient and p is the pore pressure. In many applications, b is often considered equal to 1 by simplification.

Considering now the failure envelope of a hypothetical rock and the triaxial stress state (σ_1, σ_3) as represented on the Mohr diagram in Figure II.14. Following the definition of effective stress, the presence of a fluid at a pressure p has the effect of translating the Mohr's circle to the left by the magnitude of p, while maintaining the same diameter of the Mohr circle. If pore pressure is big enough, the Mohr circle could be in contact with the failure envelope which will cause the failure of the rock. Therefore, an in-situ stress state that is "safe" in the absence of pore pressure can cause rock failure if the pore pressure is sufficient to create a critical effective stress state.

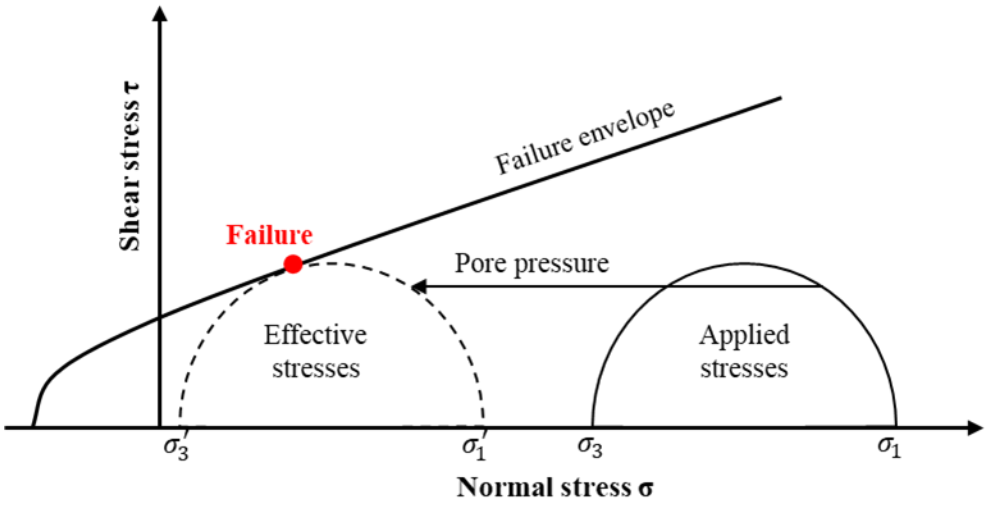

Figure II.14. Mohr diagram including Mohr-Coulomb failure envelope. Increasing fluid pressure shifts the initial stress state closer to the failure envelope.

In addition to the rock strength modification, increasing pore pressure can also change the failure mode for the same confinement. Indeed, Brady and Brown (2004) showed from data of Robinson obtained from triaxial tests on limestone at constant confinement how the behavior changes from ductile to brittle with the increase of pore pressure from 0 to 69 MPa (Figure II.15).

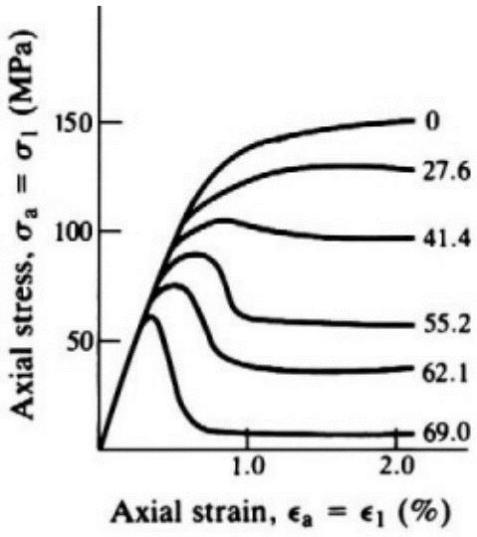

Figure II.15. Effect of pore pressure (given in MPa by the numbers on the curves) on the stress-strain behavior of a limestone tested at a constant confining pressure of 69 MPa (after Robinson, in Brady and Brown, 2004).

2.4 Effects of temperature on rock behavior

The impact of temperature on the behavior of rocks has already been widely studied in scientific literature. The range of temperature used in this topic is quite large. Indeed, some authors mention tests performed up to 100°C, while others performed tests at temperatures exceeding 1000 °C.

Based on the literature review, there are two main axes of research in this field. Firstly, research carried out on uniaxial and triaxial frames equipped with a cell to control the temperature of the sample (Descamps and Tshibangu, 2008). Secondly, the samples are subjected to controlled heating and cooling cycle in electric furnaces before being tested at ambient temperature with ordinary compressive frames (Wei et al., 2019).

While the first approach is devoted to studying rock behavior in high-depth conditions or thermo-hydro-mechanical coupling, the second is used to study the impact of the generation of microcracks or modification of the rock structure due to a thermal shock. This second approach is, for example, used to study the modification of the rock mass after a fire in a tunnel (Saiang and Miskovsky, 2012). The first approach results are of interest in the behavior of rocks in high-depth conditions. Even if the increase in temperature decreases most of the time the mechanical properties of rocks, experimental results show that the impact of temperature depends strongly on the type of rock (Wong, 1982; Houpert and

Homand-Etienne, 1984; Lion, 2008; Gu et al., 2020). Gu *et al.* (2020) studied the behavior of three rocks (granite, marble, and sandstone) up to temperatures of 800°C. Their results show that the compressive strength of granite and marble continuously decreases as the temperature increases. On the contrary, the Uniaxial Compressive Strength (UCS) of sandstone changes slightly up to 400°C. Above 400°C, the UCS increases sharply (Figure II.16). They explained this increase in the sandstone strength by a phenomenon of sintering at temperatures above 500°C. At this temperature, grains constituting sandstone start to melt partially until forming new grains. This process generates enlarged contact areas between grains that lead to an increase in compressive strength. The Young's modulus decreases continuously when the temperature increases whatever the rock.

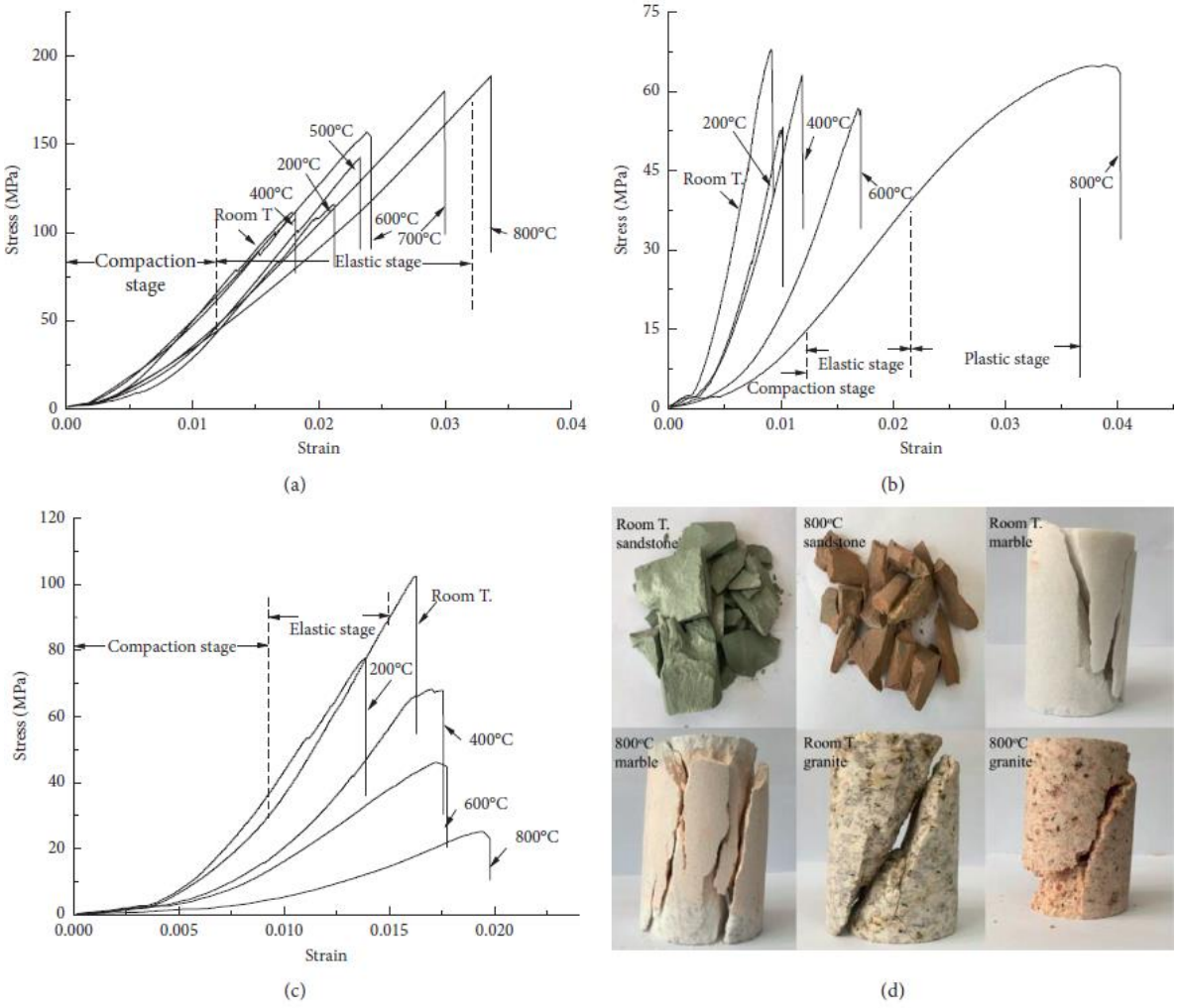

Figure II.16. Stress-strain curve and failure photographs of rock samples as a function of temperature: (a) sandstone samples, (b) marble samples, (c) granite samples, and (d) failure photograph (Gu et al., 2020).

2.5 Thermo-hydro-mechanical coupling

Presented individually, the effects of confinement, pore pressure, and temperature are however not independent but interdependent . Modifying one parameter will impact the other two. Hence the term "coupling" is used to define this interconnection (Figure II.17). In the present case, we speak of thermo-hydro-mechanical coupling.

Furthermore, while the rock is in a state of equilibrium, drilling will modify it. Indeed, the presence of the well will result in a change in the stress distribution. The drilling mud may modify the pore pressure and the temperature of the rock near the wellbore since its pressure and temperature may differ from the rock.

For example, a decrease in temperature will decrease pore pressure, changing the effective stress field. In addition, cooling will cause tensile stresses that may be sufficient to cause tensile fractures.

Although the principle of thermo-hydro-mechanical coupling is outside the scope of this work, focusing on the effects of confinement, it is interesting to mention those dependencies because it could be the basis of further developments in the study of the cutting mechanism.

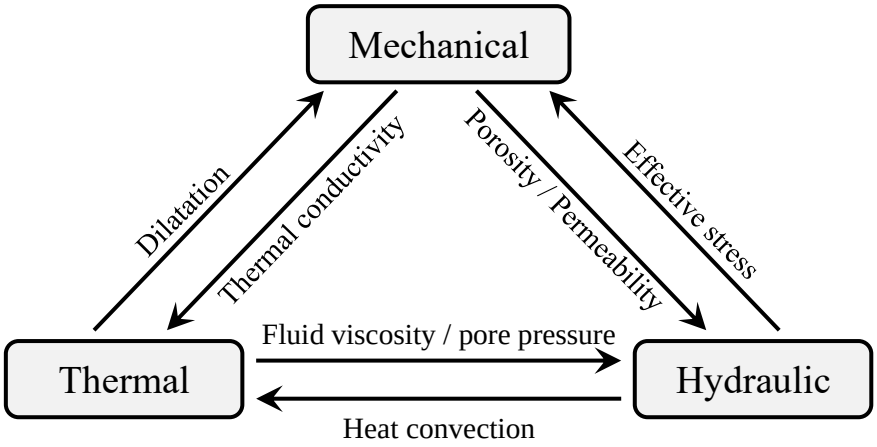

Figure II.17. Thermo-hydro-mechanical coupling (modified from Descamps (2007)).

3 Rock cutting mechanism

The term "rock cutting" is used in various fields, each with its characteristics. Indeed, this term is used in drilling, dredging, tunnel boring (with disc cutter), or mining when the extraction is made with continuous miners. Furthermore, the first studies on the cutting mechanism of rock emerged from the mining industry as did Nishimatsu (1972) who developed a phenomenological cutting model for conical picks of continuous miners.

Therefore, before going into details, this section will first define the characteristics of the cutting mechanism specific to drilling, the shapes of cutters as well as experimental devices used to study this mechanism. After that, this section will develop the current knowledge concerning the cutting mechanism in atmospheric conditions and under confinement. This section will not discuss the effects of temperature and pore pressure on the rock cutting mechanism. It is mainly due to experimental devices presented in section 3.1.3 that do not allow control of all the parameters linked to high-depth conditions.

3.1 Characteristics of rock cutting mechanism in drilling

3.1.1 General definition

In drilling, the cutting mechanism is defined as the displacement of a PDC cutter on the rock surface at a specified depth of cut d, back rake angle ω_c and cutting speed V_c (Figure II.18). The back rake angle is defined as the inclination angle of the cutting face of the cutter relative to the vertical. In third dimension, the side rake angle ω_s is defined as the angle between the velocity vector and the normal to the cutter face projected in a plane parallel to the rock free surface.

During drilling, the depth of cut depends on the Weight On Bit, but three distinct operating modes exist experimentally. During the first mode, the tests are carried out at a constant depth of cut. In the second one, a vertical force is imposed on the cutter. Therefore, the cutter starts from the surface of the rock and gradually penetrates it up to reach a corresponding depth of cut. In the third mode, the rate of penetration is imposed and the depth of cut increases continuously. In the second test mode, the depth of cut can vary depending on rock properties or if the rock is not homogenous.

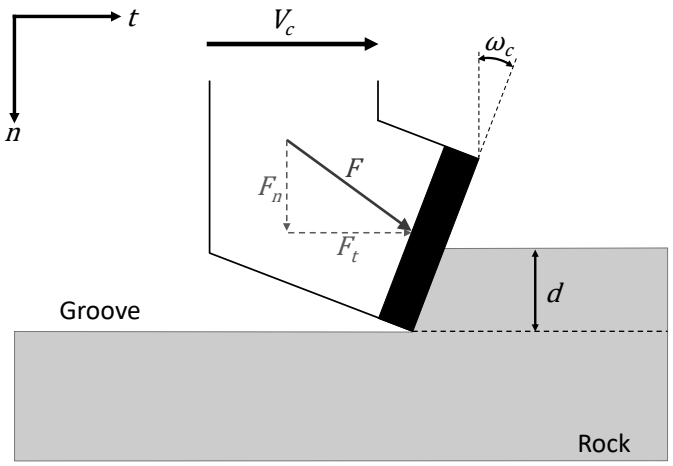

Figure II.18. 2D schematic view of the cutting parameters.

Two significant points differentiate the cutting mechanism in drilling from the one in the mining industry: the rake angle and the depth of cut. Back rake angles applied in drilling or mining are opposite and are referred as positive or negative back rakes depending on the convention used. The following convention will be considered in the rest of this work: the back rake angle is defined as negative when the cutter is inclined backward, while it is positive when the cutter is inclined forward (Figure II.19). According to this convention, the rake angles in drilling are positive and negative in mining.

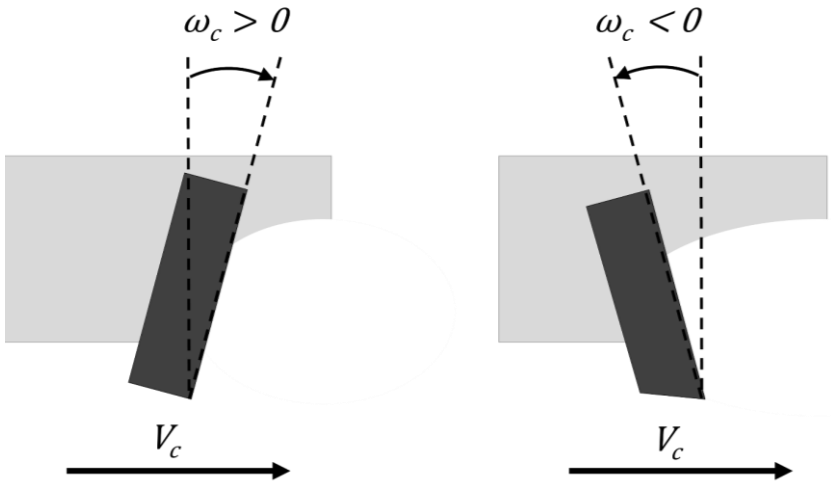

Figure II.19. Definition of negative and positive rake angle.

The typical depth of cut is in the range of centimeters or more in mining, whereas in drilling, it is in the range of sub-millimeters or millimeters. Finally, linear cutting speeds in drilling are in the order of magnitude of one meter per second.

3.1.2 Cutting forces

The total force F acting on the rock by the cutter is commonly divided into two components (Figure II.18):

- The tangential force or cutting force F_t is defined as the force needed to generate the horizontal motion of the cutter. It is parallel to the direction of movement of the cutter.
- The vertical force or thrust force F_n is defined as the force required to generate or maintain the depth of cut.

3.1.3 Experimental devices

Several types of laboratory machines have been developed to study the cutting mechanism. They can be divided into four main categories.

The first ones are laboratory devices operating under atmospheric conditions and performing linear cutting tests with a single cutter and at low speed. The cutting speed is a few millimeters or centimeters per second depending on the testing device. One of these devices is the Rock Strength Device (Richard et al., 1998) which was developed to demonstrate the theory of Detournay and Defourny (1992). This device performs linear cutting tests at a constant depth of cut and with a cutter velocity of a few millimeters per second. The advantages of this equipment are that it is small, easy to use and does not require large samples. Other devices of the same type were developed based on mechanical shapers to perform linear cutting tests but with higher cutting velocities (Menand, 2001). In addition to the devices operating at a constant depth of cut, some operate at constant vertical force applied on the cutter (Dagrain, 2006).

The second family of devices also performs tests in atmospheric conditions with one cutter but at higher cutting speeds. Linear cutting speed can reach several meters per second, corresponding to cutting speeds observed during drilling. Generally, these devices are based on mechanical lathes. Mainly wear tests are performed with these devices (Appl et al., 1993; Moseley et al., 2009). Usually, the tests carried out on these devices are performed at a constant rate of penetration.

The third category includes benches working under mud pressure and performing circular cutting tests with a single cutter; “single cutter” is often used as their nickname. There are different levels of complexity in this family. While some

machines only allow the application of mud pressure, others also control the pore pressure (Rafatian et al., 2009; Akbari and Miska, 2016; Amri et al., 2016).

The last family comprises laboratory devices that test entire drill bits in real drilling conditions, i.e., with realistic mud pressure and rotation speed (Pelfrene, 2010). This last category requires important laboratory facilities and represents high operating costs, so it is the rarest one. Besides, since these test cells use an entire drill, they are not suitable for the fundamental study of the rock cutting mechanism. Indeed, it is impossible to isolate the phenomena occurring on each cutter. Most of the experimental works presented in sections 3.2 and 3.3 of this chapter were conducted on test benches belonging to the first three families.

3.1.4 Concept of Specific Energy

To evaluate different cutting setup results or analyze cutting efficiency, Specific Energy is often used as a reference factor. This concept was initially introduced by Teale (1965) to measure the efficiency of rotary drilling. Teale defines the Specific Energy e as the work required to excavate a unit volume of rock. The work is generated by the weight on bit WOB (N) and the torque T (N.m). Considering N the rotation speed (rev/min), A the cross-section of the wellbore (m²) and ROP the rate of penetration (m/min), the total work done W and volume excavated V in one minute are given by:

$$\mathrm{W} = WOB\,.ROP + 2.\pi.N.T\ (N.m\ or\ J) \tag{II.5}$$

$$V = A.ROP\ (m^3) \tag{II.6}$$

The Specific Energy e is then expressed as:

$$e = \frac{WOB}{A} + \frac{2.\pi.N.T}{A.ROP}\ (N.m/m^3\ or\ J/m^3) \tag{II.7}$$

Based on this equation, it is possible to define the thrust energy e_t and the rotation energy e_r as:

$$e_t = \frac{WOB}{A}\ (N/m^2\ or\ N.m/m^3\ or\ J/m^3) \tag{II.8}$$

$$e_r = \frac{2.\pi.N.T}{A.ROP}\ (N.m/m^3\ or\ J/m^3) \tag{II.9}$$

Dimensionally, Specific Energy, a work per unit of volume, can also be expressed as a pressure knowing that (N.m/m³) is equivalent to (N/m²). Therefore, Specific Energy e is commonly expressed in Pa or MPa. It is important to mention that e_t is generally negligible in comparison with e_r.

This definition of Specific Energy is generally used for a drilling bit. For laboratory tests with a single cutter, an alternative definition of Specific Energy is used and is noted E. With $\vec{u}$ as the displacement vector of the cutter, $\mathcal{C}$ as its path and S_G the groove section, the Specific Energy E is defined as:

$$E = \frac{\int_{\mathcal{C}} F_t \, d\vec{u}}{\int_{\mathcal{C}} S_G \, d\vec{u}} \tag{II.10}$$

Furthermore, making the hypothesize that the section of the groove is equal to the active surface of the cutter E can be calculated by:

$$E = \frac{\overline{F_t}}{A_C} \tag{II.11}$$

With $\overline{F_t}$ = the average tangential cutting force (N), A_c = cross-section of the groove or active surface of the cutter (mm²). This formulation of Specific Energy is the most commonly used in experimental and numerical work dealing with the rock cutting mechanism.

This double definition of Specific Energy, also called Mechanical Specific Energy, often leads to confusion. However, in most work dealing with cutting mechanism, the Specific Energy terminology refers to equation (II.10). In the rest of this thesis, the term Specific Energy E refers to the equation (II.10) while Mechanical Specific Energy MSE will refer to the Teale's formulation (II.7).

As part of their work on the cutting mechanism, Detournay and Defourny (1992) introduced an additional quantity based on the vertical cutting force. This thrust energy, which they call Drilling Strength, is given by:

$$\mathrm{S} = \frac{\overline{F_n}}{A_C} \tag{II.12}$$

With $\overline{F_n}$ = the average normal cutting force (N), A_c = cross-section of the groove or active surface of the cutter (mm²).

3.1.5 Shapes of PDC cutters

Due to their use in many fields, various shapes exist for PDC cutters. In the drilling industry, cylindrical cutters are the most commonly used. When they were introduced, the PDC cutters were perfectly sharp. Unfortunately, this design tended to cause significant stress concentration on the cutter edge, resulting in chipping on the diamond table. To overcome this weakness, chamfers are often manufactured on PDC cutters to reduce the concentration of stress on the edge of the cutters and extend their lifespan.

Nowadays, design developments are mainly done on the cutting face. Indeed, PDC bit producers are developing non-planar cutting faces. These new developments aim to improve performances such as the rate of penetration or to improve the wear and impact resistance (Liu et al., 2019). Figure II.20 presents some examples of the new designs of cutting face developed.

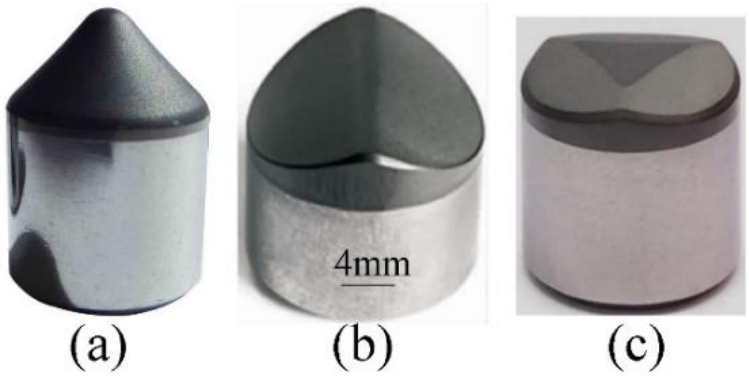

Figure II.20. Illustration of non-planar cutters: (a) Conical cutter, (b) Axe cutter and (c) 3-RDE cutter (Liu et al., 2019).

Although cutter shapes are diversified in practice, most of the work discussed in sections 3.2 and 3.3 does not involve the latest cutter geometry development but focuses on rectangular and circular flat-faced cutters. The use of rectangular cutters is linked to the definition of phenomenological cutting models developed in a two-dimensional space under the hypothesis of the plane strain state. The use of rectangular cutters for the experiments approximates this plane strain state.

3.2 Rock cutting mechanism in atmospheric conditions

The study of the cutting mechanism has led to the development of various phenomenological or experimental models based on observations and laboratory cutting test results. Before discussing these different models in section 3.2.2, the next section will focus on phenomenological aspects of rock cutting in atmospheric conditions.

3.2.1 Phenomenology of rock cutting

3.2.1.1 Failure regimes

Two fracture regimes are widely documented in the scientific literature dealing with the cutting mechanism under atmospheric conditions (Richard et al., 1998; Che et al., 2016; Liu and Zhu, 2019). The occurrence of one of these patterns depends on many factors such as the mechanical properties of the rock, the cutting parameters and the shape of the cutter. These two cutting regimes are called "scratching" and "chipping". They are characterized by the shape of the cuttings formed and the evolution of the cutting forces (Figure II.21).

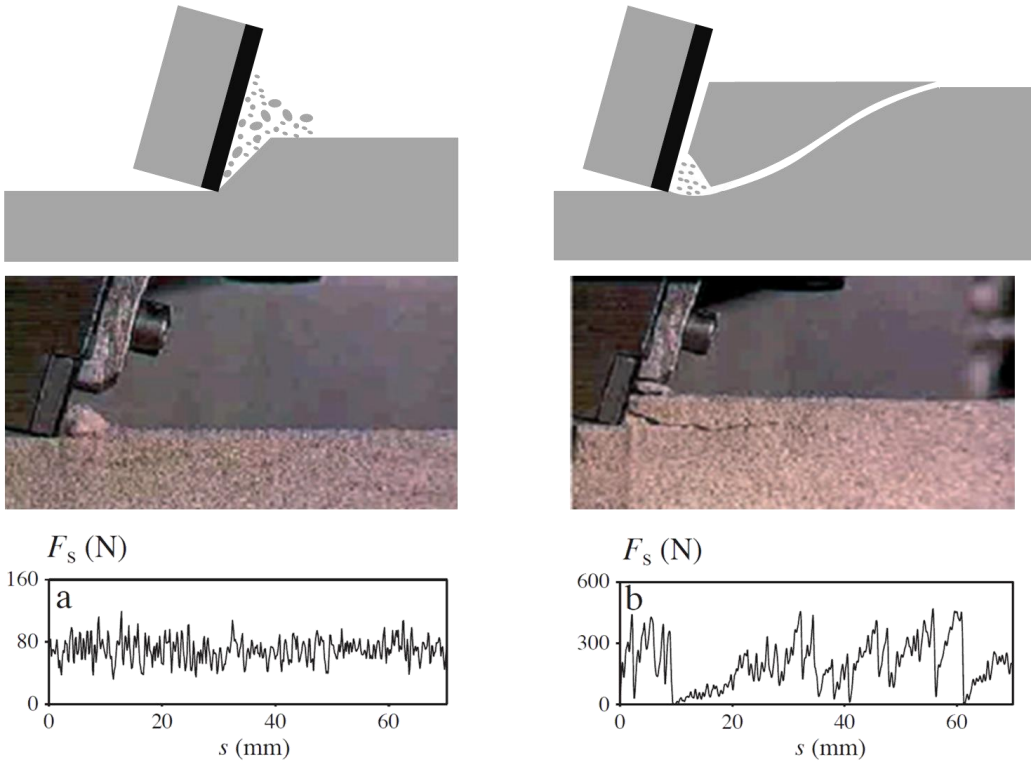

Figure II.21. Schematic views of scratching (left) and chipping (right) cutting regimes and associated force signals. Modified from Richard et al. (2012).

During the “scratching” regime, also called the “grinding” regime, cuttings are composed of rock grains ripped out of rock matrix, which generates a fine rock powder. On the other hand, cuttings formed in the “chipping” regime are composed of macroscopic chips of rock.

Concerning the cutting forces, while they looked like a continuous white noise under the scratching regime, they present a sawtooth pattern composed of peaks and releases in the chipping regime.

The chip formation process can explain the sawtooth pattern in the chipping regime, which is quite similar to the one Nishimatsu (1972) exposed for rock cutting with drag picks. This process can be divided into three successive phases (Figure II.22):

a) A crushed zone is formed at the tool tip when the cutter hits the rock.

b) Small fractures develop and generate small chips until the cutting surface takes on the shape of the cutter.

c) A macroscopic crack is formed from the crushed area to the free surface to form the major chip.

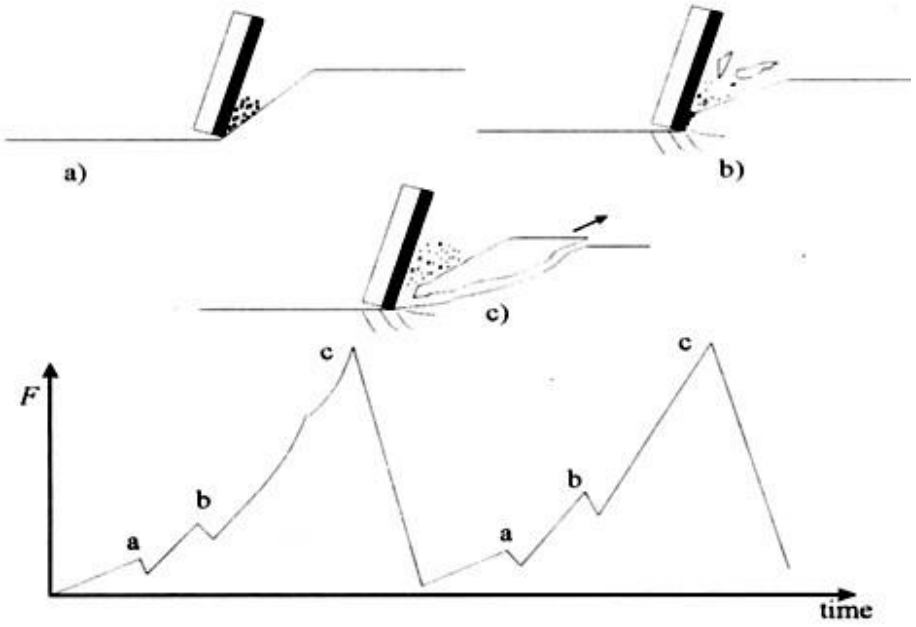

Figure II.22. Destruction cycle in chipping regime and associated force signal (Richard, 1999a).

Phases (a) and (b) are responsible for minor peaks in the force signal, while main peaks are linked to the formation of the major chips (c). After their release, cutting forces drop to 0 as the cutter is no more in contact with the rock for a short period.

In contrast, the cutter is in permanent contact with the rock and the powder formed during the scratching regime, generating a stable force signal.

In chipping mode, fractures generating chips propagate below the cutting surface and in the groove's edges. As a result, the volume of rock excavated is significantly greater than the one intercepted by the cutter active surface. This phenomenon leads to overestimating the Specific Energy calculated according to the equations (II.10).

It is necessary to mention that many researchers use the terminology “ductile” and “brittle” regimes to name these two destruction mechanisms encountered in rock cutting under atmospheric conditions. This work will not use these terms due to the following considerations. Firstly, to avoid confusion with the terms used to characterize rock behavior, which can be brittle or ductile depending on pressure or temperature conditions. Secondly, the author of this thesis does not consider that the rock powder generation is due to a ductile failure but by friction between rock and cutter.

Despite being widely studied, the two mechanisms presented above are only valid in the case of rocks exhibiting brittle behavior under atmospheric conditions. For rocks presenting ductile behavior in atmospheric conditions, the cutting process generates continuous ribbons in laboratory experiments (Cheatham and Daniels, 1979).

3.2.1.2 Impact of the depth of cut

The depth of cut is the cutting parameter that has been most widely studied and discussed in the literature. This section presents the main observations that have been made on its impact on destruction regimes, cutting forces and energies.

A Evolution of destruction mechanism

From a destructive regimes point of view, Chaput (1991) explained that cutting regimes evolution is mainly controlled by the depth of cut. While the cutting mechanism is commonly described as composed of two failure regimes, Chaput distinguished three cutting regimes from experimental observations.

According to Chaput, these failure regimes depend on the depth of cut and the resistance of the rock (Figure II.23). They are called:

- Grinding regime
- Secondary chipping regime
- Primary chipping regime

While the "grinding" and "primary chipping" regimes correspond to the modes defined as scratching and chipping, the secondary chipping regime is the transitional phase between these two regimes. Moreover, Chaput shows that the critical depth of cut between scratching and chipping regimes decreases with uniaxial compressive strength.

Many experimental studies have observed this change in cutting regimes after a certain critical depth of cut (Bifano and Fawcett, 1991; Nicodème, 1997; He et al., 2017; Wang et al., 2019). However, these studies generally mention only two cutting regimes, not three, as Chaput did.

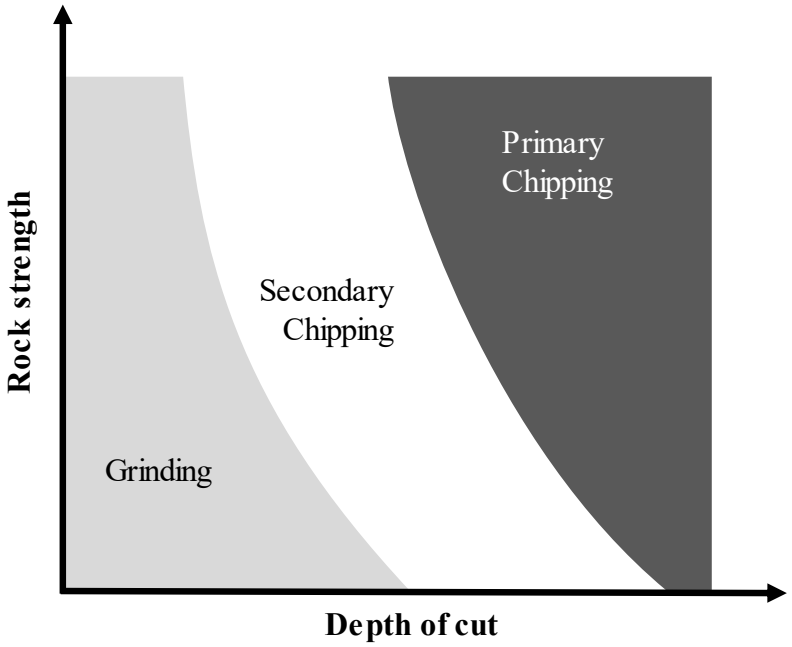

Figure II.23. Evolution of cutting mechanism from grinding to chipping, after Chaput (1991).

B Evolution of cutting forces

Based on cutting tests with sharp rectangular cutters, several researchers (Nicodème, 1997; Richard, 1999a; He et al., 2017) have shown that the evolution of peak cutting forces with respect to the depth of cut presents two different trends. At small depths of cut, measured cutting forces increase linearly as the depth of cut increases. As the depth of cut continues to increase, cutting forces deviate from the linear trend, and the increase with the depth of cut becomes less important (Figure II.24 (a)). Richard et al. (1998) explained that the second evolution of the cutting forces exhibits a scaling relationship with the square of the depth of cut. This conclusion is questioned by Pelfrene (2010). He noted that Richard's "slab" test method is very restrictive to give such conclusions. Indeed, this test method performs cutting tests with a rectangular cutter on samples having the same width as the cutter. As a result, the absence of groove sidewalls reduces the cutting forces, as shown by Dagrain et al. (2001), which does not allow to generalize Richard's conclusion. Finally, Richard explained that this break in cutting forces evolution occurs at the transition from scratching to chipping regime.

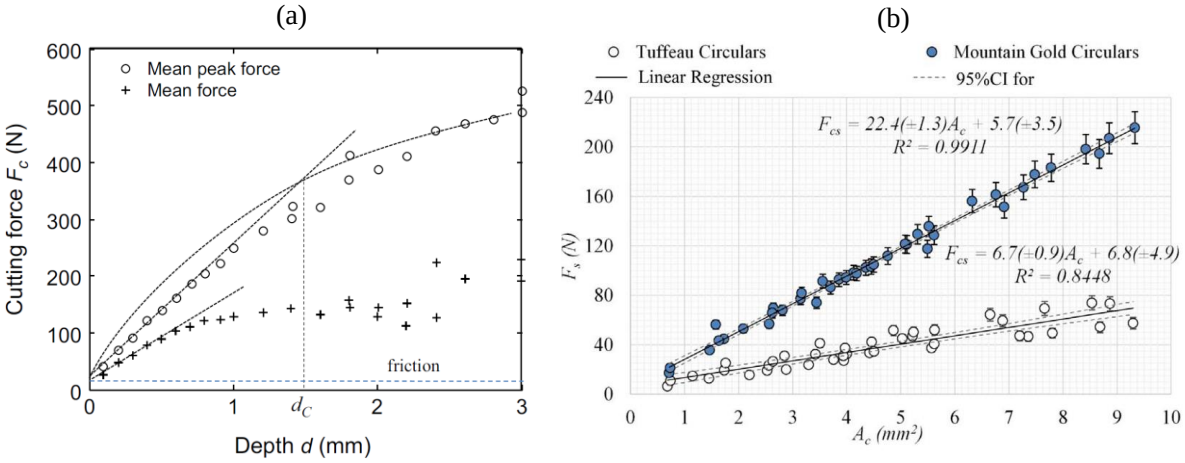

Figure II.24. Evolution of cutting forces with the depth of cut: (a), data from Richard et al. (1998) obtained with rectangular cutters and (b), data from Doshvarpassand et al. (2017) with the cutting surface for circular cutters.

Regarding mean cutting forces, experimental data of Nicodème (1997) reported by Pelfrene (2010) indicate that they reach a plateau in the second phase before increasing again at high depths of cut. However, due to the high data volatility, this interpretation must be considered cautiously and is not verified in all cases.

From tests performed with sharp circular cutters with deferent groove geometries, Doshvarpassand et al. (2017) have shown that the cutting forces evolve linearly

with the cutting area as long as the depth of cut is small enough to stay in the scratching regime (Figure II.24 (b)).

C Evolution of Specific Energy

Based on the evolution of the cutting forces presented in section B, the Specific Energy should be almost constant or present a slight decrease at shallow depths of cut while using a sharp cutter. After a depth of cut greater than the critical transition depth of cut, the Specific Energy will decrease against an increasing depth of cut. Many researchers have highlighted this decrease in Specific Energy. Figure II.25 schematizes this evolution interpreted by some studies.

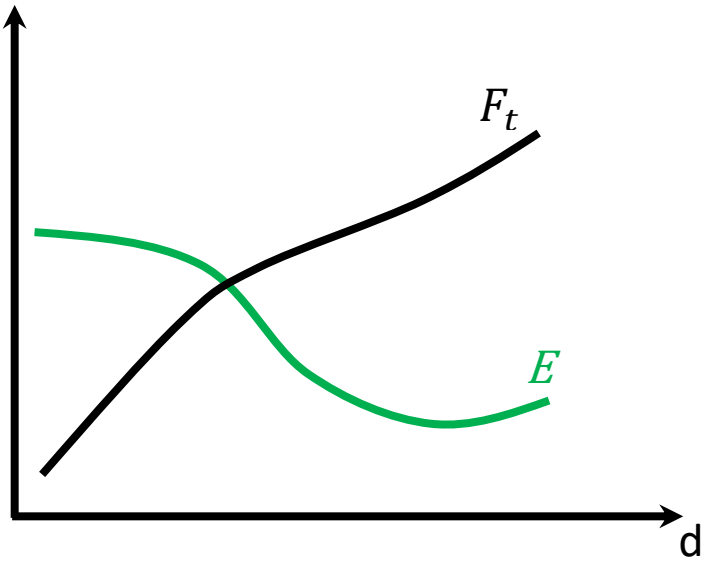

Figure II.25. Schematic evolution of cutting force (black line) and Specific Energy (green line) with the depth of cut (modified from He and Xu (2016)).

However, this decrease is not continuous and reaches a minimum even before rising again when the cutting depths are sufficiently important. Cheng et al. (2018), who performed linear cutting tests on granite, marble and sandstone, have shown that the Specific Energy (Figure II.26 (a)) decreases with the increase of depth of cut until it reaches a minimum value. However, the range of depth of cut did not allow them to observe an increase in Specific Energy after what seemed to be a minimum for cutting tests on granite (Figure II.26).

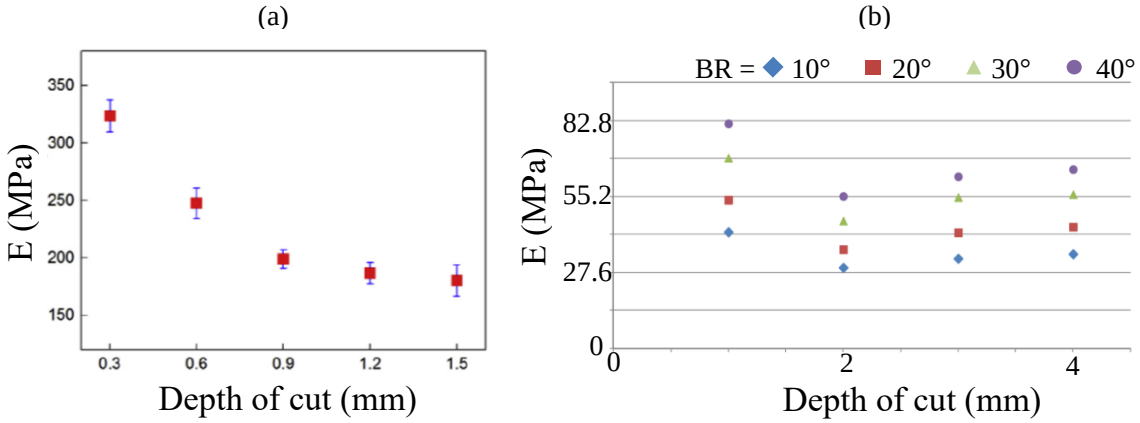

Figure II.26. Evolution of the Specific Energy with the depth of cut: (a), data from Cheng et al. (2018) and (b), data from Rajabov et al. (2012).

For their part, Rajabov et al. (2012) performed circular cutting tests with circular cutters on Torrey Buff Sandstone up to a depth of cut of 4 mm. Results in Figure II.26 show that Specific Energy decreases with increasing depth of cut up to 2 mm to further slightly increase as the depth of cut continues to increase. They explained this change in the Specific Energy trend by the evolution of the cutting area with the depth of cut. As their cutter had a circular shape, a small increase in the depth of cut at shallow DOC results in a significant increase of the active surface. However, from 2 mm, an increase in the depth of cut has less influence on the increase of the area of cut while cutting forces increase drastically.

To explain the occurrence of an optimum of Specific Energy, it is necessary to present the classic drill-off curve characterizing the relationship between Weight on Bit (WOB) and Rate of Penetration (ROP) in real drilling. This curve, presented in Figure II.27, is divided into three parts:

- Part I: due to low WOB, the depth of cut is inadequate, and an important part of the energy is lost in an inefficient frictional process leading to a low rate of penetration and an excessive wear of the bit.
- Part II: WOB is sufficient for an efficient cutting process, and WOB changes generate a proportionate change in ROP. This zone minimizes tool wear.
- Part III: the relation between WOB and ROP is no more linear. An increase of WOB could even decrease ROP due to bit balling (accumulation of cuttings in front of cutters) and bottom hole balling generating bit vibration causing excessive wear.

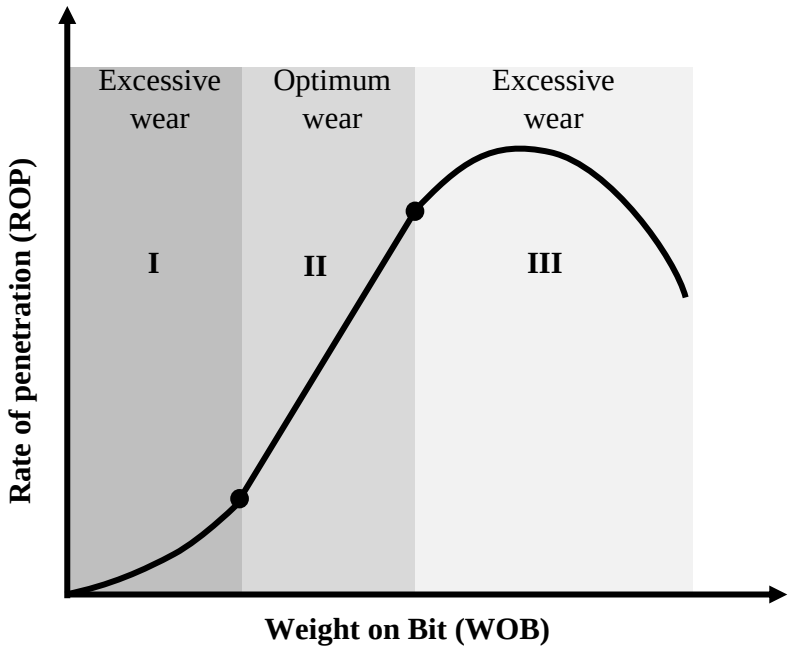

Figure II.27. Traditional relationship between Rate of Penetration and Weight on Bit.

The existence of friction and bit balling phenomena as well as the evolution of the ROP versus the WOB allow to explain the evolution of the Specific Energy according to the depth of cut (depending on the WOB) which presents an optimum corresponding to the second part of the drill-off curve.

It is also interesting to notice that some researchers observed that this minimum reached energy is in the order of magnitude of the uniaxial compressive strength of the rock tested (Teale, 1965; Pessier and Fear, 1992; Akbari and Miska, 2016). Unfortunately, they have not explained the link between these two quantities.

3.2.1.3 Impact of the back rake angle

Rostamsowlat et al. (2018) investigated the influence of the back rake angle on the magnitude of the Specific Energy. Experimental tests performed on limestone and sandstone with sharp rectangular cutters in the scratching regime showed that the Specific Energy increases with the back rake angle. Figure II.28 shows the normalized Specific Energy (Specific Energy E divided by UCS) evolution for back rake angles varying from -10° to 82.5°. While the Specific Energy remains in a narrow window for angles between -10 and 20°, the results show that the Specific Energy then increases exponentially for bigger angles. Same observations were reported by other researchers such as Detournay & Tan (2002) and Menand (2001) with tests on Vosges sandstone or Richard (1999) data on Lens limestone. Based

on the information about vertical forces, an increase in vertical forces accompanies the increase in Specific Energy.

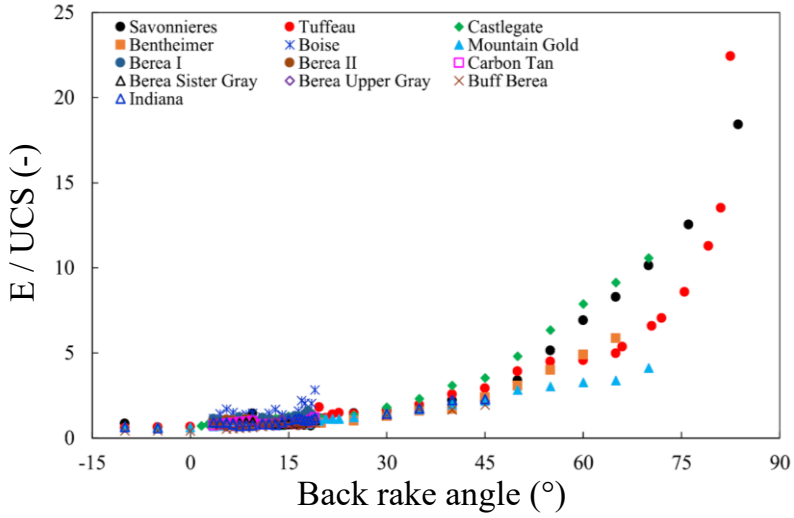

Figure II.28. Normalized Specific Energy at different back rake angles (Rostamsowlat et al., 2018b).

Moreover, the increase of the back rake inhibits a part of the forward flow of the rock crushed, which is then compressed between the face of the cutter and the rock. Richard (1999) and Rostamsowlat et al. (2018) interpreted this phenomenon as the formation of a "build-up edge" (accumulation of inert cuttings) at the bottom of the cutting face (Figure II.29). As a result, part of the flow is backward under the cutter. The increase of the back rake angle increases the backward flow at the expense of the forward one. This difficulty in eliminating the crushed rock from the cutting face is responsible for increasing Specific Energy and vertical forces.

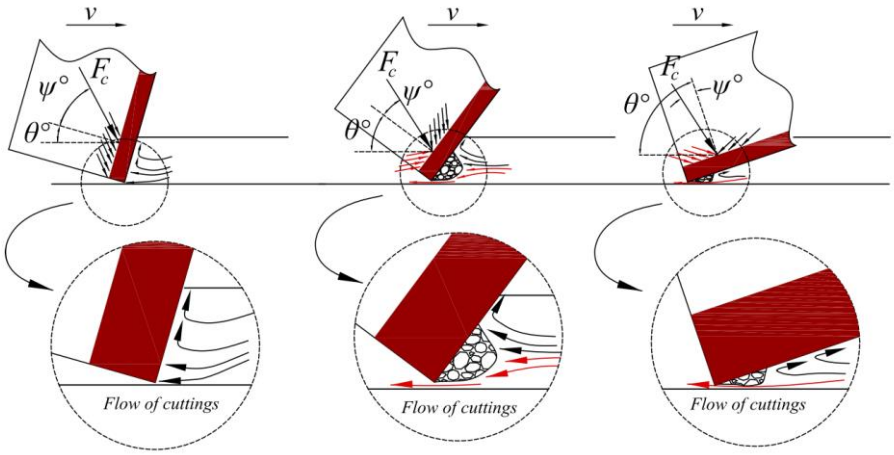

Figure II.29. The flow of the crushed material (cuttings) at different back rake angles in scratching mode (Rostamsowlat et al., 2018b).

On their side, He et al. (2017) investigated how the back rake angle influences the critical transition depth between scratching and chipping regimes. Their tests on limestones revealed first the increase of Specific Energy and Drilling Strength either in scratching or chipping regime. Moreover, they showed that the critical transition depth of cut depends on the back rake angle and increases with it. Therefore, increasing the back rake angles inhibits the formation of cracks in front of the cutter and leads to rock crushing.

3.2.1.4 Impact of the side rake angle

From linear (Coudyzer and Richard, 2005) and circular (Rajabov et al., 2012) cutting tests, it comes out that the effects of the side rake angle are negligible for angles ranging from 0 to 30°. On the other hand, Rajabov et al. (2012) showed that the Specific Energy is multiplied by 3 when the side rake angle is changed from 30 to 60° (Figure II.30).

To explain this substantial increase, they compared the evolution of the cutting surface with the increase of the cutting forces when the side rake angle increases from 30 to 60°. While the cutting surface is divided by 1.74, the tangential cutting force is multiplied by 1.5. This explains the strong increase in Specific Energy. However, they did not explain the increase in cutting forces with increasing side rake angle.

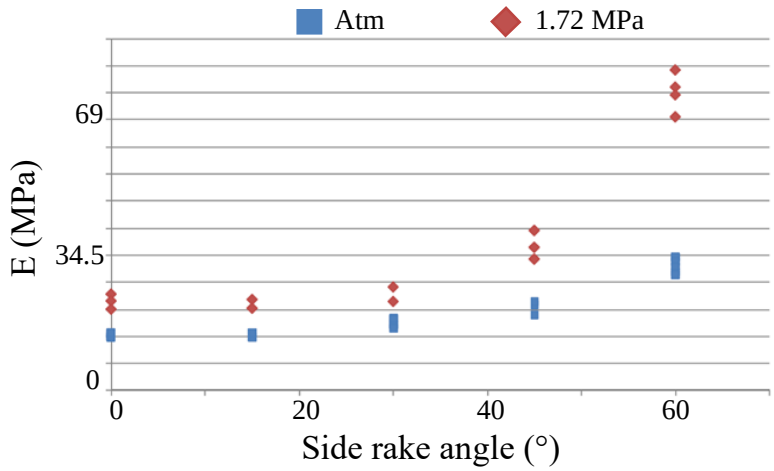

Figure II.30. Evolution of Specific Energy with side rake angle. Tests were performed on Carthage marble at a depth of cut of 1.15 mm (Rajabov et al., 2012).

3.2.1.5 Impact of the chamfer

Most of the work mentioned concerns tests carried out with sharps cutters. However, as explained in Section 3.1.5, PDC cutters used on drilling bits are chamfered to improve their resistance. Chamfers are characterized by their angle ω_{ch} relative to the cutting surface and their length L_{ch}. Although there are many chamfer designs, they generally have an angle of about 45° and a length up to 0.5 mm.

The effect of the chamfer is mainly noticeable at shallow depths of cut. Indeed, for depths of cut where the cutter is in contact with the rock only by its chamfer, the back rake angle seen by the rock is equal to the sum of the back rake angle and the chamfer angle. Akbari & Miska (2016) called this angle the "equivalent back rake angle". This situation is comparable to the one explained above regarding the increase of the back rake angle with sharp cutters. The presence of a chamfer will increase the cutting forces making the evacuation of debris difficult.

The intensity of the chamfer effect on the cutting forces will progressively decrease as the depth of cut increases. Once the rock is in contact with both the chamfer and the cutting face, Akbari & Miska (2016) calculated the equivalent back rake angle using a geometric average of the cutting face and chamfered face areas. The greater the depth of cut is, the closer the cutting forces will be to those obtained with a sharp cutter.

3.2.1.6 Impact of cutter wear

Cutters considered sharp at the beginning of their use will progressively wear out during operation, resulting in changes to their shape. The change in the shape can be caused by abrasive wear or failure mechanisms due to repeated impacts or excessive cutting forces. While abrasive wear is a continuous process that will gradually change the cutter shape to form a wear flat, failure mechanisms generate edge chipping of the diamond table or fractures through the carbide substrate that modify drastically and abruptly the tool shape. These phenomena will significantly impact drilling performance that decreases as wear increases due to the rise of cutting force. As the drill bit wears out (Figure II.31), it is therefore necessary to increase WOB to maintain efficient ROP penetration (Sinor et al., 1998).

Various researchers (Appl et al., 1993; Dagrain and Richard, 2006a; Rostamsowlat et al., 2018a) investigated the impact of cutting tool wear on the cutting mechanism regarding this field consideration. Researchers generally disregard the impact of

tool breakage because considered too uncontrollable and unpredictable to focus on the abrasive wear and the impact of the formation of a wear flat.

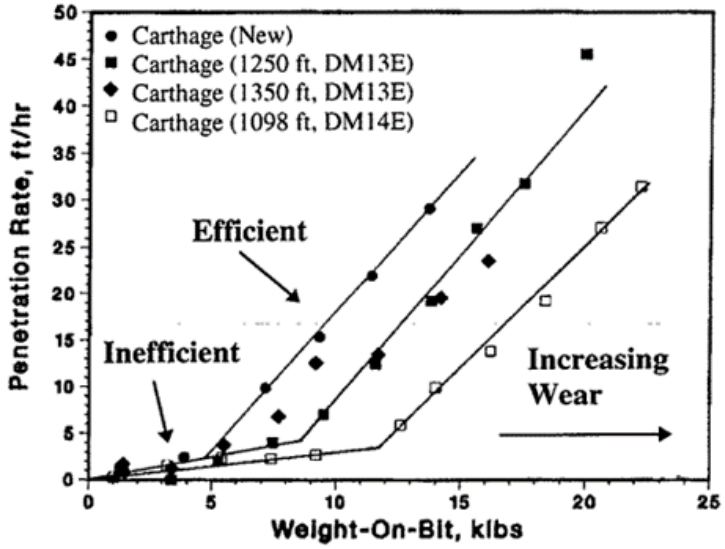

Figure II.31. Laboratory test results of a six bladed PDC bit in Carthage limestone during increasing stages of wear (Sinor et al., 1998).

Dagrain (2006) studied this problem on the scale of a PDC cutter. He performed many linear cutting tests with rectangular cutters presenting different wear flat lengths and surface conditions. These experimental results also show that minimum vertical force is necessary for efficient cutting mode (Figure II.32 (a)). It also shows that this minimum force increases with cutter wear. Besides, the literature widely documented that cutter wear increases tangential force (Dagrain and Richard, 2006a). Based on many works, the relation between Specific Energy and Drilling Strength with respect to the cutter wear is schematized as in Figure II.32 (b) when cutting is performed in the scratching regime.

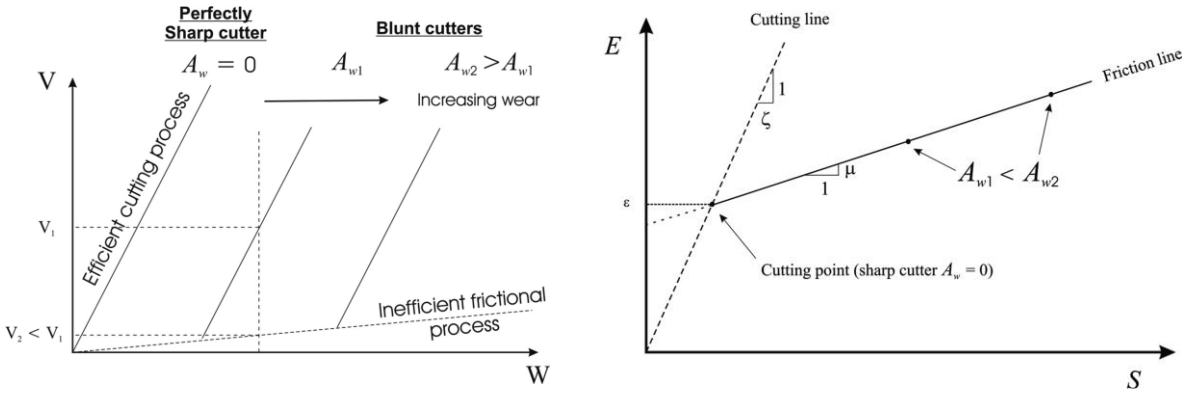

Figure II.32. Impact of cutter wear: (a) Rate of penetration (V) versus Weight on Bit (W), (b) Evolution of E-S diagram with the cutter wear (Dagrain and Richard, 2006a).

3.2.1.7 ***Impact of the cutting speed***

Since the linear cutting test benches operate at speeds ranging from millimeters to centimeters per second, the impact of cutting speed on cutting forces in atmospheric conditions has been considered negligible due to the narrow range of speeds tested. For example, Liu & Zhu (2019), who performed cutting tests at cutting speeds ranging between 8 and 24mm/s, indicated that cutting velocity has no impact on the magnitude of cutting forces or scratching-chipping regime transition. However, real cutting speeds in oil drilling are on the order of meters per second. Furthermore, many works in rock mechanics emphasize that the mechanical proprieties of rocks increase with the deformation rate (Qi et al., 2009). It suggests that such speeds could impact cutting forces.

Based on this consideration, researchers of "Mines ParisTech" performed tests on a Single Cutter Tester with cutting velocities from 0.03m/s to 2m/s (Gerbaud, 1999; Pelfrene et al., 2011; Amri et al., 2016). Their results indicate that cutting forces increase with cutting speed. Moreover, they noticed that this rate-effect is more important on the vertical cutting force than the tangential one. For instance, during Vosges sandstone tests (Amri et al., 2016), the normal force F_n is increased by 46% when RPM is raised from 10 to 120, whereas the tangential component F_t is increased by only 11%. However, based on the results presented by Amri et al. (2016), this 11% value seems low. Indeed, by observing the graph in Figure II.33, it can be noticed that the difference is much more important during the first rotation of the test than the 11% announced. Nevertheless, the difference seems to be smaller at the end of the test and after several rotations.

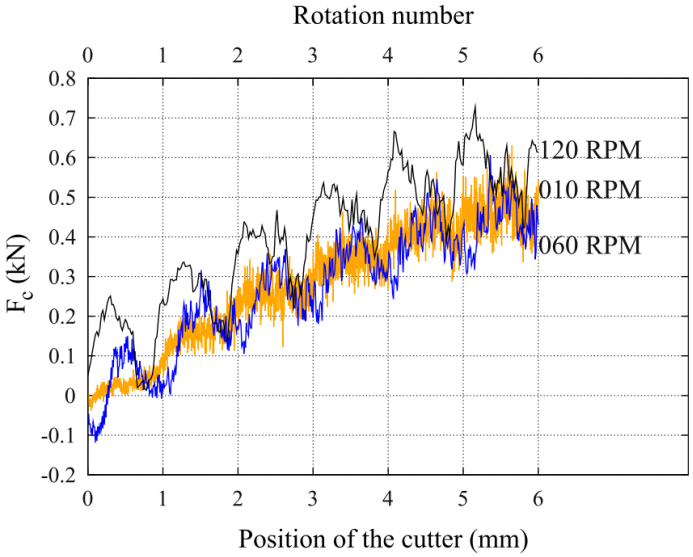

Figure II.33. Variation of the tangential cutting force component with the vertical position of the cutter at atmospheric pressure on the Vosges Sandstone (Amri et al., 2016).

3.2.1.8 Impact of the cutter size

According to Pelfrene (2010), who reported the results of Richard (1999) and Gerbaud (1999), the width or diameter of the cutters has no impact on the cutting mechanism. Richard, who has carried out tests with rectangular cutters of different widths (between 4.8 and 14.25 mm), showed that the cutter width does not influence the critical transition depth between scratching and brittle regimes. Gerbaud, who worked with circular cutters, showed that small diameter (8 mm) cutters are as efficient as larger ones (19 mm).

3.2.2 Analytical models of rock cutting in atmospheric conditions

Analytical models are based on qualitative experimental observations (phenomenological models) or quantified test results (experimental models) to build a mathematical model to estimate the cutting forces. These models generally have the mechanical properties of the rock and the cutting parameters as input parameters. Moreover, they make assumptions about the chip geometry and the failure criterion to calculate the force equilibrium between the cutter and the chip to determine the failure forces explicitly.

The first rock cutting models were strongly inspired by Merchant (1945) and Nishimatsu (1972) models, which deal with metal cutting and mining. The models presented below are only concerned with the cut under atmospheric conditions. All those involving a parameter related to confinement will be included in section 3.3.4 even if they can also be applied to the case without confinement.

For the sake of clarity, the symbols of the different parameters involved in the different models have been standardized.

3.2.2.1 Detournay & Defourny (1992) model

Detournay & Defourny (1992) developed a cutting model with a worn cutter based on the Merchant's model. They assume that the rock has a ductile behavior and that the cutting mechanism is composed of two simultaneous mechanisms: pure cutting at the cutting face and the contact between the rock and the wear flat. Therefore, the authors consider that the cutting force exerted on the worn cutter can be decomposed into a pure cutting force (F^c) transmitted by the cutting face and a frictional force (F^f) located at the wear flat (Figure II.34).

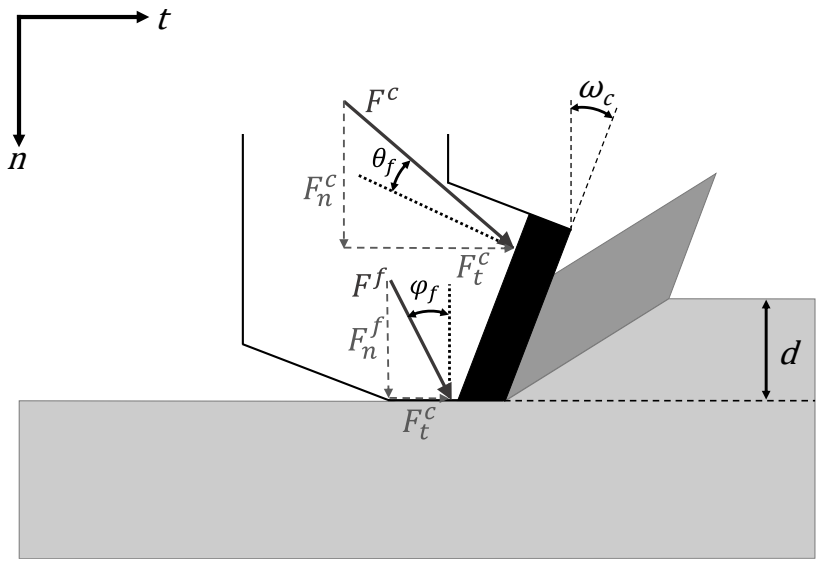

Figure II.34. Decomposition of the total force applied on the cutter in Detournay & Defourny (1992) model.

Hence, the tangential and vertical cutting forces can be decomposed into a cutting component and a friction one and are expressed as:

$$F_t = F_t^c + F_t^f \tag{II.13}$$

$$F_n = F_n^c + F_n^f \tag{II.14}$$

Where F_t^c and F_t^f are respectively the cutting and friction components of the tangential force while F_n^c and F_n^f are the cutting and friction components of the normal force. Figure II.34 presents the decomposition of the force. When the cutter is perfectly new, F_t^f and F_n^f are equal to zero.

Moreover, the authors assume that the cutting forces due to pure cutting are proportional to the active surface of the cutter, such as:

$$F_t^c = \varepsilon A_c \tag{II.15}$$

$$F_n^c = \zeta \varepsilon A_c \tag{II.16}$$

Where ε is the Intrinsic Specific Energy and ζ is the ratio between the vertical and tangential forces acting on the cutting face. ζ can be calculated by:

$$\zeta = tan(\omega_c + \theta_f) \tag{II.17}$$

Regarding forces acting on the wear flat due to frictional contact and considering the coefficient of friction μ equal to $tan\,(\varphi_f)$, component F_t^f and F_n^f are related by:

$$F_t^f = \mu\, F_n^f \tag{II.18}$$

Divided by the active surface A_c, the tangential force F_t and the normal force F_n are respectively assimilated to a Specific Energy (E) and a Drilling Strength (S). Using the equation here above, the authors then establish a linear relationship between E and S, governed by the equation:

$$E = (1 - \mu\,\zeta)\,\varepsilon + \mu\, S \tag{II.19}$$

As ε, ζ and μ depend on many cutting parameters and therefore cannot be determined a priori, this model is not designed to predict the elementary cutting forces but to follow the evolution of the drilling with the help of the two generic quantities, the Specific Energy E and the Drilling Strength S (Figure II.35 (a)).

To validate their model, Detournay & Defourny (1992) use the experimental results of Glowka (1989) performed on the Berea sandstone with new and worn circular cutters having a cutting angle of 20° and a diameter varying from 12.7 to 19.1 mm. Figure II.35 (b) shows the E-S diagram for different cutting depths. As predicted by relation (II.19), the values align on a line with a slope of $\mu = 0.82$.

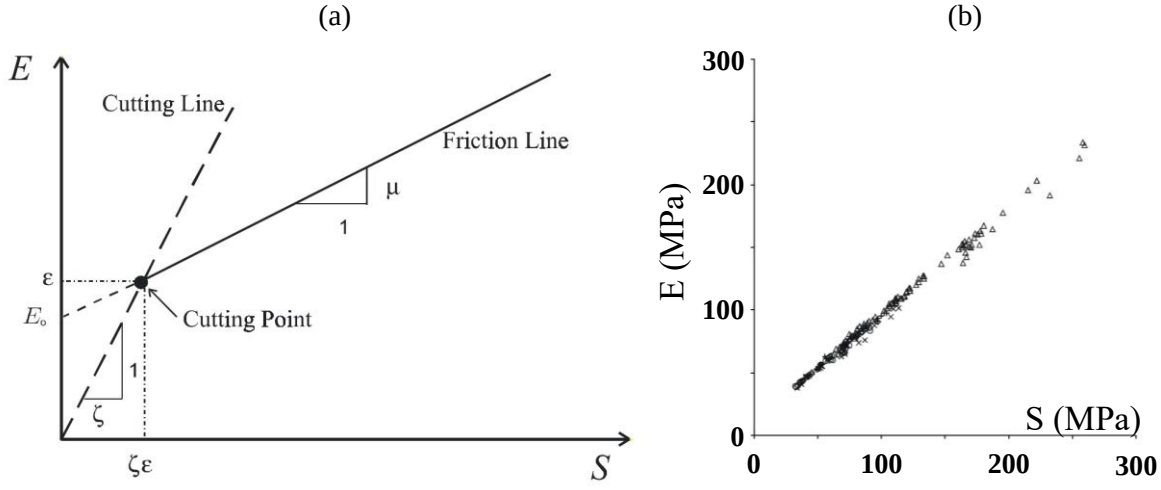

Figure II.35. Theoretical E-S diagram of Detournay and Defourny (a) and E-S Diagram based on results of Glowka (1989) (b). Images modified from Dagrain (2001).

3.2.2.2 ***Wojtanowicz & Kuru (1993) model***

Like Detournay & Defourny (1992), Wojtanowicz & Kuru (1993) consider that two forces are applied to the cutter: one to cut the rock with the cutting face and another to counter friction on the wear flat. Moreover, the total cutting force is decomposed into normal force (F_n) and tangential one (F_t) as shown in Figure II.36 and given by:

$$F_n = F_c \ sin\,\omega_c + F_{fc}\,cos\,\omega_c + \ F_w\,cos\,\omega_p + \ F_{fw} \ sin\,\omega_p \qquad \text{(II.20)}$$

$$F_t = F_c \ cos\,\omega_c - F_{fc}\,sin\,\omega_c - \ F_w\,sin\,\omega_p + \ F_{fw} \ cos\,\omega_p \qquad \text{(II.21)}$$

Where F_c is the cutting force perpendicular to the cutting face, F_{fc} is the friction force acting on the cutting face, F_w is the normal force acting on the wear flat, F_{fw} is the friction force acting on the wear flat, ω_c is the back rake angle and ω_p is the penetration angle.

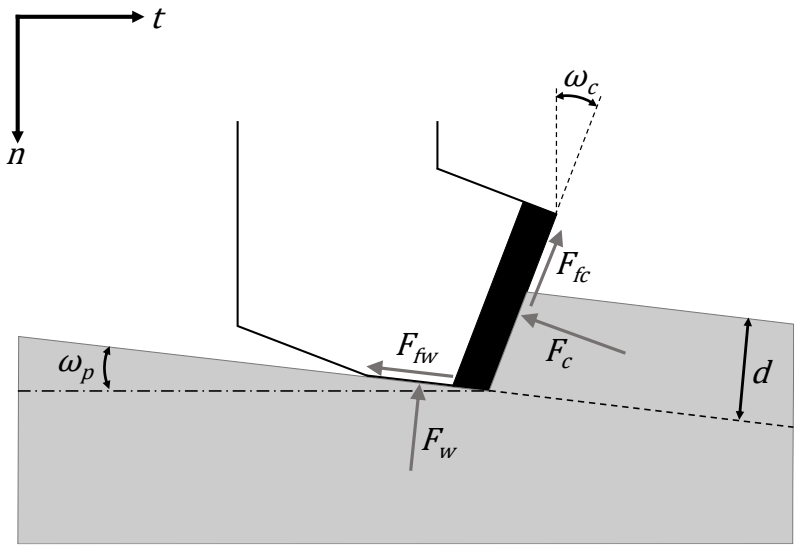

Figure II.36. Cutting model of Wojtanowicz & Kuru (1993).

Arguing that rocks present a ductile behavior in high-depth conditions, the authors assume that the rock has a ductile behavior at the cutter-rock interface. Moreover, they note that the cutting process is cyclic and assume that the cutter works in shearing mode on the cutting face and punching mode on the wear flat. Moreover, the forces responsible for shearing and punching are assumed to be directly proportional to the contact surfaces subjected to them. Finally, the authors hypothesize that the friction angle between the cutter and the rock on the cutting

face and at the wear flat are equal. They also consider that the resistance to shearing (R_s) and resistance to punching (R_p) are constant and intrinsic values of the rock.

Based on these simple assumptions, they provided the following equations:

$$F_c = R_s \ A_c \tag{II.22}$$

$$F_w = R_p \ A_f \tag{II.23}$$

Where A_c and A_f are respectively the cutting area and the area of the wear flat. Introducing the metal-rock friction coefficient μ on the two friction surfaces and considering that the penetration angle is very small for a small value of depth of cut, they obtain:

$$F_t = R_s \ A_c \ (cos\, \omega_c - \ \mu \, sin\, \omega_c) + \ \mu \, R_p \, A_f \tag{II.24}$$

$$F_n = R_s \ A_c \ (cos\, \omega_c + \ sin\, \omega_c) + \ R_p \, A_f \tag{II.25}$$

To validate this model, Kuru & Wojtanowicz (1995) realized an experimental study to measure the sliding friction between sharp PDC cutters and the rock surface. The experimental device used was composed of a rock disk fixed between two identical cutters on which they applied a small normal force (F_n). In this way, they were sure to be in pure friction without cutting rock. The contact generated a frictional tangential force (F_t) which was measured continuously. Their results show that there exists a linear relationship between the normal and tangential forces. Therefore, they conclude that the friction coefficient is small and independent of the normal force. Moreover, they found that the friction coefficient varies slightly depending on the rock tested (two sandstones, one granite, and one shale) even though they have different mechanical properties.

Unfortunately, this study did not address the friction between the wear flat and the rock. Moreover, the authors do not give any information on the determination of the stress applied on the wear flat, which they consider to be the punching strength of the rock.

3.2.2.3 ***Pelfrene's model***

Pelfrene (2010) developed his analytical model based on laboratory experiments carried out on four limestones with rectangular chamfered and unchamfered cutters. As his experimental study highlighted the dependence of the cutting forces on the cutting speed, he tried to incorporate it into his model.

Figure II.37 gives a representation of his model where the cutter cuts the rock with a velocity V_c, a depth of cut d, and a cutting angle ω_c. He defines a new cutting angle, the confinement angle ω_{co} which is a function of chamfer parameters, back rake angle and the depth of cut.

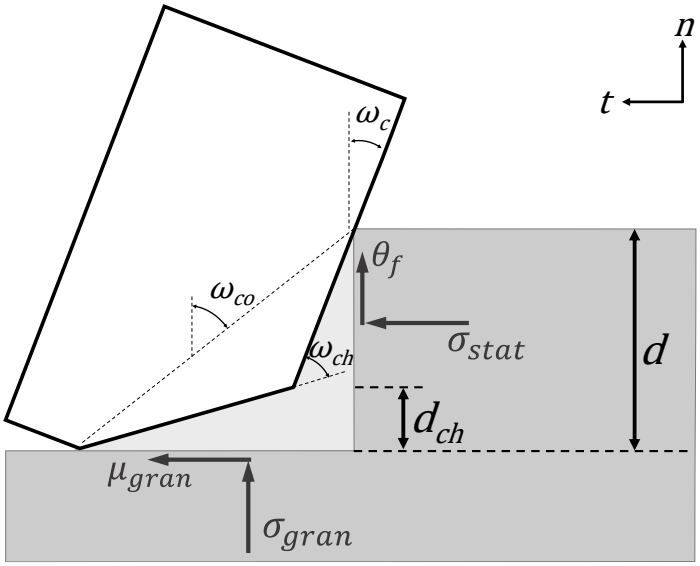

Figure II.37. Cutting model of Pelfrene (2010).

Moreover, its model considers the presence of a zone of crushed rock between the chamfer and the rock. Pelfrene (2010) assumes that this zone of crushed rock is rigid and that the limit between the crushed rock and the "virgin" one to be cut is vertical.

Finally, he decomposes the cuttings forces into two parts:

- The pure cutting forces F_n^c and F_n^c acting on the interface crushed rock/virgin rock and given by:

$$F_t^c = \sigma_{stat}\, A_c \tag{II.26}$$

$$F_n^c = \sigma_{stat}\, A_c\, tan\theta_f \tag{II.27}$$

- The friction forces F_n^f and F_n^f acting on the interface crushed rock/bottom of the groove, which are governed by a third body friction law that depends on the cutting speed, are given by:

$$F_t^f = \sigma_{gran}\, \mu_{gran}\, A_c\, tan\omega_{co} \tag{II.28}$$

$$F_n^f = \sigma_{gran}\, A_c\, tan\omega_{co} \tag{II.29}$$

$$\sigma_{gran} = \sigma_{stat} \left[1 + A_{gran} \log\left(1 + \frac{V_c}{V_{gran}}\right)\right] \tag{II.30}$$

Where σ_{stat} is the normal mean cutting stress, A_c is cutting area, θ_f is the friction angle at the cutting face, σ_{gran} is the normal stress on the bottom of the groove and A_{gran} and V_{gran} are fitting parameters to determine for each rock. μ_{gran} is the coefficient of friction on the contact between the crushed area and the bottom of the groove and depends on three fitting parameters (μ^+, μ^-, k_μ) according to the following relationship:

$$\mu_{gran} = (\mu^+ - \mu^-)\, exp\left(-k_\mu\, \sigma_{gran}\right) + \mu^- \tag{II.31}$$

3.2.3 Numerical modeling of rock cutting in atmospheric conditions

Numerical methods present the advantage that they do not require defining in advance the chip geometry, contrary to the analytical methods presented previously. The use of numerical models is more recent and has become more and more popular since the increase in the computing power of personal computers. Both continuous and discontinuous methods have been used to study the cutting mechanism under atmospheric conditions. Onate & Rojek (2004) and Mohammadnejad et al. (2017) have also used hybrid methods to simultaneously study fracture propagation in the rock and cutter wear. As their work aimed to study cutting with drag bits, it is only quoted but will not be developed further.

Inventories of different numerical modeling works dealing with rock cutting, in general, have already been made by different authors such as Jaime (2011) and Menezes (2017). Appendix A summarizes and completes their database. The following paragraphs discuss the different approaches used to determine the cutting forces and fracture propagation in the rock cutting process specifically dedicated to drilling.

3.2.3.1 Continuous method

Various numerical continuous methods such as Displacement Discontinuity Method (DDM) or Boundary Element Method (BEM), Finite Element Method (FEM), and Finite Difference Method (FDM) have been used to study rock cutting mechanism. The following paragraphs give some examples of research implementing continuous numerical models. Although these approaches have been used since the 80s, their contributions were limited for a long time.

Ingraffea (1987) studied the chipping formation with 2D FEM based on Linear Elastic Fracture Mechanics (LEFM). Due to the definition of LEFM, this work was limited to the crack's initiation and could not model the chip's motion. Moreover, this method could not simulate a scratching regime (Figure II.38).

Yu (2005) used 3D FEM. Although his study aimed at mining, it is interesting to note that using an erosion algorithm (elements are eroded when reaching failure criterium) allowed him to calculate cutting forces in scratching mode equivalent to those measured in the laboratory. Unfortunately, this method does not allow to represent the formation of chips (Figure II.39).

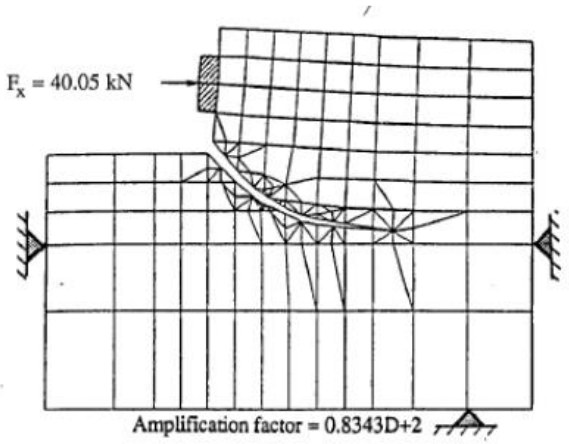

Figure II.38. Cracks propagation and chip formation with FEM based on LEFM (Ingraffea, 1987).

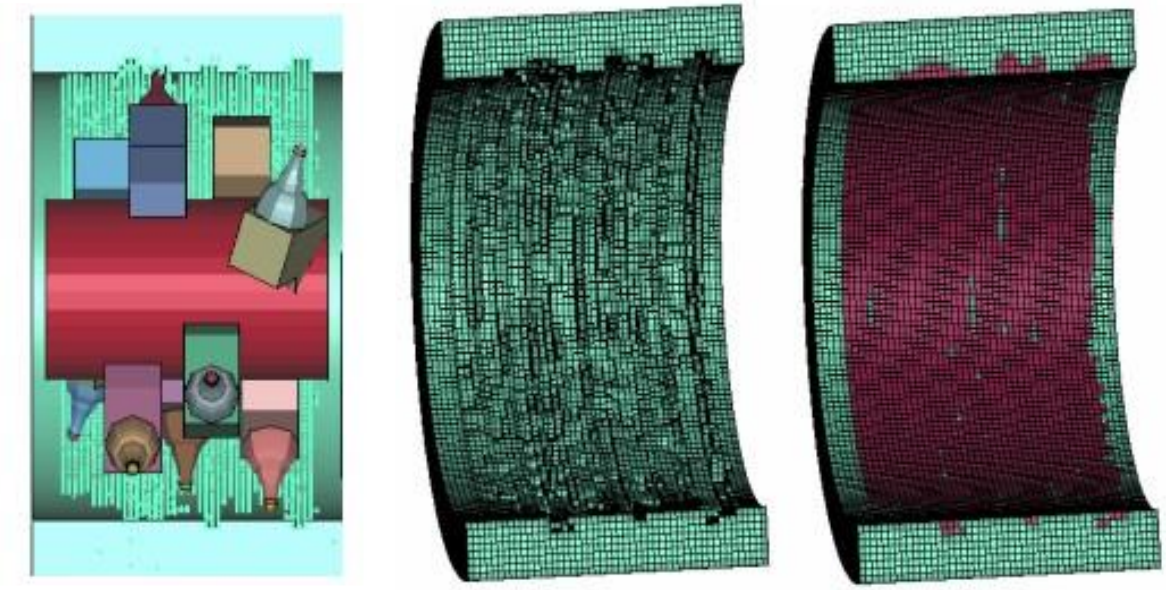

Figure II.39. Continuous mining simulation with 3D FEM: (a) total model, (b) grooves geometry and (c) deleted rock element highlighted in red (Yu, 2005).

Tulu et al. (2008) developed a numerical model based on FLAC3D to simulate circular cutting tests. As Yu (2005) did, they used an erosion algorithm but, in their case, this algorithm is based on a pre-determine amount of plastic strain. When a model element reaches this limit, it is "nulled" or removed from the model. Even if Tulu (2009) mentioned that this approach effectively represents the removal of chips, it does not allow an accurate representation of the fracture propagation and the chip evacuation. Moreover, while the trends in the evolution of the forces with the cutting parameters are qualitatively comparable with the experiments, their magnitude is far from it.

Up to there, continuous numerical models were focused on one of the two cutting regimes. They could not explicitly model the fracture propagation, the formation of the chip, and its removal. The first ones to reproduce with the same model the two failure mechanisms were Jaime (2011), Fontoura et al. (2012) and Zhou (2013).

Jaime (2011) used the Finite Element Method through LS-DYNA software to model linear cutting in 2D and 3D (Figure II.40). Thanks to the implementation of an erosion algorithm and the use of a material model allowing to represent elastic and plastic deformations as well as damage under static and dynamic loading, they were able to model the evolution from scratching failure mode to chipping one as the depth of cut increase. Jaime (2011) highlighted that the cutting forces obtained numerically show a good agreement with the experimental ones obtained during slab tests in chipping mode. However, in scratching mode, the model underestimated the cutting forces. She attributed this underestimation to the erosion algorithm that deletes model elements after failure and inhibits the presence of debris in front of the cutter. In contrast, tangential cutting forces calculated during cutting simulation in groove were found inconsistent compared to experimental ones.

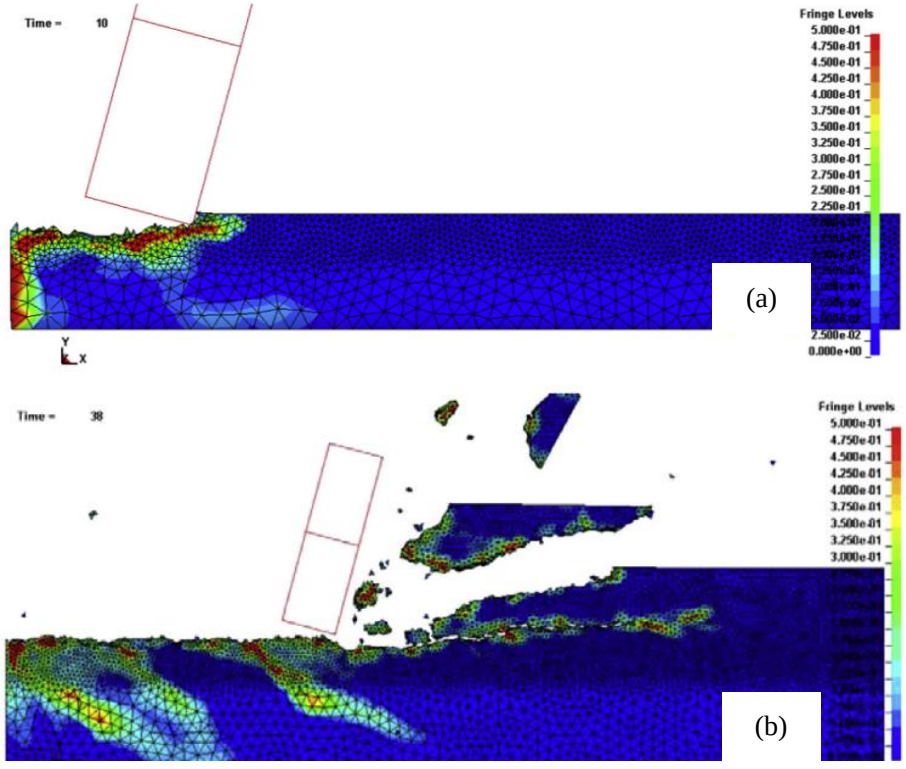

Figure II.40. Comparison of fracture patterns (a) in scratching mode (b) in chipping mode (Jaime, 2011).

Based on Jaime's numerical model, Zhou (2013) first extended the modeling to circular cutting by a single cutter and then tried to model rock drilling by a full drill bit with multiple cutting tools. As for Jaime, his modeling results for rectangular and circular cutters were consistent qualitatively with available laboratory test results. However, the cutter loses contact with the rock during simulation due to the erosion algorithm, leading to an underestimation of cutting forces and Specific Energy. His goal was to demonstrate such model feasibility regarding full bit modeling, but the results were not yet representative of the actual drilling process.

On their side, Fontoura et al. (2012) also used an element erosion criterion in their rock cutting model based on the Finite Element Method powered by the ABAQUS code. They performed 2D linear and 3D circular cutting simulations (Figure II.41). Although they successfully reproduced the two rupture modes, their forces pattern and magnitude differ substantially from the experimental ones.

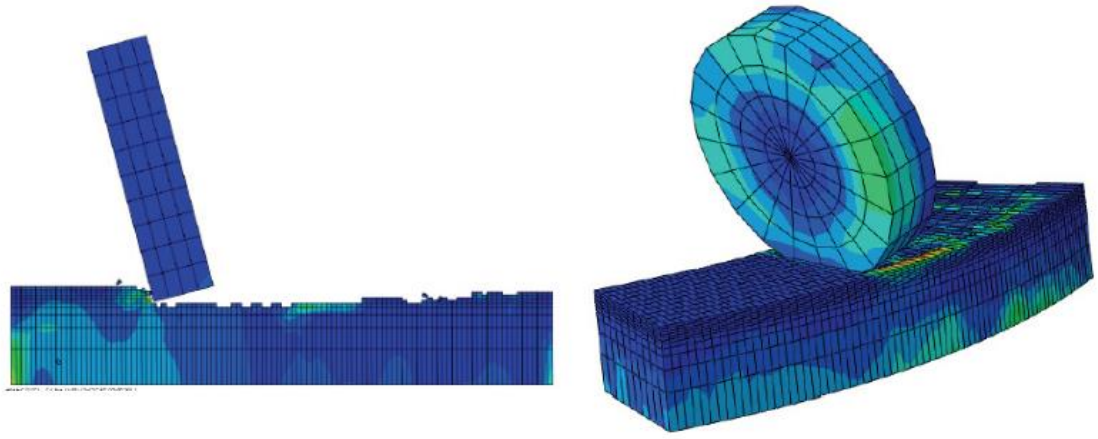

(a) (b)

Figure II.41. Cutting simulations with FEM in scratching mode in (a) 2D linear cutting and (b) 3D circular groove cutting (Fontoura et al., 2012).

Based on these encouraging results, several researchers (Carrapatoso et al., 2015; Yari et al., 2018) have continued the process by working with LS-DYNA and ABAQUS. Despite the improvements, the results of the continuous method are only qualitatively consistent with the experimental results. There is always a gap between the forces measured in laboratories and those estimated by numerical models from a quantitative perspective.

3.2.3.2 ***Discontinuous method***

The use of discontinuous methods in rock cutting modeling is more recent. Indeed, it was limited for a long time due to the high computing resources. Unlike continuous methods, whose main weakness has been for a while that they do not represent fracture propagation, discontinuous methods allow this representation by definition. This consideration makes them suitable for studying destruction mechanisms.

The first attempt to use a discontinuous method seems to be the one of Huang et al. (1999), according to Rizo (2013). Huang et al. (1999) studied rock cutting with the Discrete Element Method (DEM) using the two-dimensional Particle Flow Code (PFC) of Itasca. One of her thesis objectives was to examine if the occurrence of the two failure modes observed in rock cutting experiments can be duplicated in numerical simulation with DEM. The results show that this numerical method can reproduce scratching and chipping failure modes (Figure II.42). However, the cutting forces were not comparable to those observed in the laboratory. Nevertheless, their evolution is comparable, with a linear increase at shallow depths to reach a plateau once the chipping mode is reached (Figure II.42 (c)).

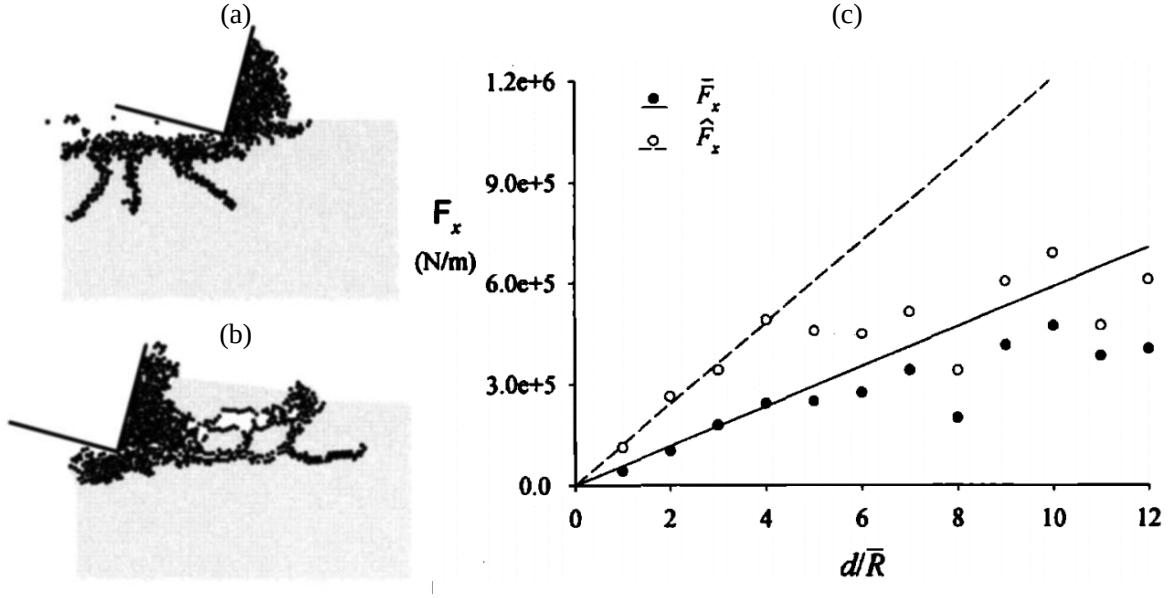

Figure II.42. Numerical results obtained by Huang et al. (1999) with Discrete Element Method: (a) and (b) show the transition between scratching and chipping mode and (c) plots the evolution of maximum and mean cutting forces with respect to the depth of cut.

Other researchers decided to develop this approach further (Joodi et al., 2012; Lin et al., 2012; Jiang et al., 2015; Liu et al., 2018). Many of these works have focused on the qualitative aspect of this modeling method allowing to study the transition

from scratching to chipping mode without requiring complex models as for the continuous methods. From a quantitative point of view, many works refer to an underestimation of cutting forces compared to those measured in the laboratory in 2D.

To overcome this limitation, researchers have tried to introduce improvements. For example, Rizo (2013) replaced the rigid and unbreakable particles generally used in the Discrete Element Method with particles that could be crushed once their strength was reached. Unfortunately, this method did not improve the problem of force estimation in 2D. On the other hand, this method did not allow to model the two failure modes without modifying the cutting parameters, such as the speed.

On the other hand, some 3D models showed a better estimation of the cutting forces despite a slight underestimation or overestimation depending on the parameters chosen to model the rock (Lin et al., 2012; Rizo, 2013; Carrapatoso et al., 2014). These models generally used particles with sizes larger than the size of the rock grains (Figure II.43). A better concordance between the two could solve this problem.

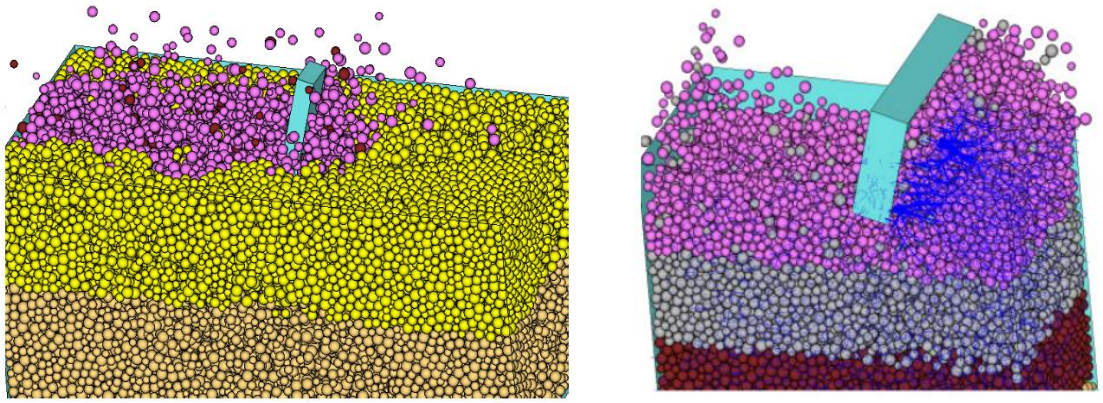

(a) (b)

Figure II.43. 3D DEM modeling of rock cutting tests (a) in groove mode (Rizo, 2013) and (b) in slab mode (Lin et al., 2012).

3.2.4 Discussion

This literature review shows that rock cutting under atmospheric conditions has already been extensively studied experimentally. It allows understanding the impact of the different parameters on the mode of destruction encountered and their qualitative and quantitative effects on the cutting forces and energies. However, many researchers were interested in the modes of destruction by scratching and chipping, but these destruction modes are characteristic of brittle rocks. Indeed, few experimental works have studied the mechanism of cutting with ductile materials, such as clay. However, rocks presenting a ductile behavior should present other failure facies than the two previously mentioned.

Despite this phenomenological knowledge, analytical models developed just for cutting in atmospheric conditions are not yet able to synthesize the complexity of this destruction mechanism. Indeed, no one considers the two failure modes and the transition from one to the other. Models are generally developed for one of these two. Moreover, these analytical models do not allow determining the cutting forces without involving parameters that must be determined through cutting tests. However, the main objective should be to determine the cutting forces and energies based only on the mechanical properties of the rocks and the geometric and dynamic cutting parameters.

Research based on the Discrete Element Method has shown promising results regarding numerical methods. Indeed, this numerical method allows representing the evolution of the destruction mechanism according to the cutting parameters, such as the depth of cut. However, the cutting forces are largely underestimated in 2D models but the 3D ones partially overcome this problem giving cutting forces and energies closer to the experimental ones. Although the erosion algorithms in the continuous methods have made them more suitable for studying the cutting mechanism, they still do not allow for simulating the scratching mechanism.

3.3 Rock cutting mechanism under confinement

While the cutting mechanism under atmospheric conditions has been extensively studied in the literature, studies dealing with its evolution under high-depth conditions are less abundant. Moreover, these studies generally focus on the impacts of the confinement due to drilling mud and ground stresses, and they do not address pore pressure or temperature effects.

This is mainly due to the test benches which, for the most sophisticated ones (Pelfrene, 2010), theoretically allow to take into account the ground pressure, the mud pressure and control the pore pressure (Figure II.44). However, the results in the literature generally refer to tests conducted at a mud pressure equal to the ground pressure and the sample was generally saturated before the test. However, the pore pressure is not controlled during the test (Amri et al., 2016).

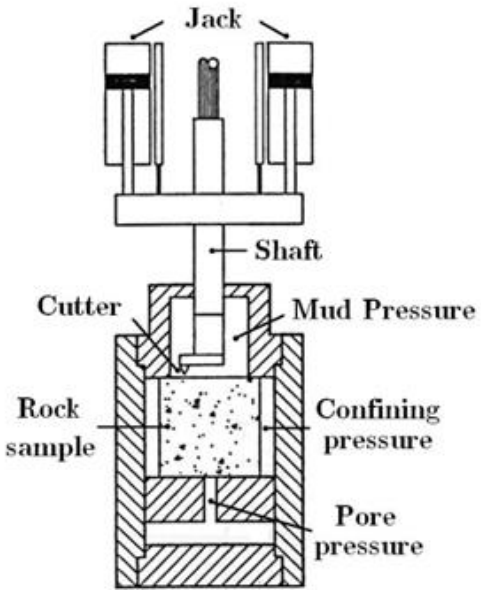

Figure II.44. Sketch of the Single Cutter Tester of Mines ParisTech laboratory (Pelfrene et al., 2011).

Finally, while many of the results presented above were obtained from linear cutting tests, those presented below are from circular tests, generally in multi-passes. This means that the cutter passes several times in the same groove. Moreover, it is not the depth of cut that is imposed here but the rate of penetration.

Based on these considerations, Figure II.45 gives a 3D representation of cutting tests performed under confinement. Before presenting analytical and numerical models of rock cutting under confinement, the following sections present the

evolution of the cutting force and destruction mechanism with respect to the increase of confinement. Moreover, section 3.3.3 discusses the influence of confinement on parameters such as back rake angle and depth of cut.

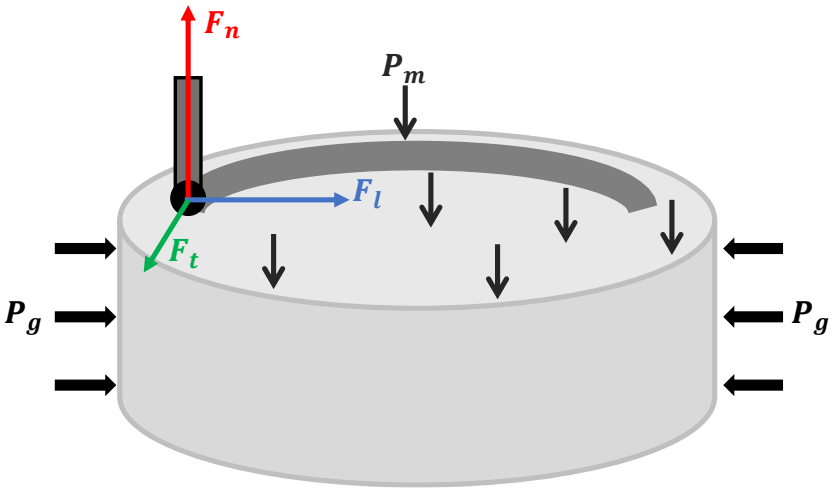

Figure II.45. 3D representation of single cutter test under confinement.

3.3.1 Evolution of destruction mechanism with confinement

The most important effect of confinement concerns cuttings morphology. While rock cutting in atmospheric conditions generates fine powder of chips depending on the depth of cut, under confinement, it generates centimetric ribbons of agglomerated rock fragments/particles whatever the depth of cut (Figure II.46).

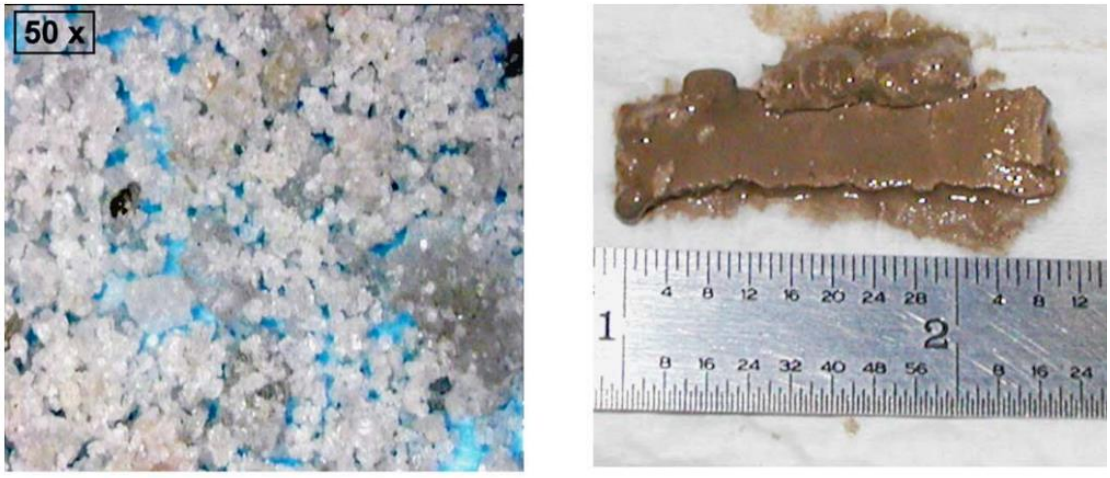

(a) Without confining pressure (b) At a confining pressure of 3.44 MPa

Figure II.46. Cuttings morphology obtained during (a) test in atmospheric conditions and (b), under a confinement of 3.44 MPa. Depth of cut was not mentioned by authors (Kaitkay and Lei, 2005).

Interestingly, this phenomenon occurs at low confinement values, as shown by the cutting of Figure II.46 (b), which was obtained during a test with a confinement of 3.44 MPa (Kaitkay and Lei, 2005). Moreover, researchers mentioned that these cuttings stick on the cutter at the end of tests. The same composition of cuttings has either also been reported in full-scale drilling experiments (Judzis et al., 2009).

These cuttings generally have a smooth face which results from the sliding of the agglomerated material along the cutting surface of the cutter. The other side of these ribbons presents a saw tooth shape (Figure II.47). Following Majidi et al. (2011), this shape comes from a cyclical process of accumulation and extrusion of debris at the cutting face. Crushed material accumulates at the base of the cutting face until the stresses generated by the new crushed rock are sufficient to extrude the previous debris. The same interpretation of the shape of the cuttings is provided by Rafatian et al. (2009), whose representation of this phenomenon is given in Figure II.48.

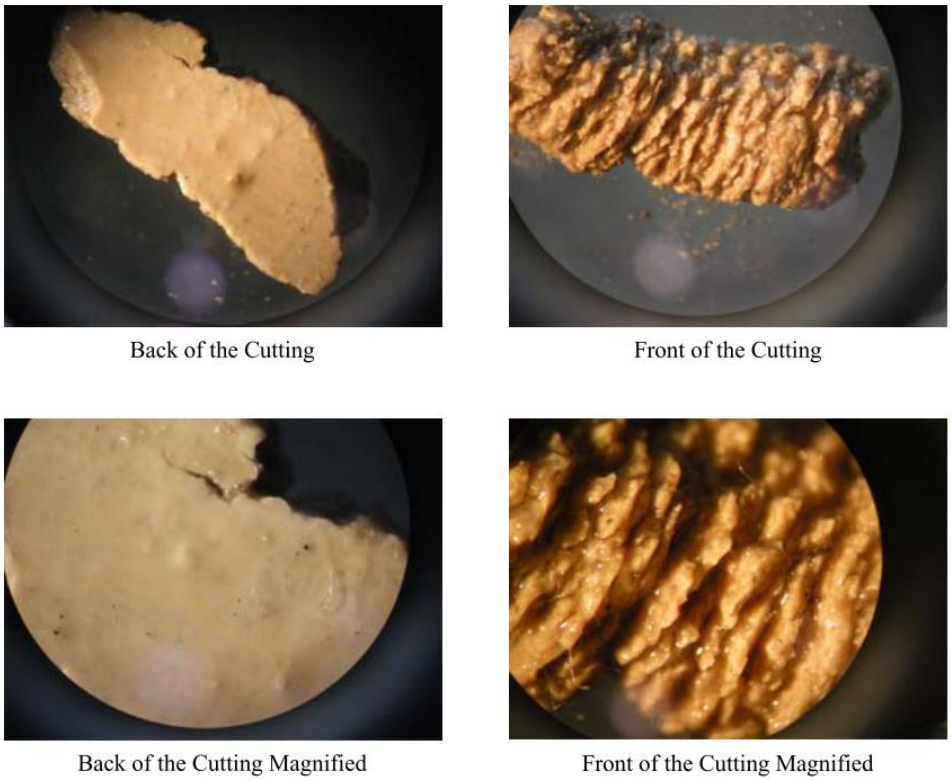

Figure II.47. Sides of cutting obtained under confinement (Rafatian et al., 2009).

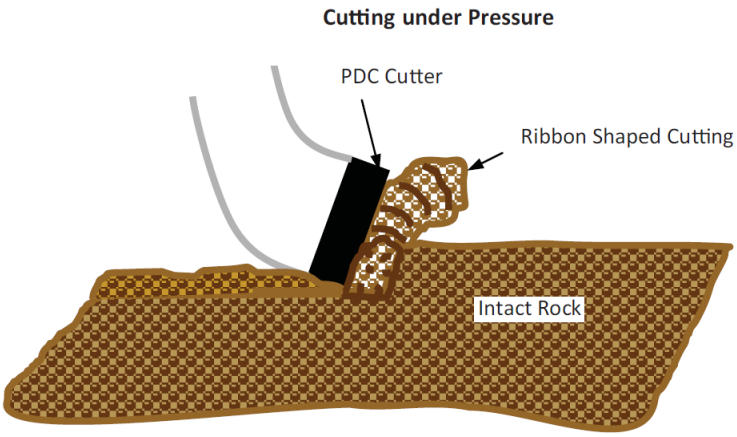

Figure II.48. Schematic representation of cutting mechanism under pressurized conditions (Rafatian et al., 2009).

3.3.2 Evolution of cutting forces and Specific Energy with confinement

As presented in Section 2.2, confinement has the effect of increasing the strength of rocks. It can be assumed that the confinement will increase the cutting forces and specific energies when performing tests under confinement. This assumption is verified by experimental results (Lei et al., 2004; Akbari and Miska, 2016; Amri et al., 2016).

Tests performed on Carthage marble by Kaitkay & Lei (2005) showed a significant increase in mean cutting forces and thrust forces increase with the increase of confining pressure, especially at low confinement values (Figure II.49 (b)). Indeed, the relationship between confinement and cutting force is not linear and presents a steep slope at low confinement. For example, Figure II.49 (a) shows that the cutting forces are multiplied by a factor greater than 3 when the confinement goes from 0 to 3.4 MPa, while they are only multiplied by about 1.7 between 3.4 and 34.4 MPa of confinement. Consequently, Specific Energy evolves in the same way.

As the Specific Energy tends to be of the same order of magnitude as the UCS in atmospheric conditions, Rafatian et al. (2009) compared the Specific Energy measured at different confinements with the theoretical Mohr-Coulomb model of Carthage Marble (Figure II.49 (b)). They showed that the apparent “rock strengthening” during cutting tests under pressure is much higher than the strengthening predicted by the Mohr-Coulomb model. They explained this substantial difference as part of the energy is used to move the cutting formed on the cutting face.

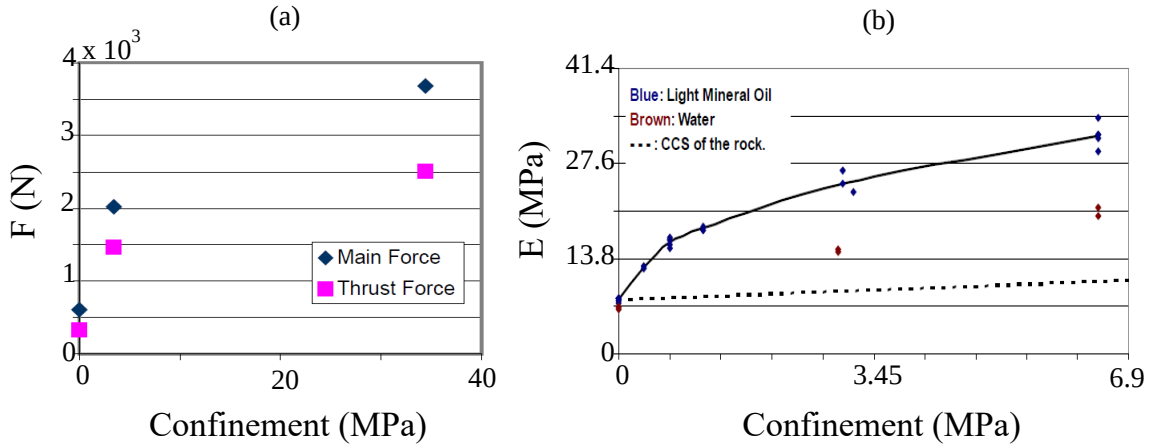

Figure II.49. Evolution of the cutting forces and Specific Energy with respect to the confinement obtained by: (a), Kaitkay & Lei (2005) and (b), Rafatian et al. (2009).

3.3.3 Interaction between confinement and cutting parameters

Section 3.2.1 showed how cutting parameters such as depth of cut or back rake angle impact cutting forces and Specific Energy under atmospheric conditions. The same trends are generally observed when a confining pressure is applied, independently of its value. Some examples are given in Figure II.50. In confined cutting tests, the Specific Energy also decreases with the depth of cut and increases with the back rake angle.

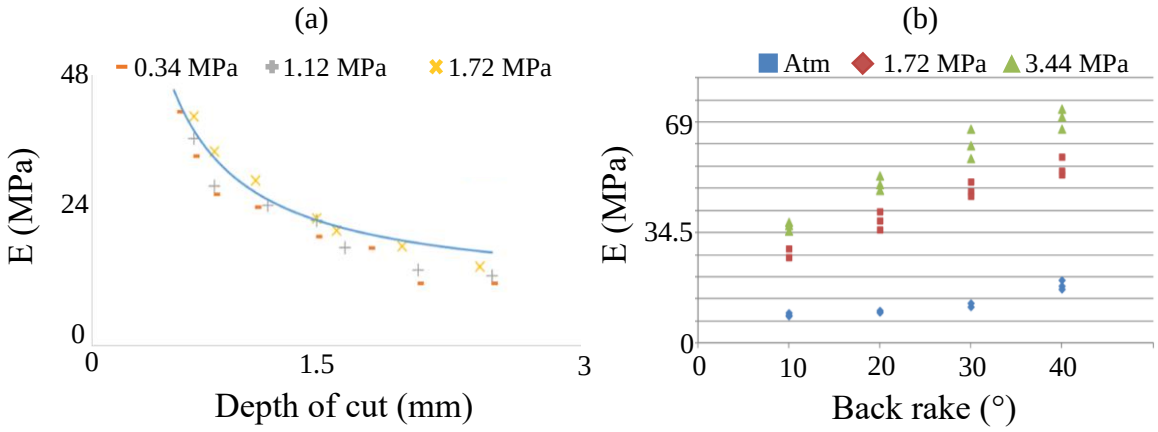

Figure II.50. Impact of cutting parameters on rock cutting under confinement: (a) impact of depth of cut (Akbari and Miska, 2017), (b) impact of back rake angle (Rajabov et al., 2012).

3.3.4 Analytical models of rock cutting under confinement

The next points present some of the main analytical models developed to model the cutting mechanism under confinement. As for section 3.2.2, the symbols of the different models have been standardized for the sake of clarity.

3.3.4.1 Cheatham and Daniel (1979) model

Cheatham & Daniels (1979) built their analytical model based on cutting tests performed on shales. During these tests, they used sharp PDC cutters with different shapes (circular, rectangular and triangular) and tested them with different cutting parameters and mud pressures. During these tests, they noticed that the chips generated were similar to those produced during metal cutting. Based on this observation, they take inspiration from Merchant's metal cutting model to build their rock cutting model. As for the Merchant's model, they consider the effect of the back rake angle and assume that the tangential stress τ exerted on the chip shear plane is independent of the normal stress σ (Figure II.51).

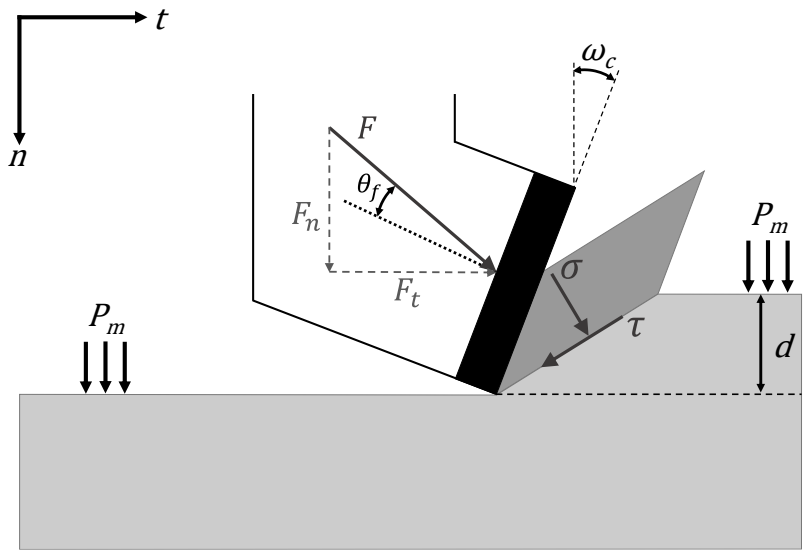

Figure II.51. Cutting Model of Cheatham & Daniels (1979).

By decomposing the average interaction force F on the cutting face into a normal force F_n and a tangential force F_t, they express the minimum cutting forces by:

$$F_t = 2\,\tau_s\,A_c\,\frac{cos\,(\omega_c + \theta_f)}{1 - sin\,(\omega_c + \theta_f)} \qquad \text{(II.32)}$$

$$F_n = 2\,\tau_s\,A_c\,\frac{sin\,(\omega_c + \theta_f)}{1 - sin\,(\omega_c + \theta_f)} \tag{II.33}$$

Where ω_c is the back rake angle, θ_f the friction angle between the cutter face and the rock, τ_s the shear strength of the rock and A_c the cross-section of the groove. The shear strength τ_s is assumed to be given by the following expression:

$$\tau_s = c\,\frac{cos\varphi}{1 - sin\varphi} + p_m\,\frac{sin\varphi}{1 - sin\varphi} \tag{II.34}$$

Where c is the rock cohesion, p_m is the confining pressure, and φ is the rock internal friction angle.

3.3.4.1 Detournay & Atkinson (2000) model

Like Cheatham & Daniels (1979), Detournay & Atkinson (2000) used Merchant's model to develop their rock cutting model under confinement with a sharp cutter (Figure II.52). However, contrary to Cheatham & Daniels (1979), they added three assumptions to the Merchant's model:

1. The effective normal stress and the shear stress across the failure plane satisfy a Mohr-Coulomb criterion.
2. A friction law relates the effective normal stress and the shear stress at the cutter-rock interface.
3. The interstitial fluid pressure along the cutter-rock interface is equal to p_m.

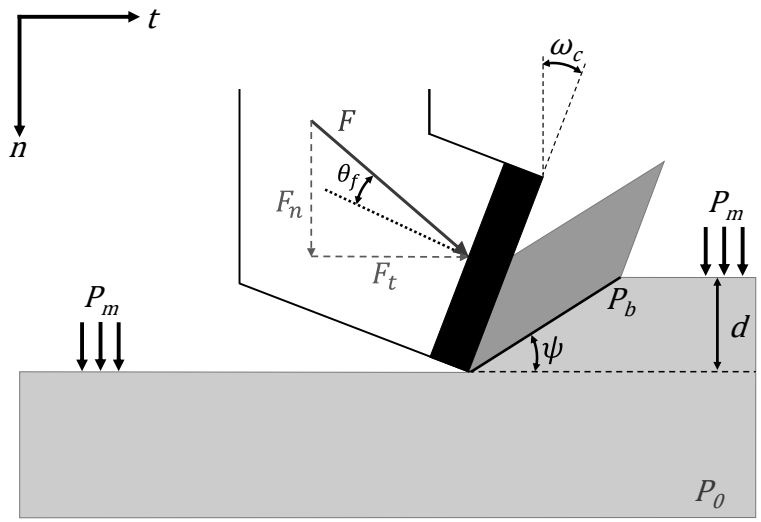

Figure II.52. Cutting model of Detournay & Atkinson (2000).

Based on the approach of Detournay & Defourny (1992), they express the tangential and vertical cutting forces as:

$$F_t = E\ A_c \tag{II.35}$$

$$F_n = \zeta\ E\ A_c \tag{II.36}$$

Where the Specific Energy E is given by:

$$E = \frac{2\ cos\varphi\ cos(\omega_c + \theta_f)}{1 - sin(\omega_c + \theta_f + \varphi)}\ [c + (p_m - p_b)\ tan\varphi] \tag{II.37}$$

This expression of the Specific Energy is obtained considering the principle of minimal external work which allows determining the inclination ψ of the shear failure plane given by:

$$\psi = \frac{\pi}{4} - \frac{\omega_c + \theta_f + \varphi}{2} \tag{II.38}$$

Based on equation (II.37), the authors mention that the Specific Energy evolves linearly with the difference between the mud pressure and the mean pore pressure at the shear plane. This equation also introduces the notion of average pore pressure along the shear failure plane p_b. The development of the authors leads them to define this pore pressure by:

$$p_b = p_0 + \Delta p \tag{II.39}$$

$$\Delta p = -\frac{\Delta\phi}{1 - \phi}\ \frac{1}{\phi C_f}\ g(\lambda; \psi) \tag{II.40}$$

Where p_0 is the initial pore pressure, Δp is the variation of pressure along the shear plane, ϕ is the initial porosity, $\Delta\phi$ is the variation of porosity along the shear plane, C_f the fluid compressibility, ψ is the inclination of the shear plane, and λ is a dimensionless number given by $V_c d/4\mathcal{D}$ with V_c the cutter velocity, d the depth of cut and $\mathcal{D}$ the diffusivity coefficient.

The function $g(\lambda;\psi)$ allows to identify of three operating regimes depending on the value of λ:

1. A "drained regime" when the cutter velocity is low ($0 < \lambda < 0.001$): the cut is made in drained conditions, which means that the pressure variation is null and $p_b = p_0$.
2. A transient regime ($0.001 < \lambda < 10$): Δp is a function of λ.
3. An "undrained regime" when the cutter velocity is high ($10 < \lambda$): in this regime, a cavitation phenomenon can occur along the shear plane ($p_b \leq 0$)

3.3.4.2 Models of Mines ParisTech

Understanding the cutting mechanism is a long story for the "Mines ParisTech" team. Since Sellami's model, researchers have developed it progressively (Sellami, 1990; Menand, 2001; Gerbaud et al., 2006; Pelfrene, 2010; Amri, 2016). Below some of these models are presented.

A Sellami's model

In his model, Sellami (1990) considers the general case of a worn PDC cutter (Figure II.53). He assumes when building his model that the cut is a cyclic process during which the cutter works at a depth of pass high enough to generate chips. His model estimates the minimum cutting forces by considering the equilibrium of a chip that breaks along a plane inclined by an angle ψ with respect to the horizontal.

His model is based on four assumptions:

1. The normal and tangential stresses acting on the cutting face and the wear flat are governed by Coulomb's friction law given by the metal-rock friction angle θ_f.
2. The ratio between normal stresses acting on cutting face and wear flat is close to 1.
3. Lateral confinement acting on the chips has no effect.
4. The chip is formed by shearing according to the Mohr-Coulomb criterion. The cohesion c and the internal rock friction angle φ are determined from triaxial tests.

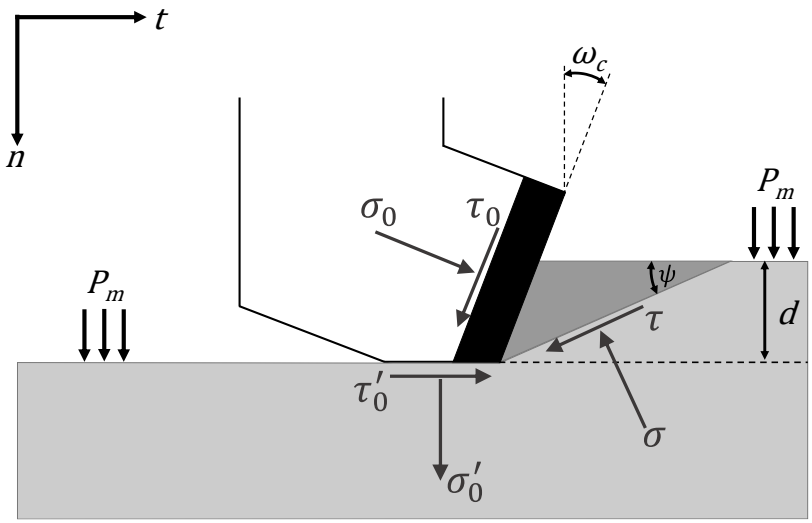

Figure II.53. Cutting model of Sellami (1990).

Writing the balance of forces on the chip and determining ψ to minimize the tangential forces, Sellami arrives at the following formulations of tangential and vertical cutting forces:

$$F_t = F_{co}\left[1 + \frac{A_f}{A_c}\frac{sin\,(\theta_f)}{cos(\omega_c + \theta_f)}\right] \tag{II.41}$$

$$F_n = F_{co}\left[1 + \frac{A_f}{A_c}\frac{sin\,(\theta_f)}{cos(\omega_c + \theta_f)}\right] tan\,(\omega_c + \theta_f) \tag{II.42}$$

With

$$F_{co} = R_{eq}\, d^{1.5} \tag{II.43}$$

$$R_{eq} = c\, A\big(\varphi, \omega_c, \theta_f, D, \psi\big) + p_m\, B\big(\varphi, \omega_c, \theta_f, D, \psi\big) \tag{II.44}$$

Where A_c and A_f are the active surface and the wear flat surface, θ_f is the metal-rock friction angle, ω_c the back rake angle, d the depth of cut, D the diameter of the cutter, φ the internal friction angle, ψ the chip failure angle and p_m the mud pressure. The failure angle ψ minimizing the rock equivalent strength (R_{eq}) is given by:

$$\psi = \frac{\pi}{4} - \frac{\omega_c + \theta_f + \varphi}{2} \tag{II.45}$$

Equations (II.41) and (II.42) determine forces to generate the chip. To be able to determine the mean forces, Sellami & Cordelier (1991) introduced the "apparent ductility coefficient" (C_{da}) that is function of the mud pressure. This coefficient his defined by:

$$C_{da} = \frac{F_{cmax} - F_{cmean}}{F_{cmean}} \tag{II.46}$$

For a brittle rock, this coefficient is near 1, while for a ductile one, it is close to 0 and varies with the confinement. However, this coefficient can only be determined based on experimental tests.

B Gerbaud et al. (2006) model

Gerbaud et al. (2006) based the development of their model on the fact that the previous models are too restrictive and do not consider certain phenomena such as the formation of a crushed zone between the cutter face and the chip, the presence of a chamfer or the existence of a backward flow of particles (Figure II.54).

Based on these considerations, they consider that the total force F acting on the PDC cutter is the sum of forces acting on the cutting face F^c, forces acting on the chamfer F^{ch}, forces acting on the back cutter surface F^b, and the ones acting on the wear flat F^f.

$$F = F^c + F^{ch} + F^b + F^f \tag{II.47}$$

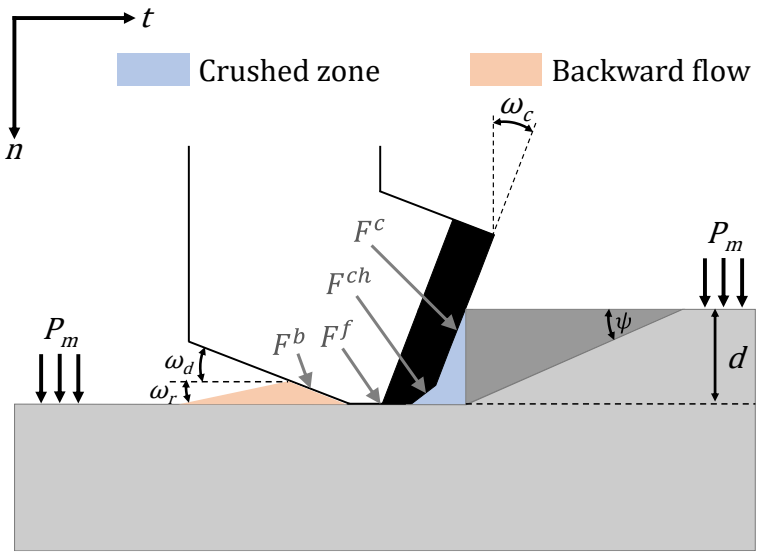

Figure II.54. Cutting model of Gerbaud et al. (2006).

They firstly introduce the rock equivalent strength σ_0. They determine this parameter considering the static equilibrium of the chip regarding the geometrical considerations in Figure II.54. σ_0 is given by:

$$\sigma_0 = \frac{c + p_m\,[(sin(\psi).cos(\psi) + cos^2(\psi)).tan(\varphi)]}{\left(1 - tan(\theta_f).tan(\varphi)\right).sin(\psi).cos(\psi) - tan(\theta_f + \varphi).sin^2(\psi)} \quad \text{(II.48)}$$

Where c is rock cohesion, φ the rock internal friction angle, θ_f the friction angle between the cutting face and rock, ψ the chip failure angle and p_m the mud pressure. ψ value is obtained by minimizing the equation (II.48):

$$\psi = \frac{\pi}{4} - \frac{\theta_f + \varphi}{2} \quad \text{(II.49)}$$

To determine the force acting on the cutting face, they suppose that the force is transmitted from the PDC to the chip through the crushed zone. It leads to the definition of φ' the friction angle between the crushed rock and the virgin one. The tangential and vertical components of F^c are then given by:

$$F_t^c = \sigma_0\,.(1 + k_G\,tan(\varphi')\,tan(\omega_c))\,.A_c \quad \text{(II.50)}$$

$$F_n^c = \sigma_0\,.\left(tan(\theta_f) + k\,tan(\omega_c)\right)\,.A_c \quad \text{(II.51)}$$

Where k_G is the ratio between the horizontal contact surface of the crushed zone and the product $A_c * tan(\omega_c)$; A_c is the cross-section and ω_c the back rake angle.

If the depth of cut is higher than the chamfer height, the chamfer forces result from the additional friction between the chamfer face and the crushed rock on the bottom of the groove and can be expressed by:

$$F_t^{ch} = \sigma_0\,tan(\varphi')\,A_{ch} \quad \text{(II.52)}$$

$$F_n^{ch} = \sigma_0\;A_{ch} \quad \text{(II.53)}$$

The cutting forces acting on the back face are not fully determined but are given by:

$$F_t^b = \sigma_0\;f(\alpha, d, \omega_c) \quad \text{(II.54)}$$

$$F_n^c = F_t^b \, f_1(\alpha, d, \omega_c) \tag{II.55}$$

Where α is the repression angle which is, according to Gerbaud et al. (2006), a rock property.

Finally, the wear forces are determined in the same way that Kuru & Wojtanowicz (1995) and are given by:

$$F_t^f = \sigma_0 \, \mu \, A_f \tag{II.56}$$

$$F_n^f = \sigma_0 \, A_f \tag{II.57}$$

Where A_f is the wear flat area and μ is the friction coefficient between wear flat and rock.

C Amri's model

The Amri (2016) model is the latest model developed by the "Mines Paristech team". Amri bases his model on the one of Gerbaud et al. (2006) that he modified to include the pore pressure along the shear plane. To do this, he changes the expression of σ_0 which becomes:

$$\sigma_0 = \frac{2\,[c + (p_m - p_b)\,tan(\varphi)]\,.cos\,(\varphi)}{1 - sin\,(\theta_f + \varphi)} \tag{II.58}$$

Compared to the model from which it is inspired, Amri's model does not consider the backward flow of crushed rock.

3.3.5 Numerical modeling of rock cutting under confinement

As for the experimental tests and analytical models, the bibliography concerning the numerical modeling of rock cutting under confinement is also less developed than the one in atmospheric conditions.

Lei & Kaitkay (2003) simulated rock cutting on Carthage Marble under confinement through Discrete Element Method in 2D with PFC2D powered by Itasca (Itasca Consulting Group, 2008a). Since they had already conducted experimental studies on Carthage Marble (Kaitkay and Lei, 2005), they decided to use this same rock for their numerical simulation. They simulate cutting tests for three confining pressures (0, 3.5, and 34.5 MPa) and two rake angles (-15 and -25 deg) with the cutting speed and depth of cut kept at 1m/s and 0.8 mm, respectively. These cutting parameters were selected to be comparable to the ones used experimentally.

The confining pressure is applied through the top row of particles. This first row act as a membrane that evolves with the cutter displacement. A force is applied to each particle of this membrane. The magnitude of this force depends on the pressure to apply and the particle's surface that could be in contact with a fluid.

From a qualitative point of view, Figure II.55 compares a cutting simulation in atmospheric conditions with another one at 34.5 MPa of confinement. Even if it is not visible in this figure, they explain that cutting simulation without confinement leads to cracks and chips formation. In contrast, simulation under confinement leads to an accumulation of rock in front of the cutter. Moreover, they notice that confinement inhibits the formation of cracks.

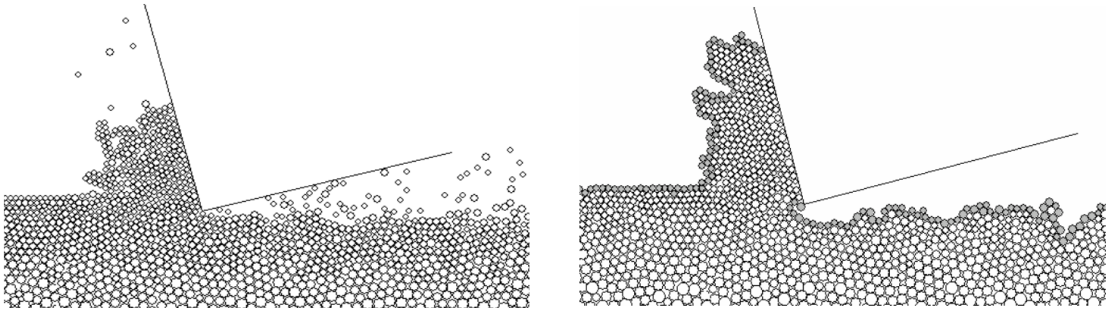

Figure II.55. Cuttings formation for cutting simulations with DEM: (a) at atmospheric conditions and (b) under a confinement of 34.5 MPa (Lei and Kaitkay, 2003).

They also compared the simulated average cutting forces with their experimental results presented before (Figure II.56). While simulated average cutting forces in atmospheric conditions are in the same order of magnitude as the experimental ones, they appear to be two times smaller when confinement is applied. Regarding the comparison of the cutting forces between simulated and experimental ones, it should be mentioned that the experimental tests were carried out with a circular cutter, while for the numerical simulations being in 2D, the cutter was considered as rectangular. This consideration could compromise the previous analyses.

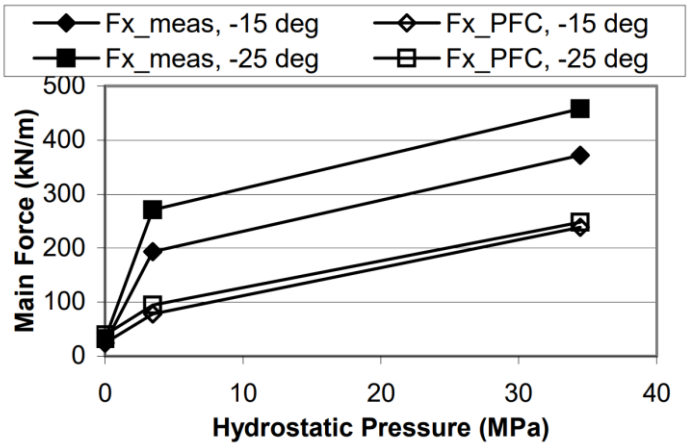

Figure II.56. Comparison of tangential cutting forces between experimental and simulation results (Lei and Kaitkay, 2003).

Ledgerwood III (2007) also studied this problem with PFC2D. He calibrated a rock model with an evolving behavior, as presented in Figure II.57. Interestingly, despite a perfectly plastic behavior at high confinement, the rock model shows a dilatant behavior at failure.

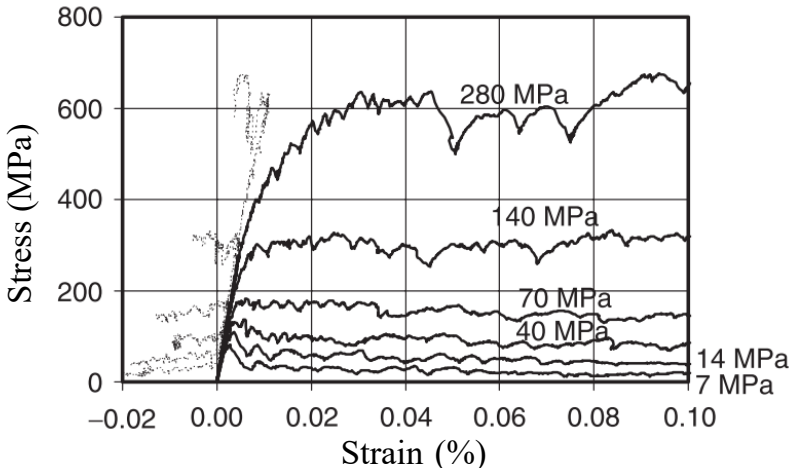

Figure II.57. Stress versus axial and volumetric strain curves of the generated PFC rock model by Ledgerwood III (2007).

His results tend to support the experimental observations:

- Cuttings evolve from chips in atmospheric conditions to ribbons of crushed material under confinement (Figure II.58).
- The flow of rock debris while cutting under confinement consists of a forward flow and a backward one flowing under the cutter.
- Specific Energy decreases with the depth of cut.

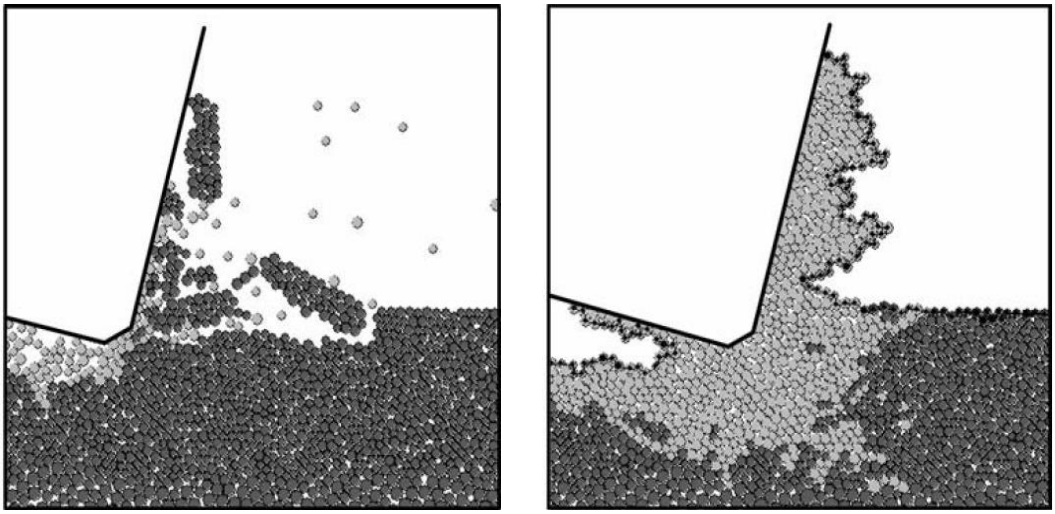

(a) (b)

Figure II.58. PFC cutting simulation at (a) atmospheric pressure, and (b) 20 MPa (Ledgerwood III, 2007).

Regarding the evolution of the destruction mechanism with respect to the confinement, it is more evident to observe this evolution in his results than in those of Lei & Kaitkay (2003).

However, the author mentions that his results of cutting forces and Specific Energy are underestimated compared to the experimental ones. He explains this incorrect estimation by the two-dimensional character of his code, which does not reflect a real flow of particles. Even if the Specific Energy estimated is wrong, he assumes that the analysis of its evolution remains relevant. Furthermore, he shows that a large part of the energy is used to move the cutting and not to cut the rock. For "numerical proof", he performed cutting tests with a model without bonds between particles but with the same friction coefficient. In this way, he models a material with zero cohesion as sand. The cutting forces obtained are then very close to those corresponding to the material with links between particles in the same conditions (depth of cut and confinement). Following this "experiment", he concludes that

inelastic properties of rock have a stronger influence on rock cutting than elastic ones.

From the continuum modeling point of view, Reyes Martinez et al. (2013) used the Finite Element Method with ABAQUS for modeling single cutter experiments on halite. Halite presents a perfectly plastic behavior and hardening at relatively low confinement of respectively 2 and 21 MPa. To represent fracture propagation, they implement a damage model characterizing the maximum strain allowed for each element of the model. When this maximum strain is reached, the element loses its strength and is removed, allowing the formation of cuttings.

From a quantitative point of view, their numerical results are in very good agreement with the experimental ones, both in 2D and 3D. The difference in terms of Specific Energy is less than 10%. From a qualitative point of view, the simulations show that the cuttings have the form of long ribbons like what can be observed for metal cutting, whatever the confinement. It is questionable whether this method would give the same good results when modeling a rock with brittle behavior.

3.3.6 Discussion

It is clear from the above elements that confinement has a very important effect on the cutting mechanism, both from the point of view of the destruction mode and of the cutting forces and energies.

Indeed, the experimental results show that the cutting mechanism is strongly impacted even at very low confinement values. The form of cuttings changes completely. It is no more about having two modes of destruction as in atmospheric conditions (scratching and chipping) but only one generating centimetric ribbons of crushed rock due to the accumulation of debris in front of the cutter. Furthermore, this phenomenon is observed whatever the depth of cut of the confining pressure. However, the qualitative impact of the cutting parameters remains the same in general. For example, the increase of the back rake increases the Specific Energy, or the increase of the depth of cut allows to decrease this energy until obtaining an optimum.

Concerning the analytical models, it is interesting to note that they differ from what is observed experimentally and still consider the formation of chips, not the one of a ribbon of rock. Moreover, the formulations proposed to calculate the angle of

failure are more or less the same regardless of the different authors' assumptions. Furthermore, it is interesting to note that these analytical models do not consider the change of behavior that the rock can present as a function of the confinement (transition from a brittle behavior to a ductile one).

As in the case of cutting under atmospheric conditions, numerical models also show an impressive ability to represent the cutting mechanism subtility under confinement. Some researchers have even tried to consider the change in rock behavior with the confinement in their simulations.

3.4 Rock cutting mechanism in real drillings conditions

Although the data collected during drilling cannot be used to analyze the impact of the different cutting parameters in detail, they provide important information on Mechanical Specific Energy (MSE) and the morphology of the cuttings. Knowledge of actual drilling data can help validate and interpret experimental or numerical research results.

3.4.1 MSE in real drilling

As he developed the concept of Specific Energy, Teale (1965) studied various laboratory tests performed with full-scale drilling tools. He showed that MSE was numerically close to the compressive strength (UCS) of the rock when the drilling efficiency was maximum (highest ROP). As these tests were performed under atmospheric conditions, the minimum MSE should be numerically close to the confined compressive strength with respect to the confinement value at the depth drilled.

In Teale's formulation of Specific Energy, the torque at the bit is the main variable. However, in real drilling conditions, torque measurements are usually made at the surface from the rotary table (Dupriest and Koederitz, 2005). It is the same for the WOB, which is always measured on the surface.

This value can sometimes be very different from the real WOB at the drill bit. It is particularly true in directional or horizontal drilling, where a significant difference between the two WOB can exist. These differences between the torque and WOB measured at the surface, and their respective values at the tool can be explained partly by friction losses between the drill collars and the well.

The lack of reliable torque and WOB measurements at the bit means that the MSE value calculated based on surface measurements is often a source of significant errors, which leads to an overestimation of the real work at the drill bit. Several researchers have worked on improving the calculation of the MSE at the tool based on Teale's formulation to take these losses into account (Mazen et al., 2021; Najjarpour et al., 2022).

In a general way, their models can be expressed as follows:

$$MSE_{adj} = MSE \,.\, EFF_m \tag{II.59}$$

where MSE_{adj} is the adjusted MSE (Teale formulation), and EFF_m is the efficiency factor.

Depending on the drilling conditions and hypothesis of the authors, EFF_m can take a very wide range of values. Indeed, Dupriest and Koederitz (2005) believed that maximum bit efficiencies were always between 30 and 40%, while Hammoutene and Bits (2012) claimed that mechanical efficiencies were between 26 and 64%. Regarding directional and horizontal drilling, Amadi and Iyalla (2012) estimated that the mechanical efficiency was 12.5%. Thereafter, these models have not ceased to be developed to consider, for example, drilling fluids and downhole motors (Mazen et al., 2021).

Each of these researchers was able to show that the MSE_{adj} was of the same magnitude as the confined compressive strength under the conditions corresponding to their models. As an example, Chen et al. (2018) developed a model in the case of directional or horizontal drilling with downhole motors. They present in their paper a comparison of different models in vertical and horizontal sections of their study well (Figure II.59 and Figure II.60).

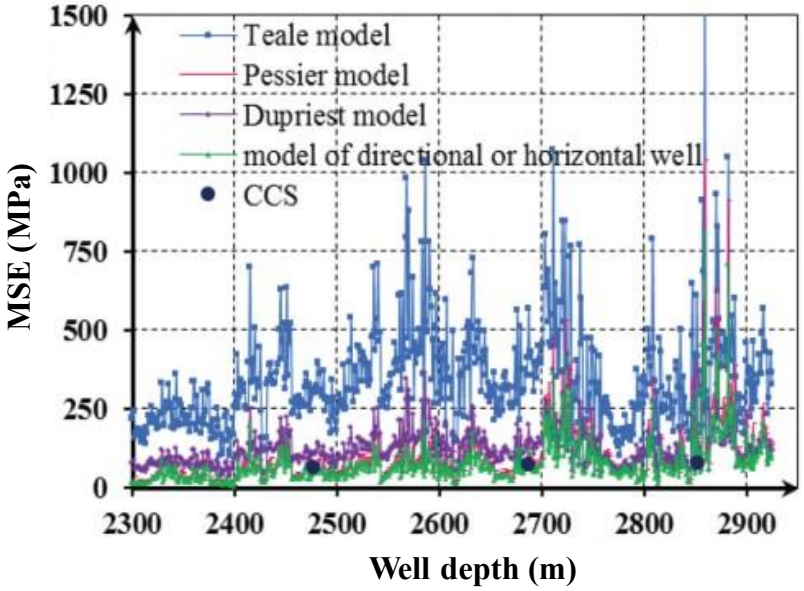

Figure II.59. Comparison of MSE calculated results and testing CCS in vertical section (Chen et al., 2018).

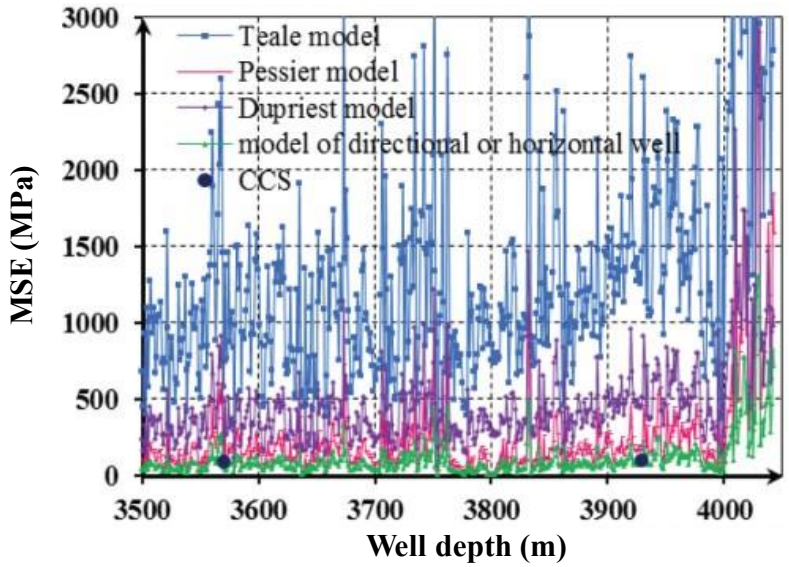

Figure II.60. Comparison of MSE calculated results and testing CCS in horizontal section (Chen et al., 2018).

Their analysis shows that Teale's model deviates strongly from the others in vertical and horizontal sections. Moreover, MSE values calculated from Teale's model deviate strongly from the confined compressive strength. In the horizontal section, Teale's MSE values are more than ten times higher than those of the CCS model.

In the vertical section, MSE values of Chen et al. (2018), Pessier and Fear (1992) and Dupriest and Koederitz (2005) models are relatively close. On the other hand, in the vertical section, the MSE values of Pessier and Dupriest are several times larger than the confined compressive strength, while the Chen model is closer.

It indicates that the determination of the MSE at the bit is not easy and that the results depend strongly on the drilling conditions and the model considered. Nevertheless, all researchers in this field agree that the MSE at the bit should be close to the strength of the rock at the confinement considered.

3.4.1 Cuttings morphology

Cuttings are an essential source of information for the good follow-up of drillings. Indeed, their analysis allows knowing the formations crossed. In addition to the geological information, the cuttings, especially their morphology, are a good indicator of the physical mechanisms occurring at the tool-roll interface.

Cuttings produced by PDC bits are generally millimetric or centimetric in size. Commonly, they consist of re-compacted fine rock particles with no primary cementation remaining (Ledgerwood III, 2007; Omland et al., 2007; Judzis et al., 2009). Moreover, these cuttings can be crushed and dislocated with fingers. The granulometric analyses of the cuttings reveal that the constitutive particles are generally in the range of several microns to a few hundred microns (Barry and Klima, 2013; Reyes et al., 2015; Kadyrov et al., 2022).

4 Conclusions

This chapter aimed to present state of the art concerning the mechanical behavior of rocks in high-depth conditions, focusing on the effects of confinement, and the cutting mechanisms in atmospheric conditions and under confinement.

Although the problem of the mechanical behavior of rocks in high-depth conditions is complex because it involves a thermo-hydro-mechanical coupling, it has already been widely studied for a long time. The impact of these three poles and their interactions on the mechanical behavior of rocks is now very well-known and documented for a wide variety of rocks. Concerning the impact of confinement, it is also very well documented how it affects the general behavior of rock materials: increase of rock strength and modification of the failure mode going from brittle to ductile as the confinement increases.

Regarding the cutting mechanism specific to drilling, its study is much more recent, and the current state of knowledge is much more limited due to the important complexity of this mechanism. Indeed, it evolves with cutting parameters, mechanical properties of rocks and test conditions (atmospheric or under confinement). Furthermore, much of the research in this field has been carried out under atmospheric conditions, which is far from the high-depth conditions that strongly impact the behavior of rocks. It means that the cutting mechanism and the impact of the different cutting parameters are very well known under atmospheric conditions but not under confinement.

Nevertheless, experimental tests performed under confinement have highlighted its impact. Indeed, the confinement impacts the shape of the cuttings and increases the cutting energies. However, these evolutions and the trend of the increase of the cutting energies are not yet clearly explained. Some phenomenological models were proposed based on these observations, but they cannot reproduce the complexity of this mechanism. They are generally limited to a particular case due

to the many assumptions required to design them. Moreover, they are not able to explain all the observations made experimentally and are very rarely able to establish a link between the evolution of the mechanical behavior of rocks and the cutting mechanism evolution with the confinement.

Finally, the emergence of personal computers with high computing power has allowed the implementation of numerical modeling to study the cutting mechanism. Although the results obtained by these methods are very encouraging, it is obvious that this approach must still be improved and complexified by 3D approaches to get closer to reality.

It appears that the subject is open and that there are numerous research opportunities (experiments, numerical modeling, use of field data) to improve the understanding of the cutting mechanism under confinement.

Chapter III Methodology

The state of the art presented in the previous chapter highlights the current state of knowledge concerning the mechanical behavior of rocks and the cutting mechanism under confinement. It has also emphasized the lack of connection between rocks' behavior and the cutting mechanism. This chapter presents the approach and methods used to better integrate the rock mechanical behavior and its evolution with confinement in studying the rock cutting mechanism under confinement.

1 Research approach

As shown in the previous chapter, different approaches can be used to study the cutting mechanism and its evolution under high-depth conditions: experimental tests, phenomenological model development, numerical modeling, or the analysis of field data.

In contrast, approaches using numerical modeling methods have shown promising results, and further developments are still possible to improve their robustness with respect to experiments. Among these developments, the calibration of models based on the rock behavior under confinement and the use of 3D numerical models are interesting perspectives.

Based on those considerations, it was decided to use a numerical approach to study the subject of this thesis. The choice of the method is discussed in section 1.1.

Once the numerical method was chosen, it was necessary to determine which material(s) to model. Several possibilities were then possible: a hypothetical material, a widely used reference rock or the implementation of several materials with different behaviors. Since the numerical model results must be verified with experimental results to be validated, the use of a hypothetical rock model was

automatically discarded. Moreover, one of the strengths of the Mining Department of the University of Mons is the characterization and the knowledge of rock behavior under high-depth conditions. Using previous in-house results obtained on some rocks would be more interesting.

Finally, the work was oriented towards the implementation of a single reference rock into numerical models. This choice is explained by the desire to develop the method to better understand the cutting mechanism with a numerical method. Once the method is validated for a rock, it could be extrapolated in the future to other rocks to validate the results obtained in this thesis. The reference rock choice is discussed in section 1.2.

1.1 Numerical method choice

Continuous and discontinuous numerical methods have been used to study the cutting mechanism, either with commercial codes or in-house ones. Each of these methods has its strengths and weaknesses. Based on the literature review, one shows a good potential to study this type of problem. It is the Discrete Element Method.

The main interest of this method is that it can be used to study the propagation of fractures in the material without introducing specific algorithms or features such as erosion algorithms, e.g., as it is the case for continuous numerical methods. Moreover, this numerical method appears to be the only one able to reproduce the evolution of the cutting mechanism depending on the depth of cut or the confining pressure. Moreover, as shown in the results presented in Chapter II, this numerical method allows to follow the evolution of the cutting mechanism from the scratching and chipping modes up to the formation of ribbons of crushed rocks under confining conditions. Unfortunately, results obtained with DEM models are still limited from a quantitative point of view due to the reduced number of 3D works and simplifications regarding the mechanical behavior of the studied rock and the size of the particles used to limit the necessary calculation time.

In this thesis, the 2D and 3D DEM methods are used. The calculation code used for this work is PFC4.0 (in its 2D and 3D versions) developed by Itasca. This commercial code has the advantage of being widely used to study the cutting mechanism. It has been developed to study materials with cohesion, such as rocks. It also offers many basic procedures that can be modified according to users' needs.

Section 2 of this chapter briefly describes the implementation of the Discrete Element Method in PFC.

1.2 Reference rock choice

Two important factors drove the reference rock choice. First, choosing a rock whose behavior and its evolution with confinement are well known was necessary. The behavior should evolve largely, i.e., passing from a brittle behavior to a ductile one with hardening as the confinement increases. This would allow the study of the cutting mechanism over all possible behaviors depending on the confinement magnitude.

Secondly, the selected rock needed to already have been extensively studied by cutting tests under both atmospheric and confined conditions. This second condition was necessary to have enough data to validate the numerical results.

Based on these considerations, the choice went to the Vosges Sandstone. This rock has the advantage of being largely studied by the Mining Engineering Department of the University of Mons, both from its behavior evolution with confinement and from cutting under atmospheric conditions point of views. Also, it is possible to find many works discussing the cutting mechanism on this rock (Dagrain et al., 2001; Zhou and Lin, 2014; Amri et al., 2016; Yahiaoui et al., 2016). Finally, this rock is made up of cemented grains; it is then suitable for modeling with the Discrete Element Method.

Section 3 of this chapter presents the general characteristics of the Vosges Sandstone from petrophysical and geomechanical points of view.

2 Discrete Element Method in PFC

The Discrete Element Method (DEM) implemented in this research is a subfamily of the Distinct Element Method proposed by Cundall (1971) to study rock mechanics problems such as stability of blocky and fractured rock masses. A few years later, Cundall & Strack (1979) developed the Discrete Element Method (DEM) to study non-cohesive media to solve soil mechanic problems.

Generally, a particle-flow model is used to study particles' mechanical behavior and interactions. These particles (also called "balls"), arbitrarily shaped and rigid, can displace independently from each other and only interact at contact points. As the particles are considered rigid bodies, a soft contact approach characterizes their contacts' behavior. The contact behavior is then defined by a finite normal stiffness representing the measurable stiffness at a contact. Newton's Law of Motion governs the overall behavior of such a moving particles system. It establishes the relationship between the particles' motion and the forces behind that motion.

Particles can be bonded together at their contact point to be able to represent a more complex behavior. In this way, tensile or shear forces can appear between particles. Then the model can be used to study the propagation of stress, the creation of cracks and the interaction of different bonded assemblies. More than particles, PFC includes "walls". These surfaces allow boundary conditions to be applied to ball assemblies for compaction and containment purposes.

2.1 Calculation cycle

As the interaction between particles is treated as a dynamic process in DEM, this dynamic behavior is numerically represented by a calculation cycle consisting of applying a time-stepping algorithm assuming that the velocities and accelerations are constant during each time step. The timestep must be chosen as small as possible to limit the propagation of disturbances from any particle to its immediate neighbors. Consequently, the forces acting on a particle are determined exclusively by its interaction with particles and walls in contact with it.

The calculation cycle, illustrated in Figure III.1, consists of repeatedly applying the law of motion to each particle, a Force-Displacement law at each contact, and updating wall positions. Contacts (ball/ball or ball/wall contacts) are formed and broken automatically during the calculation cycle.

For each time step, the calculation cycle is described as follow:

1. All contacts are updated following the known particles and walls positions.
2. The Force-Displacement law is applied at each contact to update contact forces based on the two entities' relative motion and the constitutive contact model.
3. The law of motion updates the particles' position and velocity based on the resultant force and moment acting on each particle. The walls' positions are updated following the wall motion defined by the user and are not subject to the second law of motion.

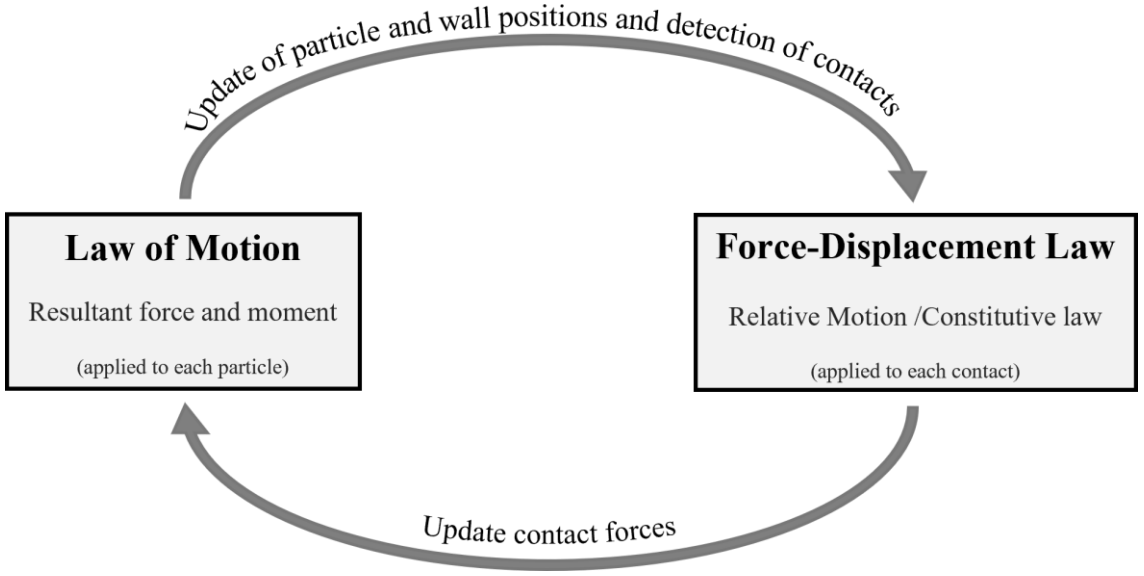

Figure III.1. Time-stepping algorithm implemented in DEM (Itasca Consulting Group, 2008b).

2.2 Constitutive models

The overall constitutive behavior of a model must be defined with at least one contact model characterizing interactions between particles in contact. Depending on the user's needs and goals, the user can complete the constitutive behavior by activating, defining a contact model, and adding parallel bonds between balls. Combining these three components defines the contact force-displacement behavior (Figure III.2). Below, a description of the different components is given.

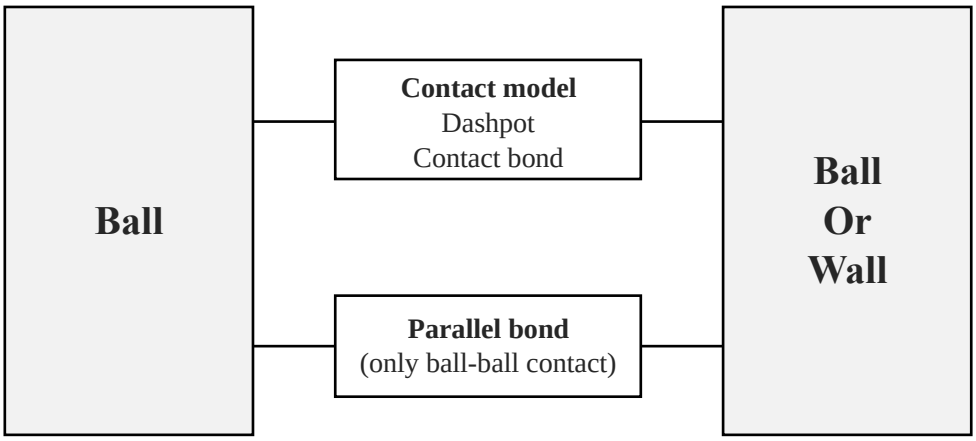

Figure III.2. Components at contacts.

2.2.1 Components of contact models

Contact models are composed of four elements which consist of stiffness (k^n, k^s), slip (μ), bonding (F_c^n, F_c^s.) and dashpot (c_n, c_s). Figure III.3 represents the different components constituting a contact model.

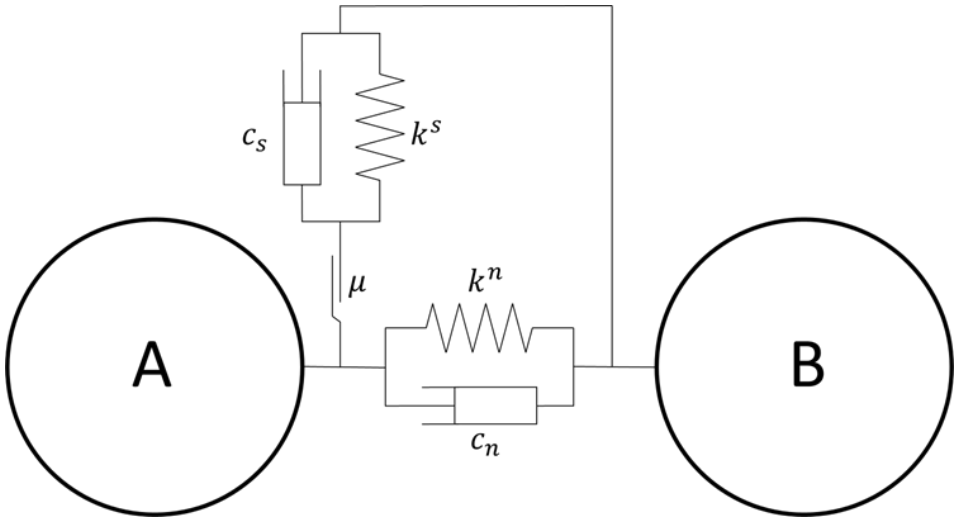

Figure III.3. Rheological model of the different components constituting contact model at ball-ball contact.

2.2.1.1 Stiffnesses

Stiffnesses, represented by springs in Figure III.3, link contact forces and relative displacements in the normal and shear displacements with respect to the Force-Displacement law.

With k^n and k^s, respectively normal and shear stiffnesses at the contact, and U^n and U^s as the normal and shear components of the contact displacement vector, normal force and shear force increment are calculated by:

$$F_{ij}^n = K^n \, U^n \tag{III.1}$$

$$\Delta F_{ij}^s = -k^s \, \Delta U^s \tag{III.2}$$

*2.2.1.2 **Slip***

The slip behavior is obtained by applying a relationship between shear and normal forces. Defining μ as the friction coefficient at contact, the slip behavior defines the maximum allowed shear contact force by:

$$F_{max}^s = \mu \, |F^n| \tag{III.3}$$

At each calculation cycle, shear force at contact $|F^s|$ is compared with F_{max}^s. If $|F^s| > F_{max}^s$, then slip is allowed to occur during the next calculation cycle and the magnitude of F^s is fixed equal to F_{max}^s. Figure III.4 gives a graphical representation of the contact behavior in the shear direction.

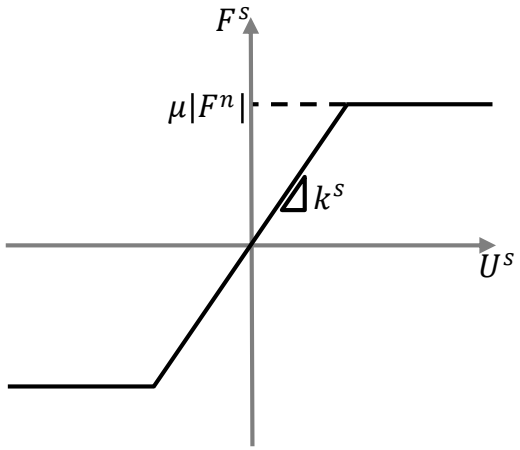

Figure III.4. Graphical representation of contact behavior in the shear direction.

*2.2.1.3 **Contact bonds***

A contact bond can be seen as a point of glue of a vanishingly small size that acts at the contact point. When contact bond is applied, springs used to define shear and normal stiffnesses at contact will also have specified shear and normal tensile strengths, respectively noted F_c^s and F_c^n.

Using a contact bond allows the development of tensile forces at contact. In the shear direction, the contact bond excludes the possibility of slip at contact.

The bond breaks when the tensile force at contact reaches the tensile bond strength. Particles are no longer in contact, and normal and shear contact forces are set to zero. However, when the shear contact force reaches the shear bond strength, the bond breaks, but the contact forces are not necessarily set to zero. If the particles remain in contact, the contact forces are not changed as long as the shear force does not exceed the friction limit, and the normal force is compressive. Otherwise, normal and shear contact forces are set to zero.

Figure III.5 presents the force-displacement behavior between two particles when the contact bond is activated. In this figure, F^n is the normal contact force, by convention $F^n > 0$ indicates tension, F^s is the shear contact force and U^s is the shear displacement.

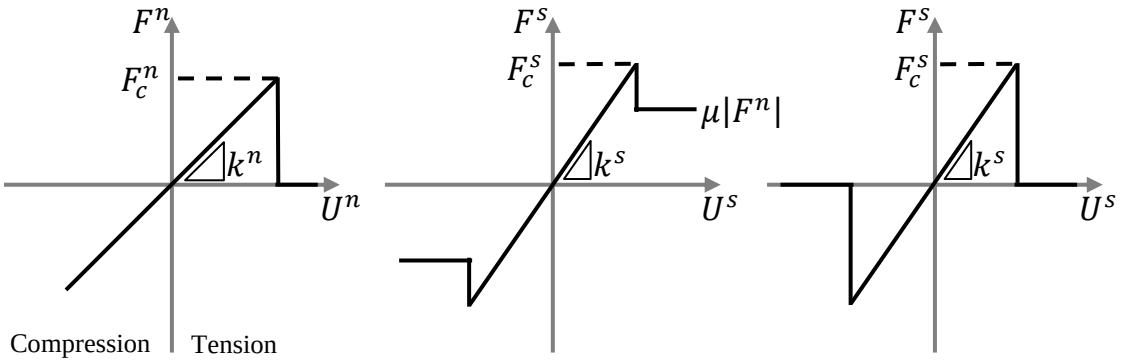

(a) Contact bond in normal direction

(b) Contact bond in shear direction with contact ($U^n < 0$)

(c) Contact bond in shear direction without contact ($U^n > 0$)

Figure III.5. force-displacement behavior between two particles when contact bond is activated.

*2.2.1.4 **Dashpots***

Normal and shear dashpots used to implement viscous damping are present at each contact and act in parallel with contact and bonding models (Figure III.2). Viscous damping adds a damping force to the contact force. This damping force acts to counter the relative motion of elements. Their role is to dissipate kinetic energy when simulating dynamic processes such as free flight and/or impacts between balls.

2.2.2 Parallel bonds

While contact bonds can be schematized as a point of glue between particles, parallel bonds approximate the behavior of a finite-sized piece of brittle and elastic cementation between two particles. The main feature of parallel bonds is to transmit both forces and moments between particles and not only force as contact bonds.

A parallel bond can be represented as a set of springs distributed uniformly over a cross-section positioned on the contact plane and centered on the point of contact. A parallel bond is defined by five parameters: normal and shear stiffnesses, $\bar{k}^n$ and $\bar{k}^n$; normal and shear strength, $\bar{\sigma}_n$ and $\bar{\sigma}_s$; and a bond radius multiplicator noted $\bar{\lambda}$ that is used to define the parallel bond radius $\bar{R}$ such as:

$$\bar{R} = \bar{\lambda} \min\left(R^{[A]}, R^{[B]}\right) \quad \text{(III.4)}$$

Where $R^{(A)}$ and $R^{(B)}$ are the particle radii.

2.3 Calibration of constitutive models

Micro-properties presented previously are not experimentally measurable and cannot be set directly based on experimental data. Therefore, a calibration procedure is needed to determine the set of micro-properties that reproduce the relevant material behavior before confidently attempting DEM simulations of interest.

In general, calibration processes consist of numerically reproducing an experimental or field test and iteratively adapting the micro-properties until the macro behavior of the simulated material matches the one observed during tests. The calibration protocol will depend on the material to be modeled (sand, rock, concrete) and on the object of interest of the numerical study.

In rock materials problems, the calibration process is generally based on unconfined or confined compression and/or tension tests. In general, Itasca proposes to use the following calibration sequence to minimize the number of iterations needed to obtain the desired behavior:

1. Match elastic properties of the material (Young's modulus and Poison's ratio) by varying elastic properties of the constitutive model.
2. Match peak strength by varying normal land shear bond strengths.
3. Match the crack-initiation stress by varying the standard deviation of bond strengths.
4. Match the post-peak behavior by varying the friction coefficient between particles

The limitation of this calibration method is that several parameters can influence the macro behavior of the numerical model. There is, therefore, no single solution, and several combinations of parameter values will result in the same macro behavior.

3 Vosges Sandstone description

The Vosges Sandstone has been widely studied through the years and the literature referring to this rock is very broad (Bésuelle et al., 2000; Descamps, 2007; Charalampidou, 2011; Couture and Bésuelle, 2019). Indeed, this rock, whose characteristics are comparable to oil and gas reservoir rocks, is generally used as a reference. Although numerous references dealing with Vosges Sandstone are available in the literature, this section mainly refers to the work of Descamps (2007) because the results gained during her thesis in our department are used to calibrate numerical models.

This section concerning the mechanical behavior of the Vosges Sandstone focuses only on the impact of confinement and does not present the impacts due to pore pressure and temperature. Indeed, these two points are not points of interest studied in this work. The reader interested in learning more about these points can refer to the references already mentioned here above.

3.1 Petrophysical properties

Vosges sandstone is a poorly cemented and quartz-rich sandstone, usually over 90% of the total composition, with some percentages of feldspars, micas and clay depending on the genesis of the rock. The porosity of this rock is around 20%. Laboratory tests carried out by Descamps showed that the samples tested had a porosity of 21.7%.

The grain size distribution of the rock depends essentially on the place of origin of the samples. Indeed, depending on this consideration, Vosges Sandstone can be made up of fine or coarse grains with a granulometry varying from 100 μm to over 600 μm (Bésuelle et al., 2000). The dimension of grains measured by optical microscope by Descamps is between 100 and 150 μm. The 3D true size of grains can be estimated with the statistical factor considering the grains as spherical. Then, the grain size distribution in 3D for the samples tested by Descamps varies between 150 and 225 μm.

These data about porosity and grain size will be used to give the synthetic rock model characteristics close to the real rock.

3.2 Geomechanical properties

During her thesis work, Descamps performed compression tests under confinement on triaxial and polyaxial (True-triaxial) devices. Below, only the tests performed on the polyaxial device are presented. Indeed, these tests highlighted the whole evolution of the behavior of the Vosges Sandstone as a function of the confinement.

Prof. Tshibangu developed the polyaxial cell during his Ph.D. thesis (Tshibangu, 1993). This test bench was developed to study the behavior of rocks in high depths conditions and highlight the effects of the intermediate principal stress. This device comprises a rigid press, a hydraulic unit and an electronic acquisition and control system, all controlled by a computer. The polyaxial cell consists of three pistons acting in perpendicular directions on 30 mm side cubic samples to conduct truly triaxial tests (Figure III.6). The entire hydraulic system has been designed such that each piston can apply maximum stress of 500 MPa on each side of the sample.

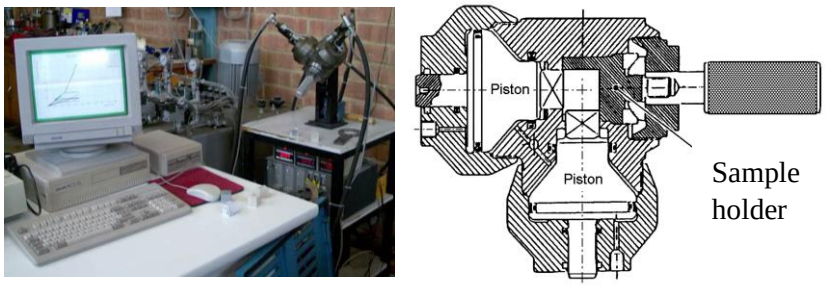

(a) (b)

Figure III.6. The polyaxial device of the Mining Department of UMONS: (a) Full device with polyaxial cell, hydraulic bench and computer and (b) cross-section of the cell. Modified from Descamps (2007).

Results of polyaxial tests performed up to 90 MPa of confinement are presented in Figure III.7. For low confinement values ranging from 0 to 10 MPa, the Voges sandstone presents a brittle behavior with a residual strength. Moreover, at failure, the rock has a dilatant behavior. From confinement of 20 MPa, the rock shows a ductile behavior with perfect plasticity and hardening at higher confining pressure. Its volumetric behavior at failure becomes then to be compactant.

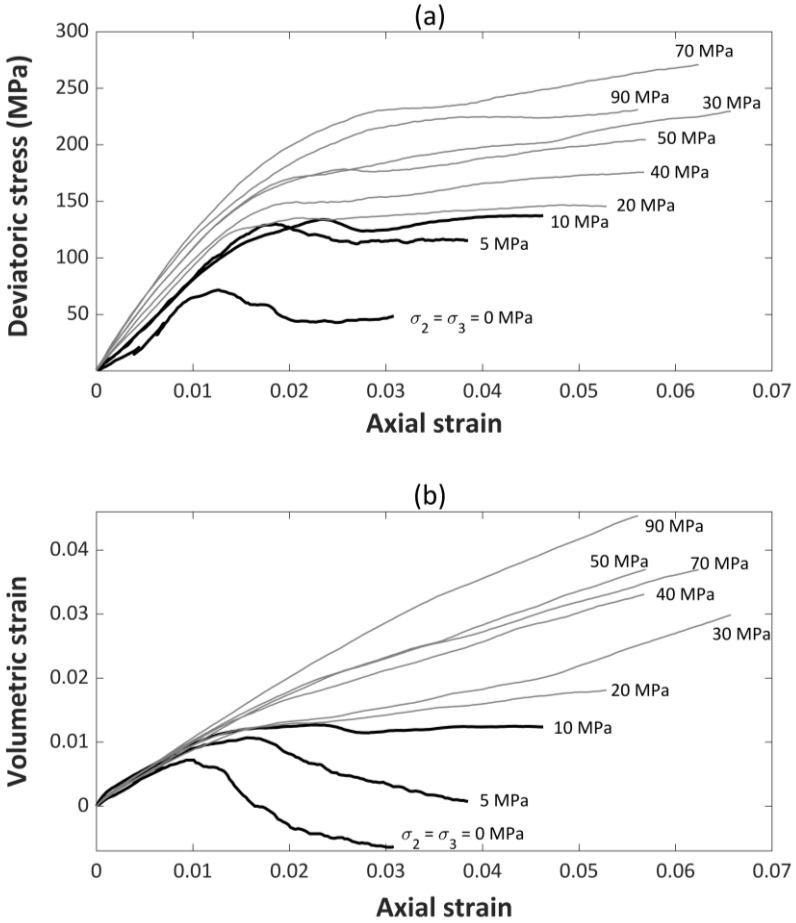

Figure III.7. Stress-strain curves of the Vosges sandstone under conventional triaxial compression conditions. Data from Descamps (2007).

From a more quantitative point of view, Table III-1 presents the values of yielding stress, compressive strength, Young's modulus, and Poisson's ratio for the different tests. The data show a clear increase in the values of these properties with confinement. It should be noted that deviations can arise compared to the tests carried out on a triaxial cell testing cylindrical samples with a 2:1 ratio (Bésuelle et al., 2000). These deviations are mainly due to the shape of the specimens and the friction between the pistons and the faces of the cubic specimen, which modify the stress field in the material. These differences are generally more important in low confinement.

Table III-1. Results of polyaxial tests on Vosges Sandstone. Data from Descamps (2007).

σ_3 (MPa)	σ_E (MPa)	σ_R (MPa)	E (MPa)	ν
0	57	71	8668	0.18
5	95	129	8327	0.13
10	101	140	7763	0.10
20	105	148	7970	0.13
30	130	190	10 039	0.24
40	141	194	10 300	0.22
50	157	221	10 019	0.32
70	176	270	11 790	0.36
90	172	304	12 578	0.39

These tests allow determining yielding and failure envelopes in 2D and 3D spaces. Figure III.8 (a) shows the failure envelope of Vosges Sandstone in the Mohr plane. Moreover, this figure shows the evolution of the cohesion and the internal friction angle of the rock with confinement. We observe that the cohesion tends to increase with the confinement while the angle of internal friction decreases simultaneously. Figure III.8 (b) shows the 3D envelope according to the Mohr-Coulomb criterion in the three-dimensional principal stresses plane.

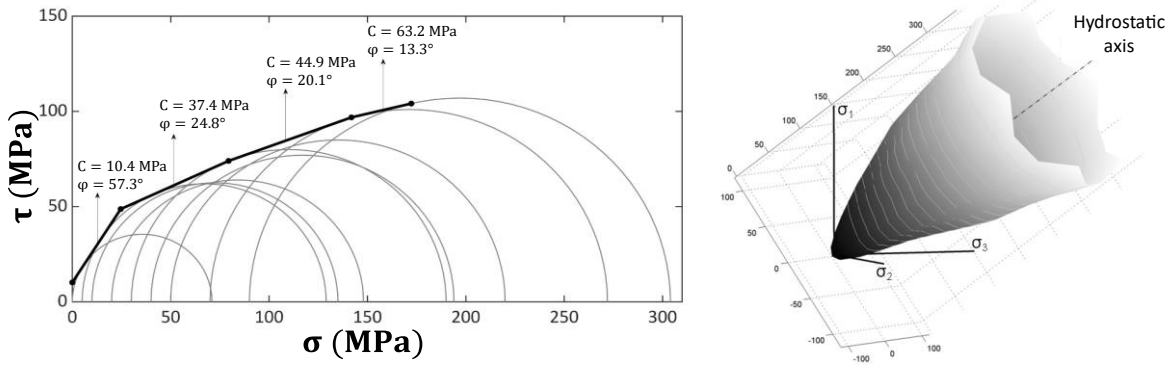

(a) (b)

Figure III.8. Failure envelopes of Vosges Sandstone: (a) 2D envelope in Mohr plane and (b) 3D envelope according to the Mohr-Coulomb criterion in three-dimensional principal stresses plane. Modified from Descamps (2007).

4 Research steps

The first step of this work consists of the calibration of the numerical model to reproduce the evolution of the mechanical behavior of the Vosges Sandstone with confinement as observed in laboratory experiments. To validate the calibrated set of parameters from the cutting mechanism point of view, simulations of cutting under atmospheric conditions will be carried out and compared to cutting tests performed on a Rock Strength Device.

Subsequently, the work will focus on the impact of confinement on the cutting mechanism. The 2D modeling will allow understanding of the propagation of fractures in the material, leading to cuttings formation. Simultaneously, 3D models will be used to study the evolution of cutting forces and energies with respect to confinement. These models will be performed with sharp cutters and standard cutting parameters to focus only on the impact of confinement.

Afterward, the models will be complexified to get closer to the real cutting conditions. In this framework, the influence of cutting angles will be studied. Different cutter geometries will also be implemented to study the effects of a chamfer and the ones due to the formation of a wear flat. These changes in geometry and parameters allow to observe and understand how these different changes interact with the increase in confinement.

Thereafter, the results of the numerical simulations will be compared to experimental ones to validate the observed trends and the orders of magnitude of the cutting forces and energies.

Finally, the results will be interpreted to relate the evolution of the cutting mechanism (qualitatively and quantitatively) to the mechanical behavior of the rock simulated.

Chapter IV Calibration, building and validation of rock cutting models

Firstly, this chapter presents and describes the calibration procedure of the 2D and 3D synthetic rock models of Vosges Sandstone. Afterward, this chapter is dedicated to the presentation of 2D and 3D cutting models. The morphology of the samples and cutters as well as their properties are introduced and discussed. The data collected during the simulations and the data processing procedures are also presented in this chapter. Furthermore, the cutting models' validation based on experimental tests performed in atmospheric conditions is detailed. Finally, this chapter concludes with the presentation of test protocols used to perform this research

1 Calibration of synthetic rock models

Any modeling project with Discrete Element Method codes starts with a first calibration step. During this step, selecting a constitutive model and calibrating its micro-properties is necessary to obtain a representative behavior of the material studied. Within the framework of this thesis, the objective is to develop a calibration method to determine a single set of micro-properties able to represent the evolution of the mechanical behavior of Vosges Sandstone.

1.1 Constitutive model choice

The Bonded Particle Model has been selected as the constitutive model for this work. This constitutive model has already been widely used in modeling related to rock mechanics problems (Cai et al., 2007; Charalampidou, 2011; Bahrani et al., 2014; Carrapatoso et al., 2016).

The Bonded-Particle Model (BPM) was developed by Potyondy and Cundall (2004) based on the description of rocks, which can be schematized as bodies composed of particles cemented together. Over time, this behavior model has become a reference for modeling rock materials in DEM. To represent these two components of a rock (grains and cement), they coupled a Linear Contact Model with a Parallel Bond Model. Figure IV.1 is a rheological representation of the Bonded-Particle Model.

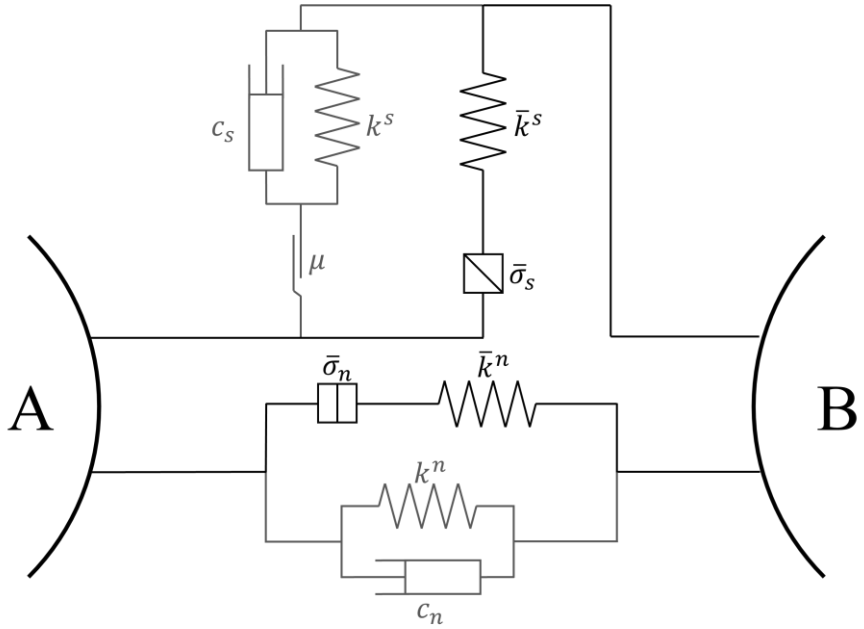

Figure IV.1. Rheological model of Bonded Particle Model. The parallel bond part is represented in black, while the linear contact model is in grey.

The stiffness and slip components of the Linear Contact Model are used to represent the grain behavior of a rock, while the Parallel Bond Model represents the cement behavior and bonds particles together. The BPM introduces the notion of grain and cement Young's moduli. Table IV-1 presents micro-properties used to define the BPM.

Figure IV.2 represents the corresponding constitutive behavior in shear and tension when subjected to external forces. If the maximum tensile stress or the maximum shear stress exceeds the tensile or shear strength, the parallel bond breaks and is removed from the model. After this bond failure, the grain-based component remains active as long as the particles remain in contact. Due to the particles' displacement during the simulation, new contacts are created and on which only the grain-based component will be activated.

Table IV-1. Definition of micro-properties of the Bonded Particles Model.

Component	Symbols	Name of the properties (unit)
Grain micro-properties	R_{min}	Minimal radius of particles (mm)
	R_{max}/R_{min}	Ratio between maximal and minimal radii (-)
	E_c	Young Modulus of contact (GPa)
	k_n/k_s	Ratio of particle normal and shear stiffnesses (-)
	μ	Friction coefficient (-)
Cement micro-properties	$\bar{\lambda}$	Radius multiplicator (-)
	$\bar{E}_c$	Young Modulus of cement (GPa)
	$(\bar{k}^n/\bar{k}^s)$	Ratio of normal and shear stiffnesses (-)
	$\bar{\sigma}_n$	Tensile strength (MPa)
	$\bar{\sigma}_s$	Shear strength (MPa)

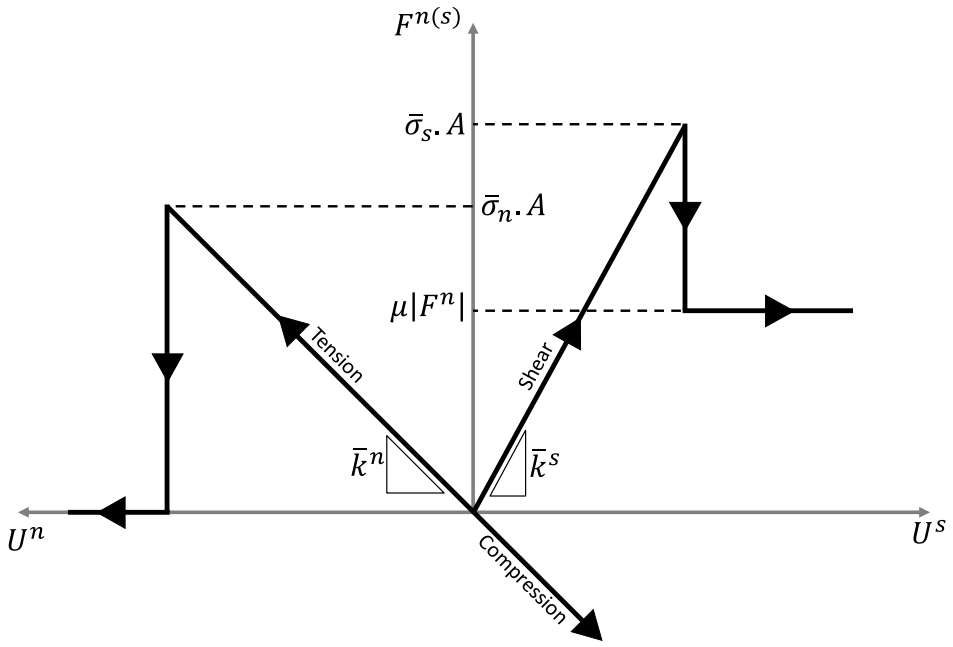

Figure IV.2. Constitutive behavior of the Bonded Particle Model in shear and tension when particles are bonded (A is the cross-section of the parallel bond).

1.2 Calibration procedure building

The calibration procedure has been built based on two compressive tests, a uniaxial one and one under confinement. This section first discusses the choice of the confinement value for which the triaxial test has been performed. Then the testing environments in 2D and 3D and the calibration steps are presented.

1.2.1 Determination of confining pressure for triaxial tests

To select the most appropriate confining pressure for the simulated triaxial test, it was necessary to base the analyses on the experimental triaxial results of Vosges Sandstone performed by Descamps (2007). As the objective of this calibration step was to reproduce the evolution of the material behavior of Vosges Sandstone from brittle to ductile as the confinement increases, it seemed interesting to choose the value of confinement at which the behavior of the rock changes from brittle to ductile. Based on the experimental tests, this transition has been highlighted at the confinement of 20 MPa. Therefore, the triaxial test part of the calibration procedure will be performed at this confinement value.

1.2.2 Compressive test environments

PFC provides an environment designed to perform unconfined and confined compressive tests in 2D and 3D.

The test environments are composed of rigid walls. The axial top and bottom walls act as loading platens while the lateral walls (2 in 2D and 4 in 3D) control and maintain constant confinement through a servomechanism while performing confined compressive tests. They are removed when performing uniaxial tests. All the walls are frictionless, and their stiffness is bigger than the ball stiffnesses. 2D compression tests are performed on rectangular models, while 3D tests can be performed on rectangular parallelepipeds or cylindrical samples.

The simulated tests are conducted in three phases. The first one (only applied for confined tests) is the seating phase, whereby axial and confining stresses are gradually increased simultaneously until the desired confinement value is reached on all the sample faces. Once this first phase is completed, the loading phase can then begin. The loading is performed by moving the axial plates towards each other at a speed determined by the strain rate given by the user. The value of the strain

rate must be chosen to ensure quasi-static solicitation and not perform a dynamic test. Finally, the test stops once the test-termination criterion is reached. There are two of them. The first one depends on the axial stress. During simulation, the deviatoric stress and its maximum value are recorded. Based on those data, the test will stop when the axial stress drops below a given percentage (defined by the user) of the maximum stress previously reached. This criterion is used when the expected behavior of the material is brittle. The second test-termination criterion is used when the user expects a ductile behavior of the model. This criterion is based on axial strain, and the test stops once the maximum strain determined by the user is reached. During the compressive tests, useful values such as stresses, strains, energies, and micro-cracks propagation are recorded. Based on these records, it is possible after simulations to plot stress-strain curves and determine properties such as the compressive strength, Young's modulus, and Poisson's ratio.

In the context of this thesis, the geometries of the models tested are comparable to the samples used experimentally. In 2D, the models are square with sides of 30 mm, while in 3D, they are cubic with sides of 20 mm. The smaller size of the 3D samples is explained by the computational time that became prohibitively large to perform the calibration in a reasonable time. Comparative tests between samples of different sizes and the same shape have shown that the size of the samples has no impact on the mechanical properties of the material. Figure IV.3 presents 2D (a) and 3D (b) triaxial test environments.

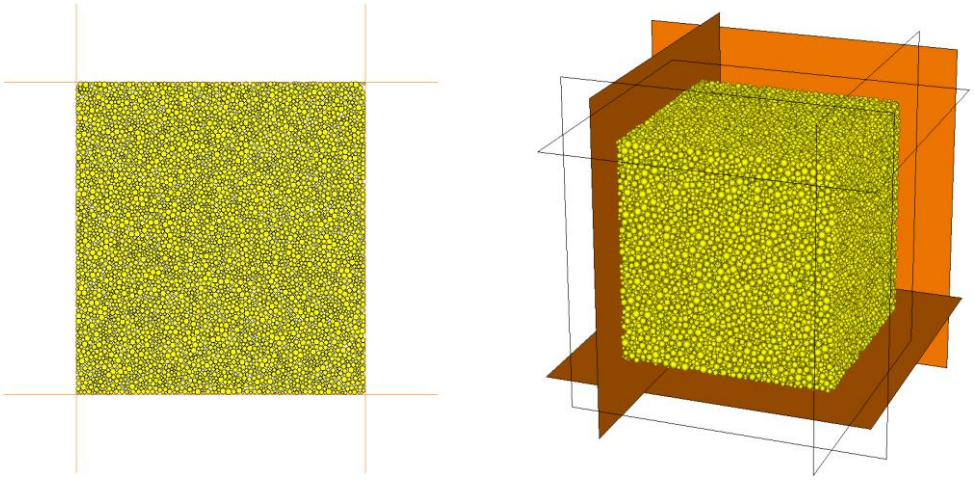

(a) (b)

Figure IV.3. Triaxial tests environment in 2D (a) and 3D (b).

1.2.3 Description of the calibration procedure

The global calibration procedure is schematized in Figure IV.4 and can be summarized as follow. Based on the first set of micro-properties, uniaxial compressive tests are performed iteratively by modifying the micro-properties until a uniaxial behavior comparable to the one observed experimentally is obtained. This calibration aims to get a compressive strength and Young's modulus for the model close to experimental values with a tolerance of 10%.

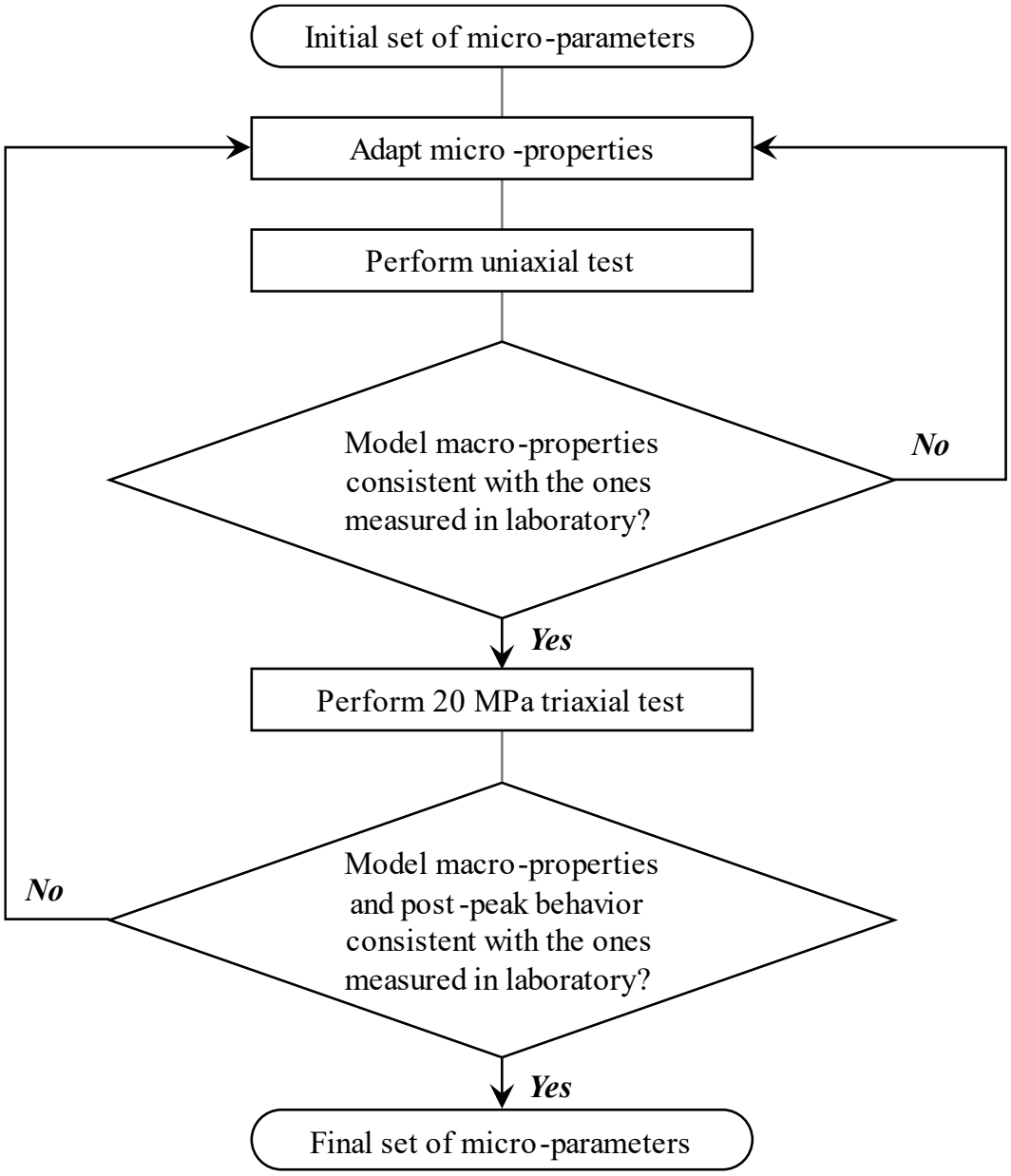

Figure IV.4. Calibration procedure based on uniaxial and triaxial tests used to find micro-properties of DEM model.

Once this first phase is completed, the set of properties is tested in a triaxial test with the confinement of 20 MPa. This test aims to verify that the set is suitable for reproducing the material's post-failure behavior while reaching a comparable confined compressive strength to the one measured in laboratory testing. Here the tolerance for the compressive strength is fixed to 10%.

The micro-properties are validated if the results obtained during the triaxial test are conclusive. Otherwise, it is necessary to go back to the "Adapt micro-properties" step and start the procedure again.

The adaptation of micro-properties is not a random process but is based on links between micro-properties and macro-properties of the model. Table IV-2 shows the micro-properties to be changed to reach desired macro-properties when using Bonded-Particle Model.

Table IV-2. Links between macro and micro -properties of PFC models using Bonded-Particle Model.

Macro-properties	**Micro-properties**
Young's Modulus	$\bar{E}_c$, E_c
Poisson ratio	$\bar{k}_n/\bar{k}_s$
Uniaxial Compressive Strength	$\bar{\sigma}_n$, $\bar{\sigma}_s$
Confined Compressive Strength	$\Delta\bar{\sigma}_n$, $\Delta\bar{\sigma}_s$
Post-peak behavior	k_n/k_s, μ

1.2.4 Results of the calibration process

The calibration started with the definition of the porosity and the particle size distribution to generate synthetic models used for the uniaxial and triaxial tests. According to Vosges Sandstone data presented in Chapter III section 3.1, the porosity has been set to 20% while the grain size distribution is uniform and comprised between 200 and 600 μm.

The entire calibration process results in the parameter sets shown in Table IV-3. The successive iterations that led to these sets of parameters are not detailed in this section but are listed in Appendix B. It is interesting to note that a dozen iterations were necessary to calibrate the 2D model, while the calibration of the 3D model required over 80 iterations. The main obstacle was the need to reproduce the post-elastic behavior under confinement.

Table IV-3. Parallel bond's micro-properties to create synthetic Vosges Sandstone models.

Component	Symbol	Microproperties	2D	3D
Grain micro-properties	R_{min}	Minimum ball radius (mm)	0.1	0.1
	R_{max}/R_{min}	Ball size ratio	3	3
	E_c	Contact modulus (GPa)	6.5	4
	k_n/k_s	Ball stiffness ratio	3	3
	μ	Ball friction coefficient	20	4
Cement micro-properties	$\bar{\lambda}$	Radius multiplicator (-)	1	1
	$\bar{E}_c$	Parallel bond modulus (GPa)	6.5	16
	$\bar{k}_n/\bar{k}_s$	Parallel bond stiffness ratio	3	4
	$\bar{\sigma}_n$	Parallel bond tensile strength (MPa)	50 ± 35	25 ± 70
	$\bar{\sigma}_s$	Parallel bond shear strength (MPa)	50 ± 35	130 ± 60

Figure IV.5 compares the stress-strain curves of the experimental tests and the numerical simulations for uniaxial and compressive tests at 20 MPa of confinement. Even though slight deviations may occur in strength and Young's modulus, these deviations are within the tolerances set by the calibration procedure. These data are summarized in Table IV-4. Besides these quantitative values, it can be observed from Figure IV.5 that the behavior of synthetic rock models changes from brittle under atmospheric conditions to ductile with slight hardening for the confinement of 20 MPa.

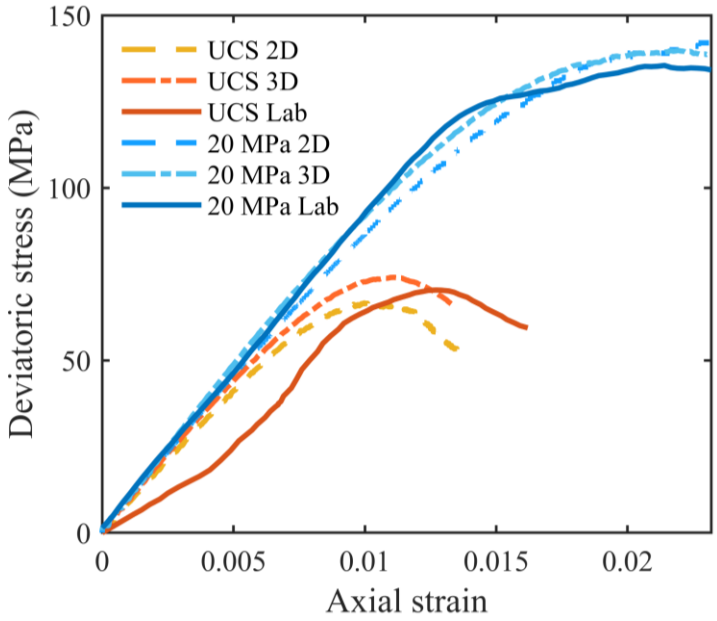

Figure IV.5. Strain-stress curve of uniaxial and triaxial tests obtained at the end of the calibration process compared to experimental ones.

Table IV-4. Comparison of compressive strength and Young's modulus between calibrated models and Vosges Sandstone.

$\sigma_2 = \sigma_3$ (MPa)	Laboratory results		2D Numerical model		3D Numerical model	
	σ_{1_rupt} (MPa)	E (MPa)	σ_{1_rupt} (MPa)	E (MPa)	σ_{1_rupt} (MPa)	E (MPa)
0	71	8668	66.7	8363	74	8892
20	148	9073	150	8709	152	9332

1.3 Failure envelope of 3D synthetic rock model

Confined compressive tests were performed with confinement ranging from 5 to 70 MPa to determine the failure envelope of the synthetic rock model of 3D, which is of interest for the quantitative aspects of this thesis. Compressive strength and Young's Modulus data from these experiments are given in Table IV-5 (strain-stress curves of these simulations are presented in Appendix B). It is noticeable that the resistance values are relatively close for the different confinements except for the 10 MPa confinement, where the model underestimates the resistance by about 20%. Regarding Young's modulus, the differences are relatively small between the model and the lab values for low confinement values but become more important from 30 MPa of confinement.

Table IV-5. Comparison between compressive strength and Young's modulus values obtained with the calibrated model and the laboratory tests from Descamps (2007).

$\sigma_2 = \sigma_3$ (MPa)	Laboratory results		3D Numerical model	
	σ_{1_rupt} (MPa)	E (MPa)	σ_{1_rupt} (MPa)	E (MPa)
0	71	8668	74	8892
5	129	8323	105	9316
10	140	8506	112	9578
20	148	9073	152	9332
30	190	10039	185	9061
40	194	10300	202	9237
50	220	10019	232	9417
70	270	11790	280	9489

Based on these data, Figure IV.6 presents the failure envelope of the synthetic rock model in the Mohr plane. The general shape of this envelope based on 3D

simulated triaxial tests is comparable with the one obtained experimentally by Descamps and presented in Figure III.8. A comparison of the parameters of this failure envelope is given in Table IV-6. These data show that differences from the experimental failure envelope are relatively small.

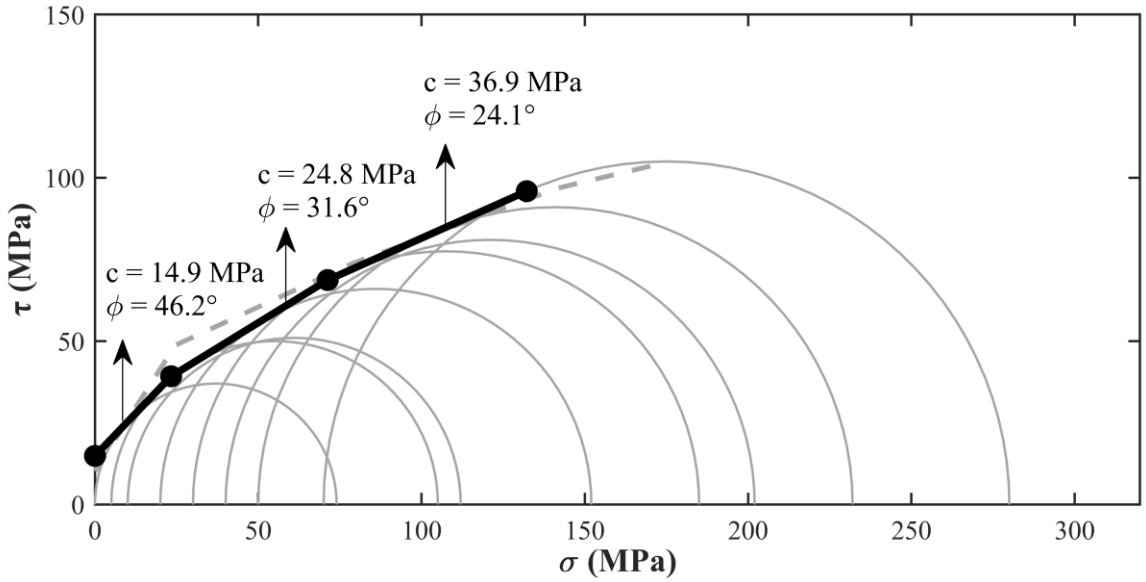

Figure IV.6. Failure envelope of synthetic 3D rock model (black lines) of Vosges Sandstone compared to experimental one (dashed grey lines).

These results show that the method used in this thesis to calibrate the DEM models to represent the evolution of rock behavior is appropriate and provides good results. To draw further conclusions on the calibration method, it would be necessary to test this approach on other rocks with different behaviors.

Table IV-6. Comparison of failure envelope parameters of Vosges Sandstone and 3D model.

Confinement range	**Vosges Sandstone**		**3D model of Vosges Sandstone**	
	***c* (MPa)**	***φ* (°)**	***c* (MPa)**	***φ* (°)**
0 – 5 MPa	10.4	57.3	14.9	46.2
5 – 30 MPa	37.4	24.8	24.9	31.6
30 – 70 MPa	44.9	20.1	36.9	24.1

2 Rock cutting models

This section gives a general overview of the physics of the problem and the different geometries and parameters used in this study for modeling rock cutting tests in 2D and 3D. The presentation of 2D and 3D models is separated because of their fundamental differences. In each case, the geometry of the rock models and the different cutter geometries used are described. Moreover, the method of applying the mud pressure to the model is discussed.

2.1 Conceptual model of rock cutting under confinement

Figure IV.7 shows the conceptual model considered to build the numerical cutting models in 2D and 3D. Although, in practice, the cutting process in drilling is a 3D process where the cutter is in simultaneous circular and vertical motion, on a small scale, the movement of the cutter can be assimilated into a linear movement at constant horizontal speeds and constant depth of cut (vertical velocity is null).

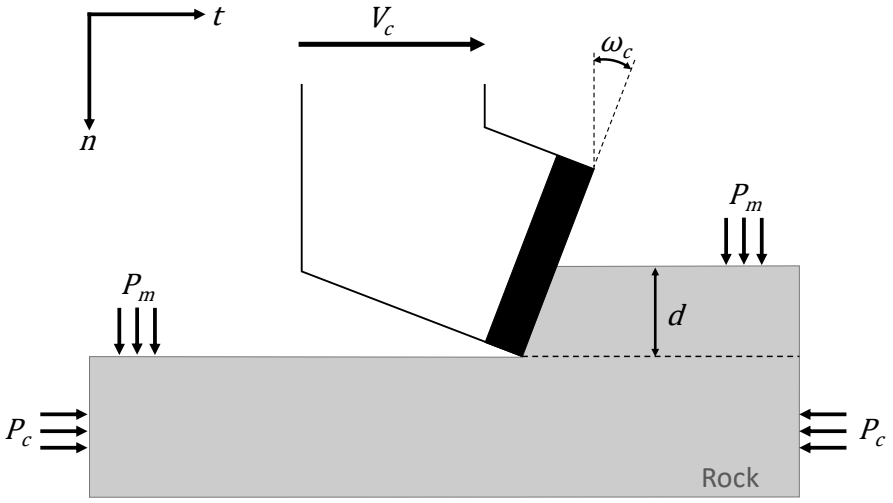

Figure IV.7. Conceptual model of rock cutting under confinement used to build numerical models.

The rock is normally subjected to a tri-dimensional state of stress where the upper surface is subjected to the mud pressure and the lateral surfaces to horizontal in-situ stresses. However, as Sellami et al. (1990) have shown, the role of lateral stress on the cutting mechanism is negligible when drilling under confinement. A 2D axisymmetric Finite Element Model was used to verify this information to determine the stress field at the cutting surface at the bottom of a wellbore.

Different models were performed considering several wellbore depths and several k ratios (σ_h/σ_v) for each depth. These models show that the stress field created near the cutting face is such that the horizontal stress is relatively close to the mud pressure. Therefore, the stresses applied to the lateral faces of the models were such that $P_m = P_c$. Since the pore pressure is not considered in the models, these are total stresses.

2.2 Two-dimensional rock cutting model

2.2.1 Model geometry

Figure IV.8 presents the general rock cutting model geometry in 2D. The model consists of a rectangular specimen, with dimensions H and L, blocked by three rigid frictionless walls on the lower, left, and right sides. These walls are used to set the boundary conditions of the model. The boundary conditions in walls are given through their motion, i.e., translational and rotational velocities. Their purpose in this numerical modeling is to fix the specimen in space. Their velocities are fixed too.

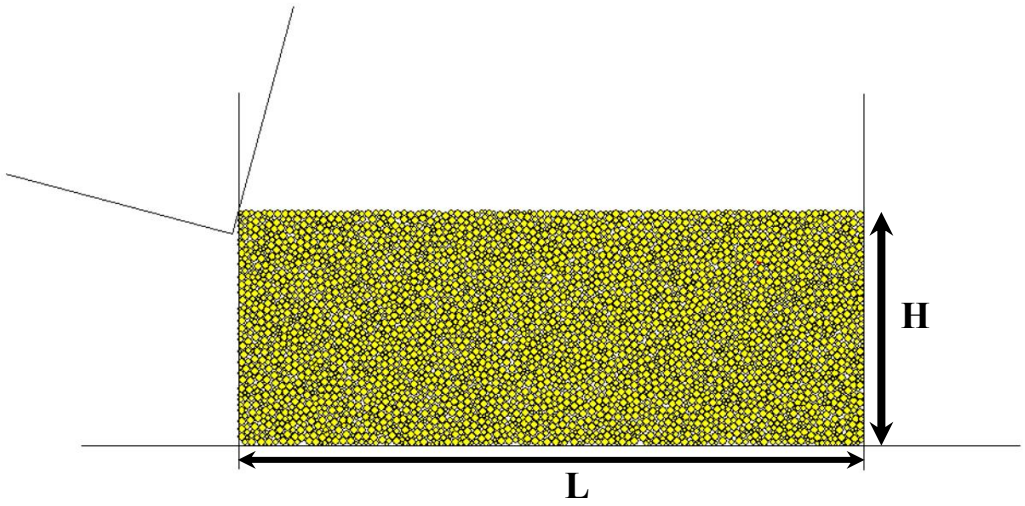

Figure IV.8. 2D model of rock cutting.

The model's dimensions remained identical for all the simulations performed with a height of 15 mm and a length of 40 mm. This sample size allows both to have a cutting length of 25mm, long enough to be in a steady-state of cutting while the results are not affected by the boundary conditions imposed by the system walls. Since PFC2D considers a plane state of deformation, it is worth mentioning that

the particles have a hidden third dimension that allows the calculation of forces in the model. This third dimension is 1m long. It means that each particle, regardless of its diameter, is a cylinder with a length of 1m. Similarly, the cutter has a third dimension of 1m too.

2.2.2 Cutter geometries

The PDC cutters are represented as a single wall with several segments. Three different cutter geometries were modeled for 2D simulations (Figure IV.9). The geometry that has been mainly used is the sharp cutter. This cutter is composed of two perpendicular segments whose length has been fixed at 13 mm. The two other geometries implemented are the chamfered cutter and the blunt one. These two cutters are made up of three segments. The chamfered cutter is characterized by its chamfer angle ω_{ch} and length L_{ch}, as shown in Figure IV.9 (b). The blunt cutter is characterized by the length L_m of its wear flat (Figure IV.9 (c)). The cutter geometry of the blunt cutter has been implemented in the code to ensure that the wear flat is always horizontal regardless of the back rake angle.

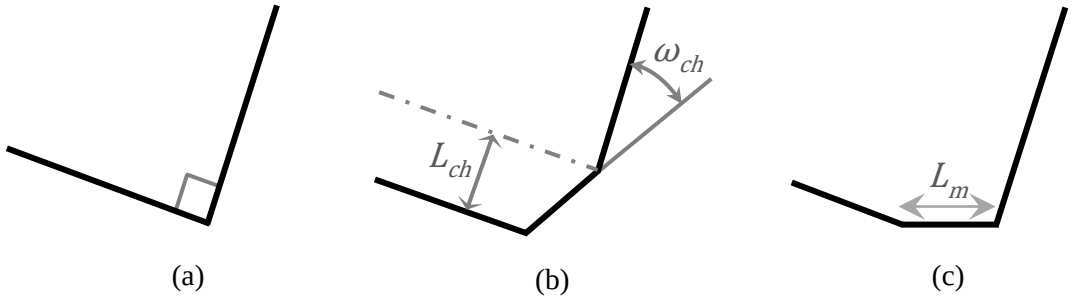

Figure IV.9. Cutter geometries used for 2D simulations: (a) sharp cutter, (b) chamfered cutter, (c) blunt cutter.

2.2.3 Implementation of mud pressure

Mud pressure applied to the surface of the specimen was implemented using the spanning-chain algorithm. This algorithm represents the drilling mud as a membrane on the surface of the rock sample and the crushed rock particles that evolve with the cutter displacement and transmits the mud pressure to the sample (Figure IV.10). This pressure is applied perpendicular to the surface of the membrane.

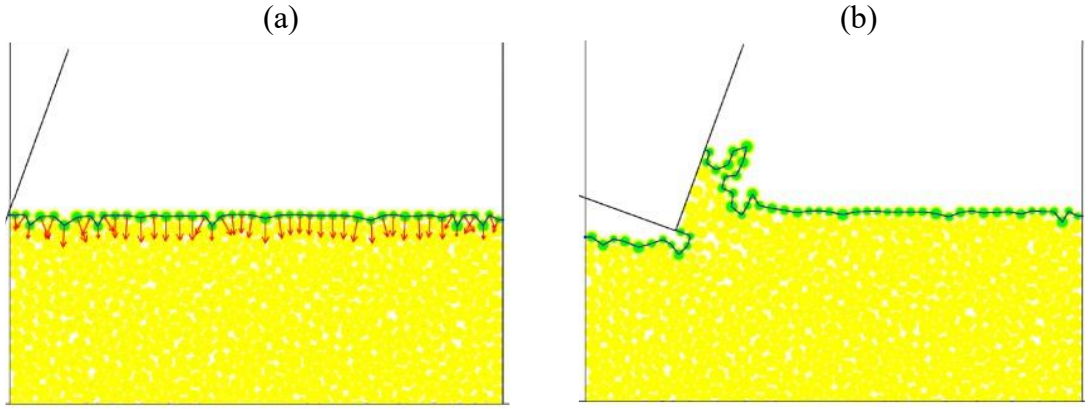

Figure IV.10. Implementation of confinement in 2D models: (a) membrane at the beginning of the test and orientation of the pressure along the surface and (b) evolution of the membrane during the test.

Practically, this procedure builds two chains of particles: the first one going from the cutter to the right-hand wall of the model and the second one from the tip or the back face of the cutter to the left-hand wall. These two chains of particles are composed of successive surfaces passing through the center of particles at the top of the model. Each of these surfaces is used to determine the direction and magnitude of the applied external force assigned to each chain particle based on the desired confining pressure. Figure IV.10 shows the evolution of such a chain during a cutting test and how the pressure is applied from each chain particle. The confinement algorithm is not implemented when the cutting simulation is done in atmospheric conditions.

2.2.4 Cutting parameters and outputs

The main cutting parameters that could be modified in two dimensions are the depth of cut, the cutting speed, and the back rake angle. From the cutter geometry point of view, the modified parameters during the study were the length of the wear flat for blunt cutters and the length and angle of the chamfer for chamfered cutters.

Since the cutters consist of a single wall, the model provides the horizontal and vertical components of the forces applied to the cutter. Therefore, it is not possible to determine the forces applied on each cutter face. During simulations, vertical and horizontal forces were monitored. Figure IV.11 shows the raw recording of the cutting forces for a confined cutting test in 2D and the color convention used to display the tangential (green) and normal (red) cutting forces.

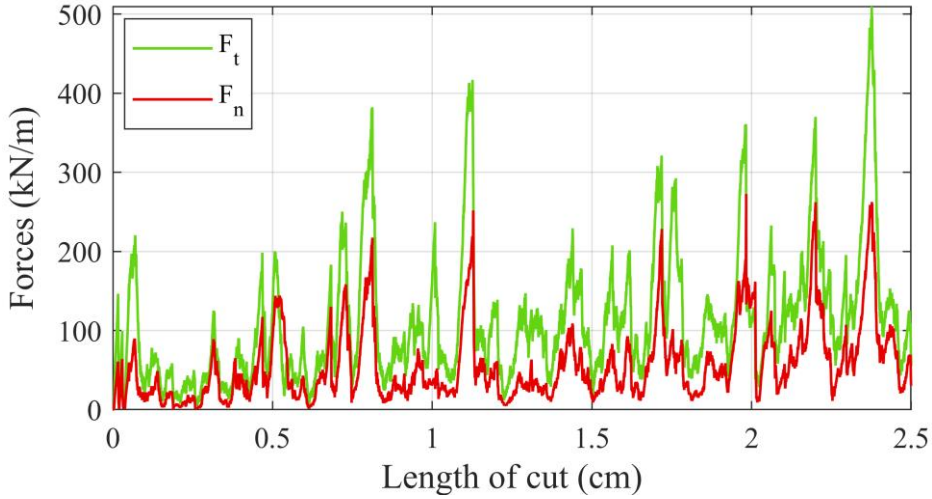

Figure IV.11. Raw 2D cutting force signals.

Moreover, each simulation has been recorded in video format. The purpose of recording these simulations was twofold. First, they allowed checking afterward if the simulation had gone properly. Moreover, these videos were used to analyze the destruction mode involved during the test. For this purpose, the broken bonds between particles were represented by red or blue lines, depending on whether the break occurred by traction or shear. Observing these micro-cracks allows following the fracture propagation in the material to qualify the destruction mode. Figure IV.12 shows several snapshots of a video recorded for a cut simulated under atmospheric conditions and for a cutting depth of 2 mm.

At the beginning of the simulation, when the cutter impacts the model (Figure IV.12 (a)), we can observe the formation of a small chip on the upper part of the model while some fractures propagate in depth. As the cutter moves forward and due to its speed, the destroyed rock accumulates on the cutter face (Figure IV.12 (b)). Some of the accumulated material is composed of rock chips as well as crushed fragments (area with a high density of red lines showing the broken bonds). Figure IV.12 (b) and Figure IV.12 (c), which are very close snapshots, highlight the propagation of a fracture under the free surface of the rock that will result in the formation of a chip. Finally, Figure IV.12 (d) illustrates the creation of a chip while another one has been released and is in free flight from the rest of the material accumulated on the cutter face.

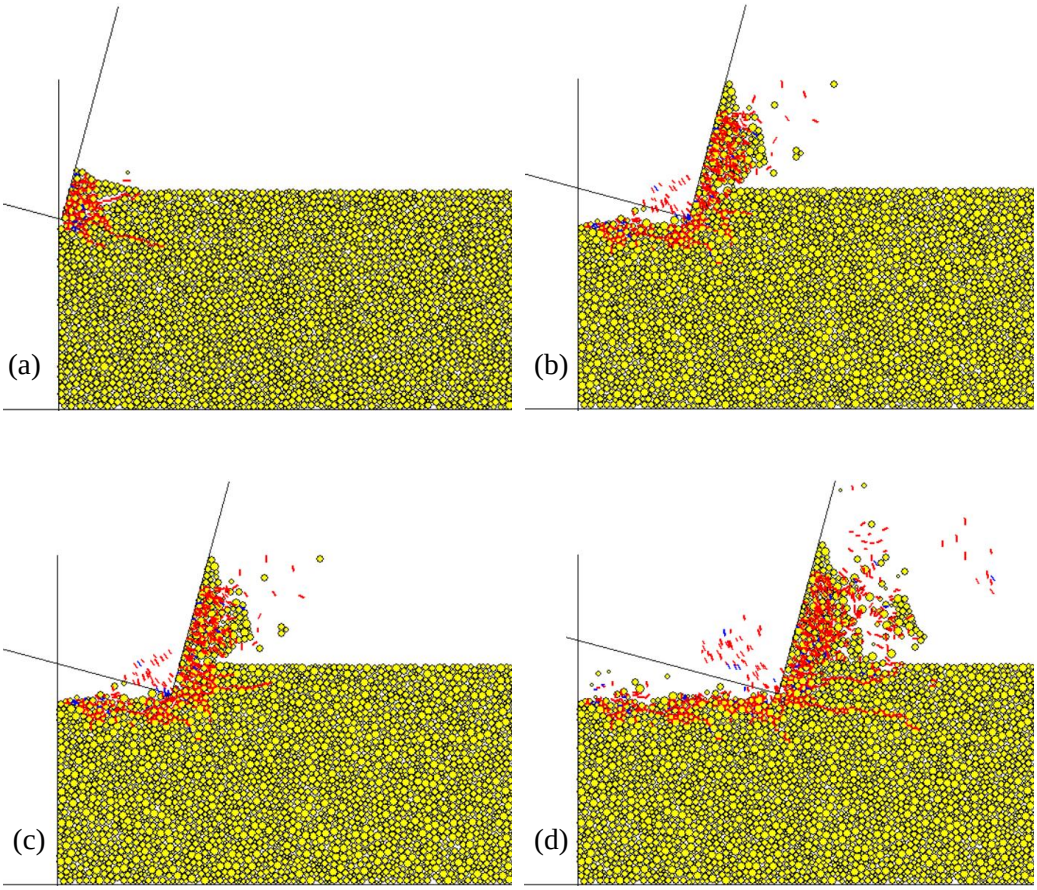

Figure IV.12. Snapshots of 2D cutting modeling at different length of cut: (a) 0.03 cm, (b) 0.77 cm, (c) 0.83 cm, and (d) 1.42 cm.

2.2.5 2D data processing

As shown in Figure IV.11, the evolution of the cutting forces in 2D is composed of multiple peaks and drops, especially at the beginning of the simulation. Two elements explain this evolution of forces. Firstly, due to the nature of the model and the cutting mechanism, the cutter may not contact a particle for a short time, causing the cutting forces to drop close to zero. However, the cutting forces can reach a very short peak when the cutter comes back into contact with the model. Secondly, due to the high data acquisition frequency, all these peaks and drops are recorded. Therefore, a moving average filtering procedure was implemented on the recorded simulated forces to mitigate the peaks.

Furthermore, since the model considers a 1m wide cutter, the cutting forces were divided by 100 to consider a 1cm wide cutter and compare them to the experimentally measured ones. Figure IV.13 shows the same signal as Figure IV.11 but after processing.

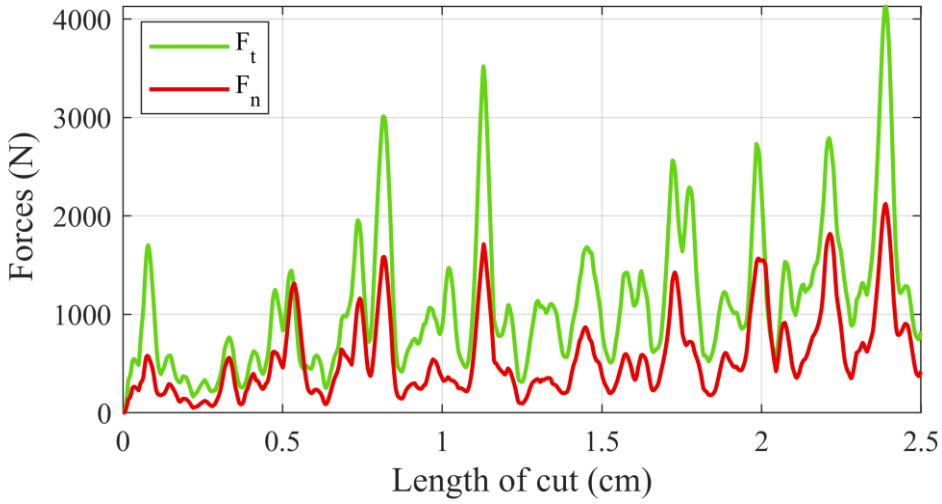

Figure IV.13. 2D cutting force signals after processing.

2.3 Three-dimensional rock cutting model

2.3.1 Model geometry

In contrast to the 2D model, the geometry of the 3D models was much more impacted by computational resources and was therefore designed to obtain accurate results at a reasonable computational cost. Figure IV.14 presents the general rock cutting model geometry in 3D. The rock sample is represented as a rectangular parallelepiped with dimensions H, L, and W. As for the 2D model, boundary conditions are imposed by the walls surrounding the specimen. The model was encapsulated between five walls: four lateral and one beneath. The height of the specimen fixes the height of three of the four side walls, while the wall opposite to the cutter is higher to avoid the rotation of the model.

While the length L and height H of the specimen were constant and fixed at 25 mm and 8 mm for all simulations, the width W was a function of the cutter geometry and cutting depth. Comparative tests showed that the model width should be at least 2.5 times the maximum groove width to avoid boundary conditions affecting the results. To limit the calculation time, the refine function of PFC3D was used to create different particle size distributions in the model by increasing the particle radius in areas not affected by the displacement of the PDC cutter. Three zones were defined with this function to progressively increase the particles' size with depth. The particles in the upper zone have the size defined during the calibration stage. The distribution is multiplied by 1.5 in the central zone and 2 in the lower

one. These three areas are represented in Figure IV.14 by three different colors given to the particles.

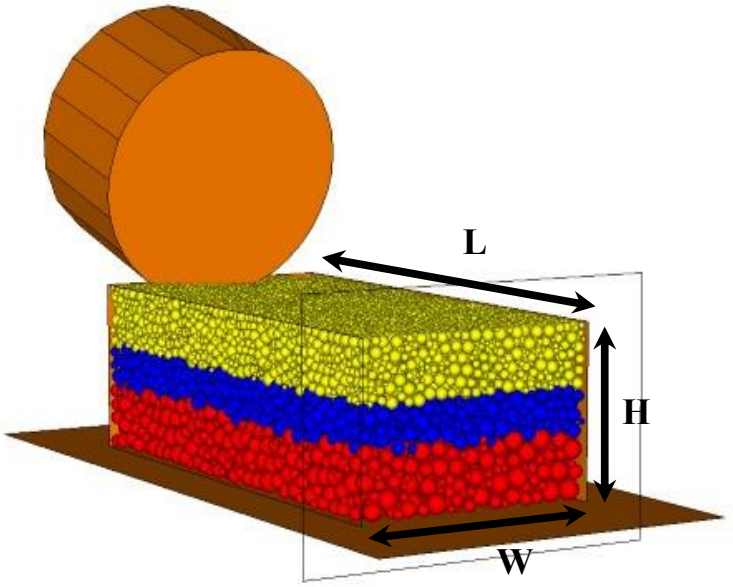

Figure IV.14. 3D model of rock cutting: the three-particle colors represent the three size distribution zones.

2.3.2 Cutter geometries

Simple surfaces such as plane, cylindrical and conical surfaces were used for cutter design. Two types of cutters were built with these surfaces: circular cutters and rectangular cutters.

Concerning the circular cutters, two different geometries were implemented: a sharp cutter and a chamfered one (Figure IV.15 (a) and (b)). These two cutters have a diameter of 13 mm, close to the dimensions of the cutters used experimentally and in industry. For the rectangular cutters, three configurations were used: a sharp cutter, a chamfered one, and a cutter with a wear-flat (Figure IV.15 (c), (d) and (e)). All these cutters have a width of 10 mm. The 3D work was mainly carried out with the sharp circular cutter. The other cutters were used to study the impact of the change in geometry and the impact of a chamfer or a wear flat on the cutting forces.

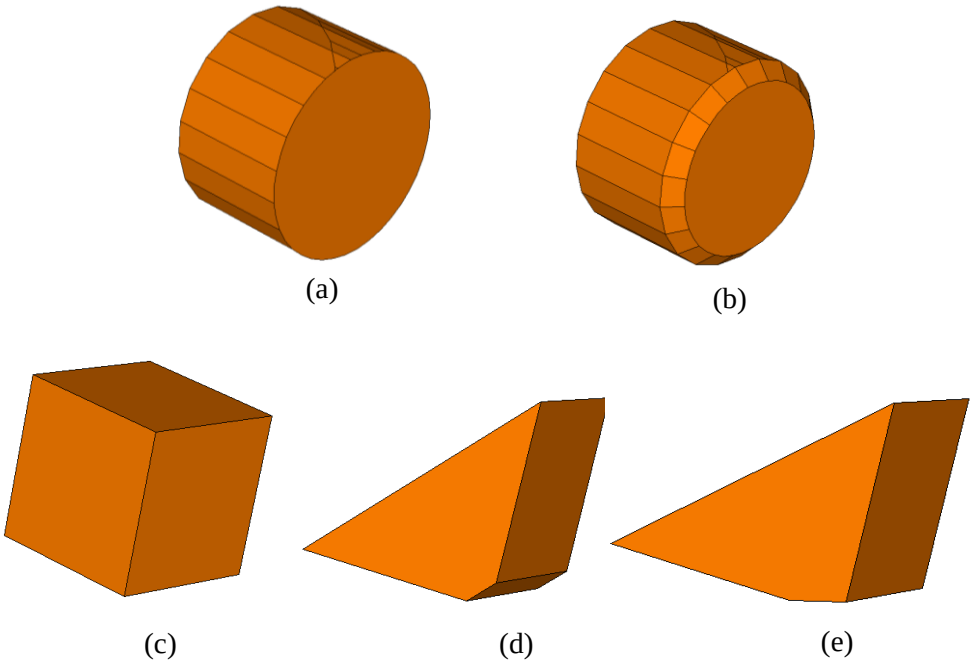

Figure IV.15. Cutter geometries used for 3D simulations: (a) sharp circular cutter, (b) circular chamfered cutter, (c) rectangular sharp cutter, (d) rectangular chamfered cutter, and (e) rectangular blunt cutter.

2.3.3 Implementation of mud pressure and confining pressure

Mud pressure and confinement were applied via the 'shinning-lamp' algorithm. This method defines particles subjected to confinement as those receiving direct illumination from light sources that shine towards the body. Each outer particle of the body is assigned to an externally applied force (F) which is related to the specified pressure (P_{conf}) and the amount of received light (which is related to its illuminated surface).

Figure IV.16 illustrates this method; it shows an assembly of particles receiving light laterally from an infinite source. For each particle, the force applied to its center is the sum of the forces contributions from each light source with $F = P_{conf} . A$, where A is the projected illuminated area. Since the program calculates the position of the particles at each time step, the pressure is always exerted on the particles located at the outer boundary of the model. In this way, the confining pressure is also applied to the particles accumulated in front of the PDC cutter.

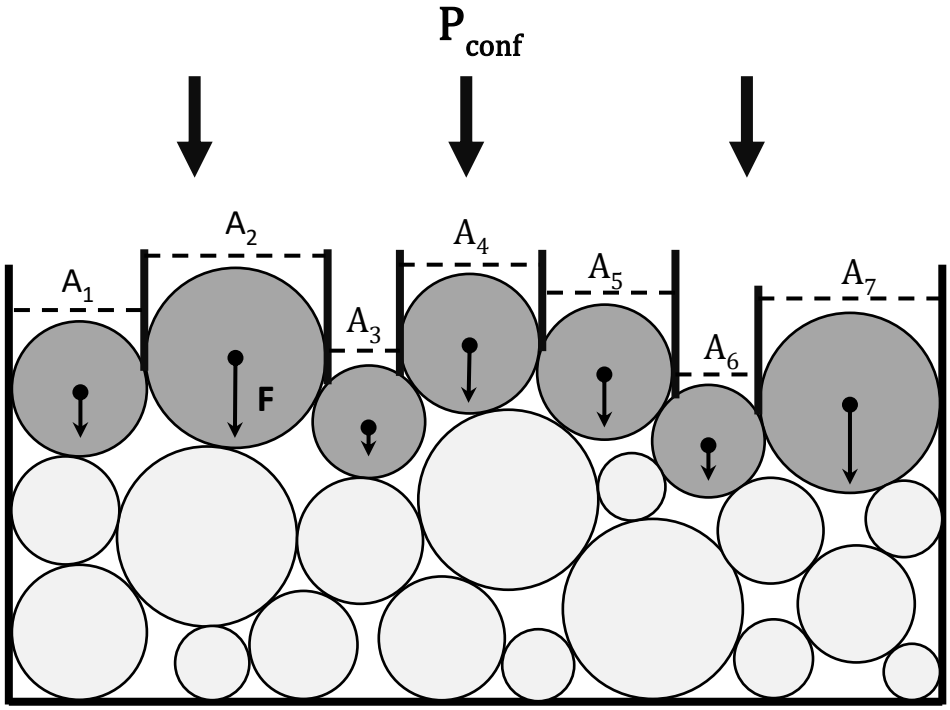

Figure IV.16. Schematic view of the shining lamp-algorithm. Applied particle forces (F) are proportional to the projected areas (A_i). Light grey particles are not illuminated.

2.3.4 Cutting parameters and outputs data

As for the 2D models, the main parameters that could be modified are the depth of cut, the cutting speed, and the back rake angle. In addition to these three parameters, the side rake angle could be studied in 3D. From the point of view of the cutter geometry, it is essentially the length and angle of the chamfer as well as the length of the wear flat that were adapted to quantify their impact on the cutting forces.

As the different faces of the cutters are independent, it was possible to monitor the forces exerted on each face and in the three main directions. Figure IV.17 shows the cutting forces measured on the cutting face of a sharp circular cutter at atmospheric conditions and for a cutting depth of 1 mm. The same color convention for tangential and normal cutting forces was used for 3D and 2D modeling. It should just be mentioned that the lateral force has been added, which by convention will be represented in blue in all cutting force charts of 3D models.

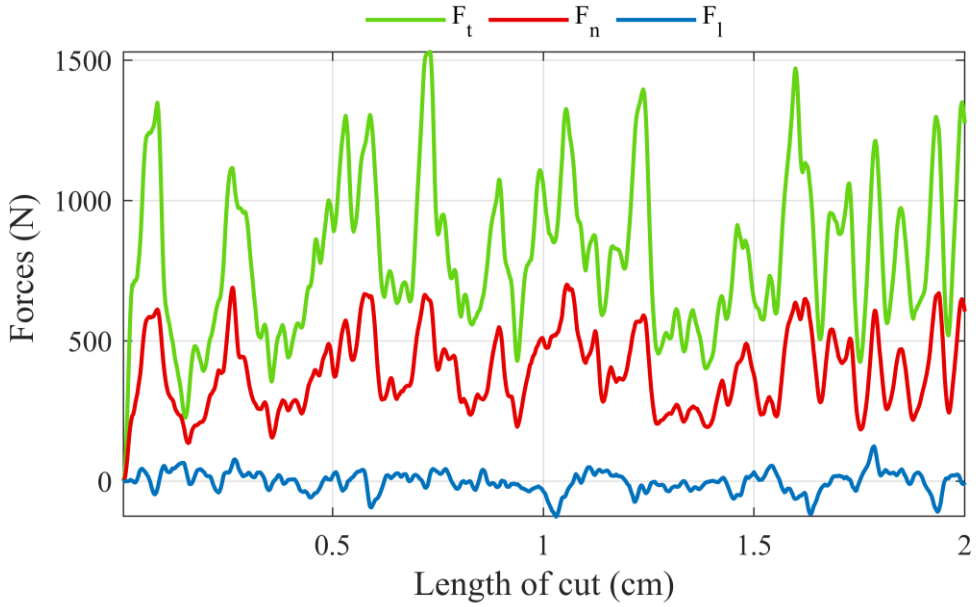

Figure IV.17. Raw 3D cutting force signals from the cutting face of a circular cutter.

As for 2D models, videos of each test were recorded. With calculation times that can exceed one day, these videos allowed to verify their good execution afterward. Unfortunately, the graphical display tool of PFC3D 4.0 does not enable obtaining a usable representation of the fracture propagation in the material. To overcome this shortcoming, the evolution of the number of cracks (bonds failed) was monitored during each simulation (Figure IV.18). These data were then used to qualify the destruction mode and will be discussed in Chapter VI.

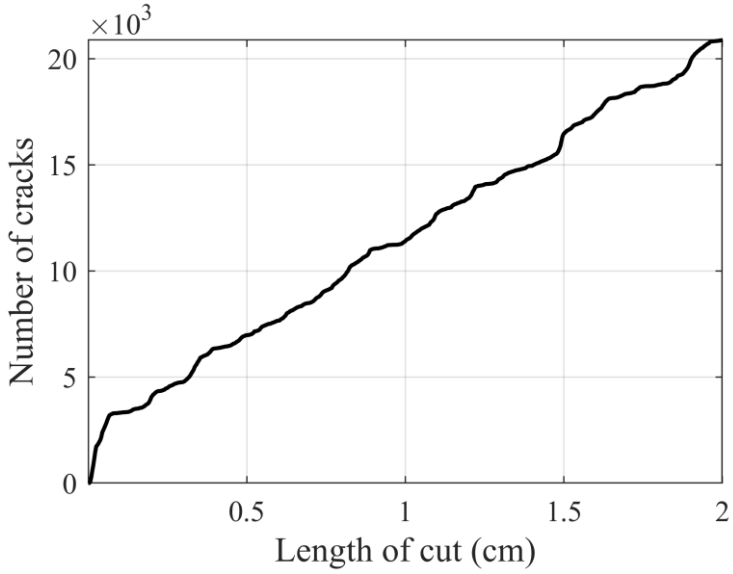

Figure IV.18. Number of cracks evolution during 3D cutting simulation.

2.3.5 3D data processing

As previously stated, 3D modeling allows us to obtain the forces exerted on each face of the cutter. This proved to be very useful during the work to understand the evolution of the forces when the cutting parameters are modified. However, in general, and unless stated specifically, the forces mentioned in this report are the total forces acting on the whole cutter. Moreover, by summing all the forces, it is possible to compare them to those measured experimentally. Figure IV.19 shows an example of this sum of forces in the case of a chamfered cutter.

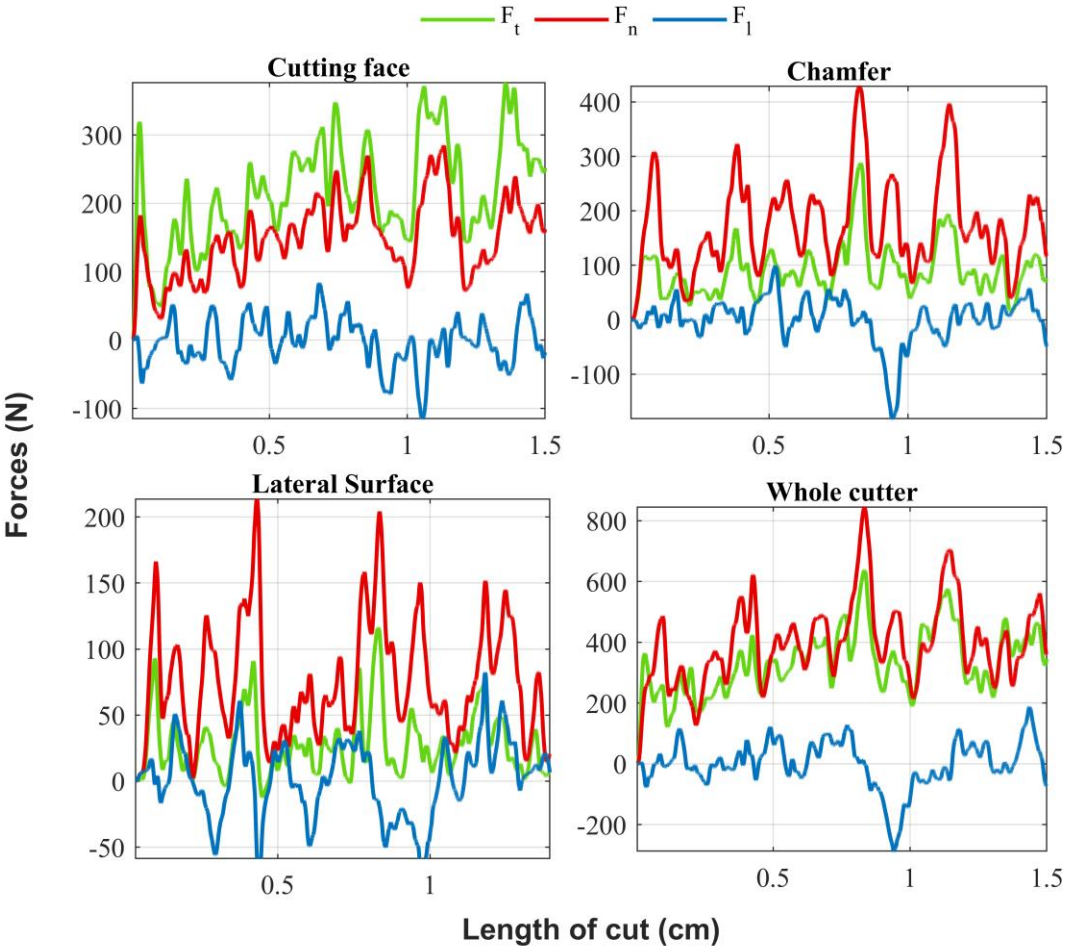

Figure IV.19. 3D cutting force signals for each face of a circular chamfered cutter and their summation.

3 Quantities determined from cutting forces

As presented in Chapter II, Specific Energy E is used to characterize and compare single cutter experiments. The same approach was used to compare simulations performed with different cutting parameters, confinement, or cutters of various shapes.

Usually, E is calculated based on the average tangential cutting forces $\bar{F}_t$ and the active surface of the cutter A_C as follow:

$$E = \frac{\bar{F}_t}{A_C} \tag{IV.1}$$

Therefore, it was necessary to define how the measurement of the average forces should be done based on output data and the calculation of the active surface, which depends on the cutter geometry and cutting parameters.

Figure IV.20 shows a typical result of a cutting test under confinement. Although the evolution of the forces will be discussed in detail in Chapter VI, it can already be observed that the cutting forces evolve in a transient phase before reaching a steady state. The average cutting forces were determined based on this steady-state.

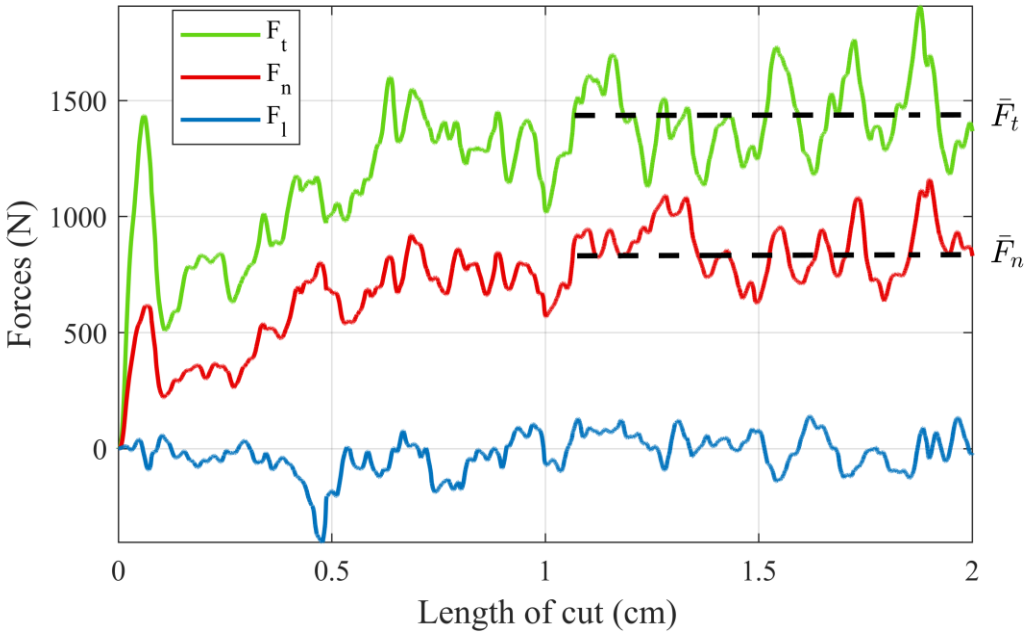

Figure IV.20. Determination of mean tangential and normal cutting forces based on force signals.

Two cases need to be distinguished regarding the determination of the active surface. The first one concerns 2D and 3D models with a rectangular cutter which is the simplest. Indeed, the active surface is the projection in the vertical plane perpendicular to the cutter path of the rectangular surface in contact with the rock. It depends on the depth of cut, the cutter width, and the side rake angle for 3D modeling (Figure IV.21). It was therefore calculated by:

$$A_C = W_c \ d \ cos\,(\omega_s) \qquad \text{(IV.2)}$$

Where W_c is the cutter width, d is the depth of cut, and ω_s is the side rake angle. This definition of the active surface for a rectangular cutter is only valid when the groove walls are vertical or in the case of slab tests.

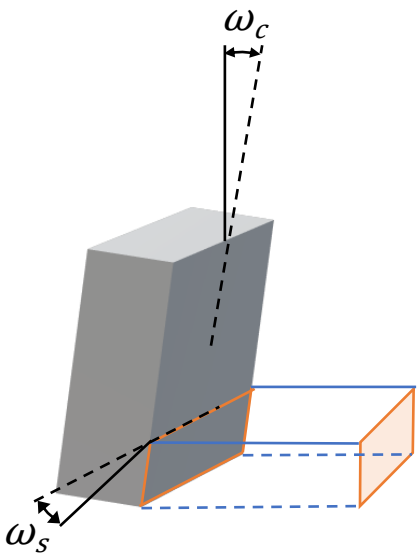

Figure IV.21. Active surface for a rectangular cutter.

The second case concerns the circular cutters used for 3D models. The part of the cutter in contact with the rock is a circular segment that depends on the cutter diameter, the depth of cut, and the back rake angle. Then the projection of this surface in a vertical plane perpendicular to the groove gives the active surface, depending on the back rake angle and the side rake angle (Figure IV.22). The formulas determining the active surface for a circular cutter can be given by:

$$C_S = \left(\left(\frac{D}{2}\right)^2 \; acos\left(\frac{\frac{D}{2} - \frac{d}{cos\,(\omega_c)}}{\frac{D}{2}} \right) - \left(\frac{D}{2} - \frac{d}{\cos(\omega_c)}\right) \sqrt{\left(\frac{D}{2}\right)^2 - \left(\frac{D}{2} - \frac{d}{cos\,(\omega_c)}\right)^2} \right) \tag{IV.3}$$

$$A_C = C_S \; cos(\omega_c)\, cos(\omega_s) \tag{IV.4}$$

Where C_S is the circular segment of the cutter, D is the cutter diameter, d is the depth of cut, ω_c is the back rake angle and ω_s is the side rake angle.

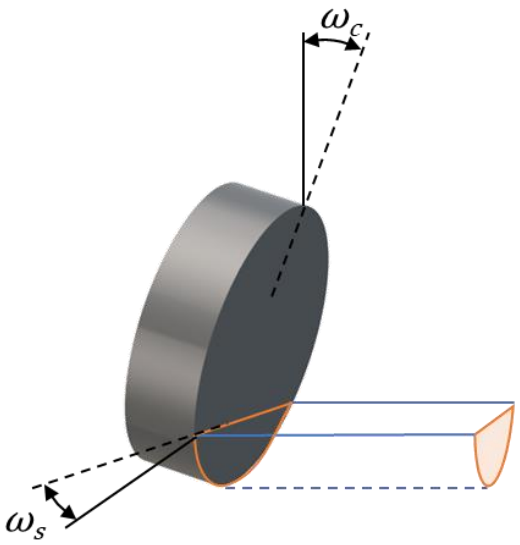

Figure IV.22. Active surface for a circular cutter.

It is also possible to determine cutter Aggressiveness based on cutting forces. Aggressiveness M is defined as the ratio between the torque and the WOB when dealing with drill bits on the field. At a given WOB, a bit with higher reactive torque is considered more aggressive (Rajabov et al., 2012). For single cutter tests, Aggressiveness can be determined as the ratio between tangential and vertical cutting forces (Carrapatoso et al., 2015). In numerical modeling, this ratio can be used as a sensitivity parameter to analyze the cutting efficiency of different cutter shapes. Aggressiveness, denoted M, is calculated in this work by:

$$\mathrm{M} = \frac{\overline{F_t}}{\overline{F_n}} \tag{IV.5}$$

4 Validation of rock cutting models

Following this step of calibration of 2D and 3D Vosges Sandstone synthetic models and the building of cutting models, it was necessary for robustness purposes to validate them from the point of view of the cutting mechanism before proceeding further. In this context, linear cutting tests under atmospheric conditions were carried out on a Rock Strength Device (RSD).

4.1 Laboratory tests

The cutting tests performed were determined based on the characteristic of the 2D cutting models due to the plane strain state in PFC2D, which imposes that the cutter is rectangular and has the same width of 1m as the sample (Figure IV.23 (a)). This characteristic of the 2D model can be assimilated to a particular cutting test: the slab tests. A slab test refers to a cutting configuration in which the width of the rectangular cutter is equal to the width of the sample (Figure IV.23 (b)). In this type of cut, the problem is geometrically two-dimensional.

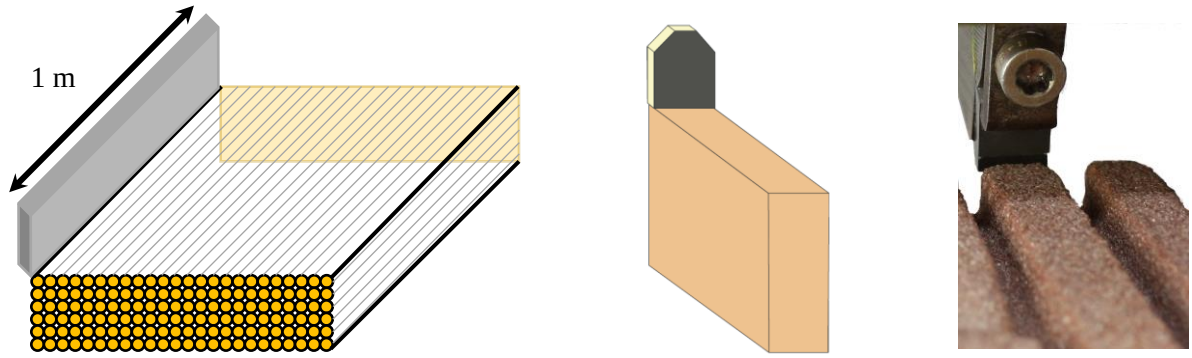

(a) (b) (c)

Figure IV.23. Slab tests: (a) fake 3D representation of 2D rock cutting simulation by DEM, (b) Schematic view of a slab test (Dagrain et al., 2001), (c) slab tests performed in the laboratory.

To perform these tests, a sample of Vosges sandstone was previously grooved with a saw to obtain test bands of 10 mm wide as the sharp rectangular cutter used (Figure IV.23 (c)).

Following cutting parameters were used to perform the slab tests on the Rock Strength Device (RSD, Figure IV.24):

- Back rake angle: 15°;
- Cutter velocity: 4 mm/s;
- Cutting length: 40 mm;
- Depth of cut: from 0.2 to 1.6 mm by step of 0.2 mm.

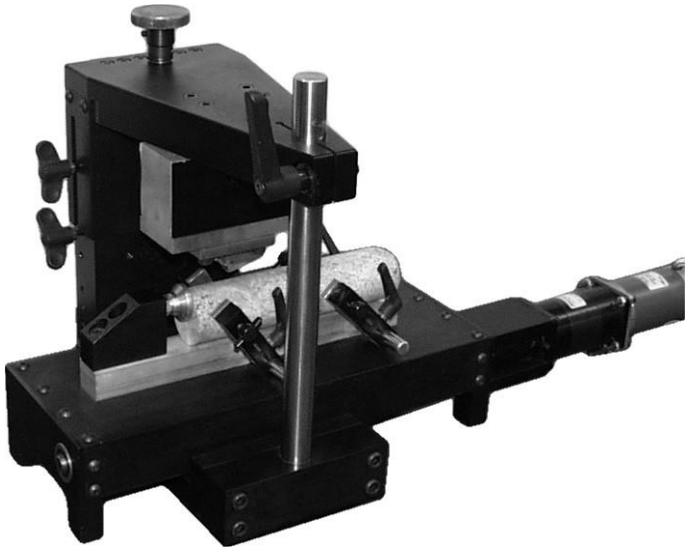

Figure IV.24. Rock Strength Device used to perform slab tests.

4.2 Numerical models of slab test

The 2D models were not modified to perform these simulations since the laboratory test geometry was designed based on them. In contrast, the 3D model had to be slightly modified to allow test modeling. The main modification concerns the side walls locking the sample in the space. As the side faces of the sample must be free, three of the four side walls have been limited to half the height of the sample. Therefore, the wall located at the end of the sample in the cutting direction was not modified. These modifications allow the lateral movement of the particles to be unrestricted while ensuring that the model remains fixed. Moreover, the cutter and sample widths were set to 10 mm. A 3D model of the slab test is presented in Figure IV.25.

The cutting parameters used to perform the cutting simulation are:

- Back rake angle: 15°;
- Cutter velocity: 3 cm/s;
- Cutting length: 20 mm;
- Depth of cut: from 0.2 to 1.6 mm by step of 0.2 mm.

Compared to experimental cutting speed, the cutting speed in numerical models was increased to perform the simulations in a reasonable time while remaining close to the experimental conditions.

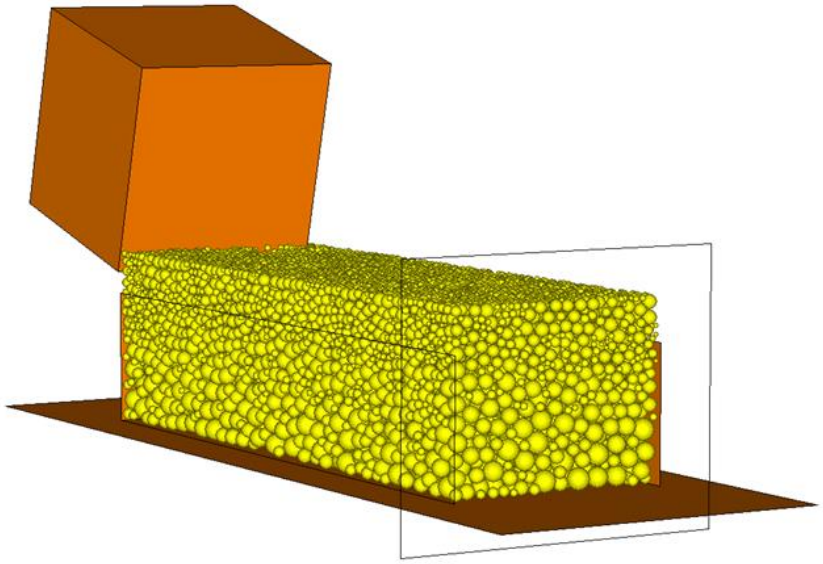

Figure IV.25. The 3D model used to simulate slab tests.

4.3 Results of the validation process

Figure IV.26 shows the results obtained during this validation phase of the numerical models. The mean tangent cutting forces determined from the numerical models agree with the experimental results. Indeed, the differences between these forces are relatively small, and their evolution with the cutting depth is comparable. This evolution can be decomposed into two parts. The first part where the forces seem to evolve linearly with the depth of cut, and the second one from 1.2 mm of DOC where the slope appears smaller. Moreover, these observations agree with the numerous experimental results under atmospheric conditions published in the literature.

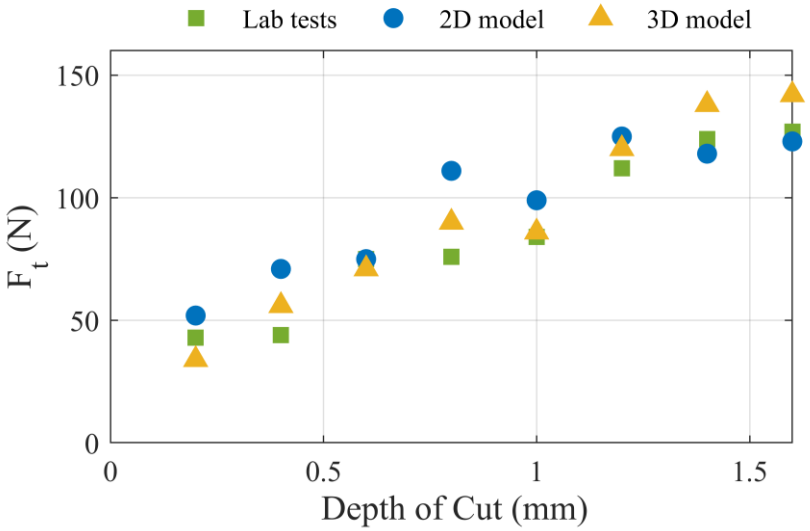

Figure IV.26. Validation of cutting models through slab tests in atmospheric conditions.

Regarding the destruction mechanism, Figure IV.27 compares the evolution between laboratory tests and 2D numerical simulations of the destruction mode from a scratching (Figure IV.27 (a) and (b)) to a chipping one (Figure IV.27 (c) and (d)) when the depth of cut increases.

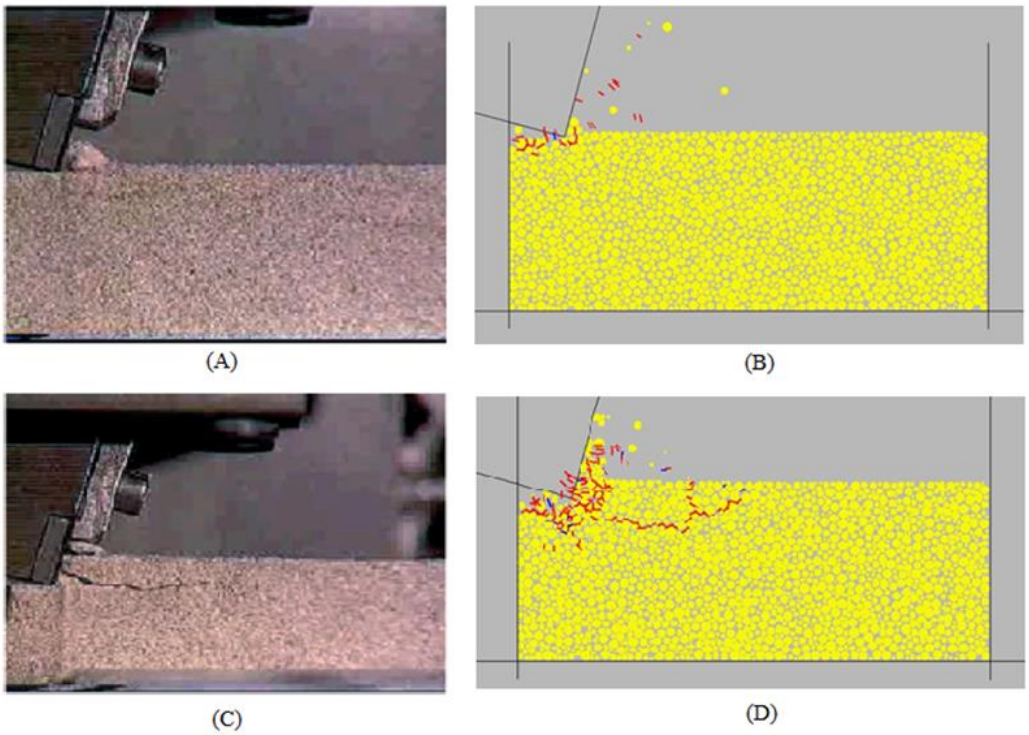

Figure IV.27. Comparison between scratching (A (Richard, 1999) and B) and chipping (C (Richard, 1999) and D) destruction mechanisms observed in lab and during numerical modeling.

5 Simulation protocols

Simulation work carried out to understand better the cutting mechanism under confinement was conducted in four phases.

In the first phase, the work focused on the impact of confinement on the cutting mechanism from qualitative and quantitative perspectives. From a qualitative point of view, the objective was to understand how this mechanism, which is characterized by two destruction modes in atmospheric conditions depending on the depth of cut (scratching and chipping modes), evolves to the formation of ribbons under confinement during experimental tests, regardless the depth of cut. Regarding the quantitative aspect, the objective was to highlight the evolution of the Specific Energy with the confinement and to relate it to the mechanical properties of the studied material. Therefore, two parameters were modified during this first phase: the depth of cut and the confinement.

Two depths of cut were considered: 0.5 and 1.5 mm. These values were chosen to obtain the two modes of destruction in low confinement conditions while remaining in ranges of values corresponding to field and experimental conditions. Concerning the confinement, the range went from 0 MPa to 40 MPa. The upper limit was chosen based on the evolution of the behavior of the Vosges sandstone, which evolves from brittle to ductile with hardening within these two bounds. The other parameters, such as the back rake angle or the cutting speed, correspond to the typical values used experimentally (Rajabov et al., 2012; Amri, 2016; Akbari and Miska, 2017). Table IV-7 summarizes the values used for these different parameters for this first phase. Concerning the cutters, only sharp ones were used in 2D and 3D (the circular one) for this first phase, as the objective was to focus only on the impact of the confinement.

Table IV-7. Cutting parameters used during the first phase of simulations to study the effect of confinement on the rock cutting mechanism.

Parameters	Values
Cutting velocity (m/s)	1
Back rake angle (°)	15
Side rake angle (°)	0
Confinement (MPa)	0 ; 10 ; 20 ; 30 ; 40
Depth of cut (mm)	0.5 ; 1.5

The second phase focused on the effects of cutting parameters (depth of cut, back rake, and side rake angles) to compare their relative influence on cutting forces and energies in different confinement conditions. The second objective of this phase was to ensure that the numerical model could reproduce the effects of these parameters as observed in the laboratory.

In this framework, 3D simulations were performed to investigate this problem. Table IV-8 shows the values for these different parameters during this second phase. These values were chosen in the same order of magnitude as those used experimentally. In this second phase, the depth of cut and the confinement values considered were the same as in the first phase.

Table IV-8. Cutting parameters used during the second phase of simulations to study the relative effect of confinement and cutting parameters on the cutting mechanism.

Parameters	Values
Cutting velocity (m/s)	1
Back rake angle (°)	15 ; 30 ; 45
Side rake angle (°)	0 ; 5 ; 10 ; 20 ; 40
Confinement (MPa)	0 ; 10 ; 20 ; 30 ; 40
Depth of cut (mm)	0.5 ; 1 ; 1.5 ; 2

The third phase focused on the effects of cutter geometry. In 2D, the work essentially consisted in changing the cutter geometry to study its effect on the destruction modes and the fracture propagation in the material. Table IV-9 presents the different cutter geometries used for this part of 2D modeling. The 3D simulations were used to quantify the effect of cutter geometry on the cutting forces. Table IV-10 presents the geometries considered.

Table IV-9. Geometrical parameters used in the third phase of simulation to study the impact of cutter shape on cutting mechanisms in 2D models.

Type of cutter	Parameters	Values
Sharp cutter	Length (mm)	13
Chamfered cutter	Chamfer angle (°)	45
	Chamfer Length (mm)	0.5
Blunt cutter	Length of the wear flat (mm)	0.5 ; 1.5

Table IV-10. Geometrical parameters used in the third phase of simulation to study the impact of cutter shape on cutting mechanisms in 3D models.

Shape of the cutter	Type of cutter	Parameters	Values
Circular	Sharp cutter	Diameter (mm)	13
		Thickness (mm)	8
	Chamfered cutter	Diameter (mm)	13
		Thickness (mm)	8
		Chamfer angle (°)	30 ; 45 ; 60
		Chamfer Length (mm)	0.25 ; 0.5
Rectangular	Sharp cutter	Width (mm)	10
		Thickness (mm)	10
	Chamfered cutter	Width (mm)	10
		Thickness (mm)	10
		Chamfer angle (°)	30 ; 45 ; 60
		Chamfer Length (mm)	0.25 ; 0.5
	Blunt cutter	Width (mm)	10
		Thickness (mm)	10
		Length of the wear flat (mm)	0.25 ; 0.5 ; 1 ; 2

Finally, simulations were also conducted in 3D to analyze the practical case of groove overlapping. Indeed, in practice, the cutter does not attack a flat surface but a surface that has been previously cut. Two general cases were considered. The first one consisted of performing two cutting tests along the same line but at different depths of cut. Typically, the first test was performed at 1 mm depth of cut and the second at 2 mm (Figure IV.28 (a)).

This situation approaches the conditions under which the tests are performed with a single cutter test bench. Indeed, during these tests, the cutter, which presents a circular path, passes several times in the same groove with a constant rate of penetration. The second case studied the partial overlap of two grooves. Two cutting tests were performed at identical pass depths but with an offset proportional to the groove width (Figure IV.28 (b)).

Three different offsets were studied, respectively, 25%, 50%, and 75% of the groove width. All simulations dealing with groove overlapping were performed

with sharp circular cutters. In this fourth phase dealing with cutter and groove geometries, the depths of cut considered were 1 and 2 mm, while the confinement varied from 0 to 40 MPa.

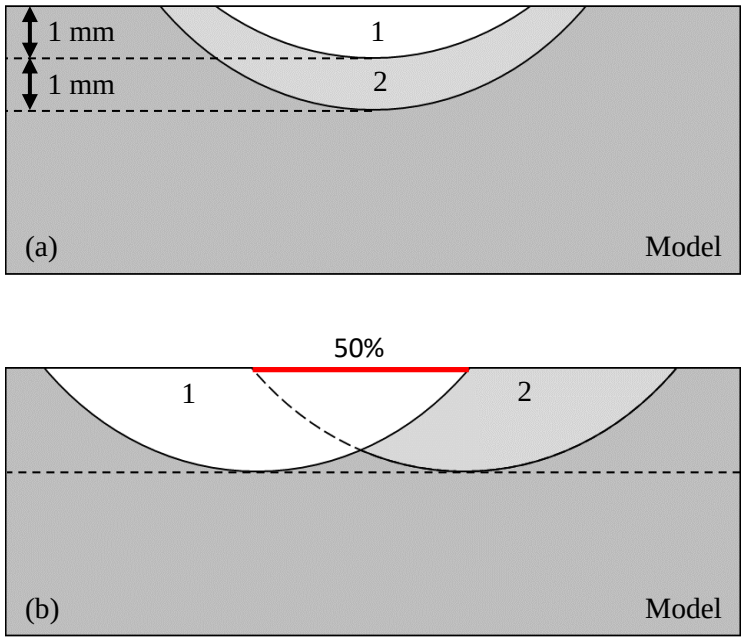

Figure IV.28. Schematic diagrams of cutting simulations of overlapping groove: (a) same path but different depth (b) partial overlap at the same cutting depth.

Chapter V Results of numerical modeling

This chapter details the results obtained following the 2D and 3D modeling performed based on the test protocols presented at the end of the previous chapter. This chapter is divided into four parts, each dealing with a specific protocol phase. The first part concentrates on the principal theme of this thesis: the effect of confinement on the cutting mechanism both from qualitative (evolution of the destruction mechanism with confinement) and quantitative (cutting forces and Specific Energy) points of view. The second section focuses on the cutting parameters and their interaction with the confinement. Finally, sections 3 and 4 are more concerned with geometric considerations related to the shape of the cutters (section 3) and the geometry of the groove (section 4).

Notice that only parts of the raw simulation results are presented in this chapter. The reader can find a listing of all test parameters and results in Appendix C.

1 The effects of the confinement on the rock cutting mechanism

This first section studies confinement's effects on the rock cutting mechanism. This section is subdivided into three points. The first one is devoted to the evolution of the destruction known to evolve from scratching and chipping mode in low confining conditions (depending on the depth of cut) to the formation of ribbons when confinement is applied. The presented results explain and analyze this transition in more details. The second section focuses on the evolution of cutting forces with confinement. The aim is to analyze the evolution of the forces during the simulation in terms of magnitude and variations. Finally, the last part will present the evolution of the Specific Energy with the confinement.

1.1 Evolution of destruction mechanism

Figure V.1 displays snapshots of 2D simulations performed at different confinements for cutting depths of 0.5 and 1.5 mm to highlight the evolution of the cutting mechanism with confinement. The two depths of cut selected to illustrate the evolution of the mechanism were chosen based on the characteristic of the cutting mechanism, which exhibits two types in atmospheric conditions. Indeed, the destruction mechanism is either scratching or chipping, depending on whether the depth of cut is small or large.

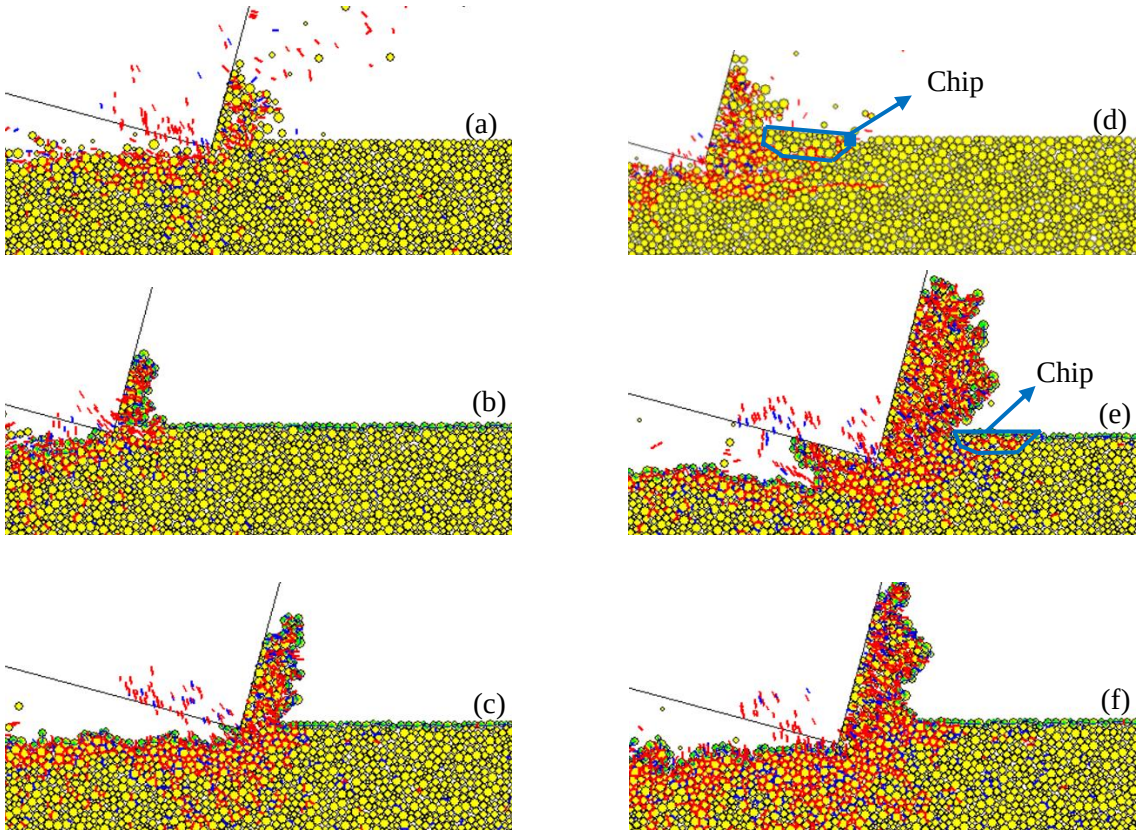

Figure V.1. Evolution of cutting mechanism at 0.5 (a, b, c) and 1.5 mm (d, e, f) depth of cut for different confinements: (a) and (d) = atmospheric conditions; (b) and (e) 10 MPa confinement; (c) and (f) 30 MPa confinement.

For the simulations performed at a depth of 0.5 mm in atmospheric conditions, the destruction mechanism observed is the scratching one (Figure V.1 (a)). Indeed, for this depth of cut, the grains are detached from the top of the model, and no major fracture is generated in the front of the cutter. On the other hand, the chipping mode was observed in the simulations at a cutting depth of 1.5 mm. This mode is characterized by long fracture propagation in front of the cutter. These fractures propagate from the cutter face in the cutting direction. Some can propagate in-

depth, while others reach the sample surface (Figure V.1 (d)). The ones joining the surface generate a chip detached from the model. This chip is then pushed by the cuttings accumulated on the face of the cutter. Therefore, the evolution of scratching and chipping modes could be studied with the confinement increase based on the simulations at these two depths of cut.

The cutting mechanism does not seem strongly impacted by the confinement increase at shallow cutting depths. Indeed, whatever the confinement value (in the ranges of values tested), the destruction mechanism remains the same. The cutter scratches the surface particles from the top of the sample. The main difference comes from the accumulation of cuttings in front of the cutter. In the atmospheric condition, the torn-off particles accumulate principally at the bottom of the cutter.

Moreover, a part of these particles is in free flight due to the cutter velocity and the high energy required to pull them out of the sample. On the other hand, the particles do not move freely and are compacted on the surface of the cutter when the confinement is applied. In addition, as the cutter progresses, the cuttings move up the cutting surface of the cutter. This phenomenon generates a ribbon of crushed material. This phenomenon is illustrated in Figure V.2, which presents three snapshots taken at different simulation intervals carried out at a depth of cut of 0.5 mm and confinement of 30 MPa. The ribbon is progressively rising on the face of the cutter due to the generation of new cuttings at the tip of the cutter. These new cuttings push the ribbon upwards due to the mud pressure, which restricts their movement. Finally, Figure V.1 (c) illustrates that the material is more impacted by the cutter run as the confinement increases. Indeed, compared to Figure V.1 (b), it is noticeable that more parallel bonds are broken under the groove when the confinement was set to 30 MPa compared to the simulation with confinement of 10 MPa.

In contrast, the evolution of the cutting mechanism for large depths of cut (when chipping is observed in atmospheric conditions) with confinement is more complex. Indeed, the cutting process generates ribbons of crushed material whatever the confinement but the physical process generating the ribbon depends on the confinement value. Simulations performed with a confinement of 10 MPa showed that chips are still formed (Figure V.1 (e)). However, these chips, smaller than those formed in atmospheric conditions, are trapped by the applied mud pressure and, therefore, cannot be removed from the cutting face. As the chips are trapped between the cutter and the mud pressure, they are crushed as the cutter moves forward.

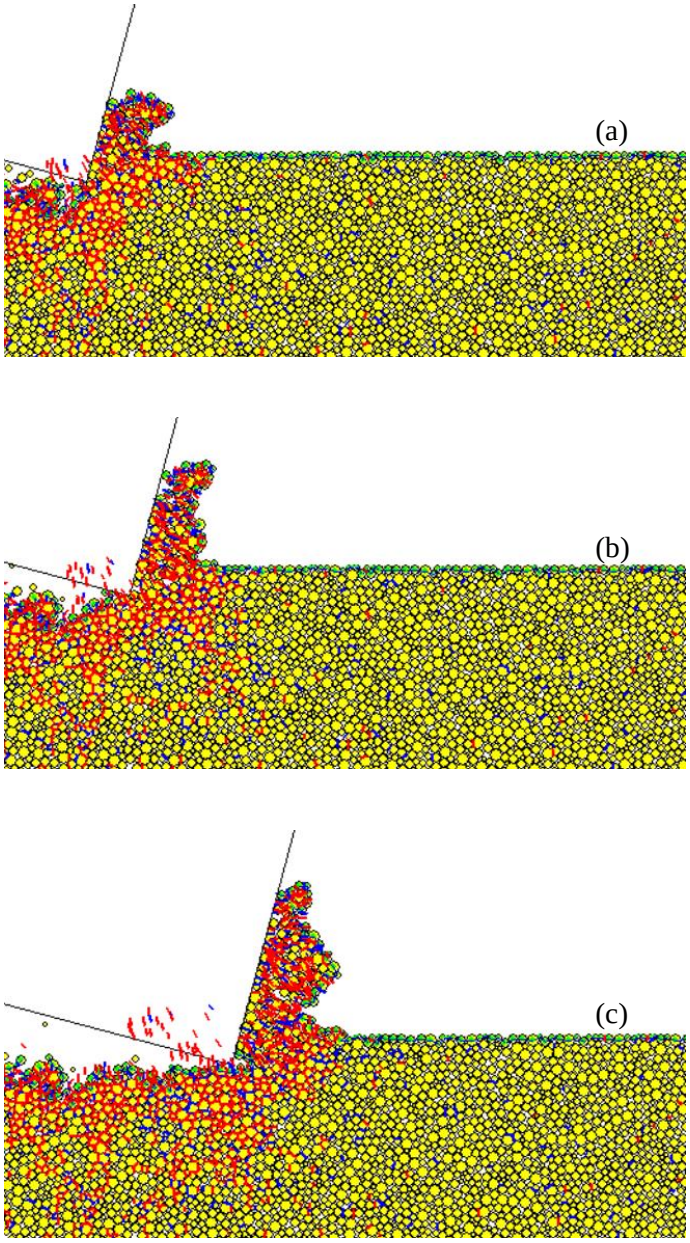

Figure V.2. Formation of a ribbon of crushed rock during the simulation at a depth of cut of 1.5 mm and confinement of 30 MPa.

On the other hand, no chips were observed from the confinement of 30 MPa (Figure V.1 (f)). The destruction mechanism that occurs then is close to the one observed at shallow depths of cut for the same confinement. Indeed, from the confinement of 30 MPa, the material is crushed during the movement of the cutter, and no more major fracture is generated in front of it. The ribbon is then formed by the crushed material, which is extruded by the displacement of the cutter.

Figure V.3 presents the evolution of the number of cracks recorded during a simulation at a depth of cut of 1.5 mm and confinement of 0, 20, and 40 MPa. On

these three graphs, two phases can be highlighted. During the first phase, the number of fractures increases rapidly and constantly. This phase co-occurs with the penetration of the cutter into the rock. Indeed, it ends after the cutter has completely penetrated the model. While the cutter penetrates the model, the contact forces are concentrated on a small number of particles in the model, which results in breaking many bonds between particles in a short time.

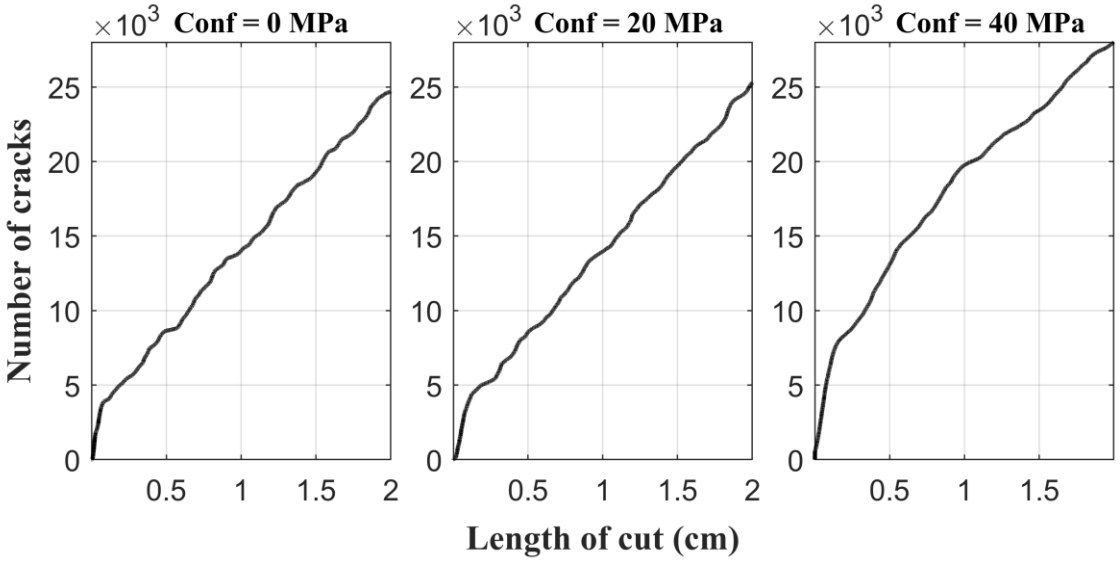

Figure V.3. Evolution of crack numbers during tests at different confinements for cutting tests at 1.5 mm depth of cut.

The number of broken bonds in this phase is similar for the different confinements, a slight increase is observed. On the other hand, the more the confinement increases, the longer this phase is. For comparison, the peak of this phase is obtained at a displacement of 0.033 mm in atmospheric conditions, while it is 0.06 mm at a confinement of 40 MPa.

In the second phase, the increase is slower and seems to be affected by the confinement. Indeed, the number of cracks increases by step in atmospheric conditions (Figure V.3 (a)). Each of these steps corresponds to the formation of a significant fracture in the model. However, between two steps, there exists a slight increase in the number of cracks. Indeed, due to the displacement of the cutter, small fractures are generated in the sample and cuttings in front of the cutter.

On the other hand, as the confinement increases, the increase of the number of cracks becomes smoother. It shows that fewer major fractures are abruptly generated for increasing confinement. Therefore, this evolution would result from a mechanism where a transition from a chipping mode to a ductile one occurs.

1.2 Evolution of cutting forces

To highlight the impact of confinement on the cutting forces, the results presented below are from 3D simulations. Firstly, the graphs in Figure V.4 illustrate the evolution of the cutting forces during simulations performed at cutting depths of 0.5 and 1.5 mm and confinement of 0, 20, and 40 MPa.

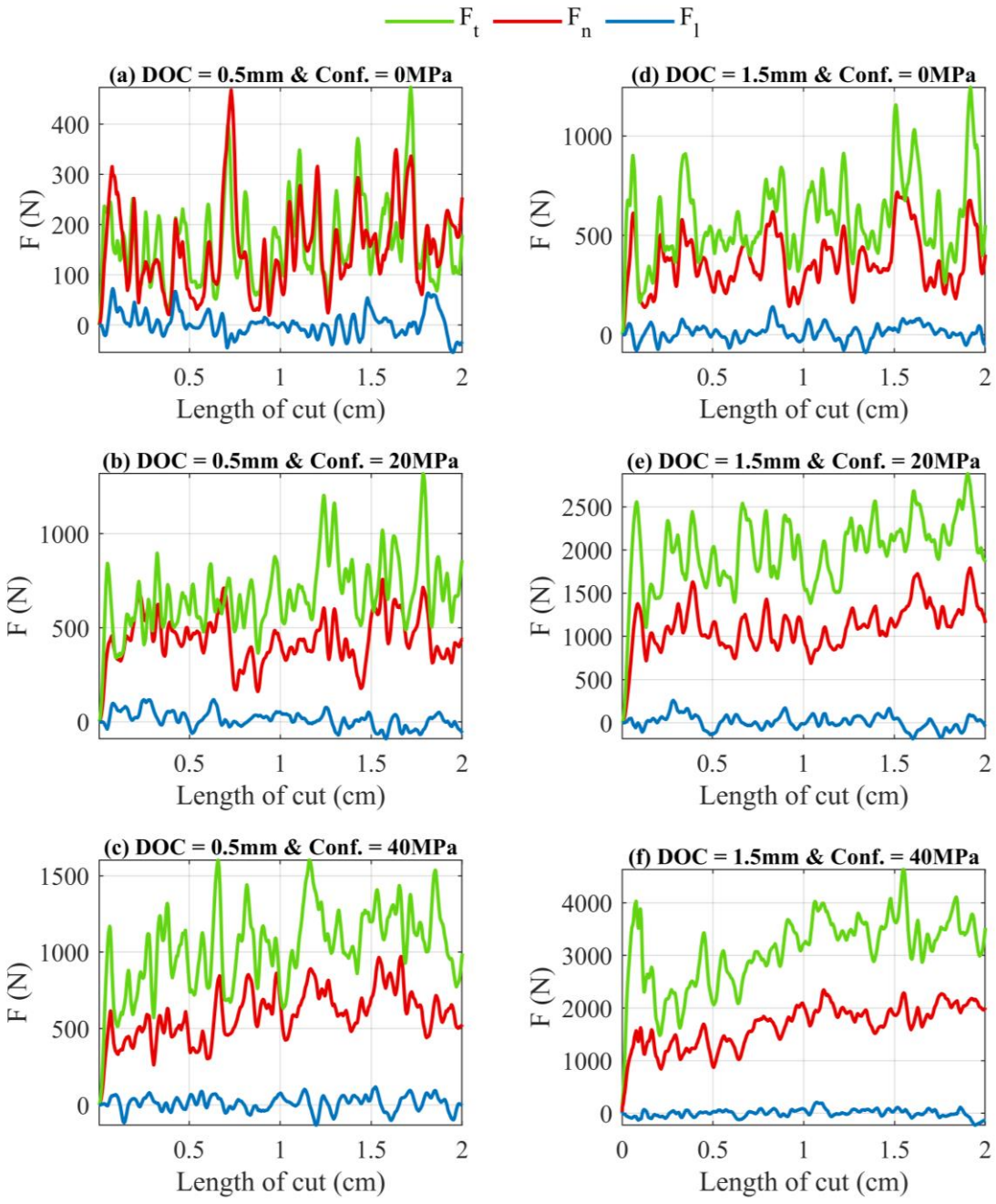

Figure V.4. Registered cutting forces during simulations at 0.5 and 1.5 mm depth of cut and confinement of 0, 20, and 40 MPa.

Under atmospheric conditions (Figure V.4 (a) and (d)), the cutting forces (tangential, normal, and lateral) fluctuate strongly, and the force signal is composed of many peaks and drops. However, these variations occur around an average value that remains constant throughout the simulation. However, the evolution of tangential and normal cutting forces shows a distinct pattern when confinement is applied. Indeed, in Figure V.4 (f), three distinct zones in the evolution of the forces can be highlighted. The first zone is defined by the force peak observed at the beginning of each simulation under confinement, whether in atmospheric conditions or under confinement. After the first peak, the forces present a transient increasing phase. This transitional phase corresponds to the distance needed for the cutter to be fully in contact with the rock sample and the one allowing the formation of a crushed ribbon in front of the cutter. Finally, the cutting forces reach a steady-state while varying around a mean value. Concerning the lateral cutting force, it does not seem to be impacted by the increase in confinement. Indeed, this force varies continuously around 0, and its standard deviation remains almost the same whatever the confinement.

Regarding cutting force magnitude and variation, graphs in Figure V.5 present the evolution of the average cutting forces (tangential and normal) and their relative standard deviation (ratio between the standard deviation and mean cutting force expressed in percentage). These results come from simulations conducted at two depths of cut of 0.5 and 1.5 mm but cover all the simulated confinement values. From the point of view of the tangential and normal cutting forces, they increase with the confinement, but the standard variation decreases simultaneously. Moreover, these observations are valid regardless of the depth of cut.

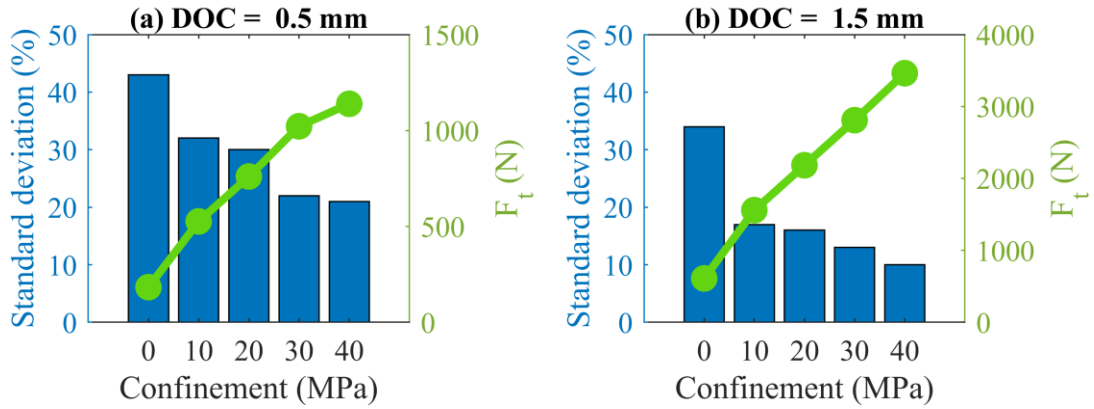

Figure V.5. Evolutions of mean tangential cutting force and its standard deviation versus confinement at a depth of cut of (a) 0.5 mm and (b) 1.5 mm.

1.3 Evolution of Specific Energy

Figure V.6 presents the evolution of E versus confinement for several depths of cut simulated. Based on cutting forces results presented before, the graphs highlight that E increases with confinement. Most importantly, E does not increase linearly with the confinement. Indeed, it is observable on these graphs that slopes reduce with confinement. Moreover, this phenomenon appears to be more pronounced at shallow depths of cut (Figure V.6 (a)).

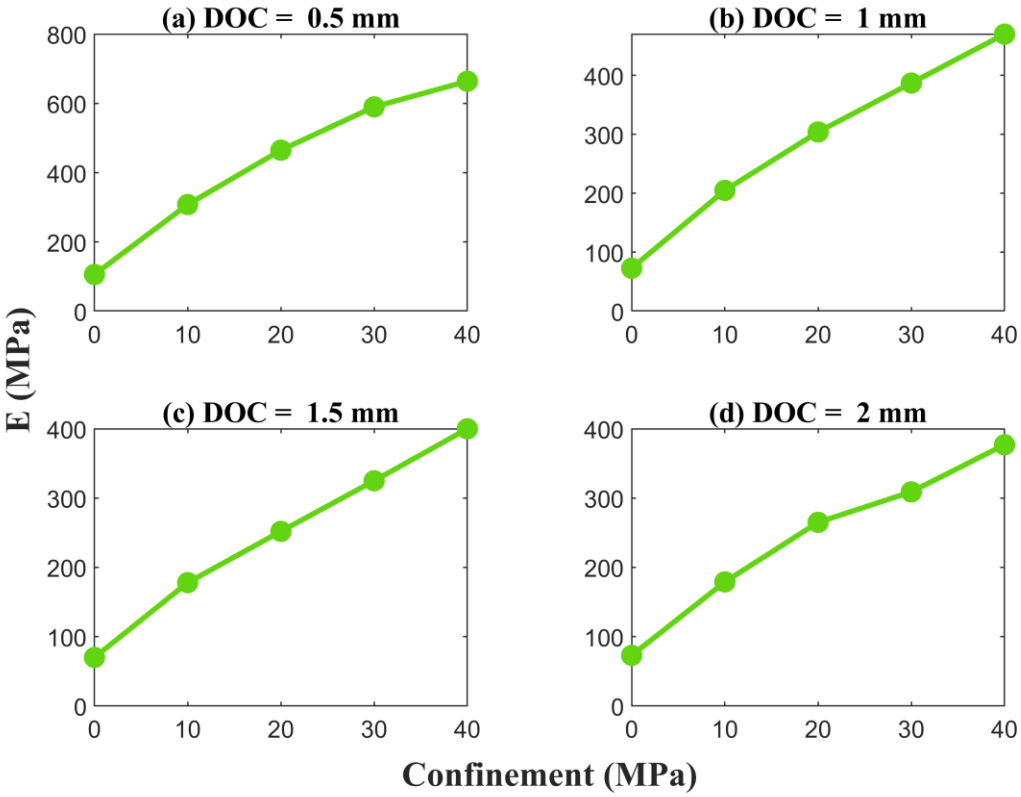

Figure V.6. Evolution of Specific Energy versus confinement for different depths of cut.

Moreover, the data indicate that the slope of E versus confinement decreases with increasing confinement for cutting depths of 0.5 and 1 mm. For a depth of 1.5mm, the data suggest that the rate of increase stabilizes when confinement exceeds 10 MPa. Finally, for simulations performed at a DOC of 2mm, the overall trend seems disturbed by the test performed at the confinement of 30 MPa. Indeed, the value of E is lower than expected based on simulations at 20 and 40 MPa confinement.

2 The effects of cutting parameters

This section considers the effect of the cutting parameters, such as the depth of cut, side rake, and back rake angles, on the Specific Energy for different confinement values. Since this section focuses on the quantitative impact of these parameters, the results come from cutting simulations performed in 3D. All the simulations used to study the effects of these parameters were performed with a 13 mm diameter circular sharp cutter.

2.1 Impact of the depth of cut

The depth of cut is one of the main factors influencing the evolution of the cutting mechanism. Nevertheless, as the literature review revealed, this parameter has an important influence on the evolution of the cutting energies. It is one of the main parameters used to optimize the cutting mechanism from this point of view.

Figure V.7 ((a) to (e)) presents the evolutions of mean and maximal tangential cuttings forces and Specific Energy for cutting simulations performed at different depths of cut (from 0.5 to 2mm) and for confinement ranging from 0 to 40 MPa.

As expected from experimental research, we observe an increase of mean and maximal cutting forces with the depth of cut. It is especially interesting to consider the evolution of the Specific Energy as a function of the depth of cut. Indeed, we notice that for each series of simulations at different confinements, the Specific Energy decreases with the depth of cut. The slope of this decrease is more significant as the depth of cut is low.

However, for confinements of 0, 10, and 20 MPa, the Specific Energy presents a minimum for a depth of cut of 1.5 mm, contrary to confinements of 30 and 40 MPa, where this minimum is not observed. It could indicate that the depth of cut at which the minimum of the Specific Energy is observed increases with the confinement.

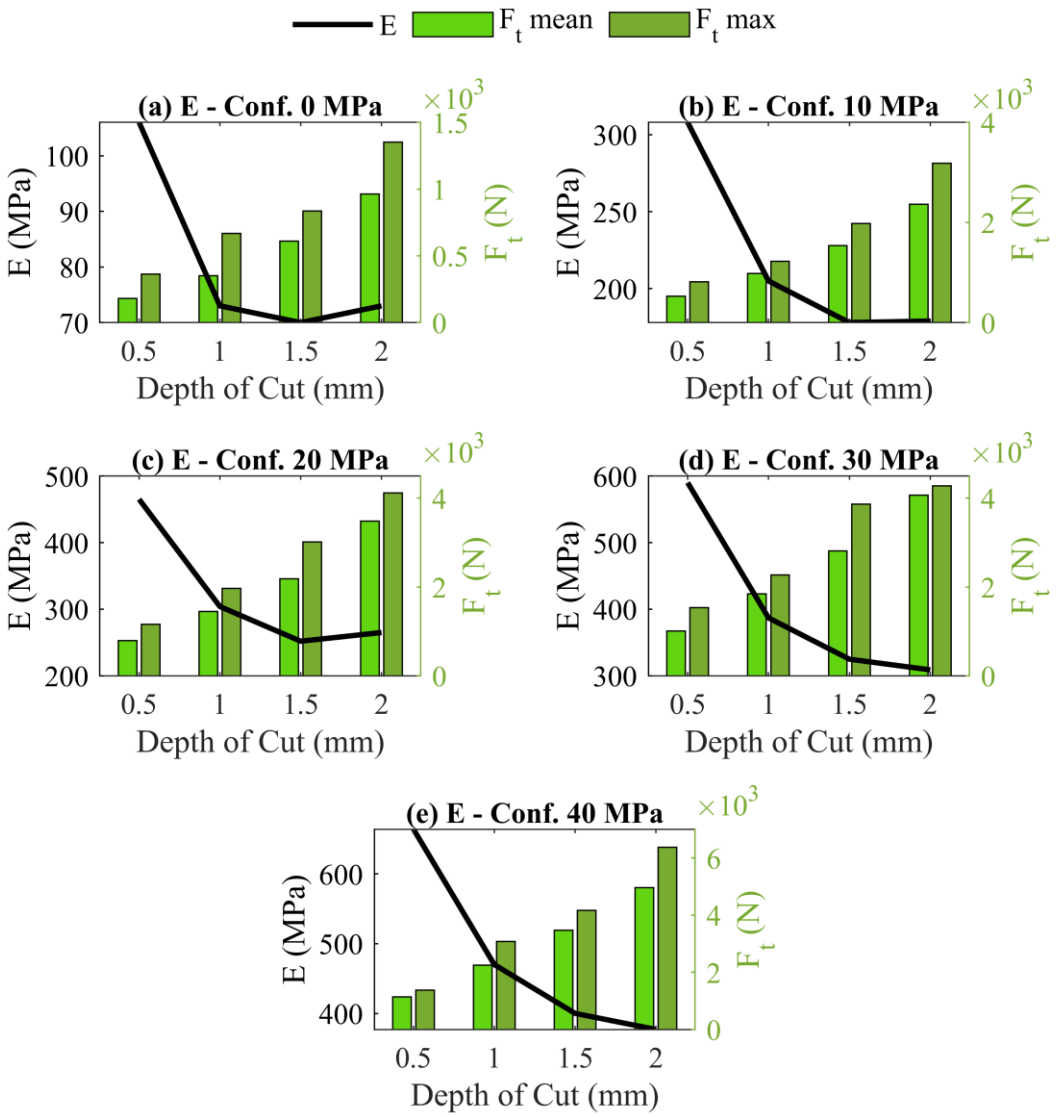

Figure V.7. Evolution of mean and maximum cuttings forces and Specific Energy versus depths of cut and confinements.

2.2 Impact of the side rake angle

The normalized Specific Energy (E_{norm_SR}) is introduced to study the impact of side rake angle on Specific Energy. It is defined by:

$$E_{norm\_SR} = \frac{E_{SR=i}}{E_{SR=0}} \quad \text{(V.1)}$$

Where E_{norm_SR} is the normalized Specific Energy with respect to the side rake angle, $E_{SR=i}$ is the Specific Energy for a side rake angle of i° and $E_{SR=0}$ is the Specific Energy at a side rake angle of 0°.

The graphs in Figure V.8 present the evolution of normalized Specific Energy (E_{norm_SR}) for different confinement values (0, 20, 40 MPa) and depths of cut (0.5 and 1.5 mm). These cutting parameters cover all the cutting mechanisms observed previously.

At a depth of cut of 1.5 mm, the impact of the side rake angle on E is negligible between 0 and 20°. In contrast, E increases strongly once the side rake angle exceeds 20°. For instance, at a confinement of 20 MPa (Figure V.8 (d)), the Specific Energy increases by 40% when the side rake angle increases from 0° to 40° while it is multiplied by 2.4 for a side rake of 60°. At shallow depths of cut, the side rake angle's effect on E is smaller and only noticeable at a side rake value of 60°.

While some experimental works explained that Specific Energy increases by the significant decrease of the active surface while cutting forces increase once the side rake angle exceeds 20° (Rajabov et al., 2012), the distribution of cutting forces exerted on the cutter faces allows completing this statement. Indeed, Figure V.8 presents the total tangential force distribution between the cutting face and the side of the cutter for different side rake angles.

While the face component is related to the destruction of the rock and the friction with the cuttings, the side component of the total cutting force is due to the friction between the side of the cutter and the edge of the groove. For side rake angles ranging between 0 and 20°, the total tangential cutting force and its distribution change slightly. However, once the side rake exceeds 20°, the magnitude of the tangential force component related to the cutting face decreases while the one related to the side face increases drastically. For example, in Figure V.8 (d), the

lateral component of cutting force represents less than 10% of the total cutting force for side rake angles between 0 and 20°, while it reaches 30% for a side rake of 40 ° and up to 70% for a side rake of 60 °.

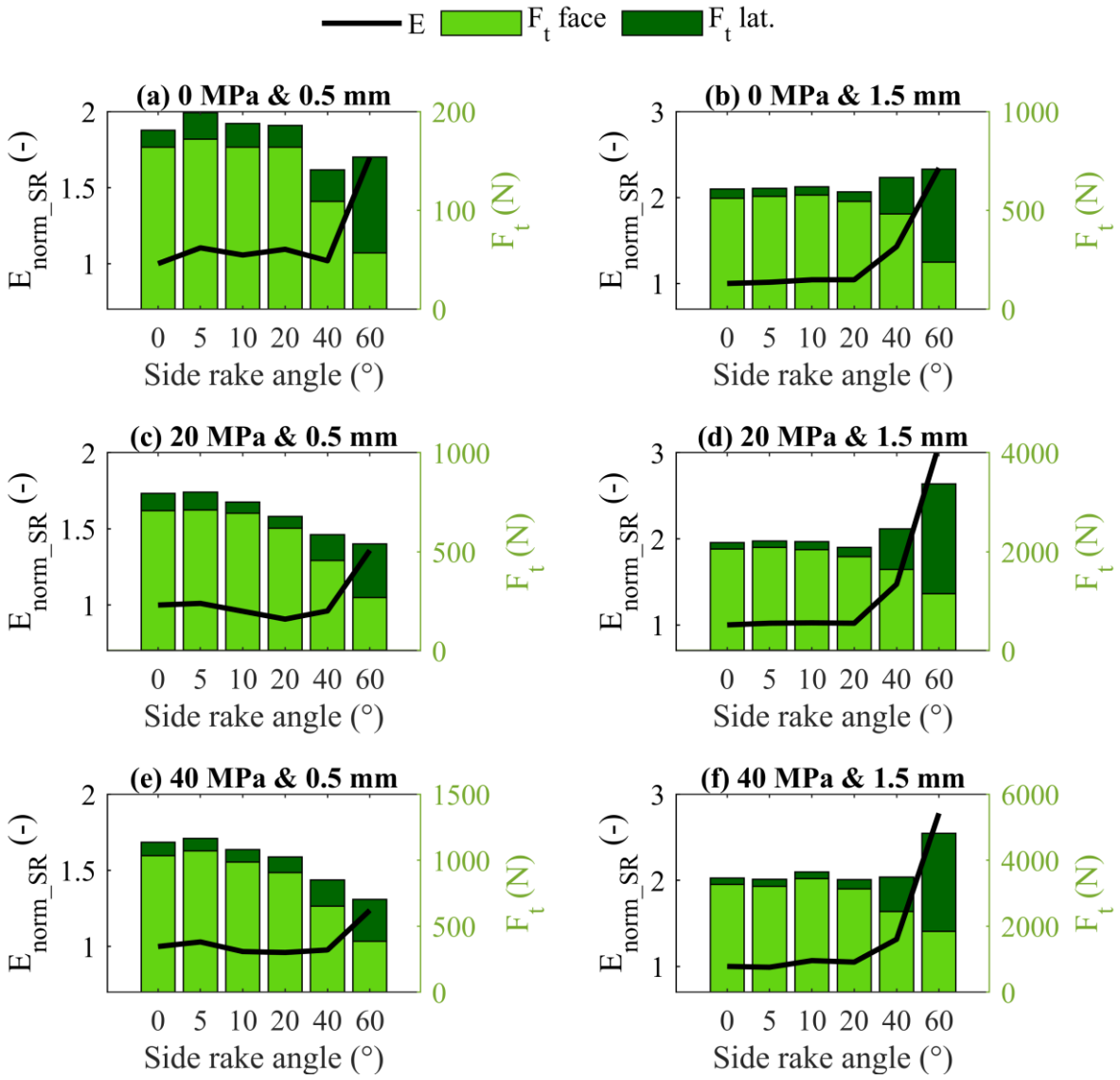

Figure V.8. Evolutions of normalized Specific Energy and distribution of tangential cutting force between cutting and lateral faces of the cutter depending on the side rake angle for different values of confinement and depth of cut.

The same picture can be drawn for normal cutting forces from Figure V.9. The main difference is that all the phenomena observed for the tangential force are amplified for the normal force. Indeed, it is characterized by a significant increase in the normal cutting forces when reaching side rakes of 40 and 60° compared to the forces measured at side rakes of 20°. Moreover, the lateral component of the

normal cutting force represents up to 85% of the total normal force for a side rake angle of 60°.

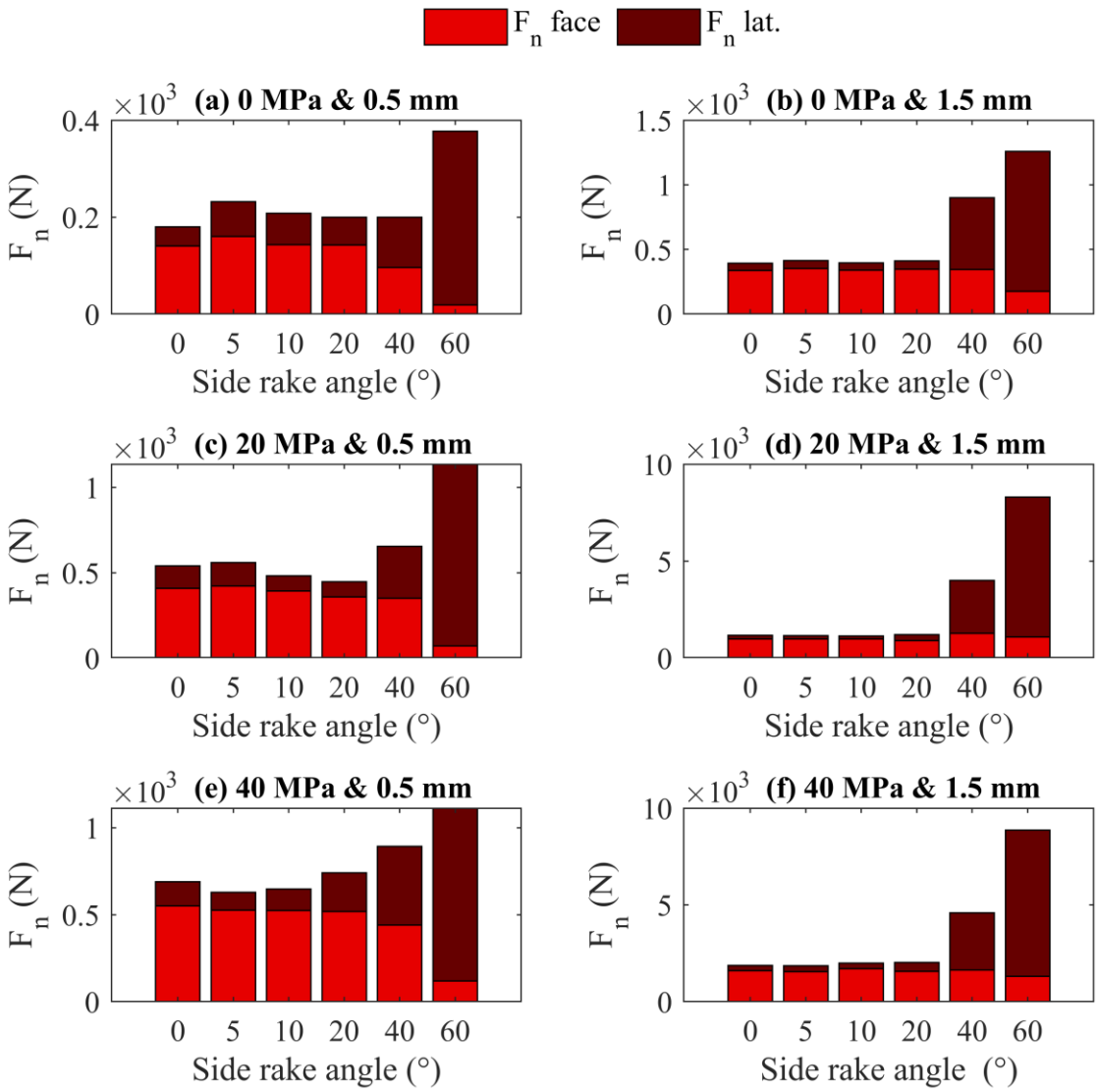

Figure V.9. Evolutions of normal cutting force between cutting and lateral faces of the cutter depending on the side rake angle for different values of confinement and depth of cut.

Figure V.10 provides a geometric explanation for the observations from Figure V.9. Indeed, at low values of side rake (up to 20°), the side face of the cutter is hidden by the cutting face and hence does not affect the shape of the groove. On the other hand, when the side rake angle becomes more important, we can observe that the cutting face no more hides the side of the cutter. Therefore, the cylindrical part of the cutter will also “cut” the rock. Moreover, the proportion of the side face that will contact the rock will be more important as the depth of cut increases.

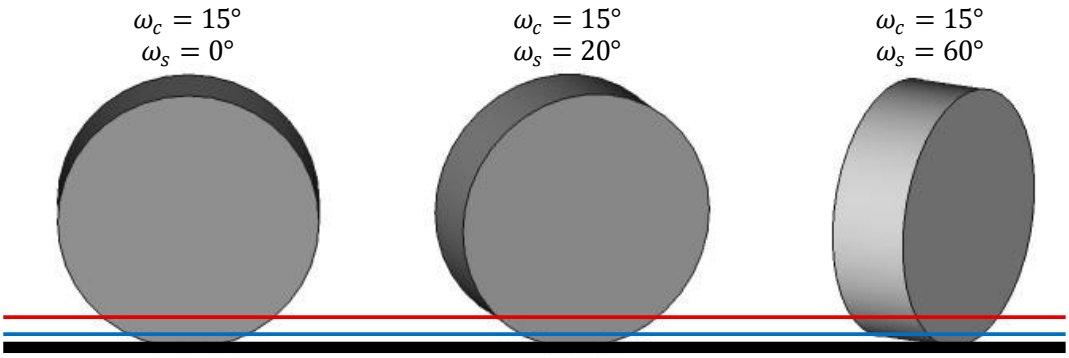

Figure V.10. Effects of side rake angle (ω_s) on the exposition on the lateral face of the circular cutter during a linear cutting test. The blue line represents the 0.5 mm depth of cut, while the red one represents the 1.5 mm depth of cut.

2.3 Impact of the back rake angle

To study the impact of the back rake, E_{norm_BR}, the normalized Specific Energy with respect to the back rake angle, is introduced. It is given by:

$$E_{norm\_BR} = \frac{E_{BR=i}}{E_{BR=15}} \tag{V.2}$$

Where E_{norm_BR} is the normalized Specific Energy with respect to the back rake angle, $E_{BR=i}$ is the Specific Energy for a side rake angle of i° and $E_{BR=15}$ is the Specific Energy at a back rake angle of 15°.

Figure V.11 presents the evolution of normalized Specific Energy and Aggressiveness versus back rake angle. These results were obtained from simulations performed at confinements of 0, 20, and 40 MPa and for a depth of cut of 1 mm. They show the rise of Specific Energy when the back rake angle increases, while the Aggressiveness decreases.

Furthermore, the Aggressiveness decreases with increasing back rake angle. This indicates that the increase in normal cutting force is more significant than the increase in tangential cutting force. This significant increase in the vertical force can be explained by the increase of the projected cutting surface in the horizontal plane. As this surface increases more rapidly with the back rake angle than the active surface for the same depth of cut, it is necessary to increase significantly the normal cutting force to maintain the targeted depth of cut.

Concerning the impact of confinement, Figure V.11 highlights that normalized Specific Energy and Aggressiveness are slightly less impacted as the confinement increases.

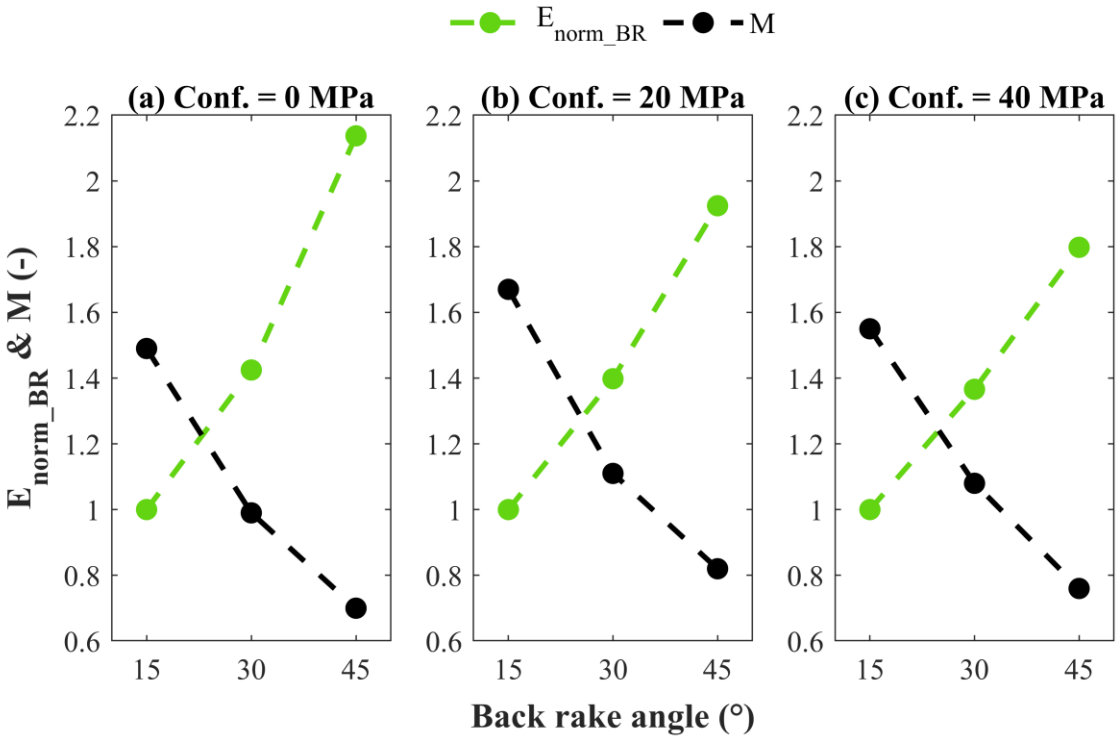

Figure V.11. Evolution of normalized Specific Energy and Aggressiveness depending on the back rake angle.

3 The cutter geometry effects on the rock cutting mechanism

This section is devoted to the study of the effects of the cutter geometry on the rock cutting mechanism. The study in 2D focused mainly on the qualitative aspects by highlighting the changes that may exist in the propagation of fractures in the material. Regarding 3D models, they were designed to study the impact of changes in geometry on cutting energy.

3.1 2D modeling

2D simulations did not highlight any modification of the destruction mechanism for the tested cutting depths with the different cutter geometries. However, these simulations have demonstrated that geometry influences the propagation of cutting forces in the rock. Figure V.12 illustrates their influence. With a sharp cutter (a), the forces propagate perpendicular to the cutting face. When the cutter is chamfered (b), the propagation of contact forces in the material is more inclined, and a high concentration of force is visible on the chamfer face. Finally, when the cutter has a wear flat (c), forces propagate from both the cutting face and the wear flat. The effect of these changes in the orientation of the cutting forces should lead to a modification of the Aggressiveness of the cutters.

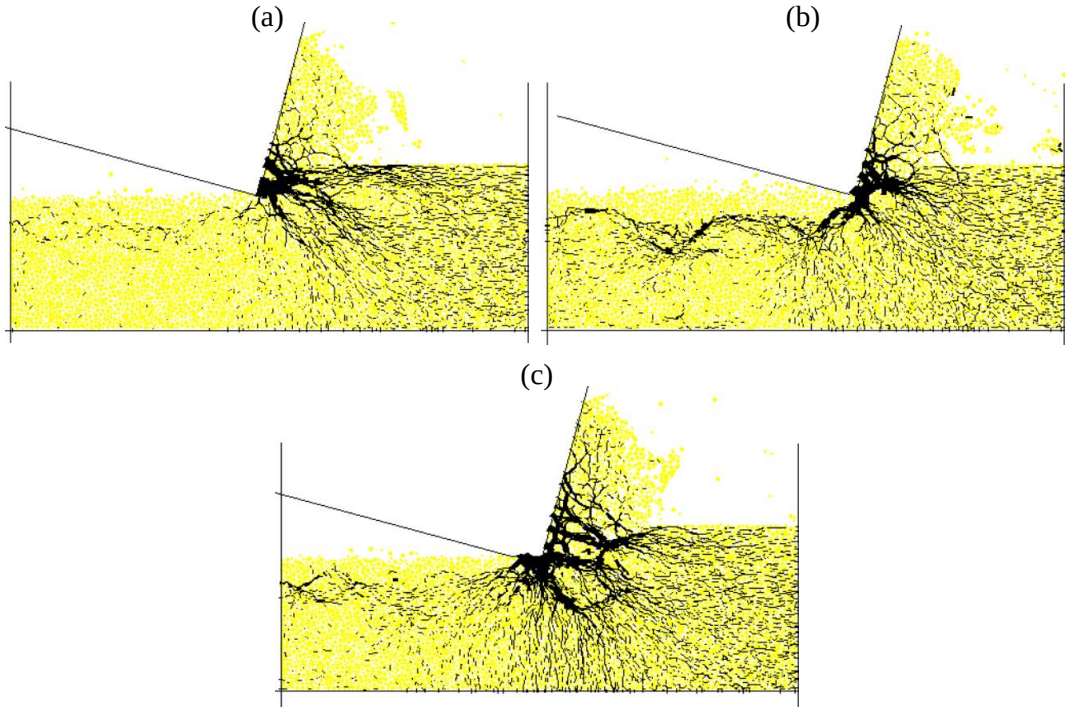

Figure V.12. Distribution of the contact forces near the cutting face of sharp (a), chamfered (b) and wear cutters (c) in atmospheric conditions.

3.2 3D modeling

As the study of the impact of the chamfer and the wear flat was done mainly with rectangular cutters (circular cutters were only used for the study of the chamfer), this section starts with a quantitative comparison of the rectangular and circular sharp cutters. Subsequently, this section focuses first on the impact of a chamfer (length and angle) and finally on the impact of the development of a wear flat.

3.2.1 Rectangular VS. Circular sharp cutters

Figure V.13 presents the evolutions for the circular and rectangular cutters of Specific Energy versus confinement for the different depths of cut tested throughout the simulations. These graphs highlight that the rectangular cutter requires less energy for an identical depth of cut than the circular one, regardless of the confinement. Moreover, the difference is more significant as the depth of cut is low.

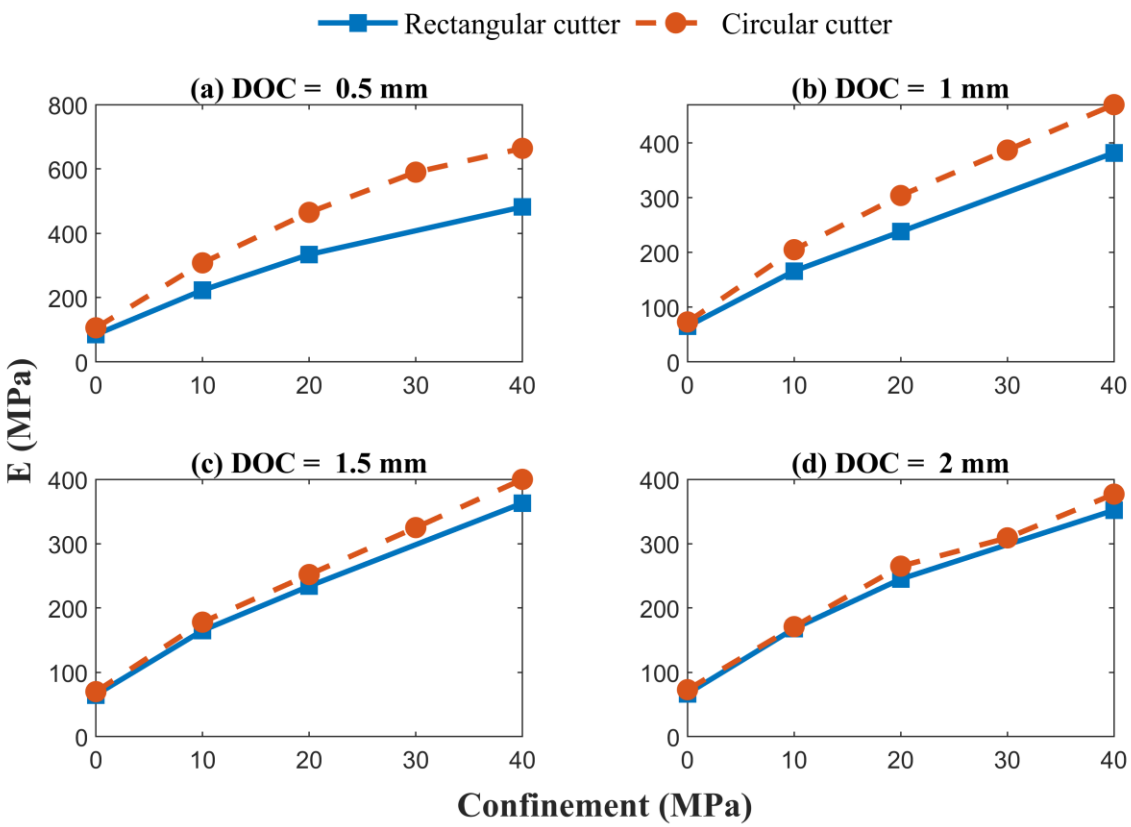

Figure V.13. Comparison between Specific Energies developed by circular and rectangular cutters under the same test conditions (depths of cut and confinements).

This difference is attributed to the average depth of cut in the groove's width. Indeed, for a rectangular cutter, the depth of cut is the same throughout the width of the cut and is equal to the fixed depth of cut. For the circular one, it varies. The depth of cut is null on the edge of the groove while it is maximum in the middle. Therefore, Table V-1 compares the active surfaces and the mean depth of cut across the groove between the rectangular and circular cutters.

Table V-1. Comparison of mean DOCs and active surface between circular and rectangular cutters for different theoretical DOCs.

Theoretical depth of cut (mm)	**Circular cutter (13 mm diameter)**		**Rectangular cutter (10 mm width)**	
	Mean DOC (mm)	**Active surface (mm^2)**	**Mean DOC (mm)**	**Active surface(mm^2)**
0.5	0.34	1.71	0.5	5
1	0.68	4.77	1	10
1.5	1.03	8.66	1.5	15
2	1.38	13.15	2	20

This table reveals the important difference between the average cutting depths or the active surface between rectangular and circular cutters for the same theoretical depth of cut. Moreover, this difference is proportionally greater as the theoretical depth of cut decreases. It explains the differences observed in the graphs in Figure V.13.

Previously, it has been shown that the Specific Energy decreases with the depth of cut and may reach a minimum for low confinement values (in the test range between 0.5 and 2mm) while using a circular cutter. The graphs in Figure V.14 compare the evolution of Specific Energy versus depth of cut between circular and rectangular cutters for confinements of 0 and 20 MPa. As highlighted for the circular cutter, we observe that E decreases with increasing depth of cut until reaching a minimum. These graphs also show that the minimum Specific Energies obtained with circular or rectangular cutters in the different cases are very close. The difference that seems to emerge is that it is possible to optimally destroy a larger volume of rock with a rectangular cutter than with a circular one. Indeed, the minimum Specific Energy is reached for a higher active surface with the rectangular cutter.

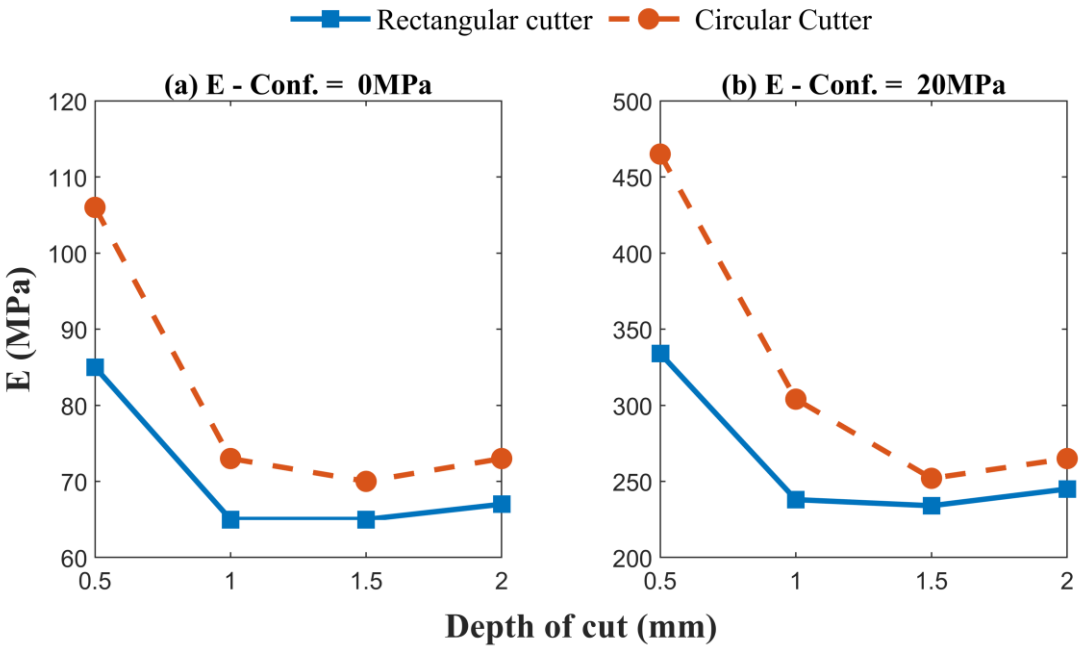

Figure V.14. Comparison of the evolution of Specific Energy versus depth of cut for circular and rectangular cutters in atmospheric and under 20 MPa of confinement.

3.2.2 Effects of the chamfer

Two chamfer lengths (0.25 and 0.5mm) and three angles (30, 45, and 60°) were tested on circular cutters. First, the presented results focus on the impact of the chamfer length for different depths of cut and confinement values. Then the impact of the chamfer angle is presented.

3.2.2.1 Chamfer length effect

Table V-2 presents the values of E and M obtained for confinements of 0 and 20 MPa and depth of cut varying from 0.5 to 2 mm. These results are also compared with the ones of sharp cutters.

Table V-2. Evolution of E and M depending on the chamfer length and the depth of cut for circular cutters.

DOC (mm)	L_{ch} (mm)	Confinement = 0 MPa		Confinement = 20	
		E (MPa)	M	E (MPa)	M
0.5	0	106	1.00	465	1.47
	0.25	123	0.59	415	0.84
	0.5	152	0.50	464	0.63
1	0	74	1.5	305	1.7
	0.25	80	0.9	336	1.0
	0.5	99	0.7	362	0.9
1.5	0	70	1.55	252	1.85
	0.25	72	1.15	269	1.32
	0.5	83	0.87	297	1.09
2	0	73	1.8	265	2.0
	0.25	71	1.4	257	1.5
	0.5	76	1.1	278	1.2

The presence of the chamfer tends to increase the specific energy and decrease the Aggressiveness of cutters, whether they are circular or rectangular. Furthermore, the greater the chamfer length and depth of cut, the greater the effects of the chamfer. Indeed, the impact of the chamfers on the specific energy is negligible for a depth of 2 mm, whereas E increases by 50% for a chamfer of 0.5 mm and a depth of 0.5 mm. It is explained by the proportion of the chamfer constituting the

active surface. Indeed, the shallower the depth of cut, the larger is the percentage of the active surface covered by the chamfer (Table V-3).

Table V-3. The proportion of the active surface covered by the cutting face and the chamfer, depending on the cutter geometry, the chamfer length, and the depth of cut.

DOC (mm)	Circular cutter			
	L_{ch} = 0.25 mm		L_{ch} = 0.5 mm	
	A_c face	A_c cham.	A_c face	A_c cham.
0.5	37%	63%	1%	99%
1	65%	35%	36%	64%
1.5	76%	24%	54%	46%
2	81%	19%	64%	36%

Comparatively, although the impact of chamfers on M tends to decrease with the depth of cut, it remains important. Indeed, while E is almost not impacted at a cutting depth of 2mm, M decreases by about 40% while using a cutter with a chamfer length of 0.5 mm compared to a sharp cutter. This reduction is about 50% for a depth of cut of 0.5 mm. This decrease in Aggressiveness implies that the increase in normal cutting force due to the chamfer is much greater than the increase in tangential force. This indicates that the optimum depth for E should not change significantly from a sharp cutter to chamfered one. However, it will be necessary to apply a substantially higher vertical force and, therefore, a higher weight on bit to achieve this depth.

The graphs in this Figure V.15 represent the distribution of tangential and normal cutting forces between chamfer, cutting, and side faces of circular cutters with a chamfer of 0.5 mm for different cutting depths (0.5 to 2mm) and confinements (0 and 20 MPa). It is noticeable that the more the depth of cut increases, the less important the chamfer component of the forces is. These graphs also demonstrate that a substantial proportion of the normal force is due to the chamfer

Based on Table V-3, one would expect that the proportion of forces attributed to the chamfer could have been greater than shown in Figure V.15. However, it is necessary to point out that the tangential and normal cutting forces are determined once the mechanism reaches a steady state. Therefore, a part of the forces related to the cutter face is used to remove the cuttings. That explains the lower impact of the chamfer as the confinement increases.

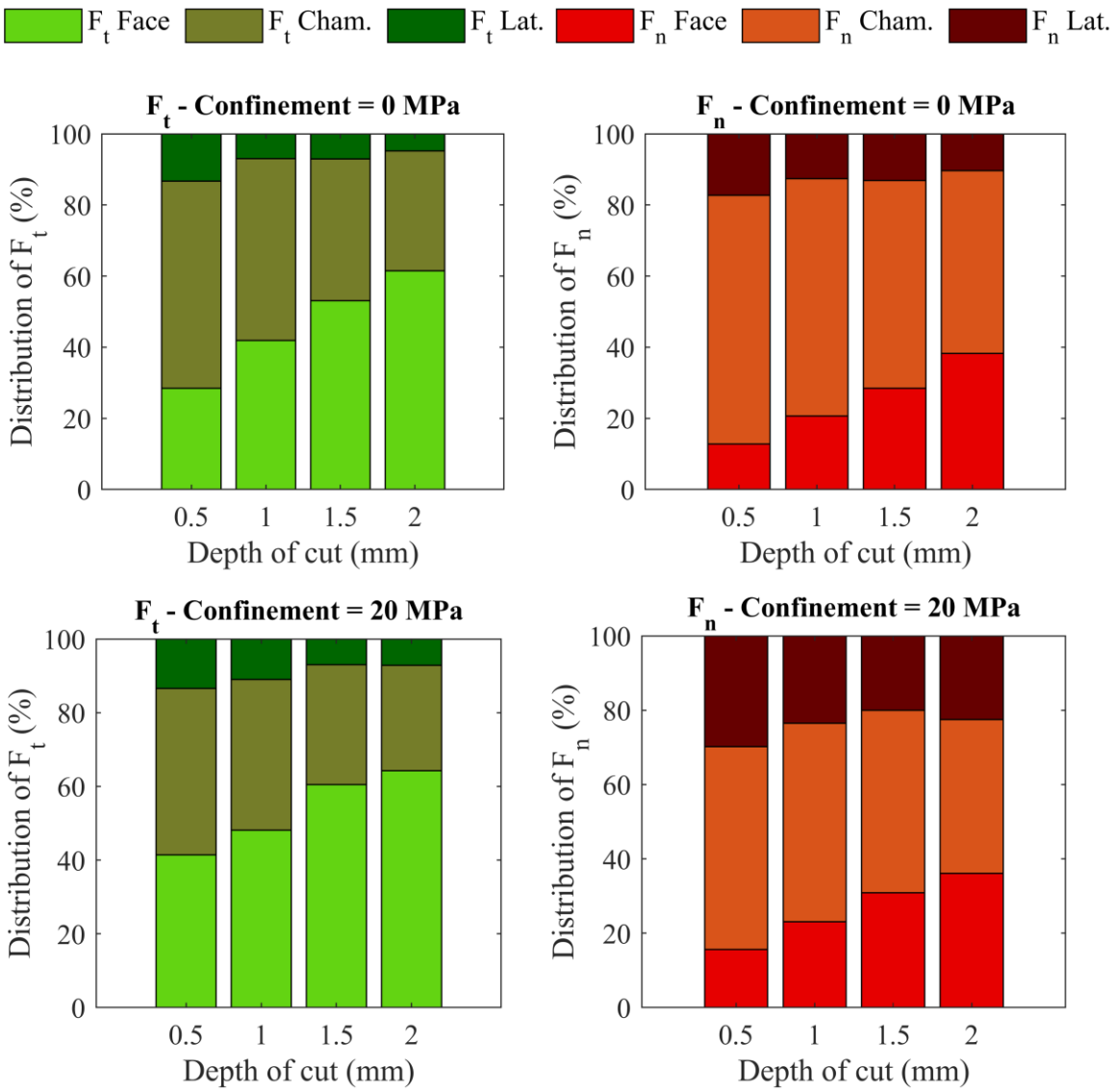

Figure V.15. Distribution of tangential and normal forces on the different faces of a circular cutter for tests performed under atmospheric conditions and confinement of 20 MPa.

3.2.2.2 Chamfer angle effect

Although the chamfer angles are typically around 45°, simulations were performed to study the impact of this parameter on cutting energies. Table V-4 presents the results obtained based on simulations with circular cutters to emphasize the impact of the chamfer angle.

Table V-4. Effects on the chamfer length of circular cutter on E and M.

L_{ch} (mm)	DOC (mm)	ω_{ch} (°)	Confinement = 0 MPa		Confinement = 20 MPa	
			E (MPa)	M	E (MPa)	M
0.25	1	30	81	1.0	337	1.1
		45	80	0.9	336	1.0
		60	79	0.9	298	1.0
	2	30	71	1.5	259	1.7
		45	71	1.4	257	1.5
		60	70	1.4	239	1.5
0.5	1	30	89	0.9	371	1.1
		45	99	0.7	362	0.9
		60	86	0.7	327	0.7
	2	30	76	1.3	277	1.5
		45	76	1.1	278	1.2
		60	77	1.0	264	1.0

The tests performed with a chamfer length of 0.25 mm did not show a real effect of the chamfer angle. Indeed, Specific Energy and Aggressiveness do not change significantly.

However, the results obtained through simulations with a chamfer of 0.5 mm have highlighted the impact of the chamfer angle. These results show that increasing the chamfer angle decreases the Aggressiveness of the cutter. Due to the significant proportion of the active surface occupied by the 0.5 mm chamfer, it has a greater influence on the cutting angle seen by the rock by increasing it. However, as seen previously, the increase of the back rake increases the cutting energies while decreasing the Aggressiveness of the cutter. This is the phenomenon that applies here with this larger chamfer. Whatever the confinement, the same trends could be observed. It is also the case for the rectangular cutters, for which the results are not presented here but are available in Appendix C.

3.2.3 Effects of the wear flat

This section dealing with the impact of the wear flat on cutting energies and the cutters' Aggressiveness only considers tests carried out with rectangular cutters. To analyze the impact of the length of the wear flat, the results obtained from simulations at 0, 20, and 40 MPa of confinement and for depth of cut of 1 and 2 mm are presented in $\overline{F_t}$ - $\overline{F_n}$ diagrams of Figure V.16.

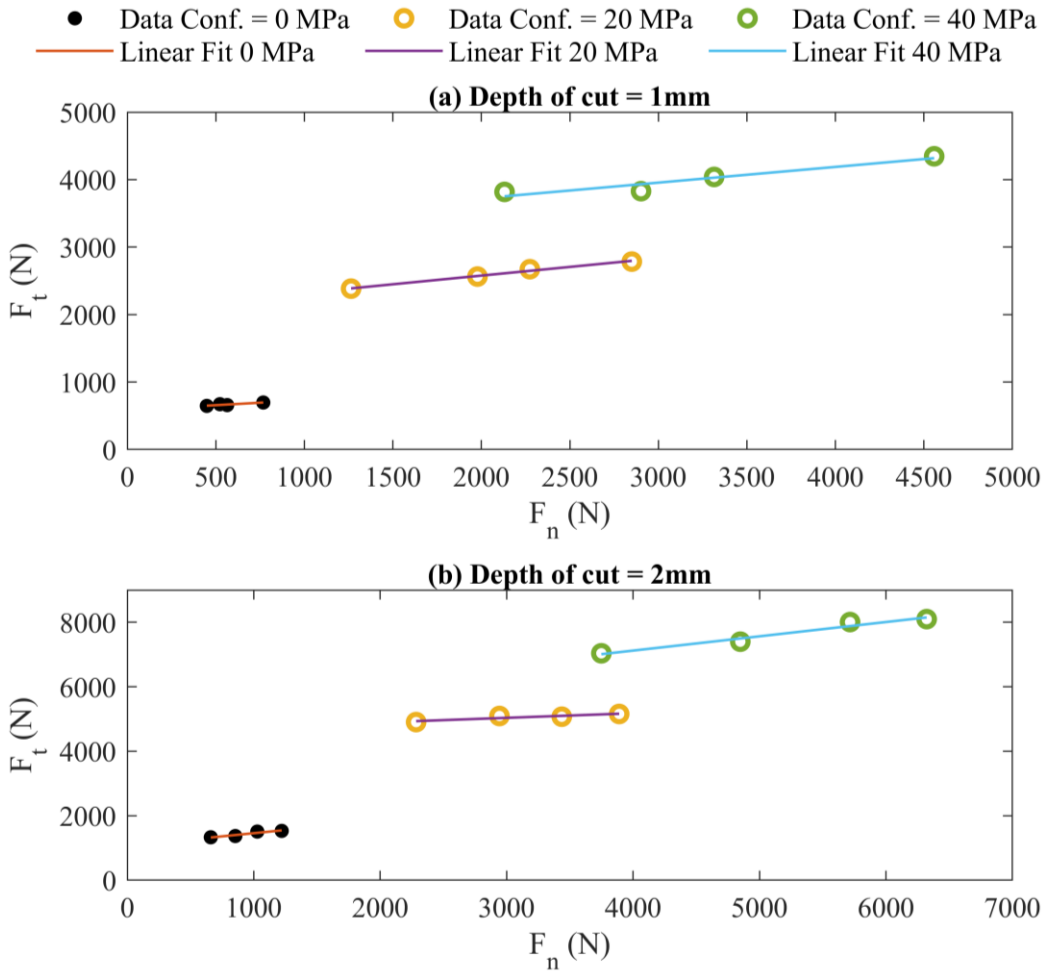

Figure V.16. $\overline{F_t}$ - $\overline{F_n}$ diagrams built from simulations carried out with increasing wear flat length for depths of cut of 1 and 2 mm and confinements of 0, 20, and 40 MPa.

These diagrams highlight that $\overline{F_t}$ and $\overline{F_n}$ are both impacted by the formation of a wear flat. Indeed, regardless of the confinement or the depth of cut, $\overline{F_t}$ and $\overline{F_n}$ increase with the length of the wear flat. Moreover, thanks to the linear fitting, it is noticeable that the test points obtained under the same conditions of confinement and depth of cut are aligned. It should be noted that the impact on $\overline{F_n}$ is more important than on $\overline{F_t}$. Since $\overline{F_n}$ increases faster than $\overline{F_t}$, the cutter Aggressiveness decreases with the length of the wear flat.

4 The groove geometry effects on rock cutting mechanism

The results presented in this chapter have been produced based on cutting tests on a virgin synthetic rock model. To get closer to the real conditions of rotary drilling during which the cutter paths are superimposed, simulations of overlapping cuts were carried out. The following sections present the results for two different cases:

1. Fully overlapped grooves from cutting at different depths of cut (1 and 2 mm from the top surface of the model).
2. Partially overlapped grooves from cutting tests at the same depth (1mm).

4.1 Case of fully overlapped grooves

The results of these successive cutting tests in the same groove are summarized in Table V-5. This table presents the Specific Energies and Aggressivenesses calculated for each simulation (the cutting number refers to the first or second groove).

Table V-5. Comparison of Specific Energy and Aggressiveness between first and second run of the fully overlapped groove at different confinement values.

# cut	0 MPa		10 MPa		20 MPa		30 MPa		40 MPa	
	E	**M**	**E**	**M**	**E**	**M**	**E**	**M**	**E**	**M**
1	82	1.42	200	1.59	293	1.73	381	1.69	461	1.52
2	37	1.70	130	2.02	204	2.17	255	1.85	332	1.95

These results highlight the reduction in Specific Energy required during the second run. This decrease is particularly significant at low confinement, exceeding 50% in atmospheric conditions. As the confinement increases, the reduction in cutting energies becomes less significant and seems to stabilize at about 30%. As Specific Energy decreases, Aggressiveness increases. This means that the thrust force decreases during the second pass but that its decrease is greater than the one of the tangential force.

This evolution in Specific Energy and Aggressiveness during the second run is explained by the fractures generated in the material during the first run. Indeed,

microcracks propagate in the material under the cutting surface during the first cut. These microcracks have the effect of reducing the strength of the material.

This pre-alteration is shown in Figure V.17, presenting a groove section after the first cut. We observe that the parallel bonds' black lines are less abundant near the groove. It reveals that part of these bonds has already been broken during the first run. Therefore, the lower reduction with increasing confinement can be easily explained. As presented previously, the confinement results in a ductile cutting mechanism that prevents the propagation of deep fractures. As a result, the material is less damaged, making it more resistant.

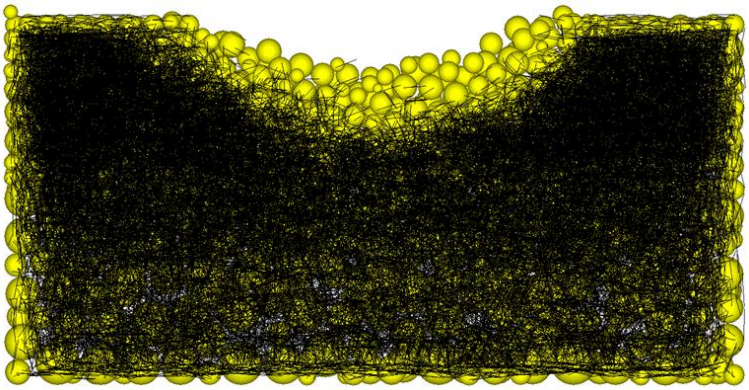

Figure V.17. Cross-section of the model after the first cut exhibiting damage to the material under the surface of the groove by the loss of parallel bonds (represented by black lines).

4.2 Case of partially overlapped grooves

The tests were conducted with non-overlapping grooves (adjacent grooves) up to 75% overlap. Table V-6 presents the results obtained for the simulations under atmospheric conditions and a 20 MPa confinement. These results highlight the decrease in the Specific Energy even for two adjacent grooves. The Aggressiveness does not vary significantly. It means that the vertical cutting force decreases proportionally with the horizontal one.

Thereafter, the more the two grooves overlap, the fewer cutting energies are consumed. This observation is valid except in the 75% overlay for the tests under a 20 MPa confinement. Indeed, we can see that the energy consumed is more important for this simulation than for the initial test. Unfortunately, this increase in Specific Energy could not be clearly explained based on the raw data of the simulations.

Table V-6. Comparison of Specific Energy and Aggressiveness for each overlapping scenario.

Cut type	Confinement = 0 MPa		Confinement = 20 MPa	
	E (MPa)	M	E (MPa)	M
Initial	73	1.31	293	1.90
0%	65	1.41	207	1.86
25%	56	1.44	222	1.63
50%	46	1.32	200	1.77
75%	39	1.55	317	1.80

5 Summary

During this chapter, important elements have been highlighted. They are summarized in this section to provide the necessary background for validating and interpreting the results that will take place in the next chapter.

In the first section of this chapter, the numerical modeling results highlighted the impact of the confinement on the cutting mechanism, both on the destruction mechanisms involved and the evolution of the cutting forces and energies.

From the destruction mechanisms point of view, the models allow understanding how the cutting mechanism evolves from two modes of destruction in atmospheric conditions (scratching and chipping) to the formation of ribbons when confinement is applied. At shallow depths of cut, the rock grains are ripped from the sample surface regardless of confinement. When mud pressure is applied, these ripped grains are compacted on the cutter face to form the crushed material ribbon. At large depths of cut, three mechanisms were observed. Without confinement, large chips are formed and pulled out of the sample. Depending on the energy released, these chips are either pulled away from the cutter or accumulated at its tip and pushed by it. When low confinement is applied, smaller chips are formed. However, they cannot be evacuated and remain in place due to the mud pressure. As the cutter moves forward, these chips are then crushed and progressively accumulated on the cutting surface of the cutter to form a ribbon. Finally, no more chips are formed for high confinement values, but the cutter crushes the rock. The crushed rock then forms a ribbon that rises on the cutting surface of the cutter.

As expected, the results indicate that cutting forces and energies increase with confinement. Nevertheless, the most important point is how these energies evolve with confinement. Indeed, this increase is not linear, but the rate of increase is more important for low confinement. Regarding the cutting forces, the main output of the numerical modeling is the highlighting of the reduction of the relative standard deviation with the confinement. It could be the meaning of a more continuous destruction mechanism.

In the second section of the chapter, the presented results focused on the cutting parameters' impact on E, $\overline{F_n}$, and M to understand how vertical force evolves comparatively to tangential. The results indicated that increasing the depth of cut allowed to reach a minimum of E. This minimum was observed up to confinement of 20 MPa. No minimum could be observed in the tested DOC range for larger confinements, but it could be assumed that an optimum DOC should be raised performing further simulations.

Concerning the side rake angle, the results showed that this parameter could be slightly beneficial by decreasing Specific Energy but only when this parameter is lower than 20°. Once this value is exceeded, the impact of this parameter is negative as it causes an increase in the Specific Energy and reduces Aggressiveness. Indeed, a part of the side face comes in contact with the rock once an angle of 20° is exceeded, generating significant friction on this part of the cutter. Indeed, a part of the lateral face of the cutter is then in direct contact with the rock, which results in important frictional efforts between the rock and the cutter. Finally, the results highlight the negative effect of increasing the back rake angle.

The third section focused on the impact of the cutter geometry. Since rectangular cutters have often been used for experimental research, simulations with rectangular and circular cutters were compared. This comparison showed that Specific Energy does not differ significantly between circular and rectangular cutters. Indeed, evolutions of E versus the depth of cut and confinement with rectangular cutters are comparable to those observed with circular cutters. However, rectangular cutters require less energy than circular ones at an identical depth of cut and confinement.

This section focused on the chamfer's impact as most PDC cutters used on drill bits are chamfered ones. Two aspects have been studied: the impact of the chamfer length and its angle. The results indicate that the presence of a chamfer decreases the Aggressiveness of the cutter due to the increase of vertical cutting forces. The presence of the chamfer only slightly impacts E. In general, the longer the chamfer

and the shallower the depth of cut, the greater the impact of the chamfer on vertical cutting forces.

The last part of this section focused on the appearance of a wear flat on rectangular cutters and its impact on cutting energies. The analysis of the results showed that vertical force is mainly impacted by the formation of a wear flat and its enlargement and increases with it. Tangential force is less impacted than vertical one, and its increase is smaller. Moreover, the data from tests at constant confinement are aligned in the $\overline{F_t}$ - $\overline{F_n}$ diagram.

Finally, the last section of this chapter focused on the complete and partial overlapping of two grooves. For two overlapped grooves, results indicated a reduction of 50% of Specific Energy. This reduction becomes less important when the confinement increases to around 30% at 40 MPa of confinement. Regarding the partial overlap, a decrease in the cutting energies was measured even in two adjacent grooves. In atmospheric conditions, the increase of the overlap leads to a decrease in E. On the other hand, the increase in overlap does not seem to show a real benefit under confinement. It even seems unproductive for an overlap of 75% where E increased.

Chapter VI Comparative analyses and interpretations

Following the presentation of the results of the numerical simulations in the previous chapter, the present chapter is divided into three parts. First, the results are compared to data available in the literature. The objective is to ensure that numerical results correspond to experimental ones qualitatively and quantitatively.

In a second step, the results will be interpreted and completed by some data to explain the evolution of the destruction mechanisms involved and the evolution of the cutting energies. This part ends with an attempt to model the evolution of the optimal cutting energy versus the confinement.

Finally, this chapter concludes with a section highlighting how DEM modeling could help set cutting parameters to optimize Specific Energy.

1 Comparative analyses

To validate the results of the numerical simulations, they are compared in this section with experimental results available in the literature. These validations will be done on different points of interest: the cutting forces, the effect of the cutting parameters, the cutter geometry, and finally, the evolution of E due to the increase of confinement. Only the results obtained with 3D models are used in this section as it focuses on quantitative aspects.

1.1 Cutting forces

Two aspects must be considered to validate the cutting forces as measured in the numerical models: the pattern and the magnitude of cutting forces.

The pattern concerns the evolution of the cutting forces throughout the simulation essentially. Whether in atmospheric conditions or under confinement, the cutting forces reach a steady state in the numerical models. In atmospheric conditions, this steady state is reached at the beginning of the test (Figure VI.1 (a) and (b)), whereas under confinement a transient phase is necessary (Figure VI.1 (c) and (d)). The steady state phase is also observed in laboratory experiments both in atmospheric and confined conditions. This transitional phase is also visible during the laboratory tests under confinement. It corresponds to the time needed during the laboratory test to reach the nominal depth of cut.

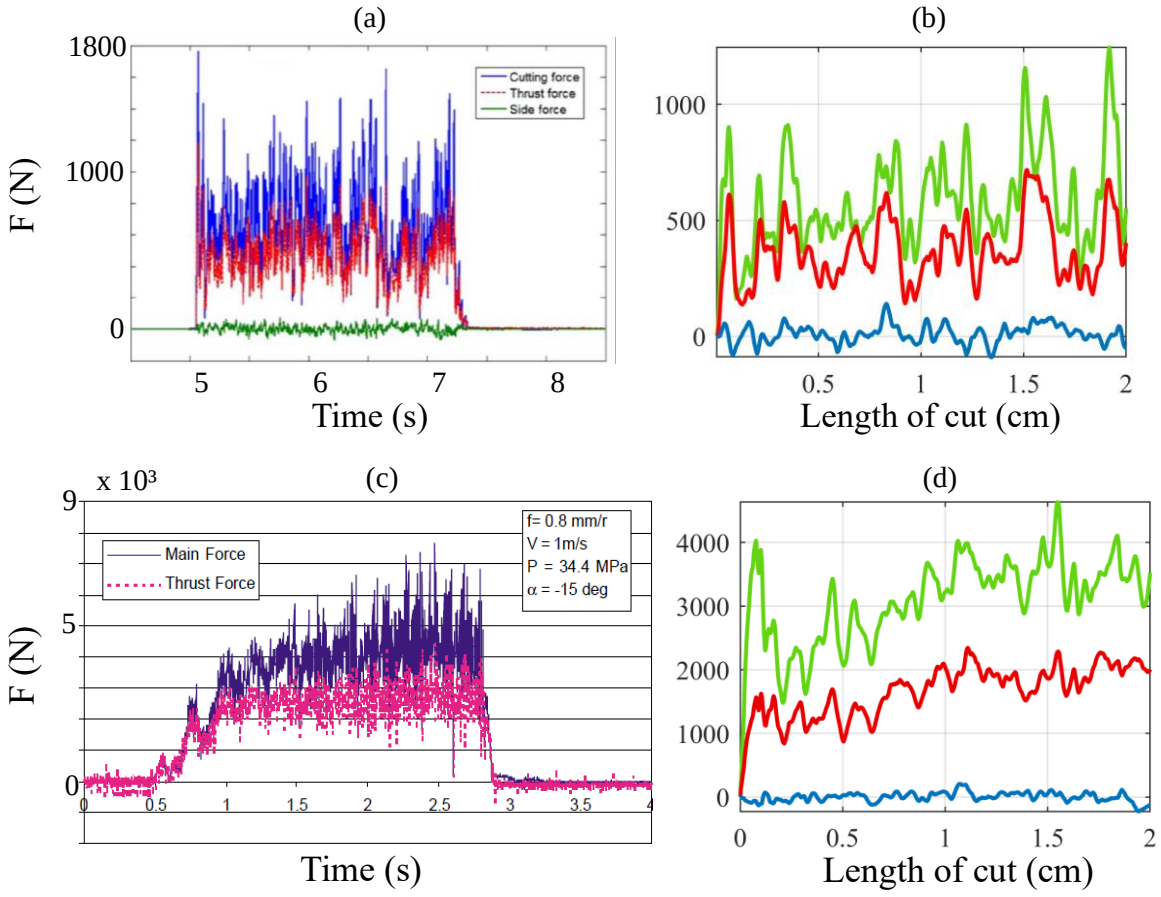

Figure VI.1. Comparison between (a - c) experimentally (Che et al. (2016) - Kaitkay and Lei (2005)) and (b - d) numerically measured forces under atmospheric conditions and under confinement.

Regarding the magnitude of cutting force, Table VI-1 compares the measured average forces obtained numerically under different confinement conditions with results published in the literature. As experimental conditions and tested materials are not always the same (experimental setups and rock properties are also considered in this table), the cutting forces are standardized based on UCS.

Table VI-1. Comparison of tangential cutting force between simulations and various lab tests available in the literature.

Source	Rock	UCS	Cutter velocity	Conf.	DOC	Mean cutting force	Standardized cutting force (N/MPa)
This work	Vosges Sandstone	70 MPa	1 m/s	0 MPa	1 mm	350 N	5
				20 MPa		1450 N	21
				40 MPa		2242 N	32
Amri et al. (2016)	Vosges Sandstone	36 MPa	0.6 m/s	0 MPa	1 mm	200 N	6
			0.9 m/s	20 MPa		750 N	21
			1.2 m/s	20MPa		750 N	21
Kaitkay & Lei (2005)	Carthage Marble	120 MPa	1 m/s	0 MPa	0.8 mm	600 N	5
				34 MPa		3600 N	30
Majidi et al. (2011)	Indiana Limestone	50 MPa	0.3 m/s	0 MPa	1 mm	400 N	8

The values of the standardized cutting force (SCF) are very interesting to compare the different works listed in Table VI-1. Indeed, for tests carried out under comparable conditions, the values of standardized cutting force are close. The SCF values for numerical models show that the forces obtained numerically are in line with experimental measurements. Although this is not proof of the exact validity of the forces measured in this work, it tends to show that they are consistent with experimental ones.

Although laboratory tests on a Vosges Sandstone with the same mechanical properties as the simulated material will be necessary to validate the simulations, this first analysis based on the literature review allows us to consider that the results of the cutting forces (pattern and magnitude) are realistic.

1.2 Impact of cutting parameters

This section aims to verify if the evolution of the Specific Energy depending on the cutting parameters as observed numerically is comparable to what is described in the literature from experimental tests. Three parameters are analyzed here: the depth of cut, the back rake angle, and the side rake angle.

For the depth of cut, the simulations showed that E and S decrease with increasing depth of cut up to reach a minimum for given confinement. It may be partly due to the limited range of depth of cut tested, going from 0.5 to 2 mm. In contrast, in the case of S, a minimum was observed only for 40 MPa of confinement. The numerical model results are in adequacy with experimental and field works published in the literature (Rajabov et al., 2012; Akbari and Miska, 2017; Cheng et al., 2018). Indeed, these works have highlighted the decrease of the Specific Energy with the increasing depth of cut up to reach a plateau or a minimum followed by a re-increase. Figure VI.2 allows comparing this evolution between numerical and experimental results. Based on the graphs in this figure, E versus DOC curve shapes are comparable between the numerical models and the experimental results.

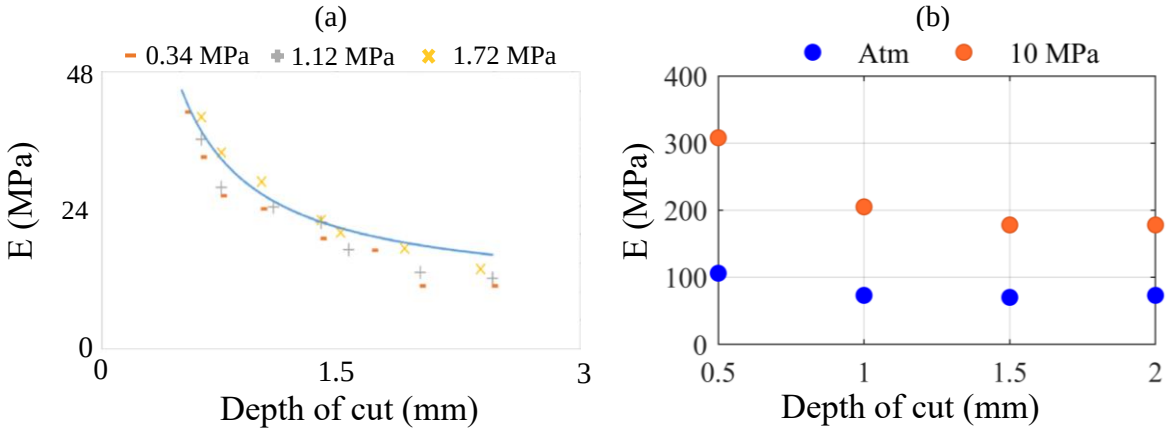

Figure VI.2. Evolution of Specific Energy with the depth of cut: (a) experimental results on Carthage Marble (Akbari and Miska, 2017), (b) numerical ones.

Concerning the impact of the back rake angle, its rise increases the energy required to cut the rock. Focusing on the magnitudes of this increase between the numerical models and the experimental results (Figure VI.3), it can be observed that they are comparable. Indeed, when the back rake angle increases from 15° to 45° under atmospheric conditions, E is multiplied by 2.2 in the numerical models. In contrast, it is multiplied between 2 and 3 for the different rocks tested by Rostamsowlat et

al. (2018). Unfortunately, no figures have been obtained in the literature for the increase of S or E under confinement.

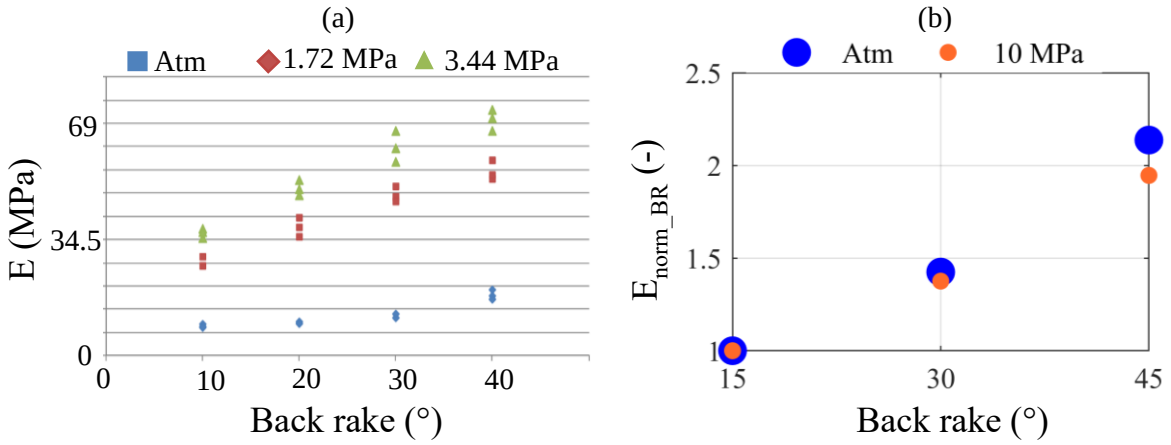

Figure VI.3. Impact of the back rake angle on the Specific Energy: (a) experimental results on Carthage Marble (Rajabov et al., 2012) and (b) numerical ones.

Finally, Figure VI.4 compares the evolution of E versus side rake angle between our numerical modeling results and experimental ones of Rajabov et al. (2012). In both cases, E remains stable up to a side rake angle of 20°. Once this value is exceeded, E increases at an increasing rate in both cases. These are comparable in terms of the orders of magnitude of this increase. Indeed, in the experimental results, E is multiplied by 2 (atmospheric conditions) and 3 (250 psi of confinement) when the side rake angle goes from 0 to 60°. While for the simulations, it is multiplied by 2.2 in atmospheric conditions and 2.4 at 20 MPa of confinement.

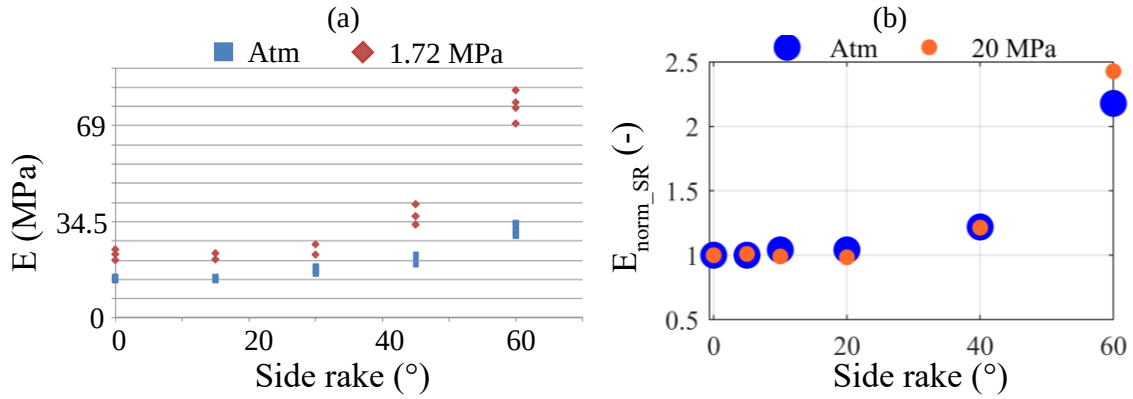

Figure VI.4. Impact of the side rake angle on the Specific Energy: (a) experimental results on Carthage Marble (Rajabov et al., 2012) and (b) numerical ones.

1.3 Impact of cutter geometries

This section focuses on validating the numerical results obtained with chamfered cutters and ones with a wear flat. Regarding the impact of the chamfer, its presence tends to increase E and $\overline{F_n}$ according to numerical results. However, these results show that the impact of a chamfer on E decreases with increasing depth of cut. Indeed, for a depth of cut of 2 mm and for any confinement, E is only slightly influenced by the presence of a chamfer. The results agree with those published by Akbari & Miska (2016) and presented in Chapter II.

The wear effect on the cutting energies was studied using rectangular cutters with increasing wear flat length. Modeling results highlighted the increase in $\overline{F_t}$ and $\overline{F_n}$ with increasing wear flat length. The $\overline{F_t}$ - $\overline{F_n}$ diagrams highlighted the linear evolution of $\overline{F_t}$versus $\overline{F_n}$, at a constant depth of cut and confinement, as the wear grows. These results are consistent with the numerous experimental results presented in the literature, where results are presented in E-S diagrams. The linear regression slope of E versus S is generally considered as the coefficient of friction (μ) between the wear flat and the rock. This coefficient can also be determined based on $\overline{F_t}$ - $\overline{F_n}$ diagrams. The results obtained for μ are presented in Table VI-2. Comparing them to the values calculated by Dagrain and Richard (2006b), who had obtained values of 0.69 with a rough wear flat and 0.25 with a polished one (tests performed on Vosges Sandstone), it can be noticed they are of the same order of magnitude than the one obtained with a polished wear flat.

Table VI-2. Friction coefficient μ between the wear flat and the rock for different confinements and depths of cut.

Depth of cut	**Confinement**			
	0 MPa	**10 MPa**	**20 MPa**	**40 MPa**
1 mm	0.14	0.20	0.25	0.23
2 mm	0.39	0.22	0.14	0.44

1.4 Evolution of E with confinement

Numerical models have shown the evolution of E with confinement for simulations performed under the same experimental conditions (same depth of cut, back and side rake angles). The most interesting is that this increase is not linear. Indeed, the rate of increase decreases with the confinement in most cases simulated. These results also agree with the experimental results published in the literature regarding

works dealing with the cutting mechanism (Lei et al., 2004; Akbari and Miska, 2016; Amri et al., 2016).

1.5 Conclusions of comparative analyses

The comparative analysis in this section highlighted the consistency of numerical results with the experimental results published in the literature. Indeed, it has shown that the numerical results are valid both quantitatively and qualitatively. Quantitatively, the numerical cutting forces are in orders of magnitude comparable to the experimental ones, while qualitatively, evolutions of cutting energies with cutting setup follow the same trends as experimentally.

Although the numerical results seem to correspond to the different trends observed experimentally on other rocks, a coupled experimental-modeling study should be necessary to validate the whole approach developed during this thesis and the veracity of the modeling results with respect to the experimental results on the same rock.

2 Interpretations

This second section focuses on interpreting the results presented in the previous chapter. Three points are studied here: the evolution of the cutting mechanism, the search for an optimal cutting depth, and finally, the evolution of the cutting energies with the confinement.

2.1 Evolution of cutting mechanism with confinement

At shallow depths of cut (0.5 mm), the cutting mechanism seems to be slightly influenced by the confinement. At this depth, the grains are scratched from the surface of the sample by the PDC cutter. The destruction mechanism is then dominated by friction between the cutter and small scratched cuttings.

In this friction-dominated mechanism, the change in cutting shapes due to the confinement is explained by applying mud pressure. Under atmospheric conditions, numerical models show that the grains are torn individually from the material to form an independent assembly. In the practical case, the grains on the surface of the material are torn or fractured by the forces exerted by the cutter. This mode of destruction then forms a fine powder of rock. When the confinement is applied, ribbons of rock are formed. The formation of these ribbons is due to the application of the drilling fluid pressure. Whether experimentally (in most cases) or numerically, the pressure applied by the drilling fluid is static. Indeed, no circulation of this fluid is done to simulate the drilling mud circulation occurring in practice. This non-circulation prevents the removal of the grains torn-off by the cutter on the face. This results in an accumulation of cutting debris at the front of the cutter. These particles of rock are then recompacted by the applied pressure and move up to the surface of the cutter as it advances. This friction-dominated destruction mode is an inefficient mechanism requiring more energy to destroy a defined volume of rock (see section 2.2).

When the cutting depth increases, the cutting mechanism will evolve from a pole essentially dominated by friction to a pole evolving with the mechanical behavior of the rock. This second pole is greatly influenced by the confinement and the evolution of material constitutive laws. In the Vosges Sandstone studied here, the cutting mechanism at a cutting depth of 1.5 mm has evolved from a brittle to a ductile mode of destruction with increasing confinement. The formation of chips characterizes the brittle destruction mode. These chips are formed in atmospheric conditions and when the confinement is low. The main difference is that when the

confinement is applied on the cutting surface, they are not evacuated (same explanation as before due to the absence of fluid circulation). These chips are then crushed because they are trapped between the membrane applying the slurry pressure and the advancing cutter. When the confinement increases, the destruction mechanism evolves towards a ductile mechanism like the material behavior. No chips are then formed due to the propagation of large fractures developing in the cutting direction. Instead, microcracks propagate between the grains composing the numerical model. This microcracks propagation occurs over an area slightly larger than the imposed depth of cut. The development of these microcracks gives relative mobility to the grains with respect to each other, allowing them to be evacuated when the cutter advances.

The diagram in Figure VI.5 summarizes the cutting mechanism's evolution depending on the depth of cut and the confinement as observed with the Vosges Sandstone synthetic model.

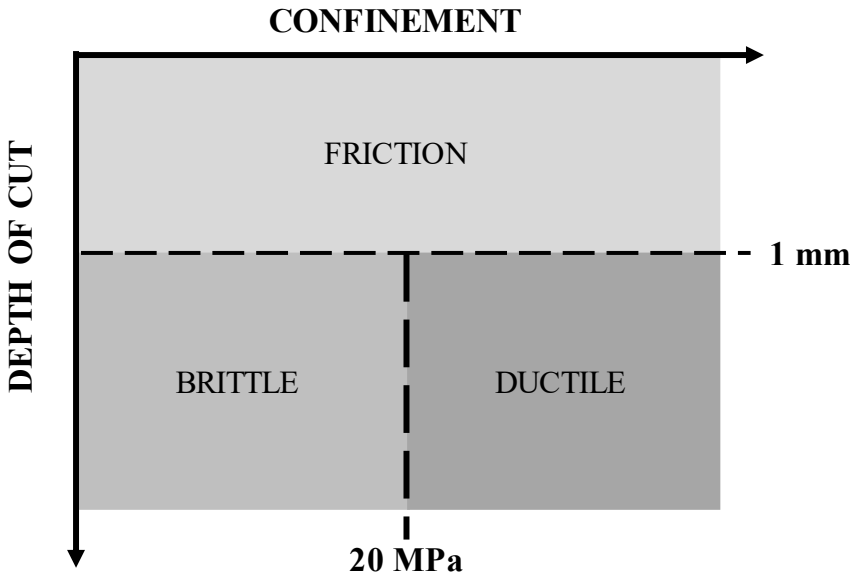

Figure VI.5. Diagram of the evolution of the cutting mechanism for Vosges Sandstone according to the confinement and the depth of cut.

The objective of this work was not to precisely determine the limits of these different mechanisms (friction-brittle-ductile). However, based on simulations, orders of magnitude can be given for these different transitions. The frictional destruction mode was observed up to a depth of cut of 1 mm. The critical depth of cut, limiting the friction mechanism, must depend essentially on the size of the grains in the model and the mechanical properties of the cement between particles.

For the brittle-ductile transition, the ductile mode was observed from a confinement of 20 MPa, which corresponds to the confinement at which the material changes from brittle to ductile behavior based on triaxial tests.

The Vosges sandstone studied here is not representative of all the rocks, and the above observations must be generalized to be applied to other rocks. Indeed, rocks do not present the same evolution, some presenting a ductile behavior at low confinement or even in atmospheric conditions (like clay and shales), while very hard ones can present a brittle behavior until a very high value of confinement (Chapter II section 2.2).

It can be assumed that the ductile destruction mode will dominate the cutting mechanism for materials exhibiting ductile behavior at low confinement. For clays, it can even be assumed that the fragile mechanism will not be met. In addition, the critical depth of cut limiting the frictional destruction mode should be low.

On the other hand, the rocks presenting a brittle behavior until high values of confinement will have their cutting mechanism dominated by the brittle cutting mode. For this type of rock, it can also be assumed that the critical depth of cut will be small.

2.2 Optimal depth of cut

Results presented in section 2.1 of Chapter VI highlighted the decrease of cutting energies with the increasing depth of cut. Further, a minimum of the Specific Energy (corresponding to an optimum depth of cut) for each confinement can be assumed according to the conventional drill-off curve (Chapter II), which highlights the existence of a range of WOB allowing to optimize the ROP. Besides, a minimum of E has been observed in the models under atmospheric conditions. This minimum corresponds to a cutting depth of 1.5 mm. A plateau seemed to be reached for the other confinements before a possible re-increase.

Additional simulations with sharp circular cutters were performed to refine the observations made in the previous chapter. Two objectives were behind this extended protocol of simulations. The first one was to define the optimal depth of cut in atmospheric conditions more precisely. The second goal was to investigate the existence of an optimal cutting depth for other confinement values. For this purpose, the range of cutting depths studied was subdivided into smaller intervals of 0.25 mm and extended up to 2.5 mm.

Based on the additional data collected, a curve fitting of the Specific Energies evolution with the depth of cut was performed for each confinement value. Figure VI.6 presents the graphs obtained with the curve fitting. They show an optimal cutting depth for each of the tested confinements.

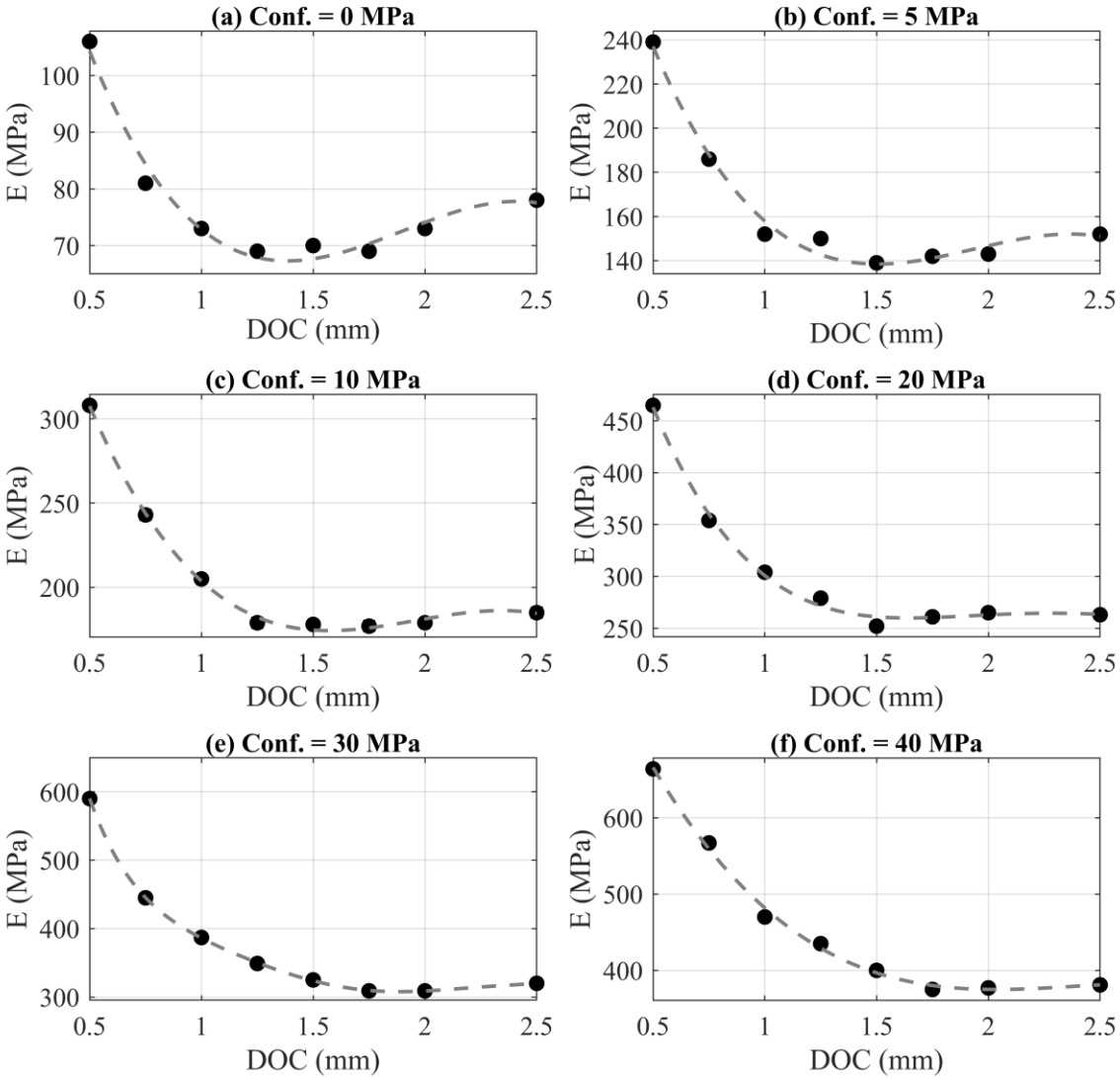

Figure VI.6. Curve fitting of the evolution of Specific Energy with confinement for different confinement values.

The curve fitting highlights the occurrence of an optimal depth of cut for each tested confinement, which is consistent with the drill-off curve. Table VI-3 gives the values of the optimal depths of cut and the values of the respective Specific Energies for each graph of Figure VI.6. It is noticeable from these data that the optimal cutting depth increases with the confinement.

Table VI-3. Evolution of the optimum depth of cut and its associated Specific Energy with the confinement.

Confinement	Optimum depth of cut (mm)	Specific Energy (MPa)
Atmospheric	1.39	68
5 MPa	1.50	138
10 MPa	1.53	175
20 MPa	1.65	259
30 MPa	1.90	312
40 MPa	1.99	375

Figure VI.7 presents the general trend in the evolution of the optimal depth obtained by linear interpolation. Although few points compose this graph, it presents a sigmoidal trend with an inflection point located at a confinement of 20 MPa. This confinement value coincides with the transition of the rock behavior from brittle to ductile. Therefore, this inflection point can be seen as the boundary between a brittle and a ductile cutting mechanism. This analysis agrees with observations made in the 2D numerical models. Indeed, the 2D models revealed that chip formation was visible up to confinement of 10 MPa. From 20 MPa, no more chips appeared to be created. The change from macroscopic fractures to micro-cracks between the particles corresponds to the transition from a brittle to a ductile mode of destruction.

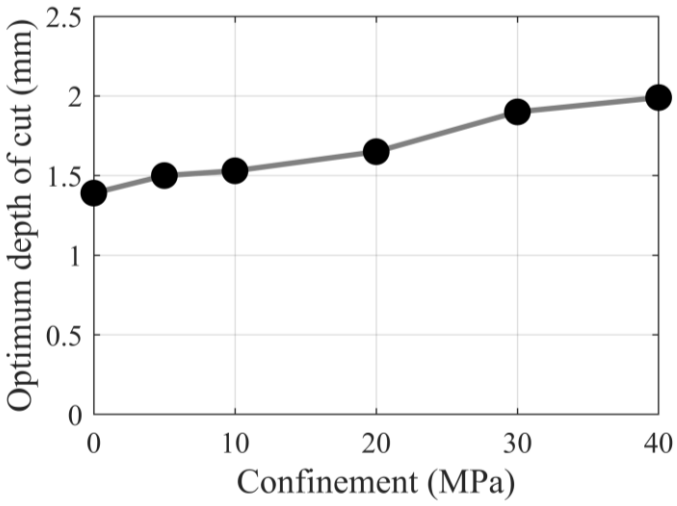

Figure VI.7. Graphical representation of the evolution of the optimum depth of cut with the confinement based on numerical simulations.

It is essential to note that the set of optimal cutting depths and the associated cutting energies given in this section are only valid for the sharp circular cutter (D=13 mm)

modeled and for specific testing conditions (V = 1 m/s; BR = 15°; SR = 0°). Indeed, results presented in Chapter V have shown the impact of the cutter shape and cutting parameters on the cutting energies. Therefore, optimum Specific Energies given in this section cannot be considered as intrinsic characteristics of the rock.

2.3 Evolution of cutting energies with confinement

Section 1.3 of Chapter VI presented the evolution of the Specific Energy versus confinement for a fixed cutting depth. As for the experimental tests from the literature, it was noticeable that the Specific Energy increases more rapidly at low confinement values (Rafatian et al., 2009).

Section 2.2 of this chapter presented the optimal cutting depths for the different confinement values tested and their associated Specific Energy values. Figure VI.8 shows the graphical representation of the evolution of the optimum Specific Energy versus confinement.

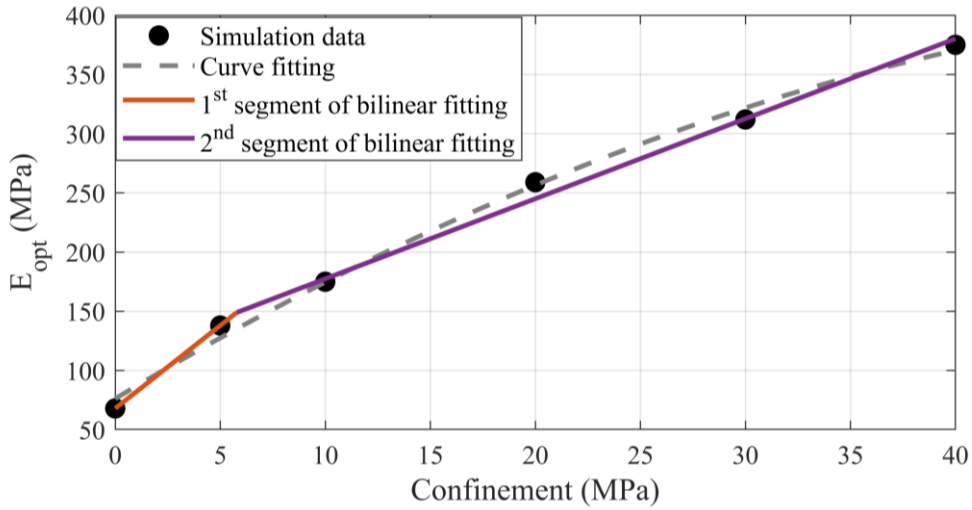

Figure VI.8. Evolution of the optimum Specific Energy with the confinement. The discontinued grey line is the curve fitting of the data, while orange and purple ones are two segments piecewise model.

The evolution of the Optimal Specific Energy does not evolve linearly with the confinement and can be fitted by a curve or piecewise models (Figure VI.8). This evolution of the Specific Energy can be related to the non-linearity of the limit envelope of the material, which evolves with the increase of the "apparent" cohesion and the decrease of the friction angle as the confinement increases. The following section tries to formulate the evolution of Optimum Specific Energy based on the mechanical properties of the rock and cutting parameters.

2.4 Attempt to model the evolution of the Optimal Specific Energy versus confinement

This section attempts to build a model of the evolution of Optimal Specific Energy with confinement based on mechanical properties of the Vosges Sandstone and cutting parameters. For this purpose, several hypotheses are formulated. Regarding the cutter geometry, only the case of a sharp circular cutter with a back rake angle of 15° is considered. Moreover, mud pressure and lateral confinement are considered equal.

Previously, we illustrated that the Optimal Specific Energy evolution can be either modeled by a curve fitting model or a piecewise model. For upcoming developments, it is considered that a piecewise model can represent this evolution and that each segment of this model can be expressed as:

$$E_{opt\_p_m} = E_{i-j} + k_{i-j}\, p_m \qquad \text{(VI.1)}$$

Where i and j are the boundaries of each domain of the model, E_{i-j} and k_{i-j} are the coefficients of each segment and p_m is the confinement.

Section 1.4 of Chapter IV determined failure envelope parameters based on the Mohr-Coulomb criterion. Moreover, considering the failure criterion as a piecewise model, the failure envelope comprises three segments in the considered confinement range (from 0 to 70 MPa). This failure criterion is presented in Figure VI.9 in the (τ, σ) and (σ_1, σ_3) planes. In (σ_1, σ_3) planes, the σ_3 limits of intervals are [0 ; 5], [5 ; 30], and [30 ; 70].

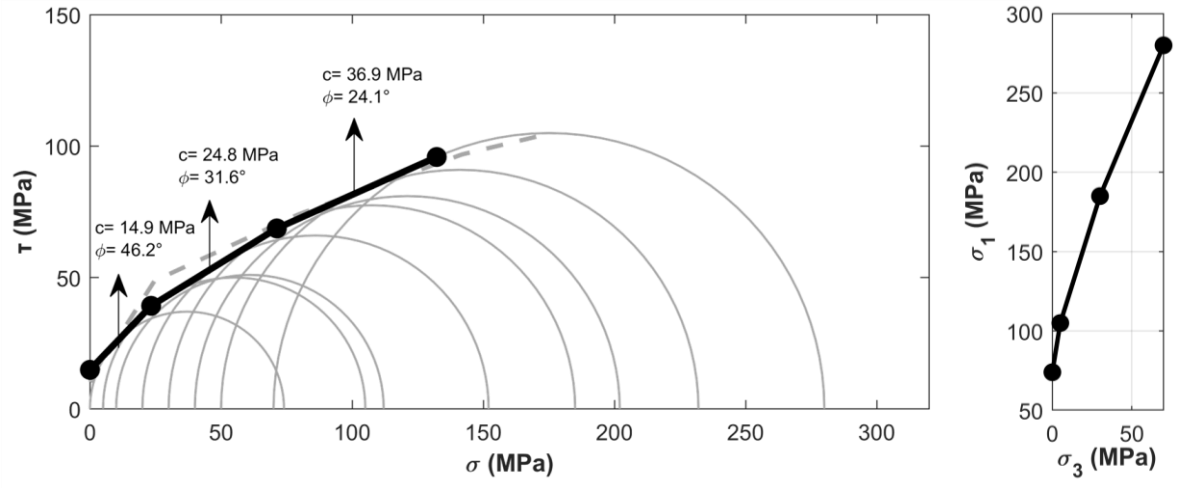

Figure VI.9. Mohr-Coulomb criterium of numerical model in (τ, σ) and (σ_1, σ_3) planes.

Assuming that these parameters govern the evolution of the Specific Energy with the confinement, the model of the Optimal Specific Energy for the confinement interval of 0-70 MPa could be divided into three segments defined as follow:

$$E_{opt} = \begin{cases} E_{0-5} + k_{0-5}\, p_m\ , & 0 < p_m < 5 \\ E_{5-30} + k_{5-30}\, p_m, & 5 < p_m < 30 \\ E_{30-70} + k_{30-70}\, p_m, & 30 < p_m < 70 \end{cases} \quad \text{(VI.2)}$$

Such model formulation, therefore, requires the definition of six coefficients: E_{0-5}, E_{5-30}, E_{30-40}, k_{0-5}, k_{5-30}, k_{30-70}. Figure VI.10 provides a schematic representation of this model.

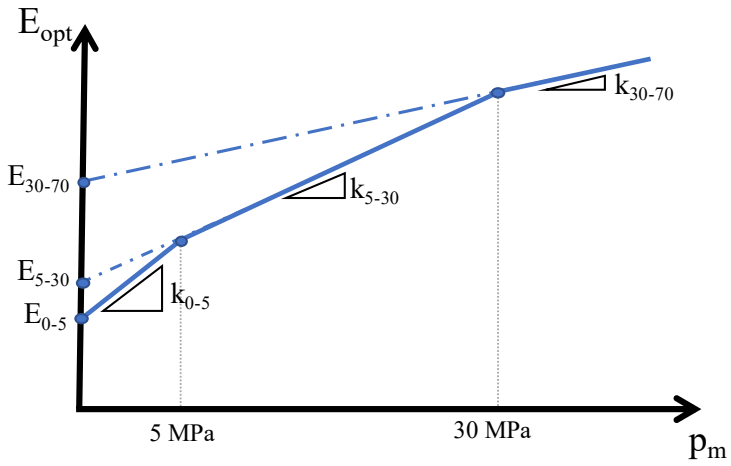

Figure VI.10. Schematic representation of the model determining the evolution of the optimal Specific Energy with the confinement.

However, by calculating the intersections between the different segments of the model based on E_{0-5} and the slopes of each interval, it is possible to reduce the number of parameters by defining the piecewise model as follow:

$$E_{opt\_pm} = \begin{cases} E_0 + k_{0-5}\, p_m, & 0 < p_m < 5 \\ E_0 + 5\, k_{0-5} + k_{5-30}\, (p_m - 5), & 5 < p_m < 30 \\ E_0 + 5\, k_{0-5} + 25\, k_{5-30} + k_{30-70}\, (p_m - 30), & 30 < p_m < 70 \end{cases} \quad \text{(VI.3)}$$

Where E_0 is equal to E_{0-5}. Therefore, only four parameters remain to be determined: E_0, k_{0-5}, k_{5-30}, k_{30-40}.

The first parameter to be determined is E_0. This parameter corresponds to the optimal Specific Energy in atmospheric conditions determined in section 2.2 of this chapter. Its value is therefore 68 MPa. Under this value are hidden parameters

such as rock and cutting properties. This value is close to the synthetic rock's uniaxial compressive strength, 74 MPa. It is consistent with the work of Teale (1965), who had already hypothesized that the optimal Specific Energy would be of the order of magnitude of the uniaxial compressive strength in atmospheric conditions. Therefore, E_0 can be approximated by the UCS of the rock.

Regarding the slope parameters (k_{0-5}, k_{5-30}, k_{30-40}), it may be of interest to take inspiration from the definition of the slope parameter of the Mohr-Coulomb criterium in the (σ_1, σ_3) plane. With respect to the Mohr-Coulomb criterium defining the angle between the shear plane and the direction of the maximum principal stress by $\psi = {}^{\pi}/_{4} - {}^{\varphi}/_{2}$ (Jaeger et al., 2007), the slope parameter in the (σ_1, σ_3) plane is given by:

$$q = tan^2\left(\frac{\pi}{4} + \frac{\varphi}{2}\right) \tag{VI.4}$$

With φ is the internal friction angle of the rock.

Following the cutting models developed by Gerbaud et al. (2006) and Amri (2016), themselves based on the Mohr-Coulomb criterion, they define the angle between tangential cutting force and the shear plane by:

$$\psi = \frac{\pi}{4} - \frac{\theta_f + \varphi}{2} \tag{VI.5}$$

Where θ_f is the apparent friction angle at the cutter face and is defined by:

$$\theta_f = \tan^{-1}\left(\frac{F_n}{F_t}\right) - \omega_c = \tan^{-1}\left(\frac{1}{M}\right) - \omega_c \tag{VI.6}$$

Based on the previous considerations, the k_{i-j} factor could be expressed as:

$$k_{i-j} = tan^2\left(\frac{\pi}{4} + \frac{\varphi_{i-j} + \theta_f}{2}\right) \tag{VI.7}$$

Where φ_{i-j} is the internal friction angle of the rock for each segment of the model. While φ_{i-j} is a parameter specific to the rock, θ_f is a characteristic of the cutter-rock interface.

Following equation (VI.6), θ_f was determined based on Aggressiveness values calculated for simulations performed at depths of cut ranging from 1.5 to 2 mm (close to optimal depths of cut) and for confinements ranging from 0 to 40 MPa. Considering the variability of M and the absence of an overall trend according to the depth of cut or confinement, an average Aggressiveness of 1.8 was considered. According to equation (VI.6), θ_f equals 14°.

Based on equations (VI.3) and (VI.7) and the values of E_0, φ_{i-j} and θ_f , the model of the Optimal Specific Energy versus confinement is presented in Figure VI.11. This model differs slightly from the optimal specific energy values, which were calculated based on the curve fitting of the numerical results in Section 2.2 of this chapter, but is within the standard deviation for each confinement.

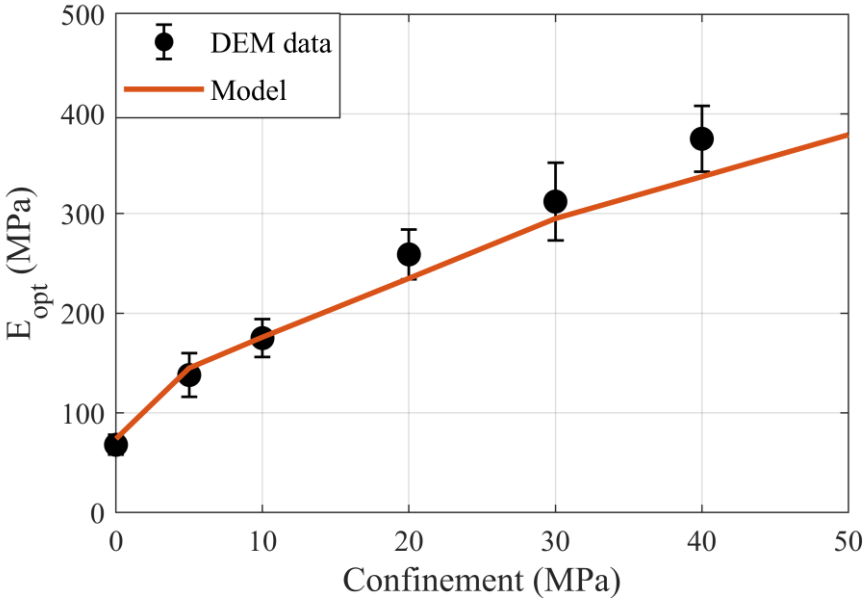

Figure VI.11. Analytical model of the evolution of the Optimal Specific Energy with the confinement compared to simulation data.

As this is a first approach, it would benefit from further validation. To be validated, this approach to estimate Optimal Specific Energy based on mechanical properties could be applied to other rocks presenting different behavior and failure envelope shape than Vosges Sandstone.

3 DEM models as a tool to optimize cutting parameters

All the simulations carried out during this thesis enabled to study the effect of the various cutting parameters on Specific Energy. But besides studying the impact of the different parameters independently, it is possible to study how they interfere together. Thanks to the factorial design used to build the simulation protocol, it is also possible to agglomerate the data to build 3D mappings of the evolution of E and $\overline{F_n}$ according to the selected cutting parameters.

Figure VI.12 (a) and (b) presents a mapping of the Specific Energy E for fixed confinement of 20 MPa. In this case, 24 simulations were realized (4 values of depth of cut [from 0.5 to 2 mm] and 6 values of side rake angles [from 0 to 60 °]). Based on the results, the best fitting surface was built. With this type of multi-parameter mapping, it is then possible to determine the set of parameters optimizing E. By carrying out the same work with the vertical force $\overline{F_n}$ (Figure VI.12 (c) and (d)), it is possible to determine the thrust force necessary to reach the optimum depth of cut.

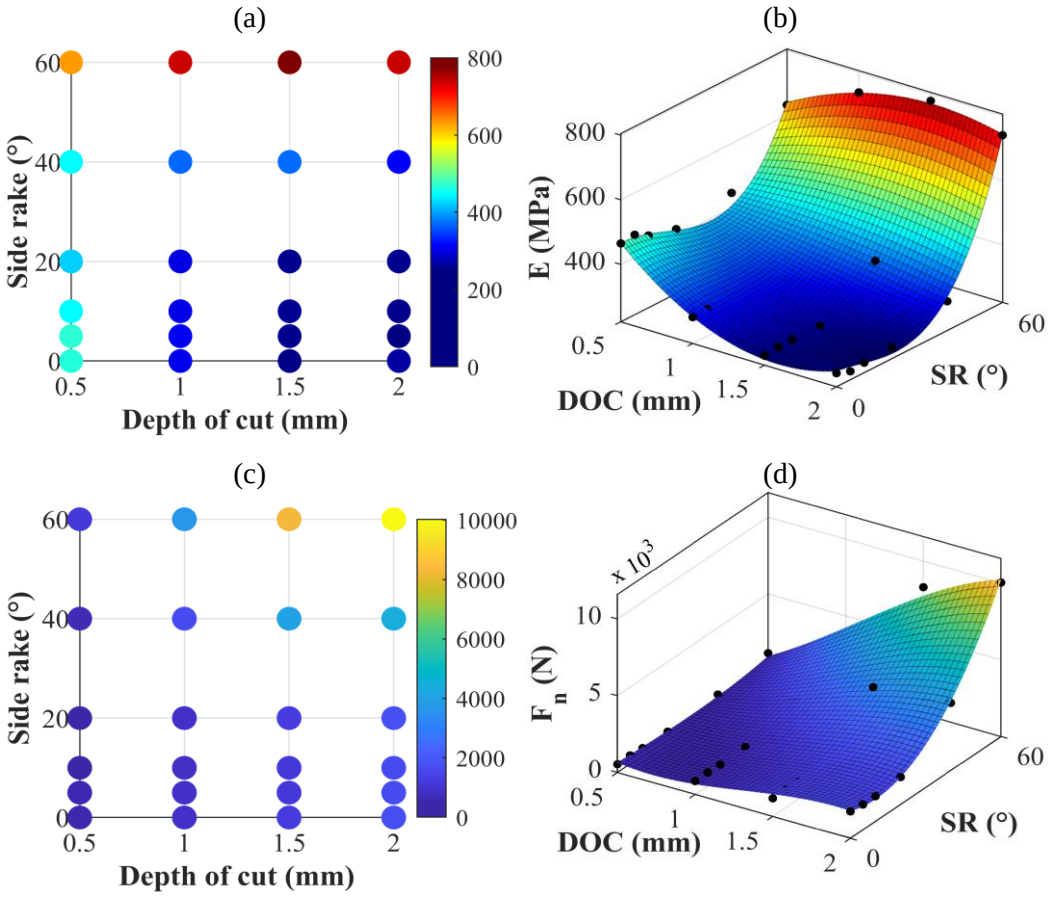

Figure VI.12. 3D mappings of E (a -b) and $\overline{F_n}$ (c-d) for a fixed confinement of 20 MPa.

Chapter VII Conclusions and outlook

1 General conclusions

While the demand for oil and gas will remain high for many years and projects, such as deep geothermal energy and geological storage of CO_2 that are expected to develop rapidly, the understanding of the rock destruction mechanisms involved in drilling operations is essential to ensure the economic and technical feasibility of these projects targeting deep reservoirs. In this context, this thesis focused on the evolution of the rock cutting mechanism in high-depth conditions, more specifically, under the effects of confinement. To address this issue, this PhD aimed to integrate the knowledge developed in the Mining Engineering Department of UMONS regarding the evolution of the mechanical behavior of rocks and their constitutive laws with confinement in the study of the cutting mechanism through numerical modeling.

The first part of this thesis presented the state of the art concerning the mechanical behavior of rocks in high-depth conditions, focusing on the effects of confinement, and the cutting mechanisms in atmospheric conditions and under confinement. This literature review highlighted the advanced state of knowledge on the impact of high-depth conditions on rock behavior, which has been studied since the end of the 19th century. By contrast, the study of the cutting mechanism is much more recent, and the current state of knowledge is hence more limited. Although this destruction mechanism has been extensively studied under atmospheric conditions, there are still weaknesses in understanding its evolution with confinement.

The literature review led to the selection of a numerical method and a reference rock. Among the different numerical methods, the Discrete Element Method had already shown encouraging results in the study of the cutting mechanism and was therefore selected to conduct the work of this study. The Vosges Sandstone was selected as a reference rock for several reasons. Firstly, the evolution of its behavior with confinement has been widely studied in the department where this thesis was conducted. It allowed access to a large amount of data to feed numerical

models. Secondly, this rock has also been widely used in experimental works studying the rock cutting mechanism.

The first step of the modeling work concerned the calibration of the numerical model. This phase is critical when implementing the Discrete Element Method. While traditional calibration methods are generally based on uniaxial or triaxial tests, a new calibration protocol has been developed. To reproduce the evolution of the Vosges Sandstone behavior (transition from brittle to ductile behavior beginning around 20 MPa of confinement), the new iterative calibration procedure simulates uniaxial and triaxial tests until a set of parameters capable of reproducing the behavior of the rock is determined. The results of this calibration method are consistent. Indeed, triaxial tests were performed up to a confinement of 70 MPa to validate the calibration. The results of these simulations were used to build the Mohr-Coulomb failure envelope of the synthetic model of the Vosges Sandstone. Comparing the numerical failure envelope with the experimental one highlighted their agreement. Indeed, the values of internal friction angle and apparent cohesion, evolving with confinement, are very close.

Following the calibration phase, a simulation protocol has been implemented to investigate the effects of the confinement, the cutting parameters, and the cutter geometry on the cutting mechanism. The objectives of this protocol were to meet the basic research objective (simulations under confinement) while ensuring that the numerical model can reproduce the evolution of cutting forces depending on the cutting parameters as observed experimentally. A comparative analysis highlighted the reliability of the numerical results compared to the experimental results published in the literature. Both qualitatively and quantitatively, the numerical model was able to reproduce the evolution of the destruction mechanism or the cutting forces depending on the different cutting parameters.

Concerning the evolution of the cutting mechanism due to confinement, the results of the 2D and 3D numerical models highlighted that the cutting mechanism is divided into three distinct regimes, whereas many authors generally consider only two of them. The prevalence of one of these regimes depends on both the depth of cut and the confinement.

At low depths of cut, the cutting mechanism is dominated by friction regardless of the confinement. During this mode of destruction, the grains composing the rock are stripped from the matrix. This phenomenon is encountered up to a critical depth, which in the case of the Vosges Sandstone model was around 1mm. However, this critical depth of cut depends on the rock studied. It is assumed that

the value of this depth depends essentially on the grain size distribution of the rock and its strength. A rock with higher strength and lower grain size distribution should have a lower critical depth of cut.

Once this depth of cut is exceeded, the mode of destruction is related to the behavior of the rock with the confinement. The regime can then be described as brittle at low confinement values and ductile from a specific higher value of confinement. The boundary between these two mechanisms corresponds to the limit confinement value at which the material begins to exhibit ductile behavior during triaxial experiments. Moreover, while the brittle mechanism is characterized by the formation of large fractures in the direction of movement of the cutter, the ductile mode is marked by the formation of microcracks between the grains of the model near the cutter.

Finally, numerical models have confirmed the occurrence of an optimal depth of cut for optimizing the Specific Energy. These models enabled us to determine the value of this cutting depth and the associated Specific Energy for each confinement tested in this work. In this context, an attempt to model the evolution of the Optimal Specific Energy based on confinement has been proposed. Based on the mechanical properties of the material, UCS and the internal friction angles of the rock evolving with the confinement, as well as the apparent friction angle between the tool and the rock, this piecewise model allowed to estimate the evolution of the Optimal Specific Energy with the confinement. The results of this analytical model were in very good agreement with the results of the numerical models. The methodology used to build this model should be tested on other rocks to be validated. This leads us to discuss the perspectives of this work in the next section.

2 Outlook

The methodology developed during this thesis and the results provide opportunities for future research topics, such as the validation of the methodology and results, the consideration of the thermo-hydro-mechanical coupling, the transposition of the results to the scale of a drill bit, and the application of the work methodology to other destruction mechanisms.

2.1 Validation of the methodology and results

The work of this thesis was essentially based on a particular rock, the Vosges Sandstone, and a comparison of numerical results with experimental results published in the literature. Therefore, a global approach is necessary to validate and universalize results and the model of the evolution of Optimal Specific Energy with confinement.

It would require a coupled experimental and numerical study on different rocks exhibiting different behavior. The experimental approach would consist of triaxial tests and cutting tests under confinement, while the numerical one would follow the same approach as this thesis. In a first step, the whole experimental and numerical approaches could be applied to the Vosges Sandstone before being transposed to different types of rocks. More specifically, we refer to rocks presenting a ductile behavior at low confinement like clays, as well as materials that can present brittle and dilatant behavior up to high confinement like limestones with low porosity.

2.2 Integration of thermo-hydro-mechanical coupling in cutting models

The work described in this thesis focused on the effects of confinement on the cutting mechanism. However, as illustrated in the state of the art, rock behavior is strongly impacted by pore pressure and temperature increase in deep drilling conditions. It would therefore be of great interest to consider these two additional parameters in the numerical study of the cutting mechanism.

Helmons et al. (2015) have already tried to consider the pore pressure in a numerical model using the Discrete Element Method. Their work, which focused on deep-sea mining, highlighted interesting qualitative results in 2D and deserves to be developed more widely in the context of the cutting mechanism in drilling.

2.3 Transposition of the results to the drill bit scale

The results of this work provide information about the evolution of cutting forces and Specific Energy with the confinement based on a single cutter simulation. They highlight the possibility of determining the vertical force to apply on the cutter to reach the optimal depth of cut, minimizing the Specific Energy.

From an industrial point of view, it is important to be able to transpose these results at the scale of the cutter into usable information for the driller. Indeed, the driller monitors the good progress of his drilling by checking the Weight on Bit and the torque based on the technical information provided by the drill bit manufacturer, who defined the optimal operating windows of his drill bit.

The development of a methodology to link the two scales appears to be of capital interest to valorize the results of this work.

2.4 Application of the work methodology to other destruction mechanisms

While this work has focused on the cutting mechanism, it would be very interesting to apply the methodology developed on other destruction mechanisms, such as the punching mechanism, for which the Mining Engineering Department of the UMONS has also developed extensive expertise based on rock indentation tests. The Discrete Element Method might allow for a better understanding of how parameters such as porosity or rock structure can influence this destruction mechanism and the forces involved.

References

Adams FD. An Experimental Contribution to the Question of the Depth of the Zone of Flow in the Earth's crust. J. Geol. 1912;20:97–118.

Akbari B, Miska S. The effects of chamfer and back rake angle on PDC cutters friction. J. Nat. Gas Sci. Eng. 2016;35:347–53.

Akbari B, Miska SZSZ. Relative Significance of Multiple Parameters on the Mechanical Specific Energy and Frictional Responses of Polycrystalline Diamond Compact Cutters. J. Energy Resour. Technol. Trans. ASME 2017;139:022904.

Amadi K, Iyalla I. Application of Mechanical Specific Energy Techniques in Reducing Drilling Cost in Deepwater Development. SPE Deep. Drill. Complet. Conf. 2012:SPE-156370-MS.

Amri M. Étude expérimentale et théorique de l ' effet de la vitesse de coupe sur la forabilité des roches sous pression de boue Mohamed Amri To cite this version : HAL Id : tel-02908810 de l ' Université de recherche Paris Sciences et Lettres É tude expérimentale. Université de Paris Sciences et Lettres, 2016.

Amri M, Pelfrene G, Gerbaud L, Sellami H, Tijani M. Experimental investigations of rate effects on drilling forces under bottomhole pressure. J. Pet. Sci. Eng. 2016;147:585–92.

Anderson TL. Fracture Mechanics: Fundamentals and Applications, Fourth Edition. vol. 76. 2017.

Appl FC, Wilson CC, Lakshman I. Measurement of forces, temperatures and wear of PDC cutters in rock cutting. Wear 1993;169:9–24.

Bahrani N, Kaiser PK, Valley B. Distinct element method simulation of an analogue for a highly interlocked, non-persistently jointed rockmass. Int. J. Rock Mech. Min. Sci. 2014;71:117–30.

Barry B, Klima MS. Characterization of marcellus shale natural gas well drill cuttings. J. Unconv. Oil Gas Resour. 2013;1–2:9–17.

Beccari M, Romano U. Encyclopaedia of Hydrocarbons: Exploration, production and transport]. ENI; 2005.

Becker GP. Finite Homogeneous Strain, Flow And Rupture Of Rocks. Bull. Geol. Soc. Am. 1892;4:13–90.

Bésuelle P, Desrues J, Raynaud S. Experimental characterisation of the localisation phenomenon inside a Vosges sandstone in a triaxial cell. Int. J. Rock Mech. Min. Sci. 2000;37:1223–37.

Bifano TG, Fawcett SC. Specific grinding energy as an in-process control variable for ductile-regime grinding. Precis. Eng. 1991;13:256–62.

Biot MA. General theory of three-dimensional consolidation. J. Appl. Phys. 1941;12:155–64.

Brady BHG, Brown ET. Rock Mechanics for underground mining. Third Edit. Dordrecht: Springer Netherlands; 2004.

Brison L, Brych J. Influence des propriétés physicomécaniques sur le processus de découpage des roches. Extr. Des Ann. Des Mines Belgique 1971.

Brown ET, Hoek E. Trends in relationships between measured in-situ stresses and depth. Int. J. Rock Mech. Min. Sci. 1978;15:211–5.

Cai M. A simple method to estimate tensile strength and Hoek-Brown strength parameter m. Rock Mech. 2009;2009:1–12.

Cai M, Kaiser PK, Morioka H, Minami M, Maejima T, Tasaka Y, et al. FLAC/PFC coupled numerical simulation of AE in large-scale underground excavations. Int. J. Rock Mech. Min. Sci. 2007;44:550–64.

Carrapatoso C, da Fontoura SAB, Inoue N, Lourenço A, Curry D. New Developments for Single-Cutter Modeling of Evaporites Using Discrete Element Method. ISRM Conf. Rock Mech. Nat. Resour. Infrastruct. - SBMR 2014, 9-13 Sept., Goinia, Brazil: International Society for Rock Mechanics; 2014.

Carrapatoso C, Lautenschläger CER, Righetto, Guilherme Lima Fontoura SA, Inoue N. Rock Cutting Analysis Employing Finite and Discrete Element Methods. J. Mech. Eng. Autom. 2016;6:100–8.

Carrapatoso C, Righetto GL, Lautenschläger CER, Fontoura SAB, Inoue N, Lourenço A, et al. Numerical modeling of single cutter tests in carbonates. 49th US Rock Mech. / Geomech. Symp. 2015 2015;3:2108–13.

Chaput EJ. Observations and analysis of hard rocks cutting failure mechanisms using PDC cutters. Imperial College, London, 1991.

Charalampidou E-M. Experimental study of localised deformation in porous sandstones. Heriot Watt University Institute, 2011.

Che D, Zhu W Le, Ehmann KF. Chipping and crushing mechanisms in orthogonal rock cutting. Int. J. Mech. Sci. 2016;119:224–36.

Cheatham JB, Daniels WH. A study of factors influencing the drillability of shales: Single—cutter experiments with STRATAPAX drill blanks. J. Energy Resour. Technol. Trans. ASME 1979;101:189–95.

Chen X, Yang J, Gao D. Drilling Performance Optimization Based on Mechanical Specific Energy Technologies. Drilling 2018.

Cheng Z, Sheng M, Li G, Huang Z, Wu X, Zhu Z, et al. Imaging the formation process of cuttings: Characteristics of cuttings and mechanical specific energy in single PDC cutter tests. J. Pet. Sci. Eng. 2018;171:854–62.

Coudyzer C, Richard T. Influence of the back and side rake angles in rock cutting. AADE Natl. Tech. Conf. Exhib. 2005:1–12.

Couture CB, Bésuelle P. Diffuse and localized deformation of a porous vosges sandstone in true triaxial conditions. E3S Web Conf. 2019;92:1–5.

Cundall PA. A computer model for simulating progressive, large-scale movements in blocky rock systems. Proc. Symp. Int. Rock Mech., vol. 2, Nancy: 1971.

Cundall PA, Strack ODL. A discrete numerical model for granular assemblies. Géotechnique 1979;29:47–65.

Dagrain F. Etude des mécanismes de coupe des roches avec couteaux usés - Approche des mécanismes de frottement sous les couteaux par le concept du troisième corps. Faculté Polytechnique de Monos, 2006.

Dagrain F. Influence of the cutter geometry in rock cutting: an experimental approach. University Of Minnesota, 2001.

Dagrain F, Detournay E, Richard T. Influence of Cutter Geometry In Rock Cutting. DC Rocks 2001, 38th U.S. Symp. Rock Mech., Washington, D.C.: American Rock Mechanics Association; 2001, p. 8.

Dagrain F, Richard T. On the influence of PDC wear and rock type on cutting efficiency. 2006a.

Dagrain F, Richard T. On the influence of PDC wear and rock type on friction coefficient and cutting efficiency. Eurock 2006 Multiphysics Coupling Long Term Behav. Rock Mech., Taylor & Francis; 2006b, p. 577–84.

Descamps F. Etude du comportement des roches poreuses saturées des roches poreuses saturées aux conditions de grande profondeur. Faculté Polytecnique de Mons, 2007.

Descamps F, Tshibangu J-P. Development of an automated triaxial system for thermo-hydromechanical testing of rocks. 42nd U.S. Rock Mech. - 2nd U.S.-Canada Rock Mech. Symp., San Francisco, USA: 2008.

Detournay E, Atkinson C. Influence of pore pressure on the drilling response in low-permeability shear-dilatant rocks. Int. J. Rock Mech. Min. Sci. 2000;37:1091–101.

Detournay E, Defourny P. A phenomenological model for the drilling action of drag bits. Int. J. Rock Mech. Min. Sci. 1992;29:13–23.

Detournay E, Tan C. Dependence of Drilling Specific Energy on Bottom-Hole Pressure in Shales. Proc. SPE/ISRM Rock Mech. Pet. Eng. Conf., 2002, p. 526–35.

Doshvarpassand S, Richard T, Mostofi M. Effect of groove geometry and cutting edge in rock cutting. J. Pet. Sci. Eng. 2017;151:1–12.

Downton G, Hendriks A, Klausen T, Pafitis D. New directions in rotary steerable drilling. Oilf. Rev. 2000;12:18–29.

Dupriest F, Koederitz W. Maximizing Drill Rates with Real-Time Surveillance of Mechanical Specific Energy. Proc. SPE/IADC Drill. Conf., Society of Petroleum Engineers; 2005.

Fertl WH. Abnormal formtion pressures - Implications to exploration, drilling and production of oil and gas resources. Elsevier; 1976.

Fontoura SAB, Inoue N, Martinez IMR, Cogollo C, Curry DA. Rock mechanics aspects of drill bit rock interaction. Harmon. Rock Eng. Environ. - Proc. 12th ISRM Int. Congr. Rock Mech. 2012:2041–6.

Gerbaud L. Optimisation de l'interaction PDC-roche application à la conception d'outils pour forage pétrolier en petit diamètre. Ecole Nationale Supérieure de Paris, 1999.

Gerbaud L, Menand S, Sellami H. PDC Bits: All Comes From the Cutter/Rock Interaction. IADC/SPE Drill. Conf., Society of Petroleum Engineers; 2006.

Glowka DA. Use of single-cutter data in the analysis of PDC bit designs: part 1-development of a PDC cutting force model. J. Pet. Technol. 1989;41:797–849.

Gu B, Wan Z, Zhang Y, Ma Y, Xu XB. Influence of Real-Time Heating on Mechanical Behaviours of Rocks. Adv. Civ. Eng. 2020;2020.

Hammoutene C, Bits S. FEA Modelled MSE/UCS Values Optimise PDC Design for Entire Hole Section. North Africa Tech. Conf. Exhib. 2012:SPE-149372-MS.

He X, Xu C. Specific energy as an index to identify the critical failure mode transition depth in rock cutting. Rock Mech. Rock Eng. 2016;49:1461–78.

He X, Xu C, Peng K, Huang G. On the critical failure mode transition depth for rock cutting with different back rake angles. Tunn. Undergr. Sp. Technol. 2017;63:95–105.

Helmons RLJ. Excavation of hard deposits and rocks on the cutting of saturated rock. 2017.

Helmons RLJJ, Miedema SA, Van Rhee C. Inclusion of pore pressure effects in discrete element modeling of rock cutting. 4th Int. Conf. Part. Methods - Fundam. Appl. Part. 2015, 2015, p. 945–56.

Houpert R, Homand-Etienne F. Comportement mécanique des roches en fonction de la température. Rev. Française Géotechnique 1984:41–7.

Huang H, Detournay E, Bellier B. Discrete element modelling of rock cutting 1999.

Ingraffea AR. Theory of Crack Initiation and Propagation in Rock. ACADEMIC PRESS LIMITED; 1987.

Itasca Consulting Group. Particle flow code in 2 dimensions manual, version 4.0. Minneapolis: 2008a.

Itasca Consulting Group. PFC3D – Particle Flow Code in 3 Dimensions, Ver. 4.0 User's Manual 2008b.

Jaeger JC, Cook NGW, Zimmerman R. Fundamentals of Rock Mechanics. 4th Editio. Malden: Blackwell, MA; 2007.

Jaime M. Numerical modeling of rock cutting and its associated fragmentation process using the finite element method. University of Pittsburgh, 2011.

Jiang M, Chen H, Crosta GB. Numerical modeling of rock mechanical behavior and fracture propagation by a new bond contact model. Int. J. Rock Mech. Min. Sci. 2015;78:175–89.

Joodi B, Sarmadivaleh M, Rasouli V, Nabipour A. Simulation of the cutting action of a single PDC cutter using DEM. WIT Trans. Eng. Sci. 2012;81:143–50.

Judzis A, Bland RG, Curry DA, Black AD, Robertson HA, Meiners MJ, et al. Optimization of deep-drilling performance - Benchmark testing drives ROP improvements for bits and drilling fluids. SPE Drill. Complet. 2009;24:25–39.

Kadyrov R, Nurgaliev D, Saenger EH, Balcewicz M, Minebaev R, Statsenko E, et al. Digital rock physics: Defining the reservoir properties on drill cuttings. J. Pet. Sci. Eng. 2022;210:110063.

Kaitkay P, Lei S. Experimental study of rock cutting under external hydrostatic pressure. J. Mater. Process. Technol. 2005;159:206–13.

Karato S -i, Wong T -f. Rock deformation: Ductile and brittle. Rev. Geophys. 1995;33:451–7.

Kuru E, Wojtanowicz AK. An experimental study of sliding friction between PDC drill cutters and rocks. Int. J. Rock Mech. Min. Sci. 1995;32:277–83.

Ledgerwood III L. PFC modeling of rock cutting under high pressure conditions. Rock Mech. Meet. Soc. Challenges Demands, Taylor & Francis; 2007, p. 511–8.

Lei S, Kaitkay P. Distinct element modeling of rock cutting under hydrostatic pressure. Key Eng. Mater. 2003;250:110–7.

Lei S, Kaitkay P, Shen X. Simulation of rock cutting using distinct element method - PFC2D. Numer. Model. Micromechanics via Part. Methods - 2004, CRC Press; 2004, p. 63–71.

Leine RI, Van Campen DH. Stick-slip whirl interaction in drillstring dynamics. Solid Mech. Its Appl. 2005;122:287–96.

Lin JS, Mendoza JA, Jaime MC, Zhou Y, Brown J, Gamwo IK, et al. Numerical modeling of rock cutting. Harmon. Rock Eng. Environ. - Proc. 12th ISRM Int. Congr. Rock Mech. 2012:461–6.

Lion M. Influence de la température sur le comportement poromécanique ou hydraulique d'une roche carbonatée et d'un mortier. Etudes expérimentales. Université des Sciences et Technologie de Lille - Lille 1, 2008.

Liu J, Zheng H, Kuang Y, Xie H, Qin C. 3D numerical simulation of rock cutting of an innovative non-planar face PDC cutter and experimental verification. Appl. Sci. 2019;9.

Liu W, Zhu X. Experimental study of the force response and chip formation in rock cutting. Arab. J. Geosci. 2019;12.

Liu W, Zhu X, Jing J. The analysis of ductile-brittle failure mode transition in rock cutting. J. Pet. Sci. Eng. 2018;163:311–9.

Ma T, Chen P, Zhao J. Overview on vertical and directional drilling technologies for the exploration and exploitation of deep petroleum resources. Geomech. Geophys. Geo-Energy Geo-Resources 2016;2:365–95.

Majidi R, Miska SZ, Tammineni S. PDC single cutter: the effects of depth of cut and rpm under simulated borehole conditions. Wiert Naft. Gaz 28 2011;28:283–95.

Mazen AZ, Rahmanian N, Mujtaba IM, Hassanpour A. Effective mechanical specific energy: A new approach for evaluating PDC bit performance and cutters wear. J. Pet. Sci. Eng. 2021;196:108030.

Menand S. Analyse et validation d'un modèle de comportement directionnel des outils de forage monoblocs PDC. Ecole Nationale Supérieure des Mines de Paris, 2001.

Menezes PL. Influence of cutter velocity, friction coefficient and rake angle on the formation of discontinuous rock fragments during rock cutting process. Int. J. Adv. Manuf. Technol. 2017;90:3811–27.

Merchant ME. Mechanics of the metal cutting process. I. Orthogonal cutting and a type 2 chip. J. Appl. Phys. 1945;16:267–75.

Mohammadnejad M, Liu H, Dehkhoda S, Chan A. Numerical Investigation of Dynamic Rock Fragmentation in Mechanical Cutting Using Combined FEM/DEM. ISRM 3rd Nord. Rock Mech. Symp. - NRMS 2017, Helsinki, Finland: Johansson & Raasakka; 2017, p. 9.

Moseley SG, Bohn KP, Goedickemeier M. Core drilling in reinforced concrete using polycrystalline diamond (PCD) cutters: Wear and fracture mechanisms. Int. J. Refract. Met. Hard Mater. 2009;27:394–402.

Najjarpour M, Jalalifar H, Norouzi-Apourvari S. Fifty years of experience in rate of penetration management: Managed pressure drilling technology, mechanical specific energy concept, bit management approach and expert systems - A review. J. Pet. Sci. Eng. 2022;208:109184.

Nicodème P. Transition between ductile and brittle mode in rock cutting. Rapport de stage d'option scientifique. Paris: 1997.

Nishimatsu Y. The mechanics of rock cutting. Int. J. Rock Mech. Min. Sci. Geomech. Abstr. 1972;9:261–70.

Nygård R, Gutierrez M, Bratli RK, Høeg K. Brittle-ductile transition, shear failure and leakage in shales and mudrocks. Mar. Pet. Geol. 2006;23:201–12.

Obradors-Prats J, Rouainia M, Aplin AC, Crook AJL. Hydromechanical Modeling of Stress, Pore Pressure, and Porosity Evolution in Fold-and-Thrust Belt Systems. J. Geophys. Res. Solid Earth 2017;122:9383–403.

Omland TH, Saasen A, Taugbøl K, Dahl B, Jørgensen T, Reinholt F, et al. Improved drilling-process control through continuous particle and cuttings monitoring. Soc. Pet. Eng. - Digit. Energy Conf. Exhib. 2007 2007:250–6.

Onate E, Rojek J. Combination of discrete element and finite element methods for dynamic analysis of geomechanics problems. Comput. Methods Appl. Mech. Eng. 2004;193:3087–128.

Paterson MS, Wong T-F. Experimental Rock Deformation — The Brittle Field. Berlin/Heidelberg: Springer; 2005.

Pelfrene G. Rôle du processus de forabilité des roches dans les vibrations de torsion des systèmes de forage pétrolier To cite this version : l ' École Nationale Supérieure des Mines de Paris dans les vibrations de torsion. Ecole des Mines de Paris, 2010.

Pelfrene G, Sellami H, Gerbaud L. Mitigating stick-slip in deep drilling based on optimization of PDC bit design. SPE/IADC Drill. Conf. Proc., vol. 1, 2011, p. 332–43.

Pessier RC, Fear MJ. Quantifying common drilling problems with mechanical specific energy and a bit-specific coefficient of sliding friction. Proc. - SPE Annu. Tech. Conf. Exhib. 1992;Delta:373–88.

Potyondy DO, Cundall PA. A bonded-particle model for rock. Int. J. Rock Mech. Min. Sci. 2004;41:1329–64.

Qi C, Wang M, Qian Q. Strain-rate effects on the strength and fragmentation size of rocks. Int. J. Impact Eng. 2009;36:1355–64.

Rafatian N, Miska S, Ledgerwood LW, Ahmed R, Yu M, Takach N. Experimental study of MSE of a single PDC cutter under simulated pressurized conditions. SPE/IADC Drill. Conf. Proc. 2009;1:330–41.

Rajabov V, Miska S, Mortimer L, Yu M, Ozbayoglu E. The effects of back rake and side rake angles on mechanical specific energy of single PDC cutters with selected rocks at varying depth of cuts and confining pressures. SPE/IADC Drill. Conf. Proc. 2012;2:910–26.

Reyes Martinez I, Fontoura S, Inoue N, Carrapatoso C, Lourenco A, Curry D. Simulation of Single Cutter Experiments in Evaporites Through Finite Element Method. SPE/IADC Drill. Conf., Amsterdam, The Netherlands: Society of Petroleum Engineers; 2013.

Reyes R, Kyzym I, Rana PS, Molgaard J, Butt SD. Cuttings analysis for rotary drilling penetration mechanisms and performance evaluation. 49th US Rock Mech. / Geomech. Symp. 2015 2015;2:1498–505.

Richard T. Determination of Rock Strength from Cutting Tests. University of Minnesota, Minnesota, 1999a.

Richard T. Determination of strength from cutting tests. University of Minnesota, 1999b.

Richard T, Dagrain F, Poyol E, Detournay E. Rock strength determination from scratch tests. Eng. Geol. 2012;147–148:91–100.

Richard T, Detournay E, Drescher A, Nicodeme P, Fourmaintraux D. Scratch test as a means to measure strength of sedimentary rocks. Proc. SPE/ISRM Rock Mech. Pet. Eng. Conf., vol. 2, 1998, p. 15–22.

Rizo JAM. Considerations for discrete element modeling of rock cutting. University of Pittsburgh, 2013.

Rostamsowlat I, Akbari B, Evans B. Analysis of rock cutting process with a blunt PDC cutter under different wear flat inclination angles. J. Pet. Sci. Eng. 2018a;171:771–83.

Rostamsowlat I, Richard T, Evans B. An experimental study of the effect of back rake angle in rock cutting. Int. J. Rock Mech. Min. Sci. 2018b;107:224–32.

Saiang C, Miskovsky K. Effect of heat on the mechanical properties of selected rock types - A laboratory study. Harmon. Rock Eng. Environ. - Proc. 12th ISRM Int. Congr. Rock Mech. 2012:815–20.

Santos IM, Hamacher S, Oliveira F. A Systematic Literature review for the rig scheduling problem: Classification and state-of-the-art. Comput. Chem. Eng. 2021;153:107443.

Sari M. A simple approximation to estimate the hoek-brown parameter "mi" for intact rocks. Rock Mech. Civ. Environ. Eng. - Proc. Eur. Rock Mech. Symp. EUROCK 2010 2010:169–72.

Scott BD, Hughes B. A bit of history : Overcoming early setbacks , PDC bits now drill 90 % -plus of worldwide footage Decades after invention of polycrystalline diamond cutters , PDC bits edge out roller cones with advances in cutters , stability , hydraulics. Innov. While Drill. 2015.

Sellami H. Etude de la fragmentation des roches par les PDC en milieu confiné - Etude du travail d'un outil stratapax en forage pétrolier profond. 1990.

Sellami H, Cordelier P. Calcul d'un outil PDC en forage pétrolier profond - Logiciel de simulation Drilsim 3D. 1991.

Sellami H, Fairhurst C, Deliac E, Delbast B. Role of in-situ rock stresses and mud-pressure on the penetration rate of PDC bits. Int. J. Rock Mech. Min. Sci. Geomech. Abstr. 1990;27:360.

Sinor LA, Powers JR, Warren TM. Effect of PDC cutter density, back rake, size, and speed on performance. Proc. IADC/SPE Asia Pacific Drill. Technol. Conf. APDT 1998:131–9.

Teale R. The Concept of Specific Energy in Rock Drilling. Int. J. Rock Mech. Min. Sci. 1965;2:57–73.

Terzaghi K. Theoretical Soil Mechanics. Hoboken, NJ, USA: John Wiley & Sons, Inc.; 1943.

Tshibangu K. Etude des effets du confinement sur le comportement mécanique des roches pour application au calcul des ouvrages souterrains. Faculté Polytechnique de Mons, 1993.

Tulu IB. Modeling PDC Cutter Rock Interaction Ihsan Berk Tulu Thesis Submitted to the College of Engineering and Mineral Resources at West Virginia University in partial fulfillment of the requirements for the degree of Master of Science in Mining Engineering Mini. West Virginia, 2009.

Tulu IB, Heasley KA, Bilgesu I, Sunal O. Modeling rock and drill cutter behavior. 42nd U.S. Rock Mech. - 2nd U.S.-Canada Rock Mech. Symp. 2008.

Wang H, Wu T, Fu X, Liu B, Wang S, Jia R, et al. Quantitative determination of the brittle–ductile transition characteristics of caprocks and its geological significance in the Kuqa depression, Tarim Basin, western China. J. Pet. Sci. Eng. 2019;173:492–500.

Wei S, Yang Y, Su C, Cardosh SR, Wang H. Experimental study of the effect of high temperature on the mechanical properties of coarse sandstone. Appl. Sci. 2019;9.

Winterwerp JC, van Kesteren WGM. Introduction to the Physics of Cohesive Sediment in the Marine Environment. vol. 1. Elsevier; 2004.

Wojtanowicz AK, Kuru E. Mathematical modeling of pdc bit drilling process based on a single-Cutter mechanics. J. Energy Resour. Technol. Trans. ASME 1993;115:247–56.

Wong TF. Effects of temperature and pressure on failure and post-failure behavior of Westerly granite. Mech. Mater. 1982;1:3–17.

Yahiaoui M, Paris J-Y, Delbé K, Denape J, Gerbaud L, Dourfaye A. Independent analyses of cutting and friction forces applied on a single polycrystalline diamond compact cutter. Int. J. Rock Mech. Min. Sci. 2016;85:20–6.

Yari N, Kapitaniak M, Vaziri V, Ma L, Wiercigroch M. Calibrated FEM modelling of rock cutting with PDC cutter. MATEC Web Conf. 2018;148:1–4.

Yu B. Numerical Simulation of Continuous Miner Rock Cutting Process Numerical Simulation of Continuous Miner Rock Cutting Process. West Virginia, 2005.

Yu W, Wu G, An B, Wang P. Experimental Study on the Brittle-Ductile Response of a Heterogeneous Soft Coal Rock Mass under Multifactor Coupling. Geofluids 2019;2019.

Zhou Y. Numerical Modeling Of Rock Drilling With Finite Elements. University of Pittsburgh, 2013.

Zhou Y, Lin JS. Modeling the ductile-brittle failure mode transition in rock cutting. Eng. Fract. Mech. 2014;127:135–47.

Appendices

Appendix A: database of numerical studies dealing with rock cutting

Numerical Method	Code	Constitutive model	Rock	Type of crack initiation and fragmentation	Reference
DEM (2D)	PFC2D	Linear contact model with parallel and contact bonds	Carthage marble	Particles are scratched	(Akbari et al., 2011)
DEM (2D)	PFC2D	Linear contact model with parallel bonds	Sandstone, homogeneous	Crack is formed. Chip is separated	(Block and Jin, 2009)
FEM (3D) + DEM (3D)	ABAQUS + PFC 3D	Drucker-Prager yield criteria / Linear contact model with parallel and contact bonds	Carbonates	Not mentioned	(Carrapatoso et al., 2016)
BEM (2D)	In-house code	Maximum tensile strength criterion	Generic, anisotropic, homogeneous	Predefined crack with incremental crack extension with piece-wise linear discretization. No fragmentation	(Chen et al., 1998)
FDM (2D)	FLAC	Elasto-plastic Mohr-Coulomb model with stiffness degradation	Generic. Heterogeneity included throughout the elements	Crack formed by smeared elements. No chip separation	(Fang and Harrison, 2002)
FDM (2D)		Mohr-Coulomb model	Granite, sandstone	No chip formation	(Fang and Harrison, 2002)
FEM (2D)		Mohr-Coulomb model		No chip formation	(Finzi et al., 2004)
FEM (2D/3D)	ABAQUS	Drucker-Prager yield criteria	Carthage Limestone	Erosion model, chip formed	(Fontoura et al., 2012)

Numerical Method	Code	Constitutive model	Rock	Type of crack initiation and fragmentation	Reference
DEM (2D)	PFC2D	Linear contact model with parallel and contact bonds with clumps and clusters	Generic rocks	A crack is formed. Chip is separated	(He & Xu, 2015)
DEM - SP(2D)	Own software	Linear contact and bond model	Carthage marble	A crack is formed. Chip is separated	(Helmons, 2017)
DEM (2D)	PFC2D	Linear contact model with contact bonds	Sandstone, homogeneous	A crack is formed. Chip is separated	(Huang and Detournay, 2008)
FDM (2D)	FLAC	Elastic perfectly plastic model with a Mohr-Coulomb yield condition and plastic potential	Generic, homogeneous	No explicit fracture. Small deformation	(Huang et al., 1998)
DEM (2D)	PFC2D	Linear contact model with parallel and contact bonds	Generics rocks: one with brittle behavior and the other with ductile behavior	A crack is formed. Chip is separated	(Huang et al., 2013)
FEM (3D)	LS-DYNA	Tensile and shear failure criterium	Sandstone	Erosion model	(Huang et al., 2016)
FDM (2D)	FLAC	Elastic Mohr-Coulomb model	Limestone, homogeneous	No explicit fracture. Small deformation	(Innaurato et al., 2007)

Numerical Method	Code	Constitutive model	Rock	Type of crack initiation and fragmentation	Reference
FEM (3D)	LS-DYNA	Concrete Damage model and the Continuous Surface Cap model	Vosges Sandstone	Erosion model, chip formed	(Jaime et al., 2010)
FEM (3D)	LS-DYNA	Concrete Damage model, Johnson Holmquist Concrete model and the Continuous Surface Cap model	Vosges Sandstone	Erosion model, chip formed	(Jaime et al., 2015)
FEM (2D)	ALGOR	Elastic-perfectly plastic model with Drucker-Prager plasticity in tension	Generic, homogeneous	Crack predefined and propagated by remeshing. No chip separation	(Jonak, 2001)
DEM (2D)	PFC2D	Linear contact model with parallel and contact bonds	Barea Sandstone	Particles are scratched	(Joodi et al., 2012)
FEM (2D)	RFPA	Mohr-Coulomb criterion	Gabbro, heterogeneity included throughout elements	No chip formation	(Kou et al., 1999)
FEM (2D)	RFPA	Mohr-Coulomb criterion with a pressure-dependent yield condition		Chip formed, no chip separation	(Kou et al., 2001)

Numerical Method	Code	Constitutive model	Rock	Type of crack initiation and fragmentation	Reference
FEM (2D)	RFPA		Gabbro, granite, marble and sandstone	Chip formed, no chip separation	(Kou et al., 2004)
DEM (2D)	PFC2D	Linear contact model with parallel and contact bonds	Generic rock	A crack is formed. Chip is separated	(Ledgerwood, 2007)
DEM (2D)	PFC2D	Linear contact model with parallel and contact bonds	Carthage marble	Particles are scratched	(Lei & Kaitkay, 2003)
DEM	PFC	Parallel bond model	Marble, homogeneous	Crack is formed. Chip is separated	(Lei et al., 2004)
DEM (2D)	PFC2D	Linear contact model with parallel and contact bonds with clumps and clusters	Granite	Cracks propagation	(Li et al., 2016)
DEM (3D)	PFC3D	FEM visco-elastic-plastic damage model / DEM Linear contact model with parallel and contact bonds	Lunar rock	Particles are scratched	(Li et al., 2017)
DEM (2D)	PFC2D	Linear contact model with parallel and contact bonds	Four generic sandstones	Crack is formed. Chip is separated	(Li et al., 2017)
FEM (3D)	ABAQUS	Drucker-Prager yield criteria	Clay	Erosion model, chip formed	(Li et al., 2018)

Numerical Method	Code	Constitutive model	Rock	Type of crack initiation and fragmentation	Reference
FEM (2D & 3D) + DEM (2D & 3D)	LS-DYNA + PFC2D & PFC3D	FEM visco-elastic-plastic damage model / DEM Linear contact model with parallel and contact bonds	Vosges Sandstone	Crack is formed. Chip is separated	(Lin et al., 2012)
FEM (2D)	R-T	Double elliptic strength criterion with elastic damage	Granite, marble and sandstone. Heterogeneity included throughout elements	Crack formed by smeared elements. No chip separation	(Liu, 2004)
FEM (2D)	R-T	Elastic-brittle model	Generic. Heterogeneity included throughout elements	Crack formed by smeared elements. No chip separation	(Liu et al., 2002)
FEM (2D)	R-T	Double elliptic strength criterion with elastic damage	Sandstone, marble, granite. Heterogeneity included throughout elements	Crack is formed by smeared elements. No chip separation	(Liu et al., 2008)
DEM (2D)	PFC2D	Linear contact model with parallel and contact bonds	Red sandstone	Crack is formed. Chip is separated	(Liu et al., 2018)

Numerical Method	Code	Constitutive model	Rock	Type of crack initiation and fragmentation	Reference
FEM (3D)	ABAQUS	Drucker-Prager yield criteria	Wusheng sandstone and Beibei limestone	No chip formation	(Liu et al., 2019)
FEM (2D/3D)	ABAQUS	Drucker-Prager yield criteria	Halite	Chip formed	(Martinez et al., 2013)
FDM (2D)	FLAC	Strain-Softening Mohr-Coulomb Constitutive Model	Generic, homogeneous	No explicit fracture. Small deformation	(McKinnon and Garrido 1998)
DEM (2D)	PFC2D	Linear contact model with parallel bonds and implementation of particle crushing	Sandstone, homogeneous	Crack is formed. Chip is separated	(Mendoza, 2010)
FEM (2D)	LS-DYNA	Elasto-visco-plastic model with continuum damage mechanics	Sandstone	Erosion model, chip formed	(Menezes, 2016)
DEM (2D)	PFC2D	Linear contact model with parallel and contact bonds	Idaho basalt	Crack is formed. Chip is separated	(Moon & Oh, 2012)
DEM (3D)	PFC3D	Linear contact model with parallel and contact bonds	Sandstones and limestone	Crack is formed. Particles are scratched	(Okan & Akcin, 2011)
DEM with FEM (2D)	In-house code	Elastic plastic with elastic damage (for FEM part)	Sandstone, homogeneous	Crack is formed. Chip is separated (DEM part)	(Oñate and Rojek, 2004)
DEM (2D)	In-house code	Elastic perfectly brittle contact model	Sandstone, homogeneous	Crack is formed. Chip is separated	(Rojek, 2007)

Numerical Method	Code	Constitutive model	Rock	Type of crack initiation and fragmentation	Reference
DEM (3D)	PFC3D	Linear contact model with parallel and contact bonds	Sandstone, homogeneous	No clear crack formed. Small chips separated, but mostly particles dispersed in space	(Rojek et al., 2011)
FEM (2D/3D)	In-house code	Quasi-brittle material model	Limestone, homogeneous	Fragmentation has been modeled analytically. There is no evidence of cracks or chip separation	(Rouabhi et al., 2005)
FEM (2D)	ANSYS	-	-	Fracture propagation	(Samui et al., 2016)
FDM and DEM (2D)	FLAC and PFC	Mohr-Coulomb plasticity model (for FDM part)	Marble, homogeneous	No explicit fracture. Large deformation	(Stavropoulou, 2006)
DEM (3D)	PFC3D	Linear contact model with parallel and contact bonds	Sandstone and Limestone, heterogeneous	No explicit fracture. Particles dispersed in space	(Su and Akcin, 2011)
FEM (2D)		Splitting fracture model/Bohus Ekeberg	Granite marble	No chip formation	(Tan et al., 1997)
DDM of BEM (2D)		Cavity model	Granite and limestone	Chip formed, no chip separation	(Tan et al., 1998)
DEM (2D)	PFC2D	Linear contact model with parallel and contact bonds	Polycrystalline SiC	Crack is formed. Particles are scratched	(Tan et al., 2009)
FEM (2D)	RFPA	Elastic-brittle model	Generic. Heterogeneity included throughout elements	No explicit fracture	(Tang, 1997)

Numerical Method	Code	Constitutive model	Rock	Type of crack initiation and fragmentation	Reference
FEM (2D)	RFPA	Coulomb with tensile strength criterion	Sandstone. Heterogeneity included throughout elements	Crack formed by smeared elements. No chip separation	(Tang et al., 1998)
FEM (2D)	RFPA	Mohr-Coulomb model	Generic. Heterogeneity included throughout elements	Crack formed by smeared elements. No chip separation	(Tang et al., 1998)
FEM (2D)	RFPA	Coulomb criterion	Heterogeneity included	No chip formation	(Tang et al., 2000)
FEM (2D)	RFPA	Mohr-Coulomb criterion with a pressure-dependent yield condition		Chip formed, no chip separation	(Tang et al. 2001)
DEM (3D)	PFC3D	Not mentioned	Carthage marble	Ribbon	(Tropin et al. 2015)
FDM (3D)	FLAC	Strain-Softening Mohr-Coulomb plasticity Model	Shale and Sandstone, homogeneous	Elements are “nulled” upon reaching failure. No crack initiated or fragmentation reported	(Tulu 2009; Tulu et al. 2008)
FEM (2D)	LS-DYNA	Elastic plastic damage – Johnson-Holmquist concrete model	Granite, homogeneous	No explicite fracture. Small deformation	(Tuomas 2004)
DEM (3D)	PFC3D	Linear contact model with parallel and contact bonds	Pearl granite and sandstone	Not studied	(van Wyk et al., 2014)

Numerical Method	Code	Constitutive model	Rock	Type of crack initiation and fragmentation	Reference
FEM (2D)	RFPA	Linear elastic damage based on tensile strain or Mohr-Coulomb criteria	Generic. Heterogeneity included throughout elements	Cracks are formed by smeared elements. No chip separation	(Wang et al., 2011)
FEM (3D)	-	-	Baiyun Granite	Erosion model, chip formed	(Xia et al., 2017)
DEM (2D)	PFC2D	Linear contact model with parallel and contact bonds	Generic rocks	Crack is formed. Chip is separated	(Xuefeng et al., 2018)
DEM (2D)	PFC2D	Linear contact model with parallel and contact bonds	Soda-lime glass	Crack is formed. Chip is separated	(Yang et al., 2018)
DEM (2D)	PFC2D	Linear contact model with parallel and contact bonds	Generic rocks	Crack is formed. Chip is separated	(Yanxin et al., 2017)
FEM (2D)	ABAQUS	Drucker-Prager yield criteria	Sandstone	Erosion model, chip formed	(Yari et al., 2017)
FEM (3D)	LS-DYNA	Elastic plastic model. Erosion of elements upon tensile or shear stress threshold	Generic, homogeneous	No explicit fragmentation	(Yu, 2005)
FEM (3D)	LS-DYNA	Concrete Damage model and the Continuous Surface Cap model	-	Erosion model, chip formed	(Zhou and lin, 2013)

Numerical Method	Code	Constitutive model	Rock	Type of crack initiation and fragmentation	Reference
FEM (2D)	RFPA	Elastic damage	Sandstone. Heterogeneity included throughout elements	Crack formed by smeared elements. No chip separation	(Zhu and Tang, 2004)
FEM (3D)	ABAQUS	Drucker-Prager yield criteria	Clay	No explicite fracture. Small deformation	(Zhu et Jia, 2014)

Appendix B: calibration procedure

B.1 Calibration steps in 2D

Calibration step	Parameters								
	E_c	k_n/k_s	μ	$\bar{E}_c$	$\bar{k}_n/\bar{k}_s$	$\bar{\sigma}_n$	$\Delta\bar{\sigma}_n$	$\bar{\sigma}_s$	$\Delta\bar{\sigma}_s$
	(GPa)	(FLT)	(FLT)	(GPa)	(FLT)	(MPa)	(MPa)	(MPa)	(MPa)
Calib 1	10	3	0.3	10	3	50	5	50	5
Calib 2	9	3	0.3	9	3	50	5	50	5
Calib 3	9	3	0.7	9	3	50	5	50	5
Calib 4	8	3	1	8	3	50	5	50	5
Calib 5	8	3	1	8	3	50	15	50	15
Calib 6	7	3	1	7	3	50	25	50	25
Calib 7	7	3	1	7	3	50	25	50	25
Calib 8	7	3	1	7	3	70	55	70	55
Calib 9	7	3	10	7	3	70	35	70	35
Calib 10	7	3	20	7	3	60	35	60	35
Calib 11	6	3	20	6	3	60	35	60	35
Calib 12	6.5	3	20	6.5	3	50	35	50	35

B.2 Calibration steps in 3D

Calibration step	Parameters									UCS		$\sigma_3 = 20\ MPa$	
	E_c	k_n/k_s	μ	$\bar{E}_c$	$\bar{k}_n/\bar{k}_s$	$\bar{\sigma}_n$	$\Delta\bar{\sigma}_n$	$\bar{\sigma}_s$	$\Delta\bar{\sigma}_s$	σ_1	E	σ_1	E
	(GPa)	(FLT)	(FLT)	(GPa)	(FLT)	(MPa)	(MPa)	(MPa)	(MPa)	(MPa)	(GPa)	(MPa)	(GPa)
Calib 1	12.5	4	0.8	13	4	76	25	76	25	91.91	11.75		
Calib 2	11	4	0.8	11	4	65	25	65	25	79.16	10.27		
Calib 3	10	4	0.8	10	4	55	25	55	25	64.55	9.25		
Calib 4	10.5	4	0.8	11	4	60	25	60	25	71.17	9.77	139.34	11.51
Calib 5	10.5	8	1	11	4	60	25	60	25	68.38	8.98	132.47	10.17
Calib 6	10.5	0.2	1	11	4	60	25	60	25	77.80	12.77	158.98	18.39
Calib 7	30	4	1	11	4	60	25	60	25	77.16	17.43	156.62	23.15
Calib 8	4	8	0.8	4	0	60	25	60	25	37.63	9.14		
Calib 9	4	8	1	11	4	60	25	60	25	60.27	6.28		
Calib 10	4	8	1	16	4	70	25	70	25	69.38	8.51		
Calib 11	8	8	1	16	4	70	25	70	25	75.39	10.29	129.12	11.03
Calib 12	1	8	1	16	4	70	25	70	25	56.00	6.93	94.17	6.55
Calib 13	4	8	1	20	4	70	25	70	25	66.74	10.09		
Calib 14	4	4	1	20	4	70	25	70	25	70.35	10.43		
Calib 15	4	12	1	20	4	70	25	70	25	62.62	9.80		
Calib 16	4	1	1	20	4	70	25	70	25	79.03	11.42	135.21	12.55
Calib 17	4	0.5	1	20	4	70	25	70	25	79.36	11.81		
Calib 18	12	2	1	20	4	70	25	70	25	87.44	16.49		
Calib 19	4	4	1	20	4	70	70	70	25	71.98	10.16	121.19	10.65
Calib 20	4	4	1	20	4	70	25	70	70	63.11	10.00	116.23	9.90
Calib 21	4	4	1	20	4	70	70	100	25	88.38	10.17		
Calib 22	4	4	1	20	4	50	50	100	50	61.58	10.04	122.66	10.48

Calibration step	Parameters									UCS		$\sigma_3 = 20\ MPa$	
	E_c	k_n/k_s	μ	$\bar{E}_c$	$\bar{k}_n/\bar{k}_s$	$\bar{\sigma}_n$	$\Delta\bar{\sigma}_n$	$\bar{\sigma}_s$	$\Delta\bar{\sigma}_s$	σ_1	E	σ_1	E
	(GPa)	(FLT)	(FLT)	(GPa)	(FLT)	(MPa)	(MPa)	(MPa)	(MPa)	(MPa)	(GPa)	(MPa)	(GPa)
Calib 23	4	4	1	20	4	50	50	100	75	59.14	9.91	120.69	10.21
Calib 24	4	4	1	20	4	50	50	150	50	69.91	10.09	0.00	0.00
Calib 25	4	4	1	20	4	60	60	125	40	80.70	10.11		
Calib 26	4	4	1	20	4	70	70	70	20	75.11	10.22	122.03	10.84
Calib 27	4	4	1	20	4	70	70	70	30	69.76	10.09	119.32	10.47
Calib 28	4	4	1	20	4	70	60	70	25	70.21	10.18	118.52	10.64
Calib 29	4	3	1	20	4	70	70	70	20	77.80	10.55	128.35	11.27
Calib 30	4	5	1	20	4	70	70	70	20	73.65	10.12	118.44	10.70
Calib 31	4	4	2	20	4	70	70	70	20	77.41	10.29	126.02	10.85
Calib 32	4	4	4	20	4	70	70	90	20	91.47	10.31	146.45	10.93
Calib 33	4	4	2	20	4	45	45	190	20	66.22	10.20	150.41	10.76
Calib 34	4	4	2	20	4	45	45	190	40	66.31	10.20		
Calib 35	4	4	0.3	20	4	45	45	190	20	57.47	9.74		
Calib 36	8	4	2	20	4	70	70	70	20	88.77	12.64		
Calib 37	1	4	2	20	4	70	70	70	20	59.49	8.28	84.14	8.31
Calib 38	4	8	2	20	4	70	70	70	20	71.74	9.94	109.75	10.39
Calib 39	4	1	2	20	4	70	70	70	20	92.96	12.06		
Calib 40	4	4	2	20	4	70	70	90	20	89.84	10.28	122.03	10.84
Calib 41	3	4	4	20	4	70	70	90	20	87.35	9.62	134.89	10.04
Calib 42	4	4	4	20	4	60	60	90	20	82.51	10.32	140.71	10.91
Calib 43	4	4	4	20	4	50	50	100	20	72.70	10.23	140.45	10.87
Calib 44	4	4	4	20	4	48	48	110	20	70.94	10.23	143.98	10.84
Calib 45	4	4	4	20	4	48	48	110	40	67.27	10.22	134.23	10.73
Calib 46	4	4	4	20	4	48	48	110	60	63.99	10.14	130.32	10.46

Calibration step	Parameters									UCS		$\sigma_3 = 20\ MPa$	
	E_c	k_n/k_s	μ	$\bar{E}_c$	$\bar{k}_n/\bar{k}_s$	$\bar{\sigma}_n$	$\Delta\bar{\sigma}_n$	$\bar{\sigma}_s$	$\Delta\bar{\sigma}_s$	σ_1	E	σ_1	E
	(GPa)	(FLT)	(FLT)	(GPa)	(FLT)	(MPa)	(MPa)	(MPa)	(MPa)	(MPa)	(GPa)	(MPa)	(GPa)
Calib 47	4	4	40	20	4	48	48	110	60	65.10	10.14	131.73	10.47
Calib 48	4	4	40	20	4	48	48	150	60	71.42	10.23	145.65	10.71
Calib 49	4	4	40	20	4	48	48	150	150	65.40	10.10	137.95	10.29
Calib 50	4	4	40	20	4	48	24	110	60	56.21	10.43	130.32	10.46
Calib 51	4	4	40	20	4	48	0	110	60	60.69	10.55	120.92	10.68
Calib 52	4	4	40	20	4	48	48	200	80				
Calib 53	1	4	40	20	4	48	48	150	60				
Calib 54	8	4	40	20	4	48	48	150	60				
Calib 55	40	4	40	20	4	48	48	150	60				
Calib 56	4	4	1	20	4	48	48	150	60				
Calib 57	4	4	4	20	4	48	48	150	60				
Calib 58	4	1	40	20	4	48	48	150	60				
Calib 59	4	8	40	20	4	48	48	150	60				
Calib 60	4	4	40	20	4	48	40	150	60				
Calib 61	4	4	40	20	4	48	24	150	60				
Calib 62	4	4	40	20	4	48	36	150	60				
Calib 63	4	4	40	20	4	48	60	150	60	77.79	10.18	151.76	10.68
Calib 64	4	4	40	20	4	45	60	150	60	75.59	10.17	150.19	10.70
Calib 65	4	4	40	18	4	45	60	150	60				
Calib 66	4	4	40	18	4	44	70	150	60	82.82	9.39	160.44	9.94
Calib 67	4	4	40	18	4	43	80	150	60	89.19	9.36	167.36	9.92
Calib 68	4	4	40	16	4	40	80	150	60	87.15	8.61	168.40	9.19
Calib 69	4	4	4	16	4	40	70	150	60	80.63	8.62	161.38	9.20
Calib 70	4	4	4	16	4	43	80	130	60	84.88	8.59	161.61	9.10

Calibration step	Parameters									UCS		$\sigma_3 = 20\ MPa$	
	E_c	k_n/k_s	μ	$\bar{E}_c$	$\bar{k}_n/\bar{k}_s$	$\bar{\sigma}_n$	$\Delta\bar{\sigma}_n$	$\bar{\sigma}_s$	$\Delta\bar{\sigma}_s$	σ_1	E	σ_1	E
	(GPa)	(FLT)	(FLT)	(GPa)	(FLT)	(MPa)	(MPa)	(MPa)	(MPa)	(MPa)	(GPa)	(MPa)	(GPa)
Calib 71	4	4	4	16	4	40	80	130	60	83.32	8.60	159.53	9.10
Calib 72	4	5	4	16	4	37	80	120	60	76.41	8.40	147.48	8.86
Calib 73	4	3	4	16	4	35	80	120	60	84.11	8.89	165.74	9.47
Calib 74	5	4	4	16	4	40	80	110	60	82.71	9.18	159.61	9.78
Calib 75	4	4	4	16	4	35	80	130	60	81.78	8.55	156.98	9.11
Calib 76	4	3	4	16	4	33	80	110	60	82.09	8.90	160.54	9.38
Calib 77	4	3	4	16	4	30	70	120	60	76.50	8.95	158.36	9.48
Calib 78	4	3	4	16	4	33	75	110	55	79.41	8.94	157.35	9.44
Calib 79	4	3	4	16	4	33	80	110	60	78.74	9.00	160.66	9.51
Calib 80	4	3	4	16	4	28	70	120	60	75.18	8.90		
Calib 81	4	3	4	16	4	28	68	120	60	72.70	8.91		
Calib 82	4	2.9	4	16	4	26	70	120	60	73.47	8.96		
Calib 83	4	2.8	4	16	4	26	66	120	60	69.15	8.91	151.62	9.43
Calib 84	4	3	4	16	4	27	70	120	60	73.23	8.92		
Calib 85	4	3	4	16	4	26	70	120	60	73.71	8.93		
Calib 86	4	3	4	16	4	25	70	125	60	73.25	8.90		
Calib 87	4	3	4	16	4	25	70	130	60	74.04	8.92	158.77	9.49
Calib 88	4	3	4	16	4	24	70	130	60	74.21	8.92	160.41	9.50
Calib 89	4	3	4	16	4	23	70	130	60	74.27	8.92	159.68	9.52
Calib 90	4	3.2	4	16	4	23	70	128	60	72.67	8.78	154.23	9.36
Calib 91	4	2.8	4	16	4	23	70	128	60	72.90	8.90	157.11	9.51

B.3 Polyaxial simulation in 3D compared to experimental tests

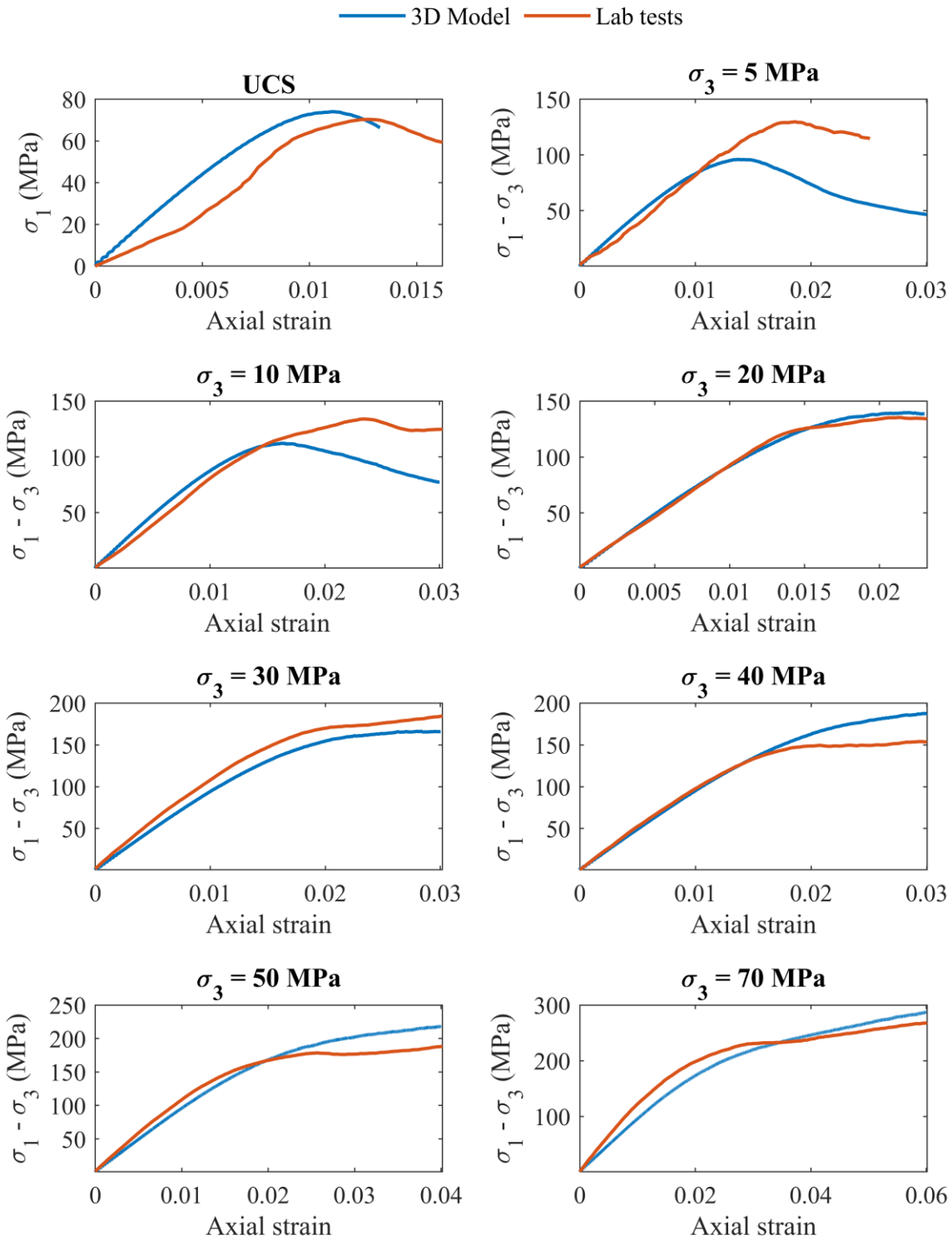

Appendix C: results of 3D numerical modeling

C.1 Results with sharp circular cutter

Depth of cut = 0.5 mm and back rake angle = 15°

Conf. (MPa)	ω_s (°)	A_c (mm²)	$\overline{F_t}$ (N)	Std $\overline{F_t}$	$\overline{F_n}$ (N)	Std $\overline{F_n}$	E (MPa)	M
0	0	1.71	181	55	181	40	106	1.00
5	0	1.71	408	73	291	215	239	1.41
10	0	1.71	526	109	421	106	308	1.25
20	0	1.71	794	136	539	90	465	1.47
30	0	1.71	1009	137	634	128	590	1.59
40	0	1.71	1134	110	690	90	664	1.64
0	5	1.70	199	53	232	172	117	0.86
10	5	1.70	569	86	420	311	334	1.36
20	5	1.70	800	106	560	415	470	1.43
30	5	1.70	978	143	632	468	575	1.55
40	5	1.70	1165	150	628	465	684	1.85
0	10	1.68	188	54	208	154	112	0.90
10	10	1.68	537	74	399	296	319	1.34
20	10	1.68	751	117	482	357	446	1.56
30	10	1.68	946	128	558	414	562	1.70
40	10	1.68	1081	122	647	480	642	1.67
0	20	1.61	186	34	201	149	116	0.93
10	20	1.61	469	68	354	263	292	1.32
20	20	1.61	678	77	447	331	422	1.52
30	20	1.61	838	118	586	434	522	1.43
40	20	1.61	1025	155	742	549	638	1.38
0	40	1.31	141	36	200	147	108	0.70
10	40	1.31	439	99	574	534	336	0.77
20	40	1.31	585	89	654	652	447	0.89
30	40	1.31	773	126	904	884	590	0.86
40	40	1.31	849	152	894	859	649	0.95
0	60	0.85	154	44	377	248	180	0.41
10	60	0.85	409	77	940	885	479	0.43
20	60	0.85	540	97	1136	1198	632	0.48
30	60	0.85	621	102	1162	1187	727	0.53
40	60	0.85	703	116	1113	1102	822	0.63

Depth of cut = 1 mm and back rake angle = 15°

Conf. (MPa)	ω_s **(°)**	**A_c (mm^2)**	$\overline{F_t}$ **(N)**	**Std** $\overline{F_t}$	$\overline{F_n}$ **(N)**	**Std** $\overline{F_n}$	**E (MPa)**	**M**
0	0	4.77	351	74	235	56	73	1.49
5	0	4.77	727	101	428	268	152	1.70
10	0	4.77	979	93	644	87	205	1.52
20	0	4.77	1452	156	870	118	304	1.67
30	0	4.77	1847	205	1147	152	387	1.61
40	0	4.77	2242	214	1449	166	470	1.55
0	5	4.75	346	76	245	135	73	1.41
10	5	4.75	957	126	606	378	201	1.58
20	5	4.75	1459	137	886	573	307	1.65
30	5	4.75	1731	186	1036	691	364	1.67
40	5	4.75	2207	262	1430	1067	464	1.54
0	10	4.70	357	53	253	139	76	1.41
10	10	4.70	944	115	639	399	201	1.48
20	10	4.70	1416	144	840	544	301	1.69
30	10	4.70	1769	165	1171	781	376	1.51
40	10	4.70	2223	226	1364	1018	473	1.63
0	20	4.49	340	60	279	153	76	1.22
10	20	4.49	906	107	584	365	202	1.55
20	20	4.49	1343	77	872	564	299	1.54
30	20	4.49	1689	272	1141	760	376	1.48
40	20	4.49	2079	211	1467	1095	463	1.42
0	40	3.66	325	48	435	264	89	0.75
10	40	3.66	926	128	1287	1085	253	0.72
20	40	3.66	1351	187	1638	1531	369	0.82
30	40	3.66	1709	209	1956	1778	467	0.87
40	40	3.66	1966	229	2101	1859	538	0.94
0	60	2.39	380	87	802	531	159	0.47
10	60	2.39	1256	156	2442	2139	526	0.51
20	60	2.39	1760	137	3645	3471	738	0.48
30	60	2.39	2132	213	3880	3609	893	0.55
40	60	2.39	2094	268	3805	3459	877	0.55

Depth of cut = 1.5 mm and back rake angle = 15°

Conf. (MPa)	ω_s (°)	A_c (mm²)	$\overline{F_t}$ (N)	Std $\overline{F_t}$	$\overline{F_n}$ (N)	Std $\overline{F_n}$	E (MPa)	M
0	0	8.66	610	83	394	63	70	1.55
5	0	8.66	1206	194	642	359	139	1.88
10	0	8.66	1539	166	864	133	178	1.78
20	0	8.66	2183	245	1177	128	252	1.85
30	0	8.66	2810	326	1470	213	325	1.91
40	0	8.66	3463	329	1880	242	400	1.84
0	5	8.62	612	128	414	207	71	1.48
10	5	8.62	1527	163	862	482	177	1.77
20	5	8.62	2214	288	1158	667	257	1.91
30	5	8.62	2826	311	1509	921	328	1.87
40	5	8.62	3419	270	1847	1199	396	1.85
0	10	8.53	619	90	396	198	73	1.56
10	10	8.53	1547	142	862	482	181	1.80
20	10	8.53	2203	206	1129	651	258	1.95
30	10	8.53	2740	210	1467	896	321	1.87
40	10	8.53	3642	305	1988	1291	427	1.83
0	20	8.13	592	97	410	205	73	1.45
10	20	8.13	1475	179	922	515	181	1.60
20	20	8.13	2089	169	1201	692	257	1.74
30	20	8.13	2615	298	1449	885	321	1.80
40	20	8.13	3416	264	2021	1312	420	1.69
0	40	6.63	666	94	899	545	100	0.74
10	40	6.63	1771	173	2745	2247	267	0.65
20	40	6.63	2461	280	3998	3587	371	0.62
30	40	6.63	2929	219	4531	3966	442	0.65
40	40	6.63	3487	252	4584	3918	526	0.76
0	60	4.33	709	83	1258	590	164	0.56
10	60	4.33	2153	186	4472	3824	497	0.48
20	60	4.33	3371	251	8296	8925	779	0.41
30	60	4.33	4331	384	8661	8707	1000	0.50
40	60	4.33	4810	450	8869	8367	1111	0.54

Depth of cut = 2 mm and back rake angle = 15°

Conf. (MPa)	ω_s (°)	A_c (mm²)	$\overline{F_t}$ (N)	Std $\overline{F_t}$	$\overline{F_n}$ (N)	Std $\overline{F_n}$	E (MPa)	M
0	0	13.15	963	149	543	84	73	1.77
5	0	13.15	1887	269	872	464	143	2.16
10	0	13.15	2361	243	1118	160	179	2.11
20	0	13.15	3482	272	1756	172	265	1.98
30	0	13.15	4069	513	2056	200	309	1.98
40	0	13.15	4959	437	2945	230	377	1.68
0	5	13.10	909	140	519	236	69	1.75
10	5	13.10	2265	197	1116	594	173	2.03
20	5	13.10	3261	332	1650	918	249	1.98
30	5	13.10	4016	401	1997	1211	307	2.01
40	5	13.10	5025	347	2860	1906	384	1.76
0	10	12.95	889	164	507	231	69	1.75
10	10	12.95	2195	221	1129	601	169	1.94
20	10	12.95	3284	366	1639	912	254	2.00
30	10	12.95	4002	345	2128	1290	309	1.88
40	10	12.95	5069	298	2986	1991	391	1.70
0	20	12.36	885	166	574	261	72	1.54
10	20	12.36	2141	168	1237	659	173	1.73
20	20	12.36	3171	210	1779	990	256	1.78
30	20	12.36	4011	305	2269	1376	325	1.77
40	20	12.36	5003	277	3113	2075	405	1.61
0	40	10.08	718	90	877	335	71	0.82
10	40	10.08	2082	141	2812	1636	207	0.74
20	40	10.08	3151	195	4399	2946	313	0.72
30	40	10.08	3975	169	4948	3189	394	0.80
40	40	10.08	4976	318	5887	3657	494	0.85
0	60	6.58	1158	105	1774	818	176	0.65
10	60	6.58	3421	304	6213	5214	520	0.55
20	60	6.58	4864	432	10028	10588	740	0.49
30	60	6.58	6277	475	11583	11428	954	0.54
40	60	6.58	7453	462	12302	11391	1133	0.61

Depth of cut = 1 mm and back rake angle = 30°

Conf. (MPa)	ω_s (°)	A_c (mm²)	$\overline{F_t}$ (N)	Std $\overline{F_t}$	$\overline{F_n}$ (N)	Std $\overline{F_n}$	E (MPa)	M
0	0	5.03	523	92	530	92	104	0.99
10	0	5.03	1419	211	1308	195	282	1.09
20	0	5.03	2137	324	1924	282	425	1.11
30	0	5.03	2609	276	2306	250	519	1.13
40	0	5.03	3225	386	2978	439	642	1.08

Depth of cut = 1 mm and back rake angle = 45°

Conf. (MPa)	ω_s (°)	A_c (mm²)	$\overline{F_t}$ (N)	Std $\overline{F_t}$	$\overline{F_n}$ (N)	Std $\overline{F_n}$	E (MPa)	M
0	0	5.53	862	101	1231	135	156	0.70
10	0	5.53	2208	211	2872	235	399	0.77
20	0	5.53	3234	282	3936	277	585	0.82
30	0	5.53	3865	336	4669	345	699	0.83
40	0	5.53	4671	492	6174	552	845	0.76

Depth of cut = 2 mm and back rake angle = 30°

Conf. (MPa)	ω_s (°)	A_c (mm²)	$\overline{F_t}$ (N)	Std $\overline{F_t}$	$\overline{F_n}$ (N)	Std $\overline{F_n}$	E (MPa)	M
0	0	13.81	1542	267	1231	230	112	1.25
10	0	13.81	3715	438	2812	370	269	1.32
20	0	13.81	5139	619	3764	375	372	1.37
30	0	13.81	6485	803	5040	458	470	1.29
40	0	13.81	7171	606	6058	402	519	1.18

Depth of cut = 2 mm and back rake angle = 45°

Conf. (MPa)	ω_s (°)	A_c (mm²)	$\overline{F_t}$ (N)	Std $\overline{F_t}$	$\overline{F_n}$ (N)	Std $\overline{F_n}$	E (MPa)	M
0	0	15.07	2434	531	2791	511	162	0.87
10	0	15.07	5905	866	6334	613	392	0.93
20	0	15.07	7892	1322	8102	869	524	0.97
30	0	15.07	9220	1408	10076	1154	612	0.91
40	0	15.07	10427	1204	12802	1031	692	0.81

Depth of cut = 0.75 mm and back rake angle = 15°

Conf. (MPa)	ω_s (°)	A_c (mm²)	$\overline{F_t}$ (N)	Std $\overline{F_t}$	$\overline{F_n}$ (N)	Std $\overline{F_n}$	E (MPa)	M
0.1	0	3.12	254	46	170	93	81	1.49
5	0	3.12	580	107	388	242	186	1.49
10	0	3.12	758	100	472	295	243	1.61
20	0	3.12	1103	144	647	417	354	1.71
30	0	3.12	1388	195	814	543	445	1.71
40	0	3.12	1767	137	1091	814	567	1.62

Depth of cut = 1.25 mm and back rake angle = 15°

Conf. (MPa)	ω_s (°)	A_c (mm²)	$\overline{F_t}$ (N)	Std $\overline{F_t}$	$\overline{F_n}$ (N)	Std $\overline{F_n}$	E (MPa)	M
0.1	0	6.63	457	69	333	183	69	1.37
5	0	6.63	993	126	614	384	150	1.62
10	0	6.63	1188	129	746	466	179	1.59
20	0	6.63	1850	171	1121	726	279	1.65
30	0	6.63	2315	233	1340	894	349	1.73
40	0	6.63	2886	150	1781	1329	435	1.62

Depth of cut = 1.75 mm and back rake angle = 15°

Conf. (MPa)	ω_s (°)	A_c (mm²)	$\overline{F_t}$ (N)	Std $\overline{F_t}$	$\overline{F_n}$ (N)	Std $\overline{F_n}$	E (MPa)	M
0.1	0	10.84	744	173	459	229	69	1.62
5	0	10.84	1542	240	850	475	142	1.81
10	0	10.84	1922	185	1050	587	177	1.83
20	0	10.84	2826	209	1553	895	261	1.82
30	0	10.84	3347	289	1713	1046	309	1.95
40	0	10.84	4067	272	2304	1496	375	1.77

Depth of cut = 2.5 mm and back rake angle = 15°

Conf. (MPa)	**ω_s (°)**	**A_c (mm^2)**	**$\overline{F_t}$ (N)**	**Std $\overline{F_t}$**	**$\overline{F_n}$ (N)**	**Std $\overline{F_n}$**	**E (MPa)**	**M**
0.1	0	15.07	1413	199	733	333	78	1.93
5	0	15.07	2749	370	1372	730	152	2.00
10	0	15.07	3355	410	1734	923	185	1.93
20	0	15.07	4768	353	2367	1316	263	2.01
30	0	15.07	5802	396	3126	1896	320	1.86
40	0	15.07	6906	540	4034	2689	381	1.71

C.2 Results with chamfered circular cutter

Depth of cut = 1 mm, back rake angle = 15°, and side rake angle = 0°

ω_{ch} (°)	L_{ch} (mm)	Conf. (MPa)	$\overline{F_t}$ (N)	Std $\overline{F_t}$	$\overline{F_n}$ (N)	Std $\overline{F_n}$	E (MPa)	M
15	0.25	0	345	81	316	107	72	1.1
15	0.25	10	915	177	713	185	192	1.3
15	0.25	20	1399	150	898	97	293	1.6
15	0.25	40	2575	154	1909	153	539	1.3
30	0.25	0	385	67	389	97	81	1.0
30	0.25	10	1001	198	924	184	210	1.1
30	0.25	20	1608	188	1499	196	337	1.1
30	0.25	40	2289	181	1904	205	480	1.2
45	0.25	0	384	97	420	122	80	0.9
45	0.25	10	966	127	962	187	202	1.0
45	0.25	20	1602	173	1586	294	336	1.0
45	0.25	40	2239	211	2387	192	469	0.9
60	0.25	0	379	68	413	88	79	0.9
60	0.25	10	929	123	961	165	195	1.0
60	0.25	20	1424	206	1431	203	298	1.0
60	0.25	40	2259	246	2295	245	473	1.0
15	0.5	0	333	90	306	110	70	1.1
15	0.5	10	979	129	751	91	205	1.3
15	0.5	20	1417	227	1074	165	297	1.3
15	0.5	40	2311	192	2006	197	484	1.2
30	0.5	0	423	89	459	103	89	0.9
30	0.5	10	1183	134	1192	165	248	1.0
30	0.5	20	1771	151	1664	150	371	1.1
30	0.5	40	2698	287	2526	263	565	1.1
45	0.5	0	470	97	685	123	99	0.7
45	0.5	10	1172	151	1537	194	246	0.8
45	0.5	20	1730	209	1968	167	362	0.9
45	0.5	40	2602	227	3312	201	545	0.8
60	0.5	0	408	61	621	110	86	0.7
60	0.5	10	1059	96	1443	138	222	0.7
60	0.5	20	1559	152	2204	252	327	0.7
60	0.5	40	2337	249	3610	305	490	0.6

Depth of cut = 2 mm, back rake angle = 15°, and side rake angle = 0°

ω_{ch} (°)	L_{ch} (mm)	Conf. (MPa)	$\overline{F_t}$ (N)	Std $\overline{F_t}$	$\overline{F_n}$ (N)	Std $\overline{F_n}$	E (MPa)	M
15	0.25	0	868	190	485	106	66	1.8
15	0.25	10	2335	381	1386	204	178	1.7
15	0.25	20	3630	456	2176	346	276	1.7
15	0.25	40	4981	395	3133	194	379	1.6
30	0.25	0	934	147	633	123	71	1.5
30	0.25	10	2179	237	1317	150	166	1.7
30	0.25	20	3405	181	2046	117	259	1.7
30	0.25	40	5098	352	3356	154	388	1.5
45	0.25	0	933	239	669	217	71	1.4
45	0.25	10	2363	213	1673	172	180	1.4
45	0.25	20	3387	308	2320	227	257	1.5
45	0.25	40	5443	166	4295	377	414	1.3
60	0.25	0	926	161	682	124	70	1.4
60	0.25	10	2403	219	1875	225	183	1.3
60	0.25	20	3140	332	2123	279	239	1.5
60	0.25	40	5242	465	3878	315	399	1.4
15	0.5	0	988	264	640	214	75	1.5
15	0.5	10	2436	158	1461	65	185	1.7
15	0.5	20	3564	476	2215	337	271	1.6
15	0.5	40	5387	382	3276	271	409	1.6
30	0.5	0	996	200	783	137	76	1.3
30	0.5	10	2423	206	1736	200	184	1.4
30	0.5	20	3647	292	2489	83	277	1.5
30	0.5	40	5633	364	4301	248	428	1.3
45	0.5	0	1000	146	885	140	76	1.1
45	0.5	10	2364	212	2025	203	180	1.2
45	0.5	20	3658	417	2995	367	278	1.2
45	0.5	40	5547	564	4892	610	422	1.1
60	0.5	0	1013	163	1049	153	77	1.0
60	0.5	10	2346	198	2259	275	178	1.0
60	0.5	20	3472	342	3456	210	264	1.0
60	0.5	40	5374	293	5259	394	409	1.0

Depth of cut = 0.5 mm, back rake angle = 15°, and side rake angle = 0°

ω_{ch} (°)	L_{ch} (mm)	Conf. (MPa)	$\overline{F_t}$ (N)	Std $\overline{F_t}$	$\overline{F_n}$ (N)	Std $\overline{F_n}$	E (MPa)	M
45	0.25	0	211	63	359	98	123	0.59
45	0.25	10	558	121	724	186	327	0.77
45	0.25	20	709	114	844	181	415	0.84
45	0.25	40	1031	212	1072	141	603	0.96
45	0.5	0	260	72	521	139	152	0.50
45	0.5	10	594	96	862	137	348	0.69
45	0.5	20	792	110	1267	104	464	0.63
45	0.5	40	1170	139	1945	209	685	0.60

Depth of cut = 1.5 mm, back rake angle = 15°, and side rake angle = 0°

ω_{ch} (°)	L_{ch} (mm)	Conf. (MPa)	$\overline{F_t}$ (N)	Std $\overline{F_t}$	$\overline{F_n}$ (N)	Std $\overline{F_n}$	E (MPa)	M
45	0.25	0	621	97	540	112	72	1.15
45	0.25	10	1669	179	1286	188	193	1.30
45	0.25	20	2329	231	1759	116	269	1.32
45	0.25	40	3411	330	2600	176	394	1.31
45	0.5	0	720	78	827	118	83	0.87
45	0.5	10	1868	229	1751	167	216	1.07
45	0.5	20	2574	220	2368	193	297	1.09
45	0.5	40	4089	271	4086	297	472	1.00

C.3 Results with sharp rectangular cutter

Back rake angle = 15° and side rake angle = 0°

DOC (mm)	Conf. (MPa)	A_c (mm^2)	$\overline{F_t}$ (N)	Std $\overline{F_t}$	$\overline{F_n}$ (N)	Std $\overline{F_n}$	E (MPa)	M
0.5	0	5	425	97	381	98	85	1.12
0.5	10	5	1116	148	794	116	223	1.41
0.5	20	5	1670	183	1057	231	334	1.58
0.5	40	5	2412	161	1403	161	482	1.72
1	0	10	646	119	449	110	65	1.44
1	10	10	1663	115	1021	49	166	1.63
1	20	10	2384	280	1264	211	238	1.89
1	40	10	3818	290	2131	211	382	1.79
1.5	0	15	977	173	594	97	65	1.64
1.5	10	15	2481	287	1199	166	165	2.07
1.5	20	15	3505	302	1759	132	234	1.99
1.5	40	15	5446	403	2609	288	363	2.09
2	0	20	1331	71	660	50	67	2.01
2	10	20	3351	322	1610	180	168	2.08
2	20	20	4904	416	2284	192	245	2.15
2	40	20	7038	411	3749	434	352	1.88

C.4 Results with chamfered rectangular cutter

Depth of cut = 1 mm, back rake angle = 15°, and side rake angle = 0°

ω_{ch} (°)	L_{ch} (mm)	Conf. (MPa)	$\overline{F_t}$ (N)	Std $\overline{F_t}$	$\overline{F_n}$ (N)	Std $\overline{F_n}$	E (MPa)	M
30	0.25	0	713	84	630	110	71	1.13
30	0.25	10	1770	211	1282	178	177	1.38
30	0.25	20	2617	213	1959	390	262	1.34
30	0.25	40	4064	331	3007	279	406	1.35
45	0.25	0	699	133	688	180	70	1.02
45	0.25	10	1774	233	1486	154	177	1.19
45	0.25	20	2449	217	1736	195	245	1.41
45	0.25	40	3848	392	2803	191	385	1.37
60	0.25	0	635	112	558	134	63	1.14
60	0.25	10	1647	159	1234	200	165	1.33
60	0.25	20	2496	269	1766	226	250	1.41
60	0.25	40	3832	301	2853	284	383	1.34
30	0.5	0	748	98	752	120	75	0.99
30	0.5	10	1861	242	1661	335	186	1.12
30	0.5	20	2800	338	2173	219	280	1.29
30	0.5	40	4217	349	3667	289	422	1.15
45	0.5	0	575	111	687	118	57	0.84
45	0.5	10	1946	208	1938	237	195	1.00
45	0.5	20	2611	232	2353	142	261	1.11
45	0.5	40	3838	376	3356	551	384	1.14
60	0.5	0	690	145	827	244	69	0.83
60	0.5	10	1663	212	1455	275	166	1.14
60	0.5	20	2562	258	2321	374	256	1.10
60	0.5	40	3801	280	3072	461	380	1.24

Depth of cut = 2 mm, back rake angle = 15°, and side rake angle = 0°

ω_{ch} (°)	L_{ch} (mm)	Conf. (MPa)	$\overline{F_t}$ (N)	Std $\overline{F_t}$	$\overline{F_n}$ (N)	Std $\overline{F_n}$	E (MPa)	M
30	0.25	0	1465	251	941	185	73	1.56
30	0.25	10	3442	282	1996	140	172	1.72
30	0.25	20	4844	325	2574	307	242	1.88
30	0.25	40	7842	283	4641	240	392	1.69
45	0.25	0	1397	204	907	165	70	1.54
45	0.25	10	3487	419	2033	268	174	1.71
45	0.25	20	4987	311	2777	220	249	1.80
45	0.25	40	7476	486	4566	305	374	1.64
60	0.25	0	1338	317	817	166	67	1.64
60	0.25	10	3257	122	1927	146	163	1.69
60	0.25	20	4874	236	2608	187	244	1.87
60	0.25	40	7627	254	4581	319	381	1.66
30	0.5	0	1506	228	1126	140	75	1.34
30	0.5	10	3487	319	2250	211	174	1.55
30	0.5	20	5187	178	3000	160	259	1.73
30	0.5	40	8237	511	5411	488	412	1.52
45	0.5	0	1349	225	1081	163	67	1.25
45	0.5	10	3725	262	2756	211	186	1.35
45	0.5	20	5067	356	3318	240	253	1.53
45	0.5	40	7737	571	5325	393	387	1.45
60	0.5	0	1353	270	982	220	68	1.38
60	0.5	10	3420	208	2164	151	171	1.58
60	0.5	20	4925	370	3169	331	246	1.55
60	0.5	40	7635	461	4653	240	382	1.64

Depth of cut = 0.5 mm, back rake angle = 15°, and side rake angle = 0°

ω_{ch} (°)	L_{ch} (mm)	Conf. (MPa)	$\overline{F_t}$ (N)	Std $\overline{F_t}$	$\overline{F_n}$ (N)	Std $\overline{F_n}$	E (MPa)	M
45	0.25	0	438	101	697	144	88	0.63
45	0.25	10	1129	160	1194	145	226	0.95
45	0.25	20	1616	185	1492	182	323	1.08
45	0.25	40	2320	218	1805	173	464	1.29
45	0.5	0	377	64	687	153	75	0.55
45	0.5	10	1179	172	1510	238	236	0.78
45	0.5	20	1742	201	2058	220	348	0.85
45	0.5	40	2370	247	2453	271	474	0.97

Depth of cut = 1.5 mm, back rake angle = 15°, and side rake angle = 0°

ω_{ch} (°)	L_{ch} (mm)	Conf. (MPa)	$\overline{F_t}$ (N)	Std $\overline{F_t}$	$\overline{F_n}$ (N)	Std $\overline{F_n}$	E (MPa)	M
45	0.25	0	1013	192	775	189	68	1.31
45	0.25	10	2368	125	1661	126	158	1.43
45	0.25	20	3583	302	2084	223	239	1.72
45	0.25	40	5888	621	3680	545	393	1.60
45	0.5	0	910	175	842	170	61	1.08
45	0.5	10	2518	160	1994	196	168	1.26
45	0.5	20	3803	404	2695	217	254	1.41
45	0.5	40	5881	490	4319	353	392	1.36

C.5 Results with blunt rectangular cutter

Back rake angle = 15° and side rake angle = 0°

L_m (mm)	DOC (mm)	Conf. (MPa)	$\overline{F_t}$ (N)	Std $\overline{F_t}$	$\overline{F_n}$ (N)	Std $\overline{F_n}$	E (MPa)	M
0.5	1	0	671	144	523	134	67	1.28
1	1	0	658	111	564	128	66	1.17
2	1	0	696	119	768	119	70	0.91
0.5	1	10	1684	183	1187	120	168	1.42
1	1	10	1763	234	1594	205	176	1.11
2	1	10	1845	136	1905	155	184	0.97
0.5	1	20	2563	200	1978	166	256	1.30
1	1	20	2672	225	2274	201	267	1.17
2	1	20	2785	267	2850	258	279	0.98
0.5	1	40	3829	455	2902	313	383	1.32
1	1	40	4040	263	3315	265	404	1.22
2	1	40	4346	257	4558	257	435	0.95
0.5	2	0	1370	165	854	123	68	1.60
1	2	0	1508	264	1028	170	75	1.47
2	2	0	1529	232	1221	128	76	1.25
0.5	2	10	3649	243	2286	218	182	1.60
1	2	10	3482	406	2472	202	174	1.41
2	2	10	3704	257	3073	174	185	1.21
0.5	2	20	5093	464	2943	272	255	1.73
1	2	20	5071	362	3436	267	254	1.48
2	2	20	5156	278	3890	264	258	1.33
0.5	2	40	7398	423	4848	453	370	1.53
1	2	40	8007	543	5716	479	400	1.40
2	2	40	8098	444	6322	348	405	1.28